PhD Thesis

COLLECTIVE ELECTRONIC AND MAGNETIC STATES IN TWO-DIMENSIONAL TRANSITION METAL DICHALCOGENIDES

Paul Dreher

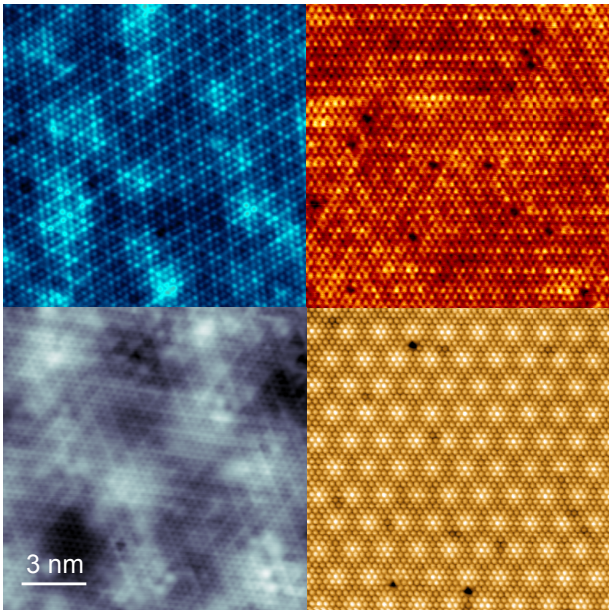

Thesis Supervisor:

Miguel Moreno Ugeda

eman ta zabal zazu

Universidad del País Vasco

Euskal Herriko Unibertsitatea

Acknowledgement

Throughout the experimental work and the writing of this dissertation I have received a great deal of support and assistance.

I would first like to express my sincere gratitude to my supervisor, Dr. Miguel M. Ugeda, whose expertise and positive mindset has truly inspired me and paved the way for this thesis. Thank you for your profound explanations on fundamental physical processes and everything you taught me about scientific writing and presenting the results at conferences. Your sharp feedback and honesty has shaped me as a researcher and also as a person outside of the laboratory.

I would like to express my special thanks of gratitude to Dr. Martina Corso and Dr. Sara Barja for their patient support and for the incredible amount of things they taught me about ultra high vacuum technology and low temperature STM, especially in my first year at CFM. Although, the STM machine we used at that time gave me many sleepless nights, your positive energy and enthusiasm kept me trying and learning about the most fundamental technical aspects of scanning tunneling microscopy, which was crucial when finally the new STM system arrived. I also would like to mention Dr. Javier Zaldivar, who introduced me to atomic force microscopy and who was a great support to me getting familiar with AFM/STM and the PhD research life.

I would like to thank Prof. Peter Liljeroth for giving me the opportunity to perform a three month research stay in his highly sophisticated laboratory at Aalto University. It was truly an incredible experience to learn from you and your amazing team of postdocs and students Shawulienu, Nurul and Benjamin.

My sincere thanks go to Dr. Wen Wan, whos dedication and motivation have been a true inspiration. Thank you for teaching me so many things about 2D materials growth and the laboratory techniques in general. Your many insightful ideas and how you describe ongoing dynamics at the nanoscale have changed my way of understanding our observations several times and have genuinely helped me on this path of becoming an independent researcher.

I would like to thank Dr. Rishav Harsh for his enthusiasm and appreciation of the most fundamental details in the experiments. Your thoughts have initiated me to reflect our data many times and were really helpful to understand very important specifics about our observations.

In addition, I would like to thank my friends outside of the laboratory and especially everybody from the Cuadrilla who have always supported me and made these years a wonderful experience. Mathias, Joscha, Stefan and Gabriele thank you for the endless surfing adventures. It was amazing. Coralie, Sara, Fernando, Alvaro, Virginia, Sahsil, Yaiza, Silvia, Emilie, thank you for the many fun nights out and the many trips we did together. Sara, thank you for introducing me to the bright side of Bilbao during stressful times writing this thesis. Severin, Erik and Sebastian, thank you for the many funny online meetings and workouts during the lockdowns, which kept me sane and in shape.

Finally, I would like to thank my grandparents Martha and Gerhard, Berta and Ernst for shaping me and helping me get here to this moment where I'm writing these words. I want to give a special thanks to my aunt and very good friend Sabine, who has been an inspiration to me all my life and without whom I would definitely not have come all the way. Lastly, I would like to thank my parents Ingrid and Wolfgang who are the most important mental support and helped me with a lot of good advices during these exciting times.

Resumen

Esta tesis presenta un desarrollo experimental en el que se han estudiado diversas fases electrónicas y magnéticas colectivas tales como la superconductividad, ondas de densidad de carga (CDW por sus siglas en inglés, charge density wave) y correlaciones de espín en dicalcogenuros de metales de transición (TMD, transition metal dichalcogenides) en el límite último de la monocapa.

El trabajo realizado en esta tesis tiene como punto de partida el crecimiento de estas monocapas atómicas de alta calidad mediante epitaxia de haces moleculares (MBE por sus siglas en inglés, molecular beam epitaxy) en condiciones controladas de ultra alto vacío. El proceso de crecimiento ha requerido de la optimización cristalina para cada material para lo cual se han usado técnicas como la difracción de electrones de alta energía por reflexión (RHEED por sus siglas en inglés, reflection high-energy electron diffraction) y la microscopía de fuerzas atómicas. Este proceso ha sido necesario llevarlo a cabo para cada distinto tipo de substrato sobre los que se han crecido estos materiales. En particular para esta tesis se han crecido monocapas de $NbSe_2$, $TaSe_2$ y $TiSe_2$, así como monocapas de aleaciones aliovalentes de $Nb_{1-\delta}Mo_\delta Se_2$ y $Ta_{1-\delta}W_\delta Se_2$. Los substratos usados han dependido del tipo de fenomenología buscada, pero los más habituales han sido el grafeno sobre SiC(0001), TMDs en volumen como el WSe_2, y superficies de metales de transición como el Au(111).

La técnica experimental principal para el desarrollo de esta tesis ha sido la microscopía y espectroscopia de efecto túnel de baja temperatura (340 mK) y altos campos magnéticos (11 T) en condiciones de ultra alto vacío. Esta técnica es conocida como STM/STS (scanning tunneling microscopy/spectroscopy). El STM nos ha permitido obtener imágenes topográficas con resolución atómica, así como medidas espectroscópicas de alta precisión energética ($\sim 100\,\mu$V) de estas monocapas bajo estudio. Además, la posibilidad de realizar estas medidas a temperaturas extremadamente bajas de 340 mK en combinación con la aplicación de altos campos magnéticos de hasta 11 T nos ha ayudado a acceder al estudio y mejor comprensión de las fases electrónicas colectivas en estos nuevos materiales bidimensionales. Las medidas de STM/STS han sido complementadas en la práctica totalidad de los experimentos descritos en esta tesis mediante otras técnicas experimentales, entre las cuales cabe destacar la espectroscopia de fotoemisión resuelta angularmente (ARPES, angle-resolved photoemission spectroscopy), el dicroísmo circular magnético de rayos-X (XMCD, X-ray magnetic circular dichroism). Asimismo, las evidencias experimentales han sido generalmente complementadas con un marco teórico con cálculos analíticos y/o ab-initio basados en la teoría del funcional de la densidad. El uso de todas estas técnicas comple-

mentarias se ha llevado a cabo en el marco de colaboraciones científicas, tal y como se detalla en la tesis en cada caso.

En el capítulo 3 de la tesis estudiamos primeramente la monocapa de $NbSe_2$. Mediante STS a 340 mK se ha caracterizado el espectro de las cuasipartículas en este sistema, así como su comportamiento con la temperatura y el campo magnético. Esto ha permitido demostrar la aparición de modos colectivos en este material correlacionado, un escenario natural para este tipo de fenómenos en el estado superconductor. Las medidas de espectroscopia STS de alta resolución verifican directamente la existencia de estos modos en el espectro de cuasipartículas. Nuestras observaciones experimentales quedan respaldadas por un modelo teórico basado en la competición entre el estado fundamental singlete (s-wave) y un triplete f-wave de mayor energía. Esta interpretación captura dos observaciones experimentales clave de nuestros experimentos, esto es, la aparición de picos en el espectro de cuasipartículas por debajo de la temperatura crítica, así como la anticorrelación observada entre la energía de los modos colectivos y el gap superconductor. La observación de modos colectivos superconductores en esta familia de materiales bidimensionales proporciona información clave sobre nuestra limitada comprensión de los mecanismos microscópicos de la superconductividad en dos dimensiones. La existencia de modos de tipo Leggett pone de manifiesto la aparición de propiedades no convencionales en el estado superconductor en los TMDs en el límite bidimensional. Además, este trabajo abre nuevas vías para la exploración de la superconductividad no convencional en entornos inexplorados mediante la combinación de monocapas de TMD con, por ejemplo, sustratos magnéticos que podrían dar lugar a fenómenos como la superconductividad topológica.

En un trabajo posterior, también en monocapas de $NbSe_2$, realizamos un estudio comparativo de las propiedades de sus fases colectivas (CDW y superconductividad) en paralelo a su estructura electrónica en cuatro substratos de naturaleza marcadamente distinta: bicapa de grafeno (BLG, bilayer graphene), monocapa de h-BN, Au(111) y WSe_2. Cada uno de los substratos representa una familia de las superficies más típicas utilizadas para el crecimiento epitaxial de metales 2D y su posterior investigación. En este caso combinamos medidas de STM/STS a 340 mK y ARPES para demostrar que, incluso cuando la estructura electrónica no se ve afectada en gran medida por el sustrato, excepto en Au(111) donde se produce una transferencia de carga, tanto la CDW como la superconductividad muestran un comportamiento dispar. En primer lugar, la CDW y la superconductividad en la monocapa de $NbSe_2$ tienen propiedades casi idénticas sobre el aislante h-BN y sobre la bicapa de grafeno. Por el contrario, estas fases electrónicas están ausentes (o muy debilitadas) sobre el substrato aislante WSe2 y sobre el Au(111) metálico. De particular interés es el caso de la heteroestructura $NbSe_2/WSe_2$, donde la superconductividad está sorprendentemente ausente a 340 mK, mientras que la CDW persiste, aunque muy deprimida en comparación con los sustratos BLG y h-BN a pesar de que todos comparten estructuras electrónicas casi idénticas. Nuestros resultados describen claramente el fuerte impacto de los efectos de proximidad inducidos por el sustrato en las fases colectivas de un sistema modelo correlacionado en dos dimensiones. Es destacable el hecho de que los sustratos de grafeno dopado juegan un papel insignificante en las propiedades electrónicas del metal 2D TMD, como lo

demuestra la comparación directa con el caso aislante h-BN. Además, el gran impacto de un sustrato TMD semiconductor observado en las fases CDW superconductora es un resultado inesperado cuyo origen queda aún abierto para futuras investigaciones. Por último, este trabajo proporciona una guía fundamental para la elección de sustratos adecuados en futuras investigaciones centradas en aspectos fundamentales de estas fases colectivas en 2D. El capítulo 4 de la tesis está centrado en el estudio del crecimiento y posterior caracterización electrónica de aleaciones TMD bidimensionales. En particular, se han estudiado dos aleaciones aliovalentes, monocapas de $Nb_{1-\delta}Mo_{\delta}Se_2$ y $Ta_{1-\delta}W_{\delta}Se_2$. El trabajo expuesto en este capítulo demuestra la viabilidad de la síntesis y la estabilidad de aleaciones aliovalentes de tipo TMD en el límite de la monocapa en todo el rango de composición. Además, se presenta la primera caracterización a escala atómica de la evolución del estado fundamental electrónico (tanto la estructura electrónica como el comportamiento de las fases electrónicas colectivas) de estos superconductores Ising bidimensionales en presencia de desorden estructural.

Para el caso de las monocapas de monocapas de $Nb_{1-\delta}Mo_{\delta}Se_2$, se han combinado medidas de STM/STS con cálculos de primeros principios para explorar tres transiciones de fase 2D diferentes, a saber, superconductor-metal, CDW-metal y metal-semiconductor. Nuestras medidas revelan una robustez inesperada de las fases CDW y superconductora frente al desorden (proporcional a la concentración de Mo, δ) en la monocapa, así como una sorprendente evolución no-monótona ésta última con el desorden, que se ve inicialmente reforzada para concentraciones diluidas de dopantes de Mo debido a la disminución de las fluctuaciones espín. Además, experimentalmente se comprueba que el CDW se debilita con el aumento del desorden debido a la pérdida gradual del orden 3x3 de largo alcance que, a su vez, es producto de la proliferación de fronteras de dominio CDW. Por último, la transición metal-semiconductor se observa para concentraciones de Nb del 25% ($\delta = 0{,}75$), lo que demuestra un amplio rango de variabilidad del gap electrónico de hasta 2.2 eV hasta la monocapa de MoSe2, lo cual es de relevancia de cara a la ingeniería de materiales para dispositivos electrónicos de baja dimensionalidad.

Con respecto a los experimentos realizados en monocapas de $Ta_{1-\delta}W_{\delta}Se_2$, estos demuestran primeramente la ausencia de superconductividad en la monocapa de $TaSe_2$ (politipo H). Sin embargo, mediante un ligerísimo dopaje de este material con átomos de W, la monocapa evoluciona al estado superconductor. La dependencia de la temperatura y el campo magnético del estado superconductor de esta aleación 2D en función del dopaje electrónico (δ) revela la aparición de un dome superconductor en el diagrama de fases con una temperatura crítica maximizada de 0.85 K, lo cual representa un aumento significativo de la de $TaSe_2$ en fase volumen ($T_c = 0.14$ K). La superconductividad se debe a un aumento de la densidad de estados a medida que la superficie de Fermi se aproxima debido al dopaje a una singularidad de van Hove en la estructura de bandas. Sin embargo, una vez que se alcanza la singularidad, la densidad de estados disminuye con δ, lo que debilita gradualmente el estado superconductor, dando forma así al dome superconductor. Por último, nuestras mediciones también nos permiten identificar y observar el desarrollo de una fase de vítrea de tipo Coulomb debida al aumento gradual de desorden en el sistema.

El capítulo 5 de la tesis, se centra en el estudio de las propiedades electrónicas y magnéticas de la monocapa de $TaSe_2$ en el politipo T, la cual no es metálica sino semiconductora. En particular estudiamos la estructura electrónica de esta monocapa así como su textura orbital con el fin de obtener información acerca del origen del gap electrónico observado. Nuestras medidas, en combinación con cálculos de primeros principios en $TaSe_2$/grafeno sugieren que el estado semiconductor no se debe a correlaciones electrónicas de tipo Mott. Asimismo, estudiamos las propiedades electrónicas y magnéticas de esta monocapa sobre un substrato metálico, la monocapa de $TaSe_2$ en la fase H. En este caso, la homobicapa 1T-$TaSe_2$/1H-$TaSe_2$ resulta ser un sistema realmente intrigante. Nuestra medidas de STS a 340 mK revelan la existencia de dos picos en la densidad de estados al nivel de Fermi y separados por $\sim$1 meV. La evolución de estos picos con la temperatura y el campo magnético (especialmente para campos bajos) descarta la aparición de fermiones pesados en una red de tipo Kondo y, en cambio, sugiere la aparición de orden magnético débil a largo alcance. Cálculos analíticos confirman este escenario.

El último capítulo de la tesis, el capítulo 6, presenta la caracterización estructural y electrónica de la monocapa de $TiSe_2$, un sistema que presenta una CDW con orden 2x2 sin ser magnético en el límite 2D. En particular, en este trabajo se sintetizan y analizan estas monocapas en dos substratos distintos, esto es, en la bicapa de grafeno y en WSe_2. Mientras que en grafeno este sistema retiene la CDW 2x2, en WSe_2, este orden se pierde, al igual que ocurre con la monocapa de $NbSe_2$. La estructura electrónica medida con STS, sin embargo, si bien presenta diferencias apreciables, cualitativamente son similares. Por último, en TiSe2 sobre grafeno, se visualiza la existencia de fronteras de dominios CDW, las cuales desaparecen en $TiSe_2$ sobre WSe_2.

Abstract

Single-layer (SL) transition metal dichalcogenide (TMD) materials possess a variety of collective electronic phases such as superconductivity (SC), charge density wave (CDW) order, and magnetic correlations, which exhibit fascinating properties in the confined space of two dimensions. In these layered materials electron-electron interactions are enhanced, which can trigger novel physical phenomena. In particular, the most fundamental properties and intrinsic parameters such as the critical temperatures (T_c) of these phases are strongly modified in most cases when reducing the dimension. Furthermore, the interplay of the electronic phases becomes crucial. Important questions on the pairing symmetry in 2D-TMD superconductors and the stability of these phases to external perturbations such as magnetic fields and doping atoms remain elusive.

This thesis presents an atomic-scale study of the collective electronic states present in selected novel TMD materials in the ultimate single-layer limit. Molecular beam epitaxy is deployed to grow highly crystalline single-layer materials and more complex TMD heterostructures. By means of low temperature scanning tunneling microscopy and spectroscopy (STM/STS) under ultra-high vacuum conditions and high magnetic fields, we are able to study the electronic structure in depth and, therefore, the phase diagrams of these 2D materials. This thesis also benefits from other experimental techniques (AFM, ARPES, XMCD, XPS, SQUID, RHEED, LEED) and calculations that provide complementary information to better understand the phenomenology of the physical systems under study.

In the first part, we examine the quasi-particle density of states of a monolayer of $NbSe_2$ to demonstrate the emergence of Leggett collective modes in the superconducting state, arising from the competition between the s-wave singlet ground state and a sub leading f-wave triplet component. Then, we study the impact of proximity effects on the electronic structure and collective states in this 2D material triggered by different types of supporting substrates. In the third part, we focus on aliovalent SL-TMD alloys. As we tune the stoichiometry of two different alloys, we examine the atomic-scale evolution of the electronic ground states and the robustness of the electronic phases against disorder. Subsequently, we explore the electronic and magnetic properties of 1T-$TaSe_2$ in single-layer form on different substrates (BLG and 1H-$TaSe_2$). On the latter, 1T-$TaSe_2$ shows evidence of long-range magnetic order. The last chapter of this thesis describes the electronic properties of single-layer $TiSe_2$ as well as the CDW order on different substrates.

Contents

CHAPTER 1

Introduction

Materials, when thinned down to the two-dimensional (2D) limit, are exhibiting fascinating electronic and magnetic properties, which are very interesting from the fundamental point of view and for a wide range of future electronic applications. In this regard, novel physical phenomena such as superconductivity (SC), charge density wave (CDW) states, topological quantum states, moiré physics and many more can be studied in the confined space of two dimensions.

In 2004 the discovery of Graphene by K. S. Novoselov and A. K. Geim opened up this new field of research.[1] Combined with the development of novel theoretical and experimental techniques, nowadays we have the possibility to experimentally create 2D materials and study their structural, electronic and magnetic properties at the atomic level in great detail. In order to design such quantum materials, basically two different strategies can be employed, which are top-down and bottom-up processes. The exfoliation of 2D materials from their bulk counterparts belongs to the class of top-down, whereas the growth of 2D materials from the pure elements is a bottom-up process and mostly deployed for this thesis. Several different methods exist. The predominately used method is chemical vapor deposition (CVD) growth. However, for this work the technique of molecular beam epitaxy (MBE) is deployed and further developed. Compared to CVD, a major advantage of MBE is the ultra-high vacuum condition where only the pure elements are involved in the process. Therefore, highly crystalline materials can be fabricated, which provide access to 2D quantum mechanical ground states.

This work focuses on a specific class of materials, namely transition metal dichalcogenide (TMD) materials. Especially since the discovery of graphene, the research interest in TMDs has strongly accelerated, because of their similar van der Waals (vdW) layered character. In that sense, it was realized that beyond graphene, there exists an entire platform of materials with diverse properties opening up the possibility to access new intriguing physics in 2D materials.

Definition of key concepts

The objective of this work is to explore the distinctive electronic and magnetic properties of collective phases of novel 2D TMD materials and related vdW heterostructures with respect to their 3D counterparts. To this purpose, the experimental work of this thesis comprises the growth of 2D TMD materials by means of molecular beam epitaxy (MBE), as well as their structural, electrical, and magnetic characterization by means of scanning tunneling microscopy & spectroscopy (STM & STS). A reflective high-energy electron diffraction (RHEED) system is deployed to analyse the growth dynamics and crystallinity of the samples in-situ. Monitoring the RHEED diffraction pattern during the growth process yields important information on the quality of the grown material. These samples can then be taken out of the MBE system and further be investigated with a room-temperature (RT) atomic force microscope (AFM). Such measurements give valuable information on the morphology and the crystallinity of the samples. A continuous optimization procedure of MBE-RHEED-AFM is performed until the desired high quality single-layer (SL) samples can be produced. Then, these samples are studied by means of a 300 mK-11 T-STM system, which, due to its topographic and spectroscopic capabilities, has access to the collective electronic and magnetic states. Additional angle-resolved photoelectron spectroscopy (ARPES), superconducting quantum interference device (SQUID), and x-ray magnetic circular dichroism (XMCD) measurements give further information on structural, electronic and magnetic properties. Density functional theory (DFT) and first-principle calculations are performed by collaborators to complement the STM/STS observations.

Structure of the thesis

Chapter 1: An introduction to the research field of TMD materials is presented. Furthermore, an overview of the properties of collective electronic phases in 2D is discussed.

Chapter 2: The working principles of the experimental techniques and how they were applied are described.

Chapter 3: Here we present the theoretical framework and experimental results of two different projects comprising SC at the SL limit of $NbSe_2$. First, the observation of a collective mode in the quasiparticle density of states (DOS) is discussed. We interpret these findings as relative phase fluctuations between two superconducting pairing channels, a so-called Leggett mode. The results are evidence for a f-wave triplet pairing channel in SL-$NbSe_2$, competing with the s-wave singlet ground state. In the second part, we investigate proximity effects on SC and CDW order introduced by underlying, electronically distinct substrates. We therefore thoroughly study the electronic structure of SL-$NbSe_2$ grown on BLG/SiC, h-BN/Ir(111), Au(111), and WSe_2 by STM/STS and ARPES experiments. One of the important outcomes of these experiments is that the BLG/SiC substrate plays a negligible role in the electronic properties of 2D TMD metals.

Chapter 4: In the first part, we study the impact of substitutional point defects in SL-$Nb_\delta X_{1-\delta}Se_2$ (X = Mo, Ti, and Cr atoms) on the electronic structure and CDW & SC states in the range of $0 < \delta < 1$. The methodical variations in the alloys stoichiometry lets us observe modifications in the DOS and reveals the dynamics of the band structure modifications in the entire alloy composition range from a superconducting material (pristine $NbSe_2$) to a semiconducting material ($MoSe_2$). Furthermore, we study the robustness of the SC and CDW order as a function of atomic doping / disorder and find a strengthening of these collective orders for low doping concentrations. In the second part, we study these collective phases in relation to the doping introduced disorder in the SL-$Ta_{1-\delta}W_\delta Se_2$ alloy. We demonstrate the emergence of superconductivity in the otherwise metallic single-layer 1H-$TaSe_2$ by electron doping provided through the W dopants.

Chapter 5: In this chapter we present a low temperature electronic and magnetic characterization, combined with DFT calculations, of single-layer $TaSe_2$ in its H-phase, T-phase, as well as in the novel heterostructure of the semiconducting 1T-$TaSe_2$ on top of the metallic 1H-$TaSe_2$. In the first section, by comparing our high resolution, spatially resolved STS measurements with DFT calculations, we discuss the nature of the observed band gap in the low lying electronic structure of 1T-$TaSe_2$. Supposed to be a Mott insulating gap, we can show that the origin of the gap is much more likely to be a conventional band structure effect. In the second part, we study the magnetic correlations in the 1T/1H-$TaSe_2$ heterostructure and discuss two different theories: the kondo lattice (heavy fermion) picture and the appearance of antiferromagnetism. STS characterization of the zero bias peak (ZBP) feature as a function of the magnetic field strongly suggests antiferromagnetic order in this material.

Chapter 6: The growth properties of single-layer 1T-$TiSe_2$ is studied for two different substrates: BLG and bulk WSe_2. Furthermore, the symmetry of the charge density wave as well as its electronic structure is studied. We compare these results with the case of bulk $TiSe_2$.

1.1 Two-dimensional TMD materials: an overview

Transition metal dichalcogenide (TMD) materials represent a large family of layered materials, which gained a lot of interest in the past years due to a widely accessible range of electronic and magnetic properties in 2D. These materials contain a broad spectrum of candidates for optoelectronic applications due to their semiconducting character and the tunability of their optical band gaps.[2–5] Moreover, this family of materials also possesses a large number of materials with metallic character that host different electronic phases such as charge density waves, superconductivity and topological order.[6–13] At the present day, many different transition metals (M) have been combined with chalcogen atoms (X) and successfully synthesized in the chemical structure of MX_2 as 2D TMD materials. Figure 1.1.1 presents an overview of the main TMD materials based on the involved transition metals and its structural and electronic phases.

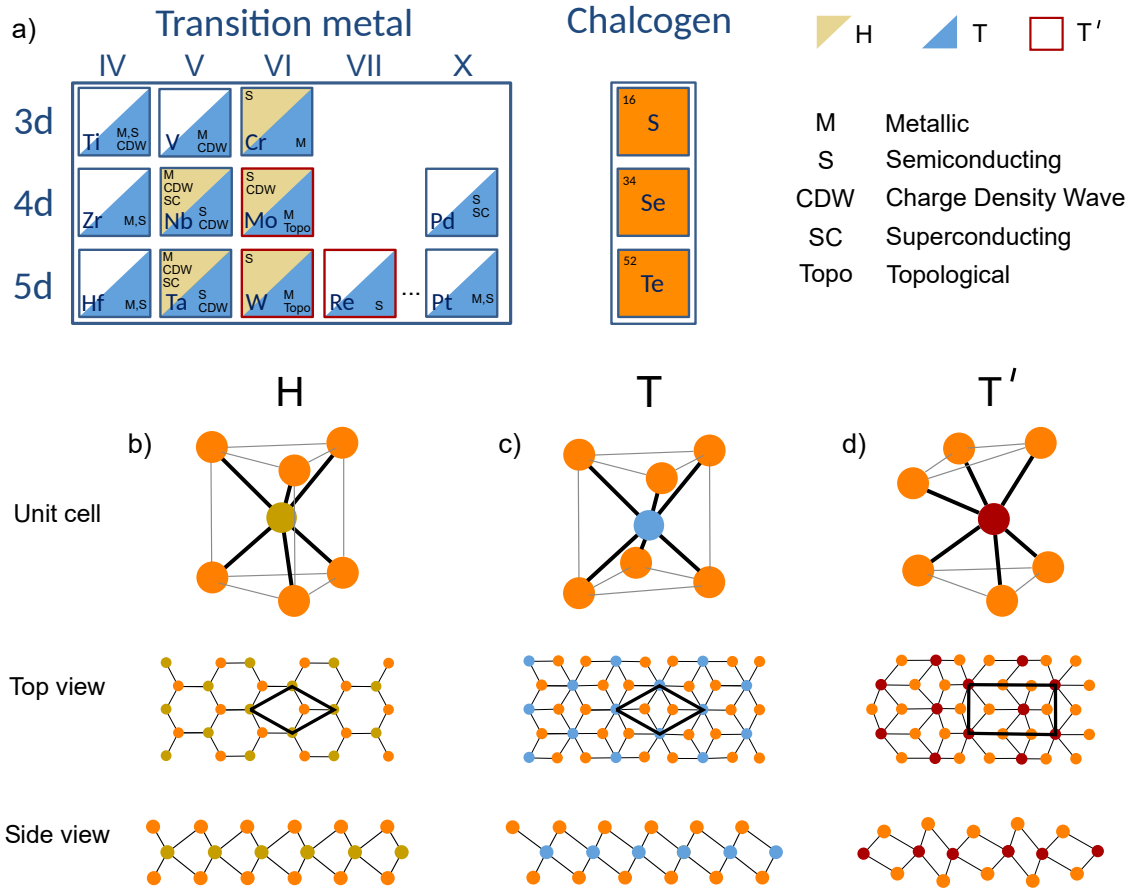

Figure 1.1.1: Overview of the main TMD structures with corresponding electronic phases and structural appearances. a) In literature reported TMD materials with its electronic phases. The unit cell, top view, and side view are illustrated for the H-phase (b), T-phase (c), and T'-phase (d).

Depending on the combination of transition metals with its chalcogen counterpart, the TMD develops a thermodynamically stable phase (groundstate): the H-phase (trigonal prismatic), the T-phase (octahedral), or the T'-phase (distorted octahedral). The three phases (H, T, and T') with their corresponding unit cells, as well as seen from the top and the side, are shown in Fig.1.1.1 b) - d). Several growth methods, in part MBE, have achieved the synthesis of metastable phases in many of these materials such as the H-phase and the T-phase of $TaSe_2$ [7, 14] or the H-phase and T'-phase of WSe_2 [15]. Typical thicknesses of such TMD layers are $3 \sim 4$ Å. For bulk TMDs these layers are bound together by the relatively weak vdW forces compared to their in-plane covalent atomic bonding. Lattice constants of the various combinations of materials are in the range of 3.15 Å - 4.03 Å, depending on the sizes of the involved atoms. The transition metal delivers four electrons, which fill the bonding states with the chalcogen atoms. In that way the oxidation states are +4 for the transition metal atom and -2 for the chalcogen atom.[16]

The electronic character of 2D TMD materials (metallic or semiconducting) is usually determined by the filling of the non-bonding d bands. In the case of partially filled bands, a metallic behaviour is observed; however, when fully occupied, the TMD material is a semiconductor. Interestingly, when reducing the dimension of TMDs from 3D to 2D, most of them undergo a transition from indirect to direct band gap, which has a strong effect on the intensity of photo luminescence due to necessary involvement of phonons (conservation of crystal momentum) in 3D, and is very interesting for optoelectronic applications.[17] The tunable bandgap in TMD materials makes them to suitable candidates for materials in photovoltaic cells, light-emitting diodes, and photo transistors.[18–21] The reduced electronic screening in 2D enhances the electron-electron interactions, what renormalizes the band gap of TMD semiconductors. In this arena, especially MoS_2, with a direct optical band gap of 1.83 eV in single-layer form, has shown to posses great potential for electronic devices.[17] It can be used as a supplement for graphene, for example in the field of low power electronics.[22] Due to the reduction of the electronic screening, coulomb interactions intensify in 2D, which can have drastic modifications of the dispersion relations in these materials.

Aside from semiconducting 2D-TMD materials, there is a big group of metallic compounds existing in a thermodynamically stable T-phase or H-phase, as it is illustrated in Fig.1.1.1. The reduced dimension and, therefore, increased Coulomb interactions has strong effects on the electronic phase diagram of these materials. In this regard, CDW and SC order can change its fundamental properties, which leads to variations in the ordering strengths. On this matter, the SC critical temperature ($T_{c,sc}$) of $NbSe_2$ is drastically reduced in the SL limit from $T_{c,sc}(3D) = 7.2\,K$ to $T_{c,sc}(2D) = 1.9\,K$.[6] For TaS_2 instead, an increase of $T_{c,sc}$ by thinning down the material was measured. In bulk $T_{c,sc} = 0.5\,K$; however, approaching the 2D limit, a steadily increase of the superconducting order was found with $T_{c,sc} = 3\,K$ for the SL sample [23, 24]. Moreover, at the 2D limit, enhanced electronic correlations are capable of triggering intriguing states of matter such as Mott insulating behaviour that can lead to unconventional superconductivity or quantum spin liquids.[25–27] The following sections will pursue on this discussion and explain the mechanisms behind these electronic phases.

1.2 Correlated electronic phases in TMD materials

This thesis is focused on collective electronic phenomena, namely superconductivity, charge density waves and magnetic order at the atomic level. The following section gives an overview of the theoretical aspects on their formation in this family of materials. Subsequently, the most important results gained in the field, which are of great importance for the later presented results, are discussed.

1.2.1 Charge density wave

In an atomic lattice described by a free electron gas, the charge density is distributed homogeneously and ions form a uniform periodic lattice. In low dimensional systems, it can be beneficial to open a gap at the Fermi surface and therefore lower the total energy of the system. Lattice distortions are usually prevented by Coulomb repulsion; however, if the gain of electronic energy can overcome the needed energy for restructuring the atomic lattice, a periodic deformation is the most stable and therefore preferred ground state.[28]

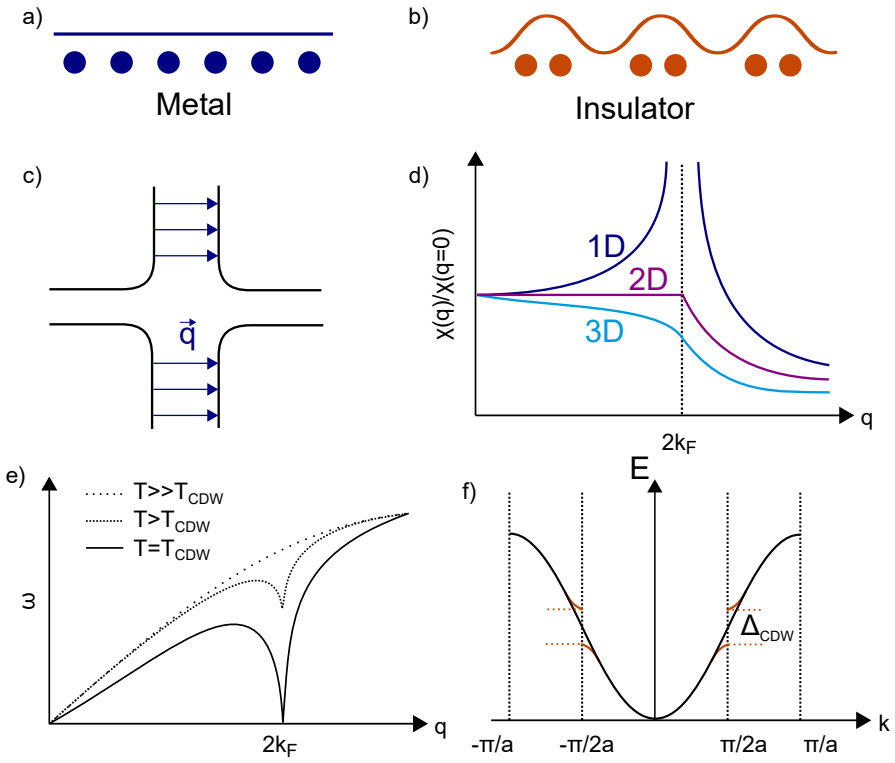

Figure 1.2.1: Peierls instability describing the CDW mechanism in a 1D-system. a) Peierls lattice distortion induced CDW before (a) (metal) and after (b) (insulator) the transition. c) Fermi surface nesting with the wave vector **q**. d) The Lindhard susceptibility as a function of wavevector **q** for the 1D, 2D and 3D case. e) 1D Kohn anomaly in the acoustic phonon branch for different temperatures, as a result from FSN. f) Band structure with gap opening for the CDW case shown in (b).

When the temperature is lowered below a certain critical temperature $T_{c,cdw}$, the Fermi surface becomes unstable and the mentioned gap opens. This leads to a reordering of the charge density to a periodic spatial modulation, the so-called charge density wave, which was first introduced by Fröhlich in the 1950s.[29] Simultaneously, the ion potential is changed and the lattice sites adapt their positions to the new equilibrium state (see Fig. 1.2.1 a) and b)). In that way the redistribution of the charge density always goes along with the distorted lattice. Peierls was the first to explain this metal to insulator transition in a 1D material as a result of electron-phonon coupling. In Fig. 1.2.1 c) the underlying Fermi surface nesting is depicted, which leads to divergence (in 1D) in the Lindhard susceptibility $\chi(q)$ at $q = 2k_F$ (see Fig. 1.2.1 d). This moreover triggers a renormalization of the phonon mode close to $q = 2k_F$, what is known as phonon softening or the so-called Kohn anomaly (Fig. 1.2.1 e).[30] There is a strong temperature dependence in the phonon energy, in a way that it reaches $\omega = 0$ for $q = 2k_F$ if $T = T_{c,cdw}$ and becomes imaginary at $T < T_{c,cdw}$. The so-called frozen phonon introduces a second order phase transition and the energy gap Δ_{CDW} shown in Fig. 1.2.1 f) is opened. This gap opening reduces the electronic energy and compensates the elastic energy required for the dimerization (see Fig. 1.2.1 b).

In two dimensions (2D) the situation is more complicated and electron phonon coupling (EPC) becomes an important parameter regarding the CDW formation. Since the 1960s, TMDs have been considered historically as model quasi-2D systems for the study of CDW phase transitions. For a long time it was suggested that Fermi surface nesting (FSN), the extension of the Peierls' picture in 2D, can explain the CDW instabilities.

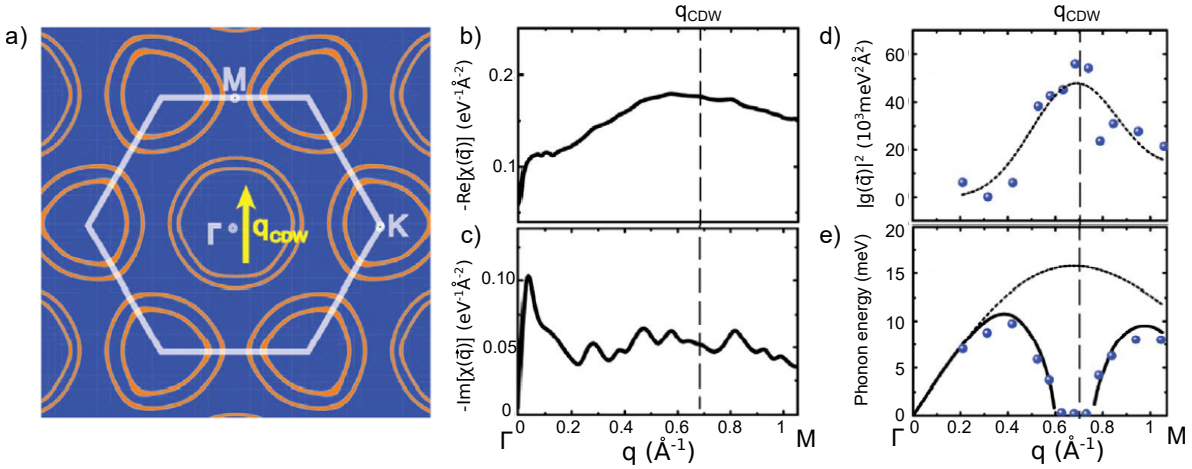

Figure 1.2.2: CDW mechanism of $NbSe_2$. a) The Fermi surface of $NbSe_2$[31] with experimental q_{cdw} [32, 33]. b-c) Real and imaginary part of $\chi(q)$ along ΓM direction calculated from experimental data.[31] d) EPC matrix element.[34] e) Soft phonon calculation (solid line), measured phonon dispersion (blue dots), and bare phonon dispersion without CDW order (dashed line). [35, 34]

However, state of the art research by angle-resolved photoemission spectroscopy studies [36, 35, 37, 38] and electronic structure calculations [39, 40] have increased the awareness that FSN might not be the right model to explain CDW in 2D TMD materials. It should be mentioned that besides EPC, the saddle point (van Hove singularity) mechanism is another process in discussion regarding the CDW formation.[41]

The study of the model quasi-2D layered material $NbSe_2$ has revealed that the Peierls's picture is not sufficient and FSN has been strongly doubted to be the origin of the CDW order in this system. Fig. 1.2.2 a) shows the FS of $NbSe_2$ with the high symmetry points Γ at the center of the Brillouin zone (BZ) as well as the M and K points on the border of the BZ.[31] The experimentally obtained CDW q-vector is indicated as q_{CDW} (yellow arrow), what contradicts to FSN as the trigger for the CDW instability.[32, 33] Furthermore, in Fig. 1.2.2 b) and c) the real and imaginary parts of the Lindhard function along ΓM direction show no sign of divergence around $q_{CDW} \cong (2/3)|\Gamma M| = 0.695\mathring{A}^{-1}$, what corresponds to a 3×3 modulation in real space. There is however a peak in the **q**-dependent EPC matrix element (d), what introduces the Kohn-like anomaly around q_{CDW} at T = 33 K and was identified as the trigger of the CDW phase transition (see Fig.1.2.2 e). The acoustic phonons soften in an extended area around the CDW wave vector. This behaviour is very different from the sharp phonon energy decrease what one would expect from a Fermi nesting process (see Fig.1.2.1 f) for comparison). Hence, the trigger of the CDW in quasi-2D $NbSe_2$ is not FSN, but it has been experimentally and theoretically shown that q-dependent EPC triggers the system.[42, 35] Important to mention is that one has to differentiate between FSN and EPC in the sense that although both are electron-lattice interactions, FSN is an elastic process, whereas EPC implies inelastic phonon scattering.[43] A more detailed description on the properties of $NbSe_2$ follows in chapter 3.

Two-dimensional TMD materials provide interesting systems for the exploration of the the origin and fundamental triggers of CDW formation, which do not follow a unique model.[44] In 2H-$TaSe_2$ a second order phase transition at 122 K can be observed to an incommensurate phase, which is close to a 3×3 superstructure. Another phase transition to a commensurate 3×3 superstructure occurs at 90 K.[33] This material is a well suited system for studying the CDW formation, because superconducting order establishes at very low temperature of $T_{c,SC} \sim 0.2$ K, therefore no special attention has to be brought to competing order of these two phases.[45] This competition and similarities between CDW and SC will be discussed in later sections of this introduction chapter. In the case of $TaSe_2$, STM measurements combined with density functional theory (DFT) calculations revealed that FS nesting is not the driving force of the CDW, because nesting vectors q_N=(1/3, 1/3,0) do not coincide with the CDW wavevector q_{CDW}.[7] However, the experimental observation of a negligible effect on the 3×3 superstructure when decreasing the sample thickness from bulk to single-layer suggests electron-phonon coupling as the CDW driving force.[7]

For 2D and 3D systems the Lindhard susceptibility does not diverge at $q = 2k_F$ like it is the case in 1D. Therefore, other mechanisms alternative to Fermi surface nesting have to be involved in the

process. However, a few systems do exist, where not even EPC is the crucial parameter. A very interesting system where electron-phonon coupling was proven not to be the driving force for the CDW transition is SL-$TiSe_2$. In this particular system, electron-electron interactiond were found to be a key regarding the CDW formation and it was proposed to be the driving force in this regard.[46] One of the mechanisms suggested to explain the CDW in $TiSe_2$ is the so-called excitonic insulator mechanism.[47] In semi-metals with small band overlap or semiconductors with a small electronic band gap, charge carriers are scarce. The few carriers form bound states between electrons and holes, the so-called excitons, if the exciton binding energy is higher than the gap. Through this process, charge carriers are removed from the Fermi surface and an insulating state is formed. If the gap is indirect, the excitons gain momentum and a CDW can form.[48]

Another process capable of introducing a CDW is the so-called band Jahn-Teller effect, which is basically a phase transition from the T-phase to H-phase triggered by the possibility of lowering the total energy of the system. This might be possible for various systems due to the difference of energies of the d bands in the two phases, where in the H-phase polytype the d_{z^2} energy is lower. If the chalcogen atoms in the T-phase below and above the transition metal rotate in the opposite direction to each other, a potential will be created on the corners of the unit cell, which attracts the positively charged metal ions and therefore distorts the lattice.[49]

Remarkably, the fundamental physics of CDW have similarities with other correlated electronic phenomena such as SC. In a few systems such as $NbSe_2$ and $TaSe_2$ instabilities at the Fermi surface open up a gap in the CDW phase as well as in the SC phase.[50] Whereas an electron-phonon condensate is formed in the CDW state, in SCs electrons condensate into Cooper pairs. One of the similarities for both cases can be seen in the form of description of the critical temperature of the two phases. From the mean-field theory one can derive

$$k_B T_{c,cdw} = 1.14\epsilon_F exp(-\frac{1}{Vg(\epsilon_F)}) \tag{1.1}$$

for the Peierls transition temperature and

$$k_B T_{c,sc} = 1.14\epsilon_D exp(-\frac{1}{Vg(\epsilon_F)}) \tag{1.2}$$

for the SC critical temperature from BCS theory.[51] In the equations k_B is the Boltzmann constant, V the electron-phonon coupling constant, and ϵ_F and ϵ_D are the Fermi and Debye energies. The energy scales of Fermi ($\epsilon_F \sim$ 1 to 10 eV) and Debye ($\epsilon_D \sim$ 0.01 to 0.1 eV) differ by two or three orders of magnitude, what indicates $T_{c,SC} << T_{c,CDW}$. However, electron-phonon coupling alone can not explain the critical temperature and transition driving mechanisms for most systems and more electronic interactions have to be taken into account. Especially the competition between CDW and SC in 2D TMD materials has manifested the believe in a deeper correlation of the two phases. This has been proven particularly for cuprate superconductors, what gives the impression that understand-

ing the mechanisms of CDW could also be a great support on the way of understanding high T_c superconductors.

1.2.2 Superconductivity

Superconductivity has been a vibrant research field since its first discovery in Mercury (Hg) in 1911 by Kamerlingh-Onnes.[52] In this revolutionary experiment, together with his coworkers Gerrit Flim, Gilles Holst, and Gerrit Dorsman, they observed a sudden fall in the resistivity curve of Hg to almost zero (see Fig. 1.2.3) below a certain temperature ($T_{c,sc} = 4.15\,K$) and they named this new phenomenon the superconducting state. Another very interesting property of superconductors was discovered soon after, namely the expulsion of an external magnetic field in the superconducting material. According to this behaviour in the presence of a magnetic field, SC can be categorized into two types: Type 1 signifies that the entire magnetic field is kept out of the superconducting material, until a certain critical field is reached, what creates ideal diamagnetism. This effect was discovered by Walther Meissner and Robert Ochsenfeld in 1933.[53] On the contrary, in type 2 SCs, quantized magnetic flux tubes (vortices) can penetrate the superconducting material with multiples of the magnetic flux quantum $\phi_0 = 2.07 \times 10^{-15}$Wb.[54]

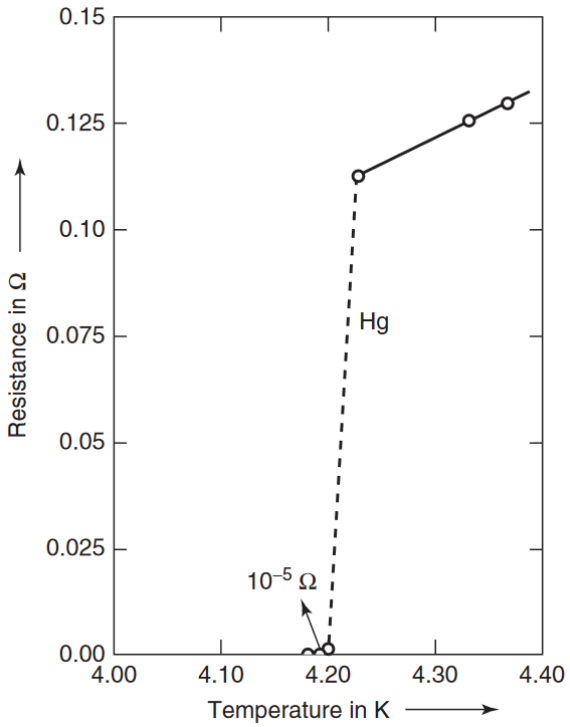

Figure 1.2.3: The superconducting state of mercury. The resistance drops to 0 at its critical temperature $T_{c,sc} = 4.15\,K$.[54]

Ginzburg and Landau (GL), in 1950, developed their phenomenological model of SC.[55] This theory was successfully applied to explain macroscopic properties of SC such as the categorization in type 1 and type 2 SCs. In the GL theory, Landaus theory of second-order phase transitions [56] is extended to a complex pseudo wavefunction ψ and introduced as an order parameter describing the superconducting electrons with $n_s = |\psi(r)|^2$ the local density of states. At $T < T_{c,sc}$ ψ is nonzero, and vanishes for $T >> T_{c,sc}$ through a second order phase transition.[57] By minimizing the GL free energy one can derive the GL equations and furthermore find two important characteristic lengths describing the superconducting state. These are the coherence length ξ, which describes the size of thermodynamic fluctuations and therefore the stability of the superconducting phase. The second one is the penetration depth λ, which describes how far an external magnetic field can penetrate into the superconducting material. The ratio of these two characteristic length scales is defined as the GL parameter $\kappa = \lambda/\xi$. It categorizes the SC materials into the two different types as $\kappa < 1/\sqrt{2}$ (type 1) and $\kappa > 1/\sqrt{2}$ (type 2).[58]

In 1954, specific heat measurements led to the discovery of another fundamental property of SC, which is the existence of an electronic gap in the ground state.[59, 60] Soon after in 1957, the BCS theory, introduced by Bardeen, Cooper, and Schrieffer, revolutionized the theory of SC.[61] Already in 1956 Cooper did the groundwork by describing a formalism, which explains the attractive force between electrons. He could show that in the Fermi sea of electrons a weak interaction of electrons will always lead to at least one bound state (Cooper pair), which is a result from the Fermi statistic and the Fermi-sea background. A very important result derivated from BCS theory is that a minimum energy of $E_g(T = 0) \approx 3.5 k_B T_c$ is necessary to break a cooper pair and therefore create two quasi-particle excitations. A more detailed description of the BSC theory follows below.

Later, in 1959, Gor'kov derivated the GL theory from the BCS theory and showed, that it is a limiting form of the BCS theory, valid near T_c. Furthermore, it was shown that the wavefunction is proportional to the superconducting gap $\psi \propto \Delta$, what means ψ can be seen as the wavefunction of the cooper pairs. In this picture, the entire superconductor can be described with one wavefunction, describing a many-body condensate of Cooper pairs by $\psi(r) = |\psi(r)|e^{i\phi(r)}$.

BCS theory

In a simplified model of two electrons in a Fermi sea at $T = 0\,\mathrm{K}$, assuming they interact only with each other but not with the other electrons of the Fermi sea, except through the exclusion principle, a two-particle wavefunction can be written as

$$\psi_0(\mathbf{r}_1, \mathbf{r}_2) = \sum_{\mathbf{k}} g_{\mathbf{k}} e^{i\mathbf{k}\cdot\mathbf{r}_1} e^{-i\mathbf{k}\cdot\mathbf{r}_2}, \tag{1.3}$$

where $g_{\mathbf{k}}$ describes the weighting coefficients. The total wavefunction is regarded to be antisymmetric, because of the attractive exchange interaction of the two electrons. Therefore ψ_0 can be converted to

a sum of products of $\mathbf{k} \cdot (\mathbf{r}_1 - \mathbf{r}_2)$ with the antisymmetric singlet spin function $(\alpha_1\beta_2 - \beta_1\alpha_2)$ to

$$\psi_0(\mathbf{r}_1, \mathbf{r}_2) = \big[\sum_{k>k_F} g_{\mathbf{k}} cos\mathbf{k} \cdot (\mathbf{r}_1 - \mathbf{r}_2) \big](\alpha_1\beta_2 - \beta_1\alpha_2), \tag{1.4}$$

with α_1 the spin up state of particle 1 and β_1 its spin down state. The energy eigenvalues E and weighting coefficients can be calculated by solving the corresponding Schrödinger equation with the defined wavefunction (1.4) as

$$(E - 2\epsilon_{\mathbf{k}})g_{\mathbf{k}} = \sum_{k'>k_F} V_{\mathbf{k}\mathbf{k}'} g_{\mathbf{k}'}, \tag{1.5}$$

where $\epsilon_{\mathbf{k}}$ are unperturbed plane-wave energies and $V_{\mathbf{k}\mathbf{k}'}$ the matrix elements of the interaction potential. It is defined as

$$V_{\mathbf{k}\mathbf{k}'} = \Omega^{-1} \int V(\mathbf{r}) e^{i(\mathbf{k}'-\mathbf{k})\cdot r} d\mathbf{r}, \tag{1.6}$$

with r the distance of the two electrons and Ω the normalization volume. If a set of weighting factors g_k can be found, which satisfies (1.5) and $E < 2E_K$, a bound state exists. Cooper assumed that $V_{\mathbf{k}\mathbf{k}'} = -V$ for k states within a cutoff energy of $\pm\hbar\omega_{cut}$, otherwise $V_{\mathbf{k}\mathbf{k}'} = 0$. Using the so-called weak-coupling approximation and converting (1.4) a bound state energy can be found as

$$E \approx 2E_F - 2\hbar\omega_c e^{-2/N(0)V}, \tag{1.7}$$

with $N(0)$ the density of states at E_F. By that he proved that a bound state exists, consisting of electrons with $k > k_F$.[61]

The origin of $V_{\mathbf{k}\mathbf{k}'} = -V$ and thus superconductivity is a result of the forces working on the electrons to couple. The repelling Coulomb interaction is outdone by an attracting force arising from movements of positive ions in the lattice. An electron is attracting positive ions and polarizes the medium, by what a second electron will be attracted (see Fig. 1.2.5 a) bottom). If this attracting force is stronger than the coulomb potential, the result is a net attractive potential, leading to Cooper pairs, and SC arises.[62, 63]

Cooper pairs located at an energy range of $\epsilon_F \pm \hbar\omega_D$ prefer to condense into the correlated state of SC than submerge into the Fermi sea as free electrons. This effect leads to a vanishing of the Fermi sea and in fact an energy gap opens around E_F. The total energy of the system is reduced. With more Cooper pairs forming they interfere with each other and the system has to be treated as a many body problem. A mathematical expression able to describe such a state is provided by the BCS wavefunction.[58]

Following description uses the $N \times N$ Slater notation to specify N-electron anti-symmetrized product functions. This notation is compact and uses the language of second quantization, where occupied

states (including spin index) are defined by using creation operators $c^{\dagger}_{\mathbf{k}\uparrow}$ as well as annihilation operators $c^{\dagger}_{\mathbf{-k}\downarrow}$, which create electrons of momentum $\mathbf{k}$ and spin up, or empty the corresponding state, respectively. With this notation the BCS many-body groundstate can be written as a superposition of Cooper pairs, with opposite momentum and spin in the conventional case:

$$|\psi_{BCS}\rangle = \prod_{\mathbf{k}} (u^2_{\mathbf{k}} + v^2_{\mathbf{k}} c^{\dagger}_{\mathbf{k}\uparrow} c^{\dagger}_{\mathbf{-k}\downarrow})|0\rangle, \tag{1.8}$$

Here, $|0\rangle$ is the vacuum state. The average occupation probability of a pair with momentum (**-k,k**) and spin $(\uparrow,\downarrow)$ is defined by $|v^2_{\mathbf{k}}|$, the average non-occupation is given by $|u^2_{\mathbf{k}}|$. The normalization condition $|v^2_{\mathbf{k}}| + |u^2_{\mathbf{k}}| = 1$ has to be valid.[58]

Pairing Hamiltonian

In order to find values for $u_{\mathbf{k}}$ and $v_{\mathbf{k}}$ and explicitly describe the behaviour of the SC state, the so-called variational method can be used.[58] For this the pairing Hamiltonian or reduced Hamiltonian is defined as

$$\hat{H} = \sum_{\mathbf{k}\sigma} \xi_{\mathbf{k}} c^{\dagger}_{\mathbf{k}\sigma} c_{\mathbf{k}\sigma} + \frac{1}{N} \sum_{\mathbf{k},\mathbf{k'}} V_{\mathbf{k},\mathbf{k'}} c^{\dagger}_{\mathbf{k}\uparrow} c^{\dagger}_{\mathbf{-k}\downarrow} c_{\mathbf{k'}\uparrow} c_{\mathbf{-k'}\downarrow}. \tag{1.9}$$

This Hamiltonian of a conventional SC describes only the electron-electron interaction and transforms a pair of electrons from one momentum state (**k'**,**-k'**) to the other (**k**, **-k**). The number of electrons in the system is defined as N. By $V_{\mathbf{k},\mathbf{k'}} = V_{\mathbf{-k},\mathbf{k'}} = V_{\mathbf{k},\mathbf{-k'}}$ spin rotation invariance is given. In the mean-field approximation BCS transforms the Hamiltonian to

$$\hat{H}^{MF} = \sum_{\mathbf{k}\sigma} \xi_{\mathbf{k}} c^{\dagger}_{\mathbf{k}\sigma} c_{\mathbf{k}\sigma} - \sum_{\mathbf{k}} \Delta^{*}_{\mathbf{k}} c_{\mathbf{k}\uparrow} c_{\mathbf{-k}\downarrow} - \sum_{\mathbf{k}} \Delta^{*}_{\mathbf{k}} c_{\mathbf{k}\uparrow} c_{\mathbf{-k}\downarrow} + const. \tag{1.10}$$

In this approximation the superconducting energy gap is defined as non-zero vacuum expectation values of Cooper pair creation and annihilation operators:

$$\Delta_{\mathbf{k}} \equiv -\frac{1}{N} \sum_{\mathbf{k'}} V_{\mathbf{k},\mathbf{k'}} \langle c_{-\mathbf{k'}\downarrow} c_{\mathbf{k'}\uparrow} \rangle \qquad\qquad \Delta^{*}_{\mathbf{k}} \equiv -\frac{1}{N} \sum_{\mathbf{k'}} V_{\mathbf{k},\mathbf{k'}} \langle c^{\dagger}_{-\mathbf{k'}\downarrow} c^{\dagger}_{\mathbf{k'}\uparrow} \rangle \tag{1.11}$$

With the known SC energy gap and the Fermi velocity of electrons condensed into Cooper-pairs, the coherence length of the correlated pairs and therefore the characteristic length scale is given as

$$\xi = \frac{\hbar v_F}{\pi \Delta}. \tag{1.12}$$

For solving the mean-field Hamiltonian and therefore diagonalizing it, the Bogoliubov-Valatin canonical transformation is deployed [64, 65]:

$$c_{\mathbf{k},\uparrow} = u_{\mathbf{k}} a_{\mathbf{k}\uparrow} + v_{\mathbf{k}} a^{\dagger}_{\mathbf{-k}\downarrow} \qquad\qquad c^{\dagger}_{\mathbf{-k},\downarrow} = -v^{*}_{\mathbf{k}} a_{\mathbf{k}\uparrow} + u^{*}_{\mathbf{k}} a^{\dagger}_{\mathbf{-k}\downarrow}. \tag{1.13}$$

By this definition, all cross-diagonal terms in the Hamiltonian are cancelled out, if $u_{\mathbf{k}}$ and $v_{\mathbf{k}}$ are written as:

$$|u_{\mathbf{k}}|^2 = \frac{1}{2}\left(1 + \frac{\xi_{\mathbf{k}}}{\sqrt{\xi_{\mathbf{k}}^2 + |\Delta_{\mathbf{k}}^2|}}\right) \qquad |v_{\mathbf{k}}|^2 = \frac{1}{2}\left(1 - \frac{\xi_{\mathbf{k}}}{\sqrt{\xi_{\mathbf{k}}^2 + |\Delta_{\mathbf{k}}^2|}}\right). \tag{1.14}$$

Through this transformation, the mean-field Hamiltonian can now be written in a simpler form as

$$\hat{H} = E_0 + \sum_{\mathbf{k},\sigma} E_{\mathbf{k}} a^\dagger_{\mathbf{k}\sigma} a_{\mathbf{k}\sigma}. \tag{1.15}$$

Here, E_0 stands for the ground state energy and $E_{\mathbf{k}}$ is the dispersion relation of the Eigenstates. This very important result describes the increase of energy above the ground state by the operators $a_{\mathbf{k}\uparrow}$ and $a^\dagger_{\text{-}\mathbf{k}\downarrow}$. Thus, the Eigenstates of this Hamiltonian after the Bogoliubov-Valatin transformation, are called the Bogoliubov quasiparticles, which are excitations of the superconductor.[58]

Bogoliubov quasiparticle

By means of the Bogoliubov-Valatin transformation, the pairing hamiltonian was diagonalized in the previous section, what has yielded the definition of a new set of eigenstates, the Bogoliubov quasiparticles. The creation of such an excitation, or Bogoliubov quasiparticle with momentum $\mathbf{k}$ and spin σ, is described by

$$a^\dagger_{\mathbf{k},\sigma} = c^\dagger_{\mathbf{k},\sigma} u_{\mathbf{k}} + sgn(\sigma) c_{\text{-}\mathbf{k}-\sigma} v_{\mathbf{k}}. \tag{1.16}$$

As it is shown in equation (1.16), the Bogoliubov excitation is a superposition of creation and annihilation of electrons with opposite spin, which are weighted by their coherence factors $u_{\mathbf{k}}$ and $v_{\mathbf{k}}$.

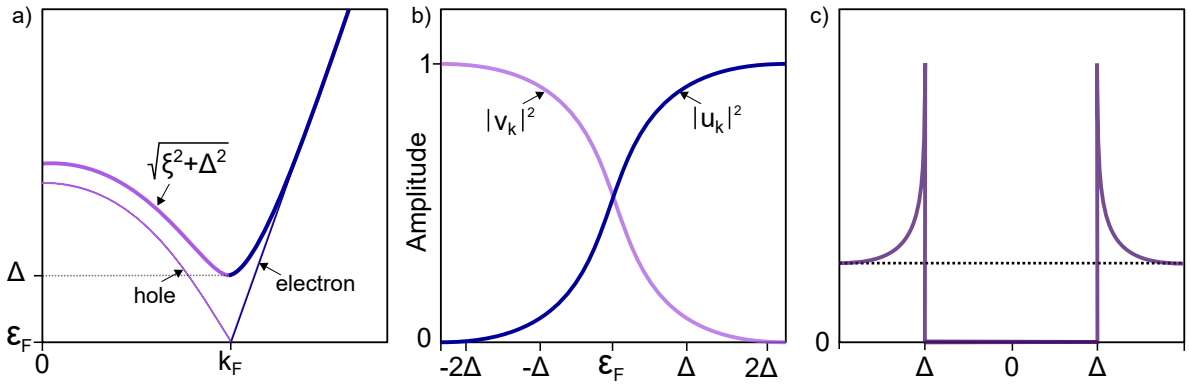

Figure 1.2.4: Quasiparticle excitations. a) The dispersion of the Bogoliubov quasiparticle. b) Amplitude of the coherence factors as a function of energy around E_F. c) DOS of a superconductor showing the coherence peaks at Δ, no excitation within the gap, and the Bogoliubov excitations outside of the gap. The marked line indicates how the DOS would look like in the normal (metallic) state.

Whereas the Cooper-pairs are condensed in the same ground state, the Bogoliubov quasi particles have energies outside of the gap, which are linear combinations of excitations of electrons (negatively charged) and electron holes (positively charged). Electron and hole bands mix to a new fermionic eigenstate with corresponding dispersion relation

$$\pm E_{\mathbf{k}} = \pm\sqrt{\xi_{\mathbf{k}}^2 + |\Delta_{\mathbf{k}}^2|}. \tag{1.17}$$

This relation is illustrated in Fig. 1.2.4 a) with a maximum excitation energy corresponding to the SC energy gap Δ. Quasiparticles with energies around Δ are mixed states of electron and hole bands, whereas the character of the excitation is determined by the energy dependent amplitudes of the coherence factors (see Fig. 1.2.4 b). The solutions of the Bogoliubov transformed Hamiltonian yields two symmetric eigenstates, which correspond to an electron and a hole. This fact exemplifies the electron-hole symmetry in superconductors, which arises from the fundamental transport characteristics, the Andreev reflections of electrons into holes and the other way around.[66] The density of states of Bogoliubov quasiparticles (Fig. 1.2.4 c) is calculated from the dispersion relation as

$$\rho(E) = \frac{1}{N}\sum_{\mathbf{k}}\Big[|u_{\mathbf{k}}|^2\delta(E - E_{\mathbf{k}}) + |v_{\mathbf{k}}|^2\delta(E + E_{\mathbf{k}})\Big]. \tag{1.18}$$

Superconductivity in 2D-TMD materials

Due to strong electronic correlations in reduced dimensions, thin films at the 2D limit are an interesting platform to study tuning parameters and the most fundamental properties of SC. By this day, especially TMDs have stood out as ideal materials to study SC. Because of their layered nature they can easily be exfoliated and transferred onto various substrates, which introduces another tuning possibility. Furthermore, molecular beam epitaxy has been proven as the perfect experimental technique for growing these materials at highest possible crystallinity and a minimized amount of defects. In this regard, in 2012, few-layer MoS_2 was shown to be able to transition from an insulating state to a superconducting state by electric field modulation.[9] Moreover, intrinsic 2D superconductivity with interesting properties was found in $NbSe_2$, TaS_2 and WTe_2.[67, 23, 12] Recent experiments have shown that SC can persist in particular SL TMD materials in the presence of in-plane magnetic fields exceeding the Pauli limit.[68, 10, 69] This effect is caused by pinning electron spins to the out-of-plane direction by spin orbit coupling (SOC) and it is called Ising SOC. For systems not having a center of inversion, the SOC is antisymmetric. SL TMD materials in the H-phase are an exceptional case, because they have out-of-plane mirror symmetry and broken inversion symmetry, what restricts the crystal electric field to be in-plane. The electron motion within this plane leads to an effective magnetic field, directed out-of-plane, what splits the energy of the spin states. Electrons within the same Cooper pair are localised in each of the two spin-split Fermi surfaces. This so-called Ising SC in SL TMD materials, where electrons with opposite out-of-plane spins in opposite K and K' valley form singlet Cooper pairs, leads to large upper critical magnetic fields, what is known as Ising protection of SC.[24]

One of the most seeked advancements is SC at room temperature, what could revolutionize many aspects of modern technologies. Studying SC at the 2D limit is a promising way to achieve this goal, as it was shown for 2D FeSe/$SrTiO_3$. This system possesses a critical temperature in the range of 60 K - 100 K depending on thickness modifications, with highest $T_{c,sc}$ at the monolayer limit.[70] It is remarkable that $T_{c,sc}$ in this system decreases drastically with increasing thickness of the sample, what is attributed to a rigorous change of the electronic structure. This behaviour could also be found in a TMD material, namely TaS_2, where the critical temperature increases from 0.5 K in bulk to $\sim$3 K in the monolayer.[24] For most TMDs and in general when thinning down superconducting materials, one would expect various quantum phase transitions, competing phases, enhanced Coulomb repulsion, localization of Cooper pairs induced by increasing disorder, weaker interlayer Cooper pairing and even changes of the band structure, which hamper the superconducting pairing strength. Furthermore, from a theoretical perspective, regarding the constraints of Cooper pair wavefunctions in 2D due to the vacuum boundary conditions one also expects a decrease of $T_{c,sc}$ with decreasing sample thickness. Indeed decreased $T_{c,sc}$ is found for most of the thinned materials, but sample cleanness and sample preparation might take an important role. In the case of $NbSe_2$, it was supposed to entirely loose its superconducting properties when thinned down below 5.5 nm, as it was optically measured for exfoliated samples in 2009.[67] Advanced exfoliation and transfer techniques and most of all ultra-high vacuum techniques, nowadays, make it possible to fabricate ultra clean samples. At the present day, for $NbSe_2$ the critical temperatures of $T_{c,sc} = 7.2$ K in the bulk, as well as 1.9 K for the monolayer are widely accepted and persistent SC was proven.[6]

The question of why some materials show a positive correlation between sample thickness and $T_{c,sc}$ and others show negative correlation is very intriguing and one of the motivational sources for this thesis. The CDW phase might play an important role as it strongly influences the density of states (DOS) around the Fermi level by opening a gap. In that sense, if a specific material suppresses its CDW phase in the 2D form, an increased availability of DOS can strengthen the Cooper pair formation and increase $T_{c,sc}$ greatly.[71]

Beyond BCS

The essential ingredient for superconductivity is a phase-coherent superfluid made up from Cooper-pairs, which can only survive at very low temperatures for most materials.[72] That is why in the last years a big effort was made in the search for new materials with higher superconducting critical temperatures $T_{c,sc}$. Especially cuprate and iron superconductors have shown to posses relatively high critical temperatures up to 160 K.[73, 74] In the scope of these research advances the theory of superconductivity had to be further developed for the so-called unconventional superconductors, in order to understand those unexpected high $T_{c,sc}$ values and other peculiar properties. The two different types, conventional and unconventional SC, differentiate in the fundamental part on how the cooper pairs are bound together.

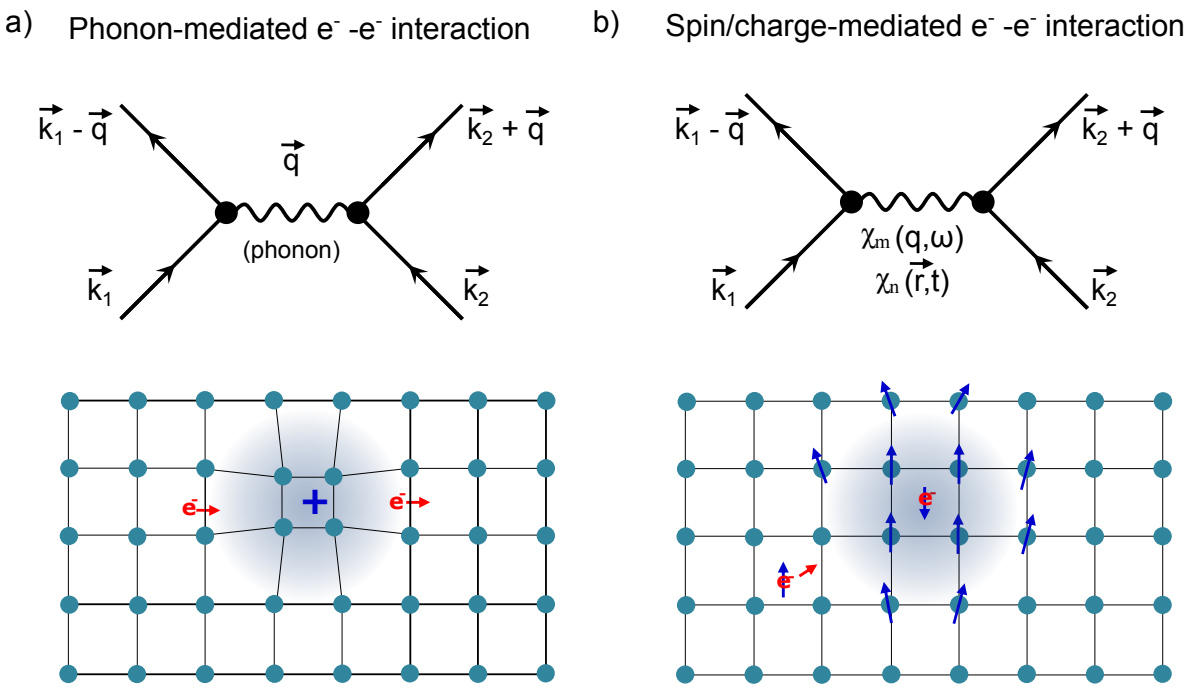

Figure 1.2.5: Conventional and unconventional superconductivity represented with Feynman diagrams (top) and phonon, or spin, interactions (bottom). a) In the formalism of conventional superconductors, two electrons form Cooper pairs mediated by lattice vibrations. b) In unconventional superconductors, instead of the phonon, the spin/charge susceptibility of the surroundings take its part and is the pairing glue for the Cooper pair.

In the BSC theory the binding glue for Cooper pairs are phonons; however, beyond this conventional pairing mechanism, quasiparticles can form Cooper pairs and thus superconductivity either by charge density or magnetically mediated interactions.[75] The two fundamentally different pairing processes are illustrated in Fig. 1.2.5 a) conventional and b) unconventional. Interestingly, the spin-spin interactions can be orders of magnitude stronger compared to the phonon mediated electron charge interactions.[75] High critical temperatures have triggered the idea of superconductivity without phonons, but instead with spin interactions of quasiparticles in a similar manner than it was thought to explain the superfluidity in liquid ^{3}He.[76, 77] This was believed to be especially significant on the border of magnetism, where spin-spin interactions are enhanced.[78] Superconductivity on the verge of ferromagnetism was found in rather recent history in a layered perovskite as well as in UGe_2.[79, 80] However, a lot of research output in years before had already suggested that there might be a close relationship between superconductivity and anti-ferromagnetism, what was found in low-dimensional organic metal and heavy electron compounds.[81–84] In those materials, the properties of their normal state and superconducting state were discovered to be remarkably different compared to the known conventional metallic superconductors at the time. These findings led to the believe that antiferromagnetic instabilities in these system might be the reason for superconductivity in those materials.

Doping effect on superconductivity

Various doping techniques make it possible to change the charge density and the conductivity of TMD materials. Approaches like electrostatic gating, chemical intercalation, and doping by proximity can drastically tune the electronic, magnetic and chemical properties of such materials. These methods shift the Fermi energy and can therefore modify the electronic and magnetic properties of the material. Although conventional SCs are not sensitive to local defects or lattice impurities, as described in the Anderson theorem, with growing disorder in the system superconducting properties are greatly modified.[85]

In that sense, it was shown for 2D $NbSe_2$ (bilayer) that the critical temperatures of SC as well as CDW order can be tuned by electrostatic gating and therefore modifying the carrier density of the material.[86] Another important observation by electric field control was reported on thin layers of $TiSe_2$, where by electronic gating, control over the strength of its electronic phases (SC and CDW) could be achieved.[87] This method allows to study details of electronic phase transitions between many body states and can possibly help to understand its most fundamental connections.

Two very interesting approaches to study the interaction between disorder through doping and the electronic phases were found to be substitutional doping, which is basically chemical doping, by interchanging atoms from the lattice with a specific similar element, capable of containing the atomic lattice. Another one is to distribute adatoms on the surface. It was shown for SL $NbSe_2$, that for both of these approaches, the superconducting properties can be changed drastically, what results in modified $T_{c,sc}$. Si adatoms on the $NbSe_2$ surface have a magnifying effect on SC at low defect densities $< 1.5\,\mathrm{nm}^{-2}$, where at higher concentrations, the SC order is destroyed. Similar behaviour was found for substitutional doping by interchanging Se atoms by S atoms. In this case it was possible to increase $T_{c,sc}$ by a factor of ~ 3.[11]

Intercalation is a very promising approach to tune CDW and SC transition temperatures, as it was shown e.g. in the controlled intercalation of $TiSe_2$ with Cu atoms. Remarkably, the CDW transition could be suppressed, and SC could be introduced at an intercalation rate of $x = 0.04$ with a maximum $T_{c,sc}$ of 4.15 K at $x = 0.08$.[88]

Another approach to tune SC might be to use specific types of substrates underneath the 2D superconducting material. Substrates can trigger numerous "proximity effects" of various nature in the 2D material such as screening[89], charge transfer[90], hybridization[90, 91], strain[92, 93], etc. Although proximity effects are known to affect the fundamental properties of 2D materials, the study of their impact on collective electronic phases in 2D materials remains sorely lacking. Depending on the type of substrate, which could be an insulator, semi-conductor, semi-metal, or a metal, the interaction is different. As it was shown for SL NbS_2 on Au(111) and, in another work, also for SL

TaS_2 on Au(111), heavy doping induced by hybridization with the substrate changes the Fermi surface remarkably.[94, 95] How electronically distinct substrates influence the SC properties remains an open question and shall be elaborated in chapter 3.2.

CHAPTER 2

Methodology

Following, the approach of creating 2D quantum designer materials using molecular beam epitaxy (MBE) is specified. Furthermore, the working principle and functionality of the most important and major tool for this work, the 300 mK Scanning Tunneling Microscope (STM), is explained.

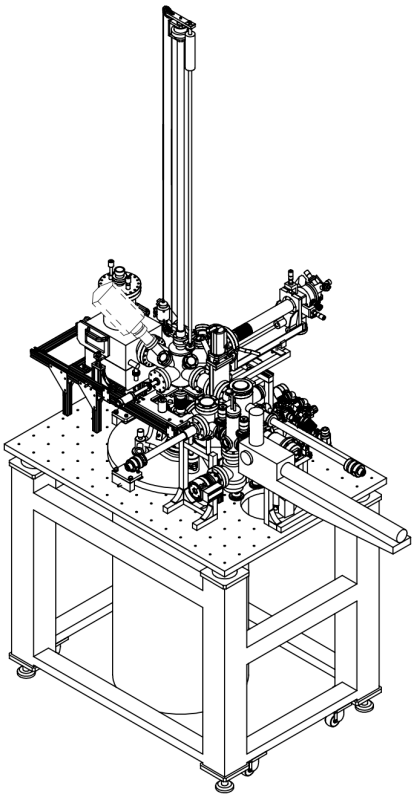

2.1 Molecular beam epitaxy (MBE)

Molecular beam epitaxy is a UHV technique used for growing thin film materials as layer-by-layer, or, ultra thin nanostructures of non-layered materials. It is regarded as one of the cleanest methods for material growth, because it is usually carried out in UHV conditions ($<10^{-9}$mbar) and only high purity elements of the desired chemical compounds are involved in the process. Nevertheless, this makes it also to one of the most delicate techniques.[96]

For many years, MBE growth has been constituted one of the most powerful techniques for the growth of crystalline thin films, and more recently also for the growth of materials at the 2D limit. The synthesis of high quality single-layer (SL) materials has opened up the possibility to study novel electronic phases in 2D, which, in specific materials, possess different properties than seen in their 3D (bulk) counterparts.[6, 97–100] Furthermore, MBE is capable of high-quality growth of vertical vdW heterostructures, comprised of different kinds of SL materials.[101, 102] The growth of rotationally aligned vdW materials without interlayer covalent bonding is known as vdW epitaxy.[103] Without such interlayer covalent bonding, the substrate and the vdW material can maintain their lattice constants. However, the lattice mismatch of the two materials on top of each other introduces the formation of lateral moiré patterns, which may modify the electronic structure.[104] Such heterostructures can also be grown in-plane (lateral), where two different kinds of SL materials are connected to each other.[105]

Another very interesting capability of MBE is to grow atomically sharp interfaces in between different phases of the same material. In material dependent temperature ranges it is possible to grow different structural phases at the same time.[27, 106] In this regard, it was shown that in the scenario where the 1T'-phase of SL WSe_2, a quantum spin hall insulator (QSHI) material, crystallographically aligns laterally with a semiconducting 1H-WSe_2 domain, topological edge states are created.[15] Furthermore, such interfaces are intriguing structures for the study of different kinds of proximity effects.

Due to its capability of large scale, single crystalline growth, MBE is not only a very versatile tool in the field of fundamental condensed matter physics, but has attracted a lot of interest in research areas connected to application developments such as photovoltaics, micro and nanoelectronics as well as optoelectronics.

2.1.1 Experimental setup

A sketch of the utilized home-made MBE system is shown in Fig. 2.1.1 a). In Fig. 2.1.1 b) a photograph with overlaid components is presented. In the scope of this thesis, in total four material evaporators were available. One of them is a standard Knudsen effusion cell (K-cell), which consists of a high temperature stable crucible, filled with the desired material in the form of powder or pellets.

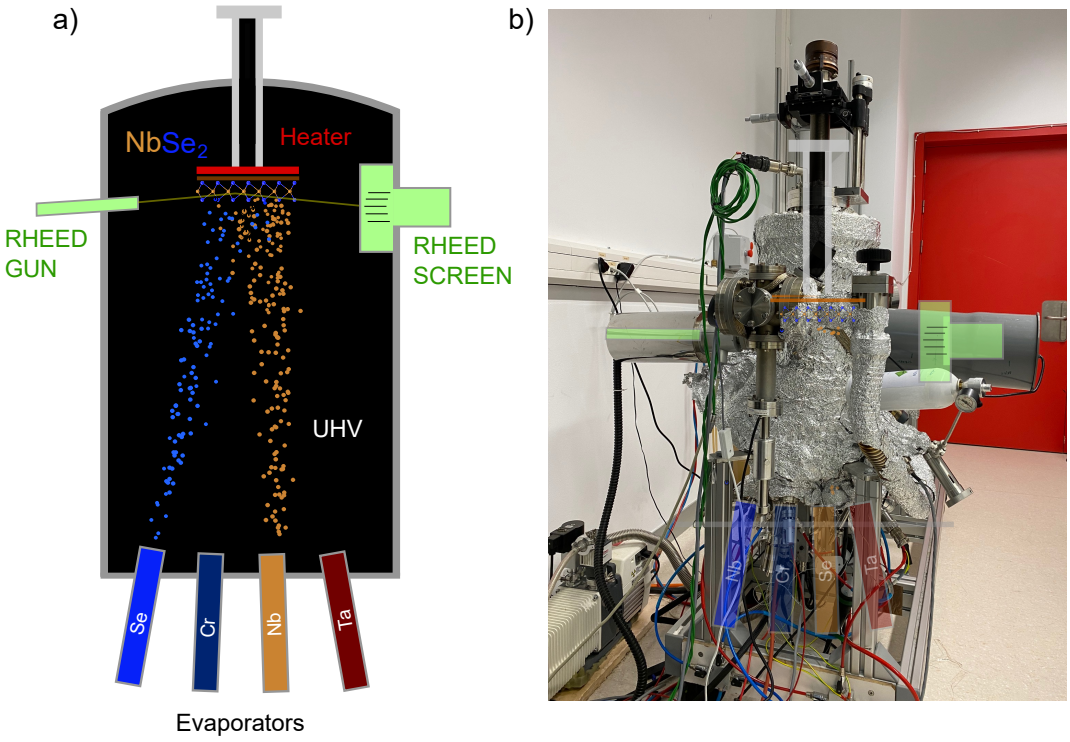

Figure 2.1.1: The MBE system. a) Sketch of the home-built MBE setup. b) Photograph of the MBE with overlaid experimental components.

This kind of evaporators are mainly used for low partial pressure elementary sources, which was Se in the scope of this thesis. A temperature of 150°C is enough to evaporate the Se into the chamber to the direction of the substrate. The other three evaporators are electron-beam (e-beam) evaporators. Contrary to the K-cell, the e-beam evaporators make use of a high voltage ($\sim 2\,\mathrm{kV}$), applied between a tungsten filament and the material source, which is a high purity metal rod in this case. The electron beam extracted from the filament is accelerated and bombarded onto the rod through the application of the high voltage, where it causes atoms to sublimate and evaporate to the chamber. This kind of evaporator is capable of heating material rods to temperatures up to ~ 2500°C. Such high temperatures are necessary to sublime robust elements such as tungsten (W) with a melting point of 3422°C. A water cooling system is installed and designed to cool the evaporators in a way that the heating of the rod is optimally localized at the tip. Thus, the surroundings are kept at low temperature and a high purity evaporation is guaranteed. Another important characteristic of these evaporators is their ion suppression tool, which is basically an additional voltage applied at the so-called suppressor electrode. It is used to remove ions from the beam and to guarantee that the atoms arriving at the substrate are neutral. Thus, defects can be prevented. All evaporators are aligned such that the beams of elements arrive at the same location on the substrate. In this experimental setup, uniform layer growth can be achieved up to an area of $\sim 1\,\mathrm{cm}^2$.

2.1.2 RHEED analysis

The reflective high-energy electron diffraction (RHEED) helps to analyse and monitor the material growth of our 2D materials in-situ and in real-time. Electrons in the energy range of 10 - 100 keV are irradiated with a glancing angle with respect to the plane of the substrates surface where they scatter in a specific way, depending on the atomic lattice, and interfere with each other. As it is shown in Fig. 2.1.1 a) the diffraction pattern of these electrons can then be made visible on a fluorescent screen on the opposite side of the RHEED gun. The so-called Ewald sphere construction is used to describe the interference process (Fig. 2.1.2). An incident electron wave with wave vector $\mathbf{k}_0$ scatters elastically on the sample surface, which is then transformed to $\mathbf{k}_1$ or $\mathbf{k}_2$ (first and second order of interference), the diffracted electron waves. Thus, they have the same amplitude and their end points are on a sphere (Ewald sphere) with radius $|\mathbf{k}_0|$. Assuming a sample with atoms equidistantly arranged on a line along the incoming electron waves, the Fourier transformation gives equidistand reciprocal lattice planes, which are perpendicularly arranged to the row of atoms. The requirement for constructive interference is specified by the intersections of the Ewald sphere with the reciprocal lattice planes. The smallest circle is defined as the 0th Laue zone (L_0). Real diffraction patterns, arising from distinct lattices have more complicated real space structures and contain valuable information.[107]

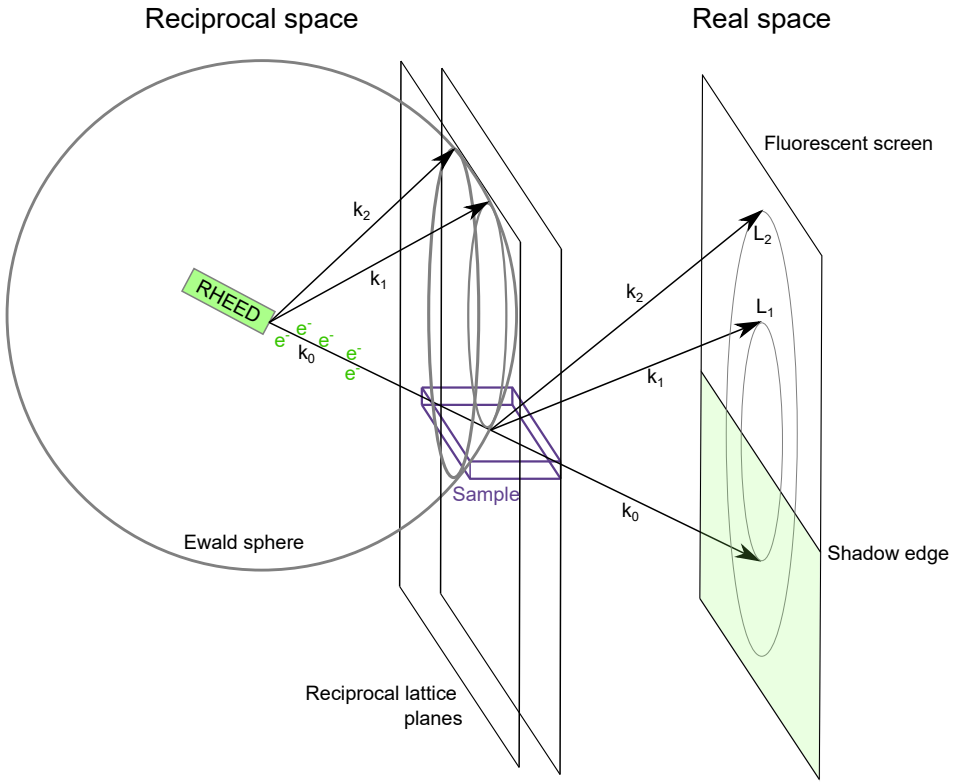

Figure 2.1.2: Working principle of RHEED. Direct space and reciprocal space of the RHEED system. Reproduced from [107].

From the constructive interference pattern, monitored by a camera, one can obtain information on:

(i) Periodicity (unit cell) in atomic arrangements.

(ii) Flatness of the surface.

(iii) Sizes of the grown domains.

(iv) Epitaxial relation between the grown islands and underlying substrate.

(v) Parameters characterizing structural phase transitions.

(vi) Growth mode (Volmer-Weber (VW), Frank-Van der Merwe (FM), Stranski-Krastanov (SK)).

(vii) Number of layers.

The lattice parameter a_2 of a grown material, on top of a substrate with lattice parameter a_1, can be extracted from the ratio $r_1/r_2 = a_1/a_2$, where r_1 and r_2 are the distances from the center of the RHEED pattern to the first order interference point for the substrate and the grown structure on top, respectively. Despite the fact that the RHEED technique is versatile and powerful in providing information of the grown thin films, during the course of this thesis we have combined it with other

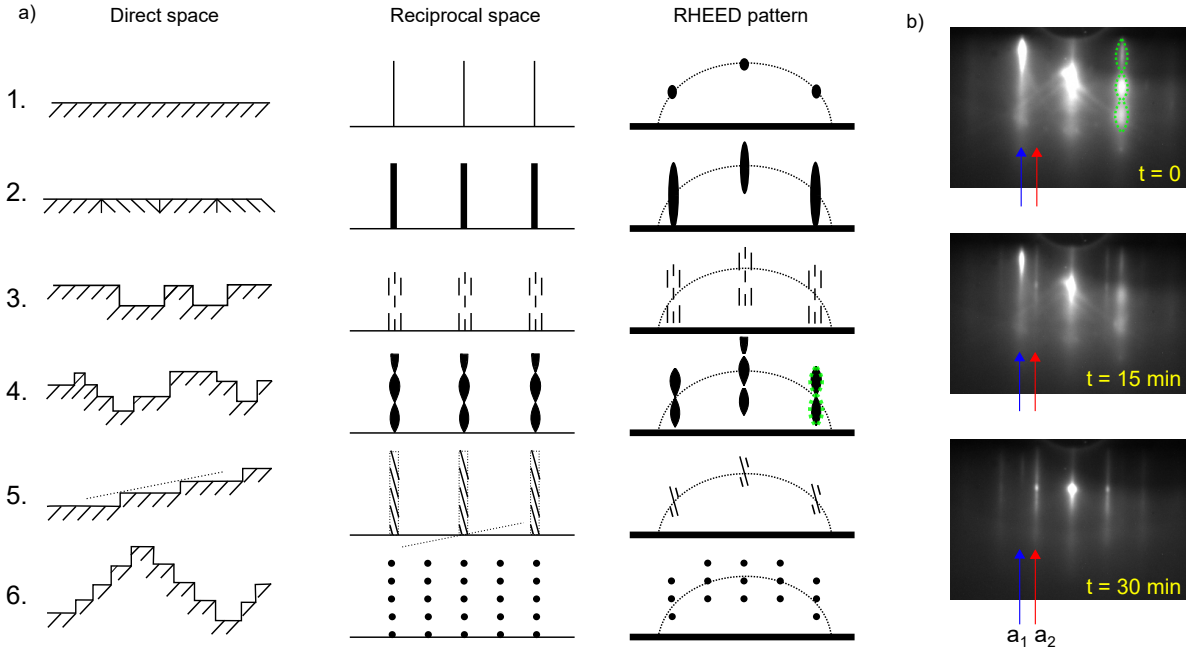

Figure 2.1.3: RHEED patterns. a) Comparison between direct space, reciprocal space, and appearing RHEED pattern. Reproduced from [107]. b) Example pattern of a grown single-layer $NbSe_2$/BLG/SiC(0001) sample fabricated in the scope of this thesis. The blue arrows indicate the structure of graphene. The red arrows indicate the lines of $NbSe_2$. With evolving time the film grows on top, the $NbSe_2$ pattern starts to form and simultaneously the BLG patterns weakens.

techniques (AFM, STM) that provide direct information regarding the atomic structure in real space. Therefore, the RHEED was mostly used for (ii), (iii), and (iv) during the actual growth. Few examples for different surface modifications and how they appear as RHEED patterns are shown in Fig. 2.1.3 a). Also shown is an actual example (Fig. 2.1.3 b) of a RHEED measurement during the growth of SL $NbSe_2$/BLG/SiC. At the starting time of the growth (t = 0) only the graphene pattern, indicated by the blue arrows, is visible. After ~ 5 min enough material has formed on the surface to produce a measurable diffraction signal. Simultaneously, the graphene pattern faints away with progressing time. After 15 min, the coverage amounts to $\sim$ 0.5 ML, as the intensities of the graphene pattern and the $NbSe_2$ pattern reach about the same value. Comparing these patterns to the theoretical illustration in Fig. 2.1.3 a) one can immediately identify a few characteristics of the growth dynamics. First, the elongated, curved lines of the graphene pattern (indicated in green in the first RHEED image) reveals the single crystalline, but stepped surface (compare to 4th structure of direct space) of the BLG/SiC substrate. Second, the $NbSe_2$ film grows in the FM mode, i.e., layer-by-layer growth, however, the domains are not rotationally aligned (compare to 2nd structure of direct space), as it is indicated by the elongated lines (red arrow). After 30 min, almost 1 ML has been grown, what is implied by the bright $NbSe_2$ pattern, compared to the almost non-visible BLG pattern.

2.1.3 Growth procedure

All substrates introduced to UHV have to be outgased in order to remove residual gases prior to the epitaxy. In order to do this, the substrates are heated up to a specific temperature, which is at least the growth temperature. With this procedure it can be made sure that moisture, oxide layers and hydrocarbons from ambient conditions are removed from the surface of the substrate, where the subsequent material growth takes place. Following, the basic steps of the growth process are listed:

1. The used evaporators are heated up to their specific temperatures and flux ratios are stabilized.
2. The substrate is heated up to its intended temperature and outgased.
3. The RHEED gun is used for monitoring of the evolution of the growth.
4. The evaporators are opened and the growth is conducted for the defined growth time. Simultaneously, the RHEED pattern changes and the progression of the layer growth can be observed.

Subsequently to the growth, the samples are measured in an ambient condition atomic force microscope (AFM). This experimental probe is a fast, nm-resolution imaging tool mainly used for the purpose of checking, if a desired material can be grown flat and crystalline on a specific substrate. AFM was frequently used after a sample was grown in the MBE. The information gained with these measurements help to optimize the growth parameters and therefore the crystal quality. Especially when trying to grow a new SL TMD material, the AFM measurements contain valuable information about the growth dynamics, which help towards a successful synthesis. Thus, the process of optimizing the MBE growth of a new TMD material is comprised of a continuous cycle of synthesis and AFM characterization.

After the material growth can be controlled in a way that the desired phase of the material appears highly crystalline and with a suitable coverage, the samples are ready to measure in the STM.

2.2 Low-temperature scanning tunneling microscopy

The STM is a versatile tool in the field of nanoscience. Since its invention in 1981 by Binning and Rohrer (Nobel laureates in physics, 1986) the technique has been developed and striking research has contributed in many different fields of fundamental research. Its atomic scale resolution imaging capability in combination with its ability to perform ultra fine spectroscopy of the electronic structure makes it to one of the key experimental probes in condensed matter physics.[108] In the scope of this thesis, the main experimental tool is a STM, which can operate at strikingly low temperatures of 340 mK and at high magnetic fields up to 11 T. In the following sections I will first describe the fundamental working principles of the STM, followed by the methods of operation, and lastly, I will give details on the experimental setup and its specifics.

2.2.1 Physics of STM

The working principle of the STM is based on the quantum mechanical tunneling effect. In a first approximation to the electron tunneling junction in the STM, a square potential barrier V(z) of height V_0 is considered between two electrodes at a point z = 0 and z = d, illustrated in Figure 2.2.1. It is possible to solve the time-independent Schrödinger equation for the one-dimensional case, which is written as

$$\frac{\hbar^2}{2m}\frac{\delta^2}{\delta z^2}\psi(z) = [V(z) - E]\psi(z), \tag{2.1}$$

assuming $\psi = e^{ikz}$ to be a plane wave travelling in +z direction. Here, m is the electron mass, $\hbar$ is the reduced Planck constant, k is the wave vector (scalar in the 1D approximation), and E the energy. Solving the equation, k is obtained as

$$k = \sqrt{\frac{2m}{\hbar^2}(E - V(z))} \tag{2.2}$$

outside of the potential barrier where V = 0. Thus, the solution is an oscillating wave for a free electron and has the form

$$\psi_{free} = e^{ikz} \qquad with \qquad k = \sqrt{\frac{2m}{\hbar^2}E}. \tag{2.3}$$

Inside the barrier (region II), V = V_0 and E - $V_0 < 0$. Therefore, k is imaginary and can be written as k = $i\kappa$. Thus, it can be rewritten as

$$\kappa = \sqrt{\frac{2m}{\hbar^2}(V_0 - E)}. \tag{2.4}$$

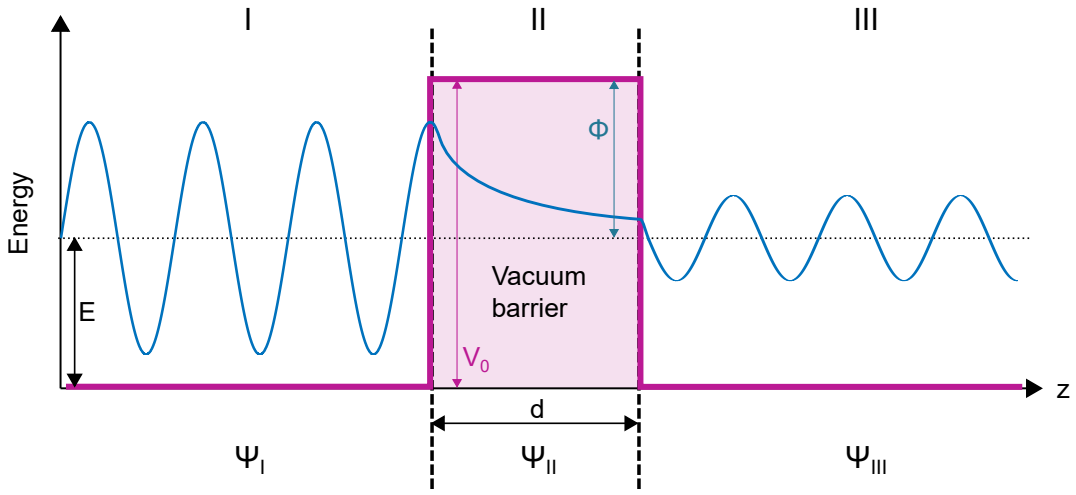

Figure 2.2.1: One-dimensional metal-vacuum-metal tunneling junction. The wave function can tunnel through a thin vacuum barrier and reach the metal on the other side. Figure adapted from [109].

It follows that inside of the potential barrier, the solution of the Schrödinger equation yields the wavefunction $\psi = e^{-\kappa z}$, if E < V_0. Thus, in region II, the solution is given as

$$\psi_{barrier} = e^{-\kappa z}. \tag{2.5}$$

This wavefunction represents the exponential decay inside the vacuum barrier. In classical physics, an electron can not enter this potential barrier. However, within the framework of quantum mechanics, such a particle is not only able to enter, but can even pass through a thin barrier, what is referred to as quantum tunneling. The square of the absolute value of the solution of the time-independent Schrödinger equation gives the tunneling probability as

$$|\psi(z)|^2 = |\psi(0)|^2 e^{-2\kappa z}, \tag{2.6}$$

where $\psi(0)$ and $\psi(z)$ represent the electron wavefunction at positions 0 and z. The decay rate is given by κ.

Bardeen model for tunneling

At this point it is not yet clear what is meant by surface topography on the atomic scale, because the simple model of tunneling through a one-dimensional barrier does not describe where the electrons are tunneling to. A long time before STMs were built, Bardeen presented a model for electron tunneling in a metal-insulator-metal junction.[110] In his model, he considered two metals with a vacuum barrier in between. Both metals have distinct electronic states, which can be calculated through the time-independent Schrödinger equation. As explained in the previous section, the solutions are oscillatory wave-functions exponentially decaying in the potential barrier. In the framework of the tunneling

process inside the STM, the tunneling happens between initial tip states and final sample states, which is considered within the time-dependent perturbation theory. As illustrated in Fig. 2.2.2 a positive bias is applied to the sample, which leads to a down shift of its states with respect to the states of the tip. Furthermore, here, zero temperature is assumed, so all energy levels up to the Fermi level are filled and empty above. In this case, tunneling happens only in the bias window of $E_{F,tip}$ and $E_{F,sample}$. Bardeen used a variant of Fermis golden rule in order to calculate the transition rate between the two electrodes. He found that the transition rate of an initial tip state i at $E_{tip,i}$ and a final sample state f at $E_{sample,f}$ can be stated as

$$w_{tip,i\to sample,f} = \frac{2\pi}{\hbar}|M_{fi}|^2\delta(E_{sample,f} - E_{tip,i}), \tag{2.7}$$

where the matrix element M_{fi} is the integral over a high-handedly surface and can be written as

$$M_{fi} = \frac{\hbar^2}{2m}\int\limits_{S_{tip/sample}} \left[\psi_{tip,i}(\mathbf{r})\nabla\psi^*_{sample,f}(\mathbf{r}) - \psi^*_{sample,f}(\mathbf{r})\nabla\psi^*_{tip,i}(\mathbf{r})\right]\cdot d\mathbf{S}. \tag{2.8}$$

In (2.7) one can see from the delta function that energy conservation is preserved and only elastical tunneling is allowed in this approach. The total transition can be stated as the sum over all pairs of initial and final states as

$$w_{tip\to sample} = \frac{2\pi}{\hbar}\sum_{i,f}|M_{fi}|^2\delta(E_f - E_I). \tag{2.9}$$

In the next step one can multiply the transition rate with two times the electron charge (spin degeneracy), which gives the tunneling current as

$$I = \frac{4\pi e}{\hbar}\sum_{i,f}|M_{fi}|^2\delta(E_f - E_I). \tag{2.10}$$

Taking into account the energy dependence of the density of states of tip (ρ_{tip}) and sample (ρ_{sample}), assuming a one-dimensional barrier and including the effects of different tip and sample work functions (ϕ), the Bardeen equation for the tunneling current transforms to

$$I = \frac{4\pi e}{\hbar}\int_0^{eV}\rho_{tip}(\epsilon - eV)\rho_{sample}(\epsilon)T(\epsilon, V, d)d\epsilon, \tag{2.11}$$

with T the transmission factor.[109] From this equation one can see that the tunneling current is proportional to the products of the density of states of tip and sample as

$$dI \propto \rho_{tip}\rho_{sample}d\epsilon. \tag{2.12}$$

As it is indicated in Fig. 2.2.2, the transmission factor is decreasing exponentially towards lower energies (shorter green arrows), what leads effectively to a larger energy barrier and therefore a lower tunneling probability for the low-lying states.[109]

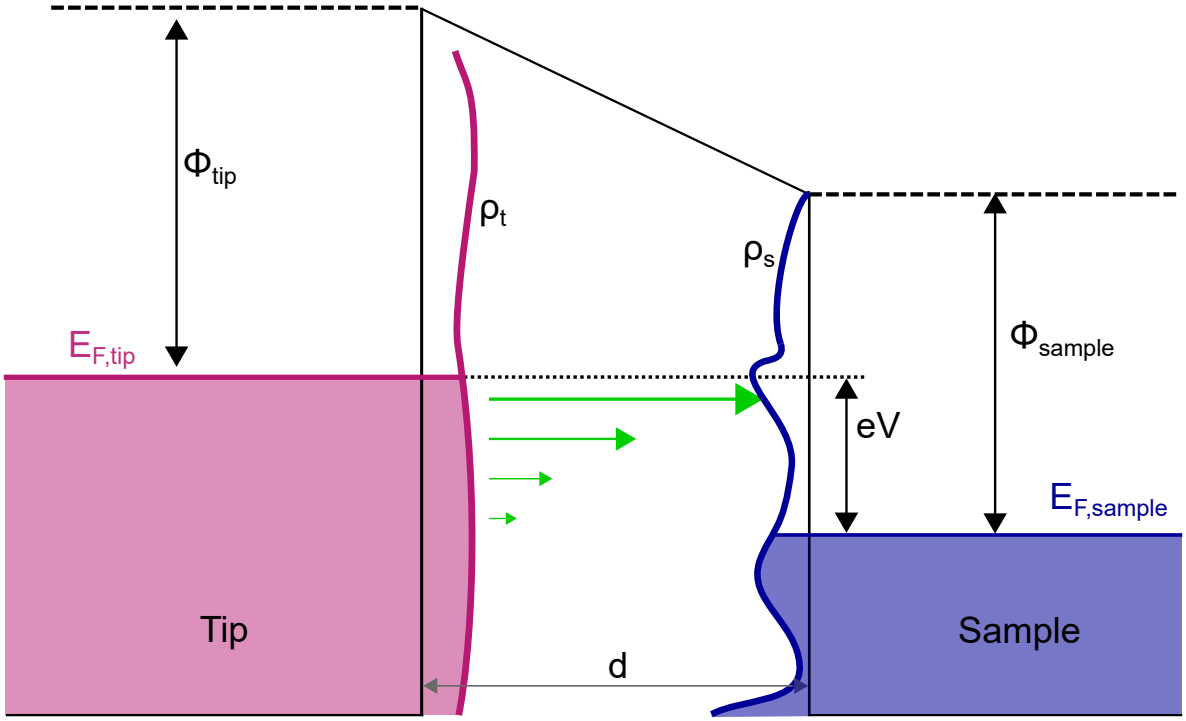

Figure 2.2.2: Energy level diagram of the tunnelling process. The applied bias voltage shifts the Fermi level by eV. The coloured areas represent the density of states of tip (pink) and sample (blue). Figure reproduced from [109].

At finite temperatures one has to include the Fermi-dirac distribution, which is a broadened step function and expressed as

$$f(eV - E_F) = \frac{1}{1 + exp[(eV - E_F)/k_bT]}. \tag{2.13}$$

It yields the occupied filled states at an energy $eV - E_F$ at temperature T.

Tersoff-Hamann approximation

Tersoff and Hamann further developed the Bardeen model, which was initially developed to explain metal-insulator-metal tunneling junctions, in order to get a more realistic tunneling picture for the STM. Instead of the simplified one-dimensional barrier, Tersoff and Hamann included realistic surface wave function to their model. They could evaluate the matrix elements (2.8) in the approximation of low bias voltages around the Fermi level. In order to calculate the integral of the matrix element, specific wave functions for tip and surface have to be defined. The wave function of the surface can be written as a plane wave Fourier expansion, where the surface structure is specified by the Fourier components of the expansion. The wave function of the tip is typically unknown, because the structure is unknown.

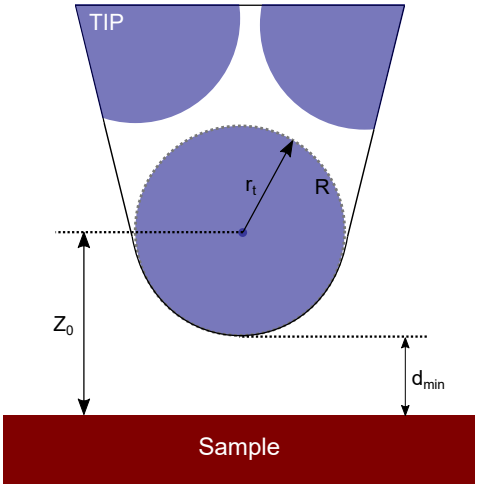

Figure 2.2.3: STM tip in the Tersoff-Hamann approximation. The tip with a single atom at its apex is assumed as a spherical object with radius r_t and curvature R. Reproduced from [109].

Thus, in the approximation Tersoff and Hamann defined an optimized tip with only one single atom at the apex. By this approximation the tip can be mathematically described as a point source at position $\mathbf{r}_t$. With this simplification they could show that the current at small bias simplifies to

$$I \propto \sum_n |\psi_n(\mathbf{r}_t)|^2 \delta(E_n - E_F). \tag{2.14}$$

Again, this holds for elastic tunneling as the Dirac delta function ensures energy conservation on both sides. The surface wave functions are given by $\psi_n(\mathbf{r}_t)$ and their squares of absolute values describe the probability of finding a surface state electron at the same energy level of the tip. As shown in Fig. 2.2.3 the tip measures the sample surface at the position $\mathbf{r}_t$, therefore the tunneling current (2.14) is equivalent with the local density of states at the Fermi level. Furthermore, the tunneling current simplifies to

$$I \propto \sum_n |\psi_n(\mathbf{r}_t)|^2 \delta(E_n - E_F) \equiv \rho_{sample}(E_F, \mathbf{r}_t). \tag{2.15}$$

This equation is valid as long as the tip wave function can be described by a spherical wave, which holds for a single atom terminated tip. As it is shown in Fig. 2.14 the tip position is given as $\mathbf{r}_t$, which is the center of the last atom and the origin of the s-wave. LDOS are measured at the Fermi level at a distance of z_0.

Tunneling spectroscopy

The strength of the STM technique, besides surface imaging, is the capability of performing energy-resolved atomic resolution spectroscopy. Considering now the energy dependence of the LDOS of tip and sample, the tunneling current (within the Bardeen model) is described in eq. (2.10). The LDOS

of the sample can be acquired by measuring the current as a function of the voltage, the so-called I-V curve. A small increase of voltage dV increases the available sample states and corresponds to an increased current dI. The additional current can be approximated by solving the integral from eq. (2.10) at the limits of an increased voltage eV, what results in

$$\frac{dI}{dV} \approx \frac{4\pi e^2}{\hbar} \rho_{tip}(0)\rho_{sample}(eV)T(\epsilon, V, d)d\epsilon. \tag{2.16}$$

Within this approximation it is ignored that lower-level current contributions and also the transmission factor change, because of a higher tunneling barrier. However, what can be seen from here, if assumed the density of states of the tip and also the transmission factor are constant with respect to dV, the differential conductance is proportional to the energy dependent density of states

$$\frac{dI}{dV} \propto \rho_{sample}(eV). \tag{2.17}$$

2.2.2 Basic operation

The operating principle of the STM is based on the quantum mechanical tunneling effect as it is described in the previous section. In simplified terms, this process is realized by applying a bias voltage V between the two electrodes, which are the metallic tip and the sample, separated by the addressed potential barrier, which is usually vacuum. The STM tip consists of a sharpened metallic needle, ideally ending in only one single atom at the tip apex. In that case the highest accuracy can be reached. Piezoelectric actuator elements are used as an extension of the tip to move it in x-, y- and z-directions. These elements are capable of moving the tip with pm precision by applying voltage pulses to the electrodes of the piezoelectrics.

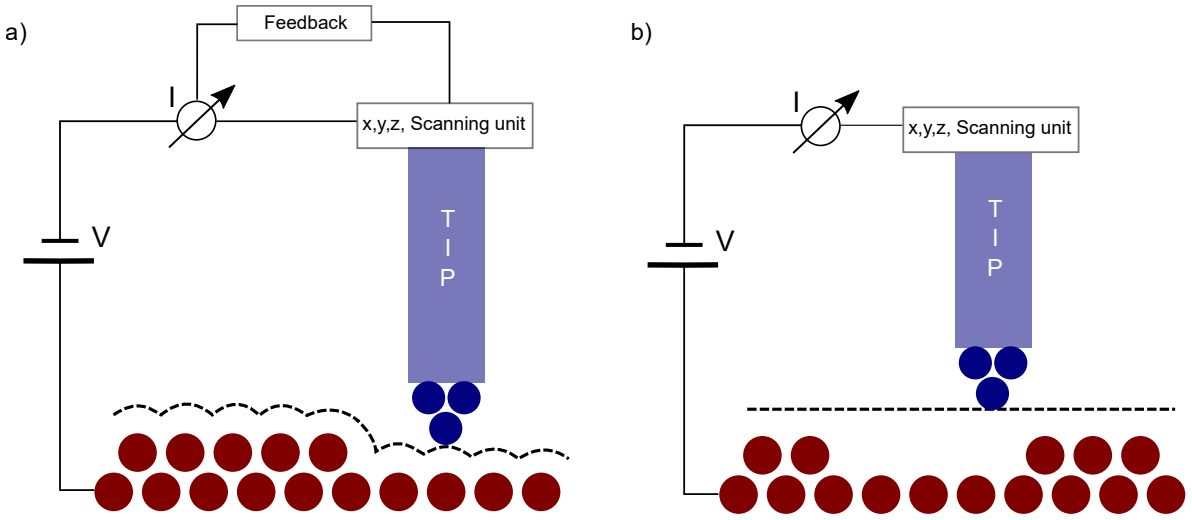

Figure 2.2.4: Measurement modes of STM. a) Sketch of the constant current mode. b) Sketch of the constant height mode.

For standard operational distances of 1 nm, electrons can tunnel from the last atoms of the tip through the vacuum barrier into the sample with a probability that decays exponentially with the distance between tip and sample (see eq. (2.6)). The scanning of the tip can be performed with two distinct measurements modes. In the most common mode, i.e. the constant current mode (see Fig. 2.2.4 a), the tip scans in x- and y-direction over the sample surface, while a PI feedback loop is regulating the tip z-movement to keep the current at a defined set point. An image of the surface can then be constructed by rendering the z-movement of the tip at every pixel in a n×m matrix. The second measurement mode is the constant height mode (see Fig. 2.2.4 b). In this mode no feedback loop is used and the tip does not move vertically. The tip is scanned in x- and y-direction and the varying tunnel current generates the contrast of the sample topography. The high resolution of this technique is given by the exponential change of tunneling current by a factor of ∼10 corresponding to a distance change of 0.1 nm, which is about the size of one atom.

Spectroscopic measurements are acquired as single curves, line-spectra or grid-spectra. For that, dI/dV curves are measured at defined pixel locations in an area of interest.

2.2.3 Experimental setup and cooling operations

The scanning tunneling microscope used during this thesis is a commercial Unisoku 300 mK - 11 T - STM operated at ultra-high vacuum conditions ($< 10^{-10}$ mbar). The experimental design and its cooling mechanism for reaching the three different regular operation modes at 4.2 K, 1.2 K and 0.3 K as well as its capability to vary the temperature in the range of 0.3 K < T < 15 K are discussed in the following sections.

The STM system

The most important parts of the STM system are labelled in Fig. 2.2.5. The entire system is mounted on a table, which is kept floating through vibration damping legs filled with nitrogen gas (indicated in light blue). The STM system is equipped with a loadlock chamber (yellow), where samples and tips can be introduced, and the preparation chamber (red), which contains a sputter gun, a sample heating stage, a tip heater, and a pre cooling mount. In the preparation chamber we perform the Se-decapping process of our samples, clean crystals by consecutive cycles of sputtering and annealing, and prepare new tips through sputtering and high temperature annealing. A mass spectrometer (light green) is mounted in case of appearance of a vacuum leak. It can be used to locate such a leak by carefully blowing He-gas to the flanges of the system and monitoring the He amount in the chamber. The cryostat (pink) is located underneath the vacuum chamber, hanging on the floating table. At the bottom of the cryostat is the STM head. The samples are transferred down via the long transfer rod (dark green) on the top. The STM head is a Pan-design, which is known for its high stability at low temperatures and high magnetic fields.[111]

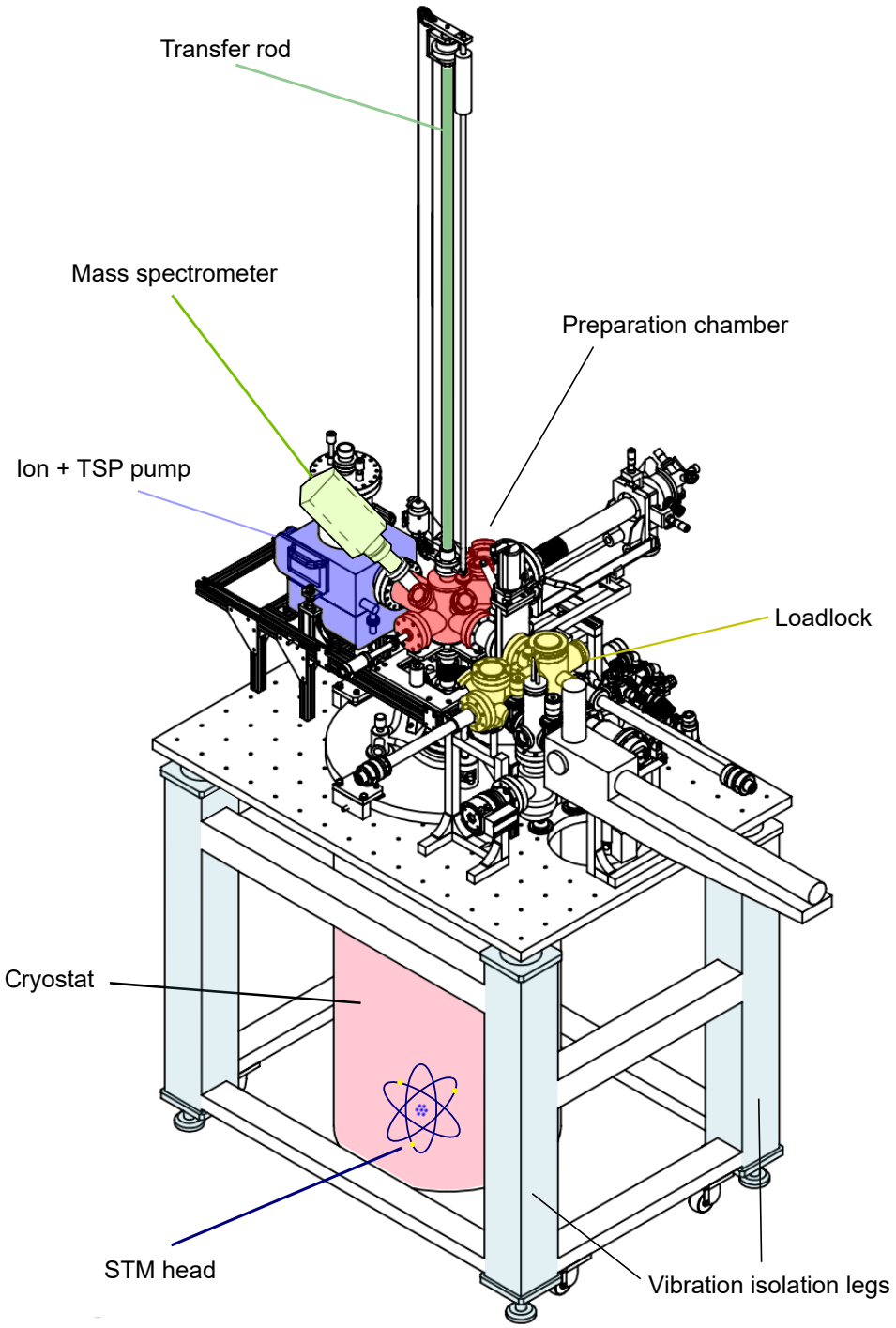

Figure 2.2.5: The STM system. Highlighted are the operation components and most important parts of the machine. Figure adapted from Unisoku USM1300 manual.

Operation modes

The STM system enables several stable operation modes at temperatures of 4.2 K, 1.2 K and 0.3 K. In standard operation, the temperature is kept at 4.2 K by using liquid helium-4 (L^4He) for cooling the inner cryostat and liquid nitrogen (N_2) for cooling the outer cryostat. The thermal insulation layer is filled with ^4He gas to increase the heat exchange between the cryostat and the sample stage. In order to reach the 1.2 K measurement mode, it is necessary to pump ^4He gas through the so-called 1K pot (see Fig. 2.2.6) and thermally isolate the STM head from the rest of the setup by pumping out the thermal insulation layer. By decreasing the vapor pressure in the 1K pot, the evaporation temperature of ^4He can be decreased to 1.2 K and therefore measurements at this temperature are possible. The needle valve, which is a tiny inlet for the L^4He into the 1K pot has to be opened until an equilibrium state between L^4He flowing in, and gaseous ^4He pumping out, is reached. That being the case the temperature is stabilized at 1.2 K. For some particular research tasks it is necessary to cool down even further. This is done by introducing ^3He, which has an evaporation temperature of 0.3 K at a vapor pressure of $1.3 \cdot 10^{-5}$ bar.

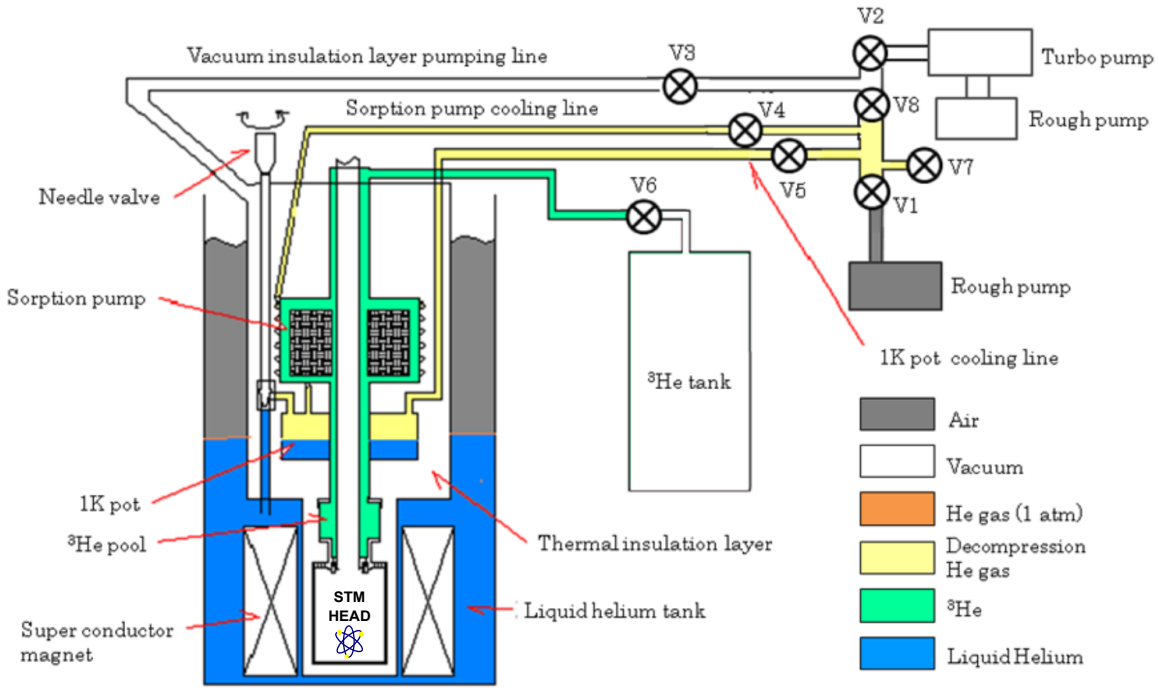

Figure 2.2.6: A sketch of the cooling operations of the STM system and the cryostat, respectively. In this situation the thermal insulator layer is in vacuum condition and the STM operates in the 0.3 K mode. Figure adapted from Unisoku USM1300 manual.

The gas is filled and kept in a closed circular line, which has the so-called ^{3}He pool directly attached at the top of the STM head. By heating up the sorption pump to 50 K, and simultaneously keeping the temperatures of the 1K pot and head below 2 K, it can be made sure that all ^{3}He in the line is in its gas phase and conditions for ^{3}He condensation are satisfied. Then, by stopping to heat the sorption pump it will automatically cool down by thermalization and start to trap the ^{3}He gas in its porous material. The ^{3}He gas condenses and drops down into the ^{3}He pool, where it thermalizes at ~ 0.3 K with the STM head.

A filament located at the STM head can be used to heat the sample in the range of $0.3\,\mathrm{K} < \mathrm{T} < 15\,\mathrm{K}$. This is a very important feature of our STM, because it allows us to perform temperature dependent measurements, which potentially contain valuable information on quantum phase transitions, e.g., the critical temperature of a superconducting material.

Magnetic field

Another relevant capability of this STM is the superconducting magnet, which is capable of generating a vertical (z-direction) magnetic field of up to ± 11 T and is located at the bottom of the cryostat wired around the STM head. It is composed of two coils made from several gauges of NbSn and NbTi wires on stainless steel and aluminium formers, respectively. The windings are wired with a superconducting persistent mode switch connected in parallel across the whole magnet, connected to the main input and output current terminals. A heater is fabricated into the switch, which enables it to be either resistive or superconducting. Two different operation modes do exist, where in one of them the supercurrent is trapped inside the magnet, by turning of the heater. In the other operation mode, the switch is constantly heated and current can flow in and out.

CHAPTER 3

Collective electronic states in 2D Ising superconductors: $NbSe_2$

$NbSe_2$ has been serving as a model 2D material for the exploration of collective electronic phases such as superconductivity (SC), charge density wave (CDW) order, magnetic order, and their interplay. Due to the possibility of growing this TMD material in UHV by MBE, CVD, and ALD with high crystallinity as well as the opportunity to exfoliate and transfer it, great progress could be achieved studying its electronic and magnetic properties in 2D. Since it was shown that SC and CDW order coexist, especially important breakthroughs such as the revelation of Ising superconductivity, a continuous paramagnetic-limited superconductor-metal transition, and the visualization of multifractal superconductivity were identified.[10, 112, 11, 113]

In this chapter two different approaches are deployed in order to investigate SC and the CDW phase in this material. In the first section, the electron pairing mechanism is discussed. The experimental analysis of STS data at varying temperatures and magnetic fields are supported by a developed theoretical model, which proofs the existence of a so-called Leggett mode. These observations are evidence for a f-wave triplet pairing channel competing with the s-wave singlet ground state in SL-$NbSe_2$. In the second section, proximity effects of the supporting substrate on the 2D material are explored.

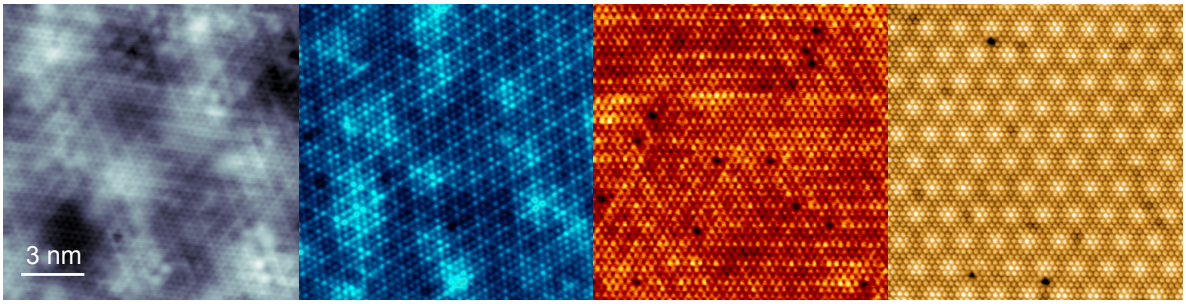

3.1 Atomic structure and electronic properties of 1H-$NbSe_2$

This chapter focuses on the H-phase of SL-$NbSe_2$. In Fig. 3.1.1 the unit cell (a), top-view (b) and side-view (c) of the atomic structure is illustrated. The delineated unit cell has an atomic lattice parameter of $a = 3.44\,\text{Å}$. The trigonal prismatic crystal structure (point group D_{3h}) of SL-$NbSe_2$ is non-centrosymmetric, which has crucial consequences for its collective electronic phases discussed at a later point in this section. While the Se and Nb atoms form strong covalent bonds within the plane, the weaker van der Waals forces between the layers allow mechanical [114, 67] and liquid exfoliation [115] of ultrathin sheets.

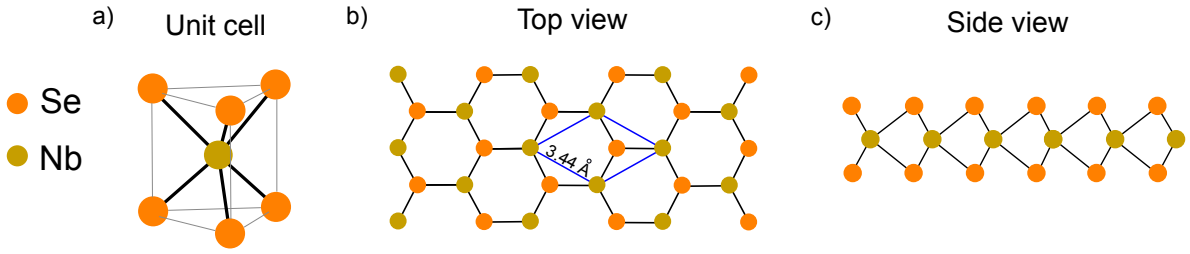

Figure 3.1.1: The atomic structure of H-phase SL-$NbSe_2$. a) Unit cell, b) Top view and c) side view.

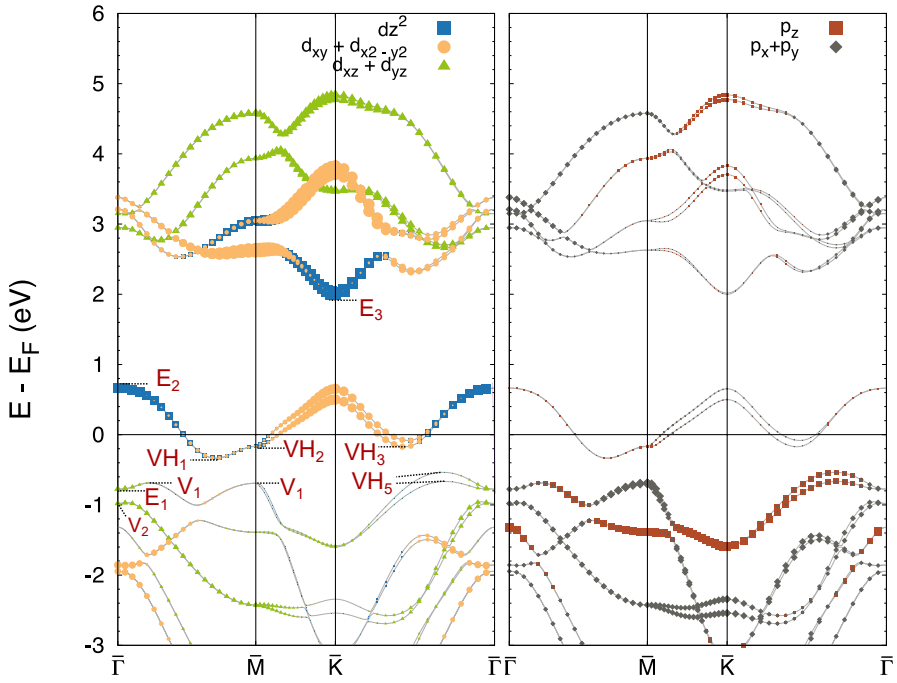

Figure 3.1.2: Calculated electronic band structure of SL-$NbSe_2$. Prominent electronic features (VH_i, E_2, V_1, V_2) of the band structure are indicated.

Fig. 3.1.2 presents the electronic band structure with spin-orbit coupling of SL-1H-$NbSe_2$. The orbitals contributing to each state (listed in the legend in the top right) are projected on to each band. It is dominated by a Nb-derived 4*d* band crossing the Fermi level (E_F) that sustains both the CDW and SC.[116, 117] The Nb 4*d* states crossing the E_F form two hole pockets around the $\overline{\Gamma}$ and $\overline{K}$ points. This band is separated from the fully occupied Se p_z bands (V_1), whose onset is located at -0.8 eV, by a bandgap of ∼0.4 eV. The band structure shows several characteristic features such as van Hove singularities (VH_i) as well as flat regions above (E_1, E_2, E_3) and below (V_1, V_2) E_F that can be identified and tracked in STS and ARPES spectra.[6] We will refer back to this important Figure in the following chapters, especially for the study of substrate induced proximity effects (see section 3.4) as well as for the discussion of $Nb_\delta Mo_{1-\delta}Se_2$ alloys (chapter 4), as we can track its modification by these external perturbations.

Following, a comparison of the electronic band structure between the bulk $NbSe_2$ and the SL-$NbSe_2$ is presented and discussed. The band structure changes significantly when reducing the dimension from 3D to 2D, as illustrated in Fig. 3.1.3 a) and b). In the case of bulk $NbSe_2$ three bands cross the Fermi level E_F. Two of these bands are Nb-derived and are degenerate in the A-H-L plane; however, spin-orbit interaction removes the degeneracy.[116] The third one is a Se-derived p_z band, which disperses along k_z and is not corssing E_F in the A-L-H plane. Due to interlayer coupling, the degeneracy is lifted, which leeds to a 3D Fermi surface for the bulk Nb bands. Thus, in the 3D case, hopping between the layers has to be considered.[31] In the bilayer, the Se-Se interaction is already reduced, where in the SL limit it vanishes. Subsequently, the Se-band shifts below E_F in the SL and only one Nb-derived band crosses E_F, which has a strictly 2D Fermi surface (compare Fig. 3.1.3 a) and b).[116]

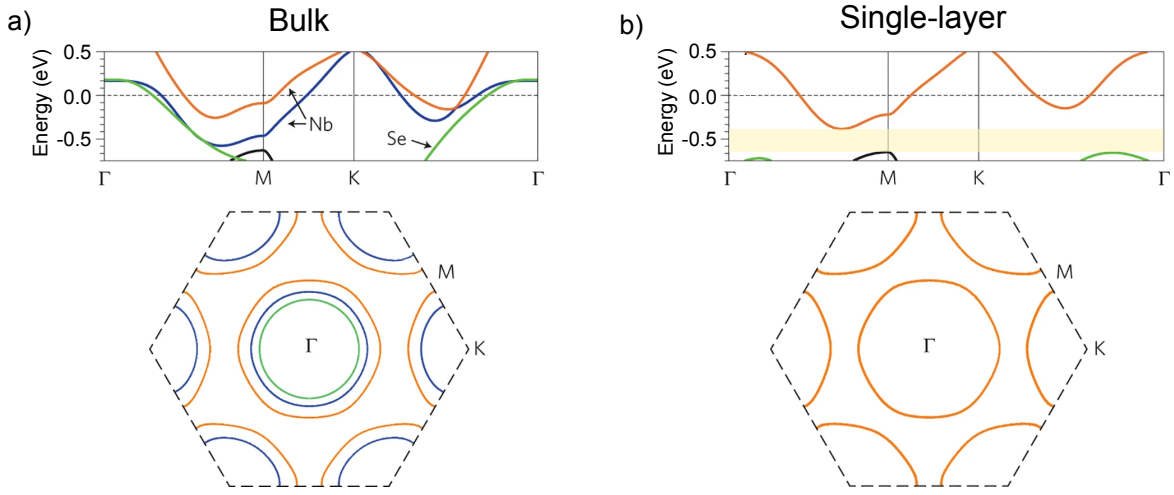

Figure 3.1.3: Comparison of electronic band structure of bulk $NbSe_2$ and SL-$NbSe_2$/BLG/SiC(0001). DFT calculated band structures (top) and Fermi surfaces (bottom) for a) bulk $NbSe_2$ and b) SL-$NbSe_2$/BLG/SiC(0001), respectively. Figure adapted from [6, 116].

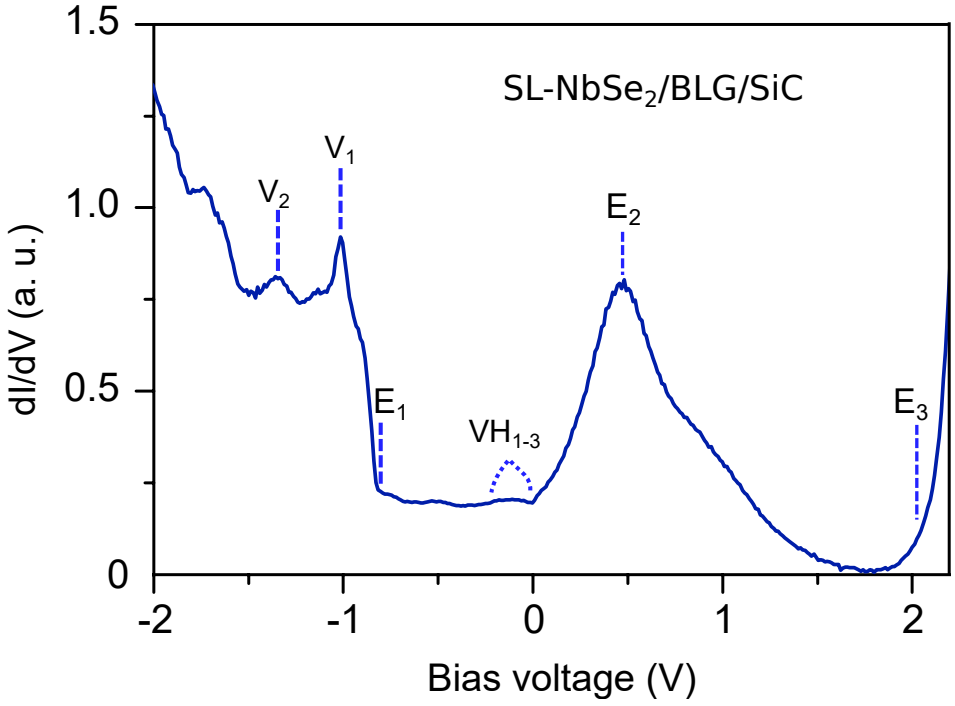

Figure 3.1.4: STS measured dI/dV curve of SL-$NbSe_2$/BLG/SiC with major features indicated. Measurement parameters: f = 833 Hz, T = 4.2 K, $V_{a.c.}$ = 3 mV.

Next, we show the large bias-voltage range dI/dV curve measured by STS for SL-$NbSe_2$ (grown on BLG/SiC(0001)). The characteristic features identified in the calculated electronic band structure (Fig. 3.1.2) can be attributed to the STS measurements and are marked as VH_i, V_i and E_i. The most significant feature for SL-$NbSe_2$/BLG/SiC in the positive bias range is a peak with its maximum at $E_2 = +0.46 \pm 0.05$ V, which can be associated to the flat region at the top of the Nb-derived band at $\overline{\Gamma}$ (E_2 in Fig. 3.1.2). Another prominent feature is the increase of DOS at an onset energy of $E_3 = +1.92 \pm 0.05$ V. In the negative bias range (filled states), several features are present: (i) Although only faintly visible in this scale, low intensity DOS arise at $VH_{1-3} \sim$ -0.25 $\pm$ 0.05 V, (ii) a flat region of DOS corresponding to the band gap, (iii) a steep onset of DOS at $E_1 = -0.81 \pm 0.16$ V, (iv) a peak V_1 slightly below this energy, which is consistent with the top of the Se-derived band at the $\overline{M}$-point, and (v) another peak at V_2 = -1.32 $\pm$ 0.12 V, which belongs to the next lower valence band.

At low temperatures, SL-$NbSe_2$ exhibits a 3×3 CDW order and SC with critical temperatures of $T_{c,cdw} \approx 33$ K and $T_{c,sc} \approx 1.9$ K, respectively [6, 118]. While the strength of superconducting order is reduced in the 2D limit manifested in the reduction of $T_{c,sc}$ from 7.2 K to 1.9 K, the 3×3 CDW ordering remains constant in the SL-limit.[6] Recent experiments have shown various exceptional behaviours regarding the superconducting state in this material. For instance, SC in SL-$NbSe_2$ can persist in the presence of large in-plane magnetic fields exceeding the Pauli limit.[10] As described in the introduction

of this thesis, this effect is caused by pinning electron spins to the out-of-plane direction by spin orbit coupling (SOC) and it is called Ising SOC. Furthermore, the absence of inversion symmetry in SL-$NbSe_2$ enables singlet-triplet mixing, what remains so far of unknown magnitude.[119] More recently, transport experiments have revealed a two-fold anisotropy of the superconducting state under in-plane magnetic fields, which has been interpreted in terms of a competing nematic superconducting instability.[120, 121] In parallel, tunneling junction experiments also claimed the existence of a subleading triplet order parameter to explain the dependence of the gap to in-plane fields in the thin film limit. [122]

3.2 Epitaxial growth of single layer $NbSe_2$

In this chapter we describe two different research projects, one focused on the SC pairing mechanism, and the second one focused on substrate induced proximity effects to the SL-$NbSe_2$. In order to study the symmetry of the SC pairing, we want to minimize the substrate interaction. Therefore, in the first section, particular interest is on SL-$NbSe_2$ grown on BLG/SiC(0001). The growth procedure has only minor differences when the TMD is grown on the distinct substrates. Thus, in this section the fabrication is explained in detail for the case of 1H-$NbSe_2$/BLG/SiC(0001). In the following section, the subtle, but important differences when growing the material on various electronically distinct substrates, are discussed (see table 3.1).

Single layers of $NbSe_2$ were grown on 6H-SiC(0001) by MBE at a base pressure of $5{\cdot}10^{-10}$ mbar in our home-made UHV-MBE system described in the methodology section. We have used SiC wafers with resistivities of $\rho \sim 120\,\Omega \cdot cm$. Before they are inserted to the UHV system, they are cleaned with an Isopropyl solution in an ultrasonic bath. After inserting the wafers into the MBE chamber they have to be outgassed for ~ 60 min at 700°C. Subsequently, we start the graphitization process. For that we have used an automatized method to produce the graphene, which was inspired by the study of Wang et al.[123] A cycling mechanism was developed to epitaxially grow the BLG on top of SiC. With this method, implemented in MATLAB, the power supply is ramping between 700°C and 1350 °C at a defined ramp speed, with the pyrometer temperature, power output and pressure as feedback parameters. The maximum temperature is reached after 30 s. The SiC crystal is kept at this temperature for another 30 s, while the graphitization is performed. In this situation the pressure is rising up to $\sim 2{\cdot}10^{-7}$ mbar. Therefore, after 30 s, the temperature is ramped down again. After a certain threshold of $5{\cdot}10^{-8}$ mbar could be reached, another cycle is performed. In total 80 cycles were needed, in order to get the best quality BLG terraces. For later projects we used a simplified approach to grow the graphene, where we kept the substrate for 35 min at the desired graphitization temperature of $1400\,°C$. This was possible due to a longer (~ 2 hours) outgassing procedure before the actual growth of the material. Therefore, during the growth, the pressure does not rise that high. With this method, we can also reach large SiC terraces $> 0.5\,\mu$m and therefore high quality SL-$NbSe_2$ domains (see Fig. 3.2.1 c).

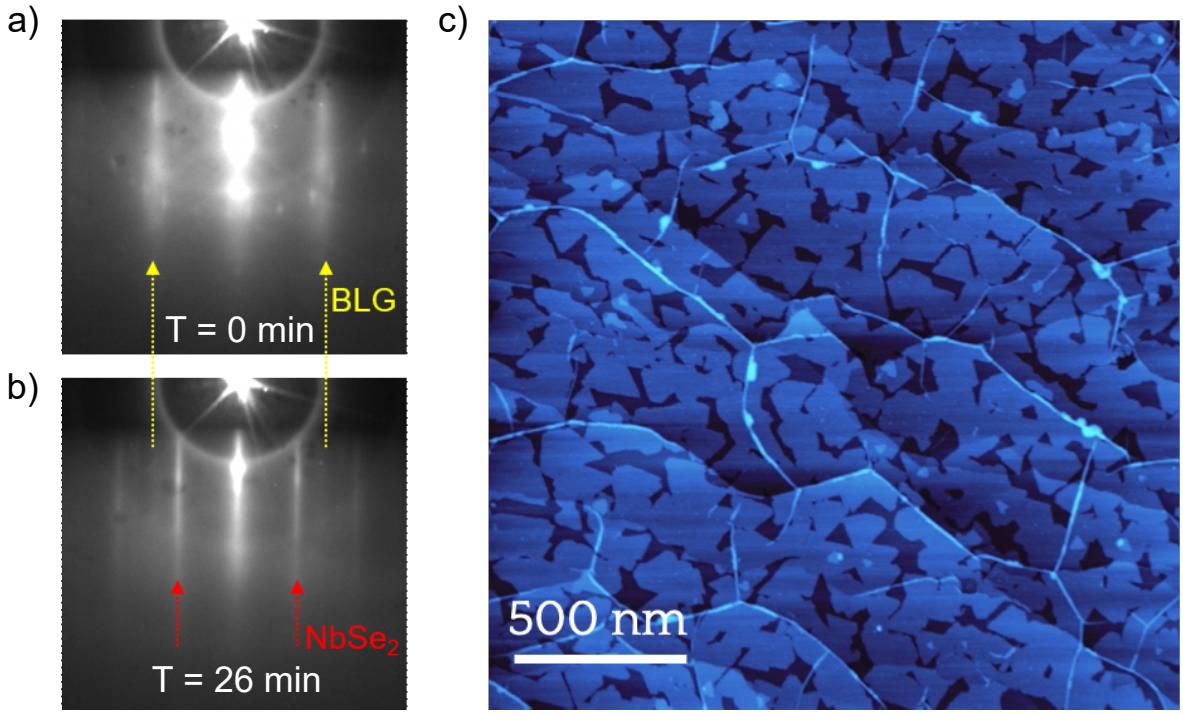

Figure 3.2.1: Growth of single-layer $NbSe_2$. a) At t = 0 before the growth of the material, only the BLG structures (yellow lines) are visible in the RHEED pattern. During the growth the diffraction pattern of SL-$NbSe_2$ gradually becomes more prominent. b) After 26 min, the intensity of the $NbSe_2$ reaches close to a maximum and thus a nearly full monolayer is grown. c) AFM image of the SL domains.

For an optimized SL-$NbSe_2$ growth we have used high purity Nb (99.99%) and Se (99.999%). At a substrate temperature of 570 °C the Nb:Se flux of 1:30 was found to be ideal in order to grow an almost full ML with an evaporation time of 26 min. Important to mention is that we have used an extra 5 min after the initial growth, where we kept the Se evaporator open. In this process we aimed to minimize the density of Se vacancies. Selenium has an evaporation temperature of 150°C. Therefore, at typical growing temperatures (570°C) the Se sticking coefficient is negligible and the Se atoms are immediately re-evaporated, unless they can instantly bind with a Nb atom.

The RHEED system can be used to monitor the formation of the graphene as well as for the synthesis of the SL-$NbSe_2$. RHEED measurements before and after the growth of SL-$NbSe_2$ are shown in Fig. 3.2.1 a) and b), where the newly appearing lines indicate the layer formation. In Fig. 3.2.1 c), a large scale AFM image illustrates the surface morphology. One can see the typical BLG terraces ($\sim 0.5\,\mu$m), with SL-$NbSe_2$ islands (100 - 400 nm) grown on top of it. All the sample used for characterization by AFM were not further used for STM measurements, as oxidation instantly degrades the sample surface when it is taken out from the UHV chamber. In order to avoid contamination of the samples during their transfer in ambient conditions from the MBE to other probe systems, we have

used Se capping layers, which are capable of protecting the samples in ambient conditions. Therefore, we have evaporated $\sim 20\,\text{nm}$ of additional Se onto the surface, while the sample was kept at room temperature. After the sample was transferred to any other UHV system (STM, ARPES, XPS, etc.), the capping layer could easily be removed by annealing the sample at $\sim 250°\text{C}$.

MBE growth of SL-$NbSe_2$ on various substrates

In order to investigate proximity effects on SC and CDW ordering (see section 3.4), we have grown and studied SL-$NbSe_2$ on various substrates, namely BLG on 6H-SiC(0001), h-BN on Ir(111), Au(111), and bulk WSe_2. The growth processes slightly vary in each case, especially in regard of the substrate temperature and the growth time. Table 3.1 shows the applied growth parameters for each substrate.

Table 3.1: Optimized growth parameters of single-layer $NbSe_2$ on various substrates.

Substrate	Temperature [°C]	Growth time [min]
BLG/SiC(0001)	580°C	30
WSe_2	550°C	25
Au(111)	560°C	20
h-BN/Ir(111)	590°C	45

3.3 Superconducting Leggett modes from competing pairing instabilities

In certain unconventional superconductors with sizable electronic correlations, the availability of closely competing pairing channels leads to characteristic soft collective fluctuations of the order parameters, which leave fingerprints in many observables and allow to scrutinize the phase competition. Superconducting layered materials, where electron-electron interactions are enhanced with decreasing thickness, are promising candidates to display these correlation effects. In this section we study the superconducting properties of SL-$NbSe_2$ with focus on characteristic features in STS spectra (at 0.35 K), which we prove to be a soft collective mode by comparing our experimental results with a developed theoretical model.

3.3.1 State of the art

In the Migdal-Eliashberg theory [124, 125] of superconductivity, electron-phonon coupling is responsible for the attraction that binds Cooper pairs together in the standard s-wave channel. In superconductors with significant electronic correlations, however, the Coulomb repulsion can be detrimental for pairing and other mechanisms need to be invoked to explain the emergence of "unconventional" superconductivity, which often occurs with different pairing symmetry in the spin or orbital sectors. Several classes of correlated electron systems such as the cuprates [126–129], iron-pnictides [130–132], iron-chalcogenides [132–134], and several heavy-fermion compounds [135, 136] have been identified as unconventional superconductors. Recently, superconductivity with unconventional features has also been identified in twisted bilayer graphene (TBLG) [137]. The different experimental complexities to produce and probe these materials make the study of their unconventional superconductivity a formidable problem.

In this arena, transition metal dichalcogenides (TMDs) are promising candidates to provide an alternative route to unconventional superconductivity. Electronic correlations are intrinsically present in this family of layered materials, which manifest in various ways such as in Mott phases [106], magnetic order [138, 119, 139], charge/spin density waves [6], quantum spin liquids [27] and superconductivity [9, 140, 6, 10, 112, 11]. Furthermore, in 2D electron–electron interactions are markedly enhanced due to reduced screening, which can enable non-phononic Cooper pairing mechanisms.

Among 2D TMD SCs, SL-$NbSe_2$ has received the most attention and its superconducting properties have been extensively studied [11, 113]. Recent findings have identified this SL-TMD as an ising SC [10] with enhanced robustness to in-plane magnetic fields [112]. Furthermore, singlet-triplet mixing in the superconducting pairing was reported [119, 141], what remains so far of unknown magnitude. Another very interesting characteristic about the superconducting state of SL-$NbSe_2$ is the recently reported nematic instability.[120, 121]

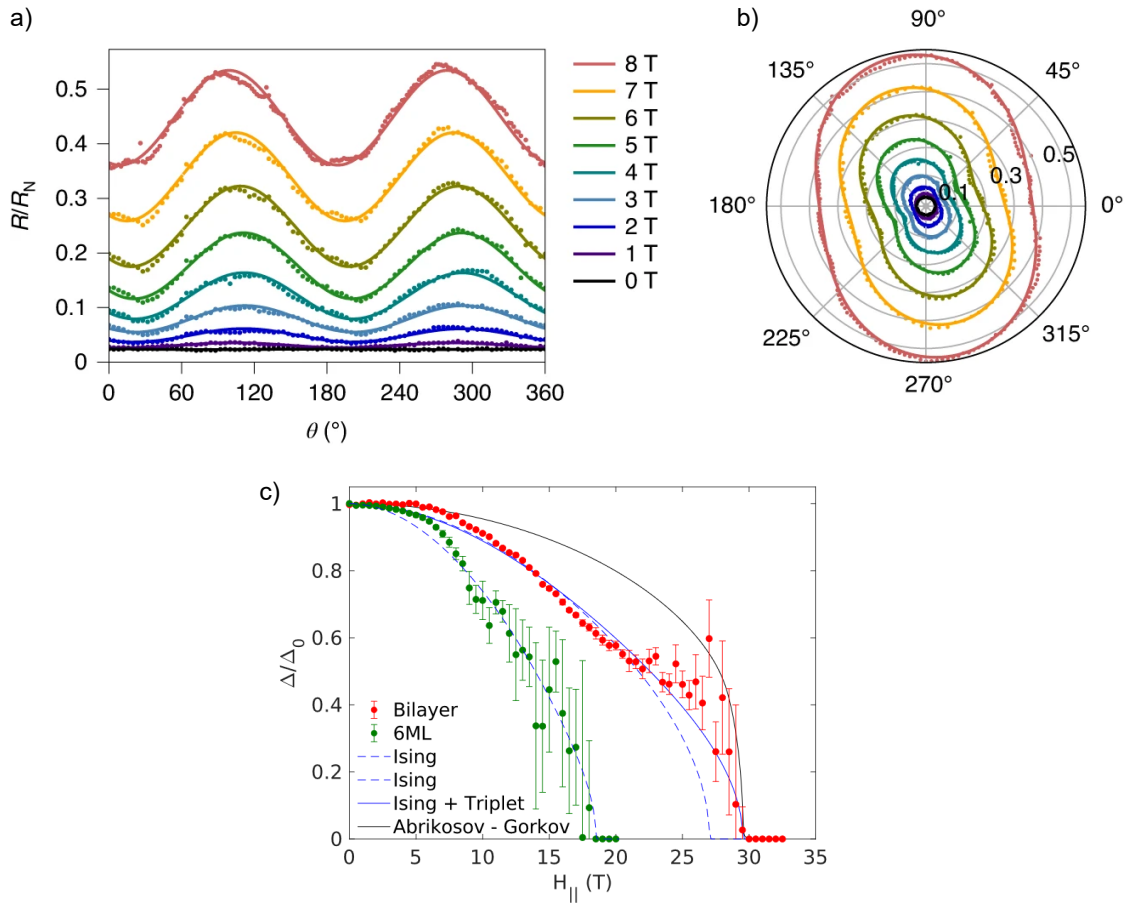

Figure 3.3.1: Closeness of superconducting pairing channels in few layer $NbSe_2$. a) Field dependence (T = 4.2 K) of the magnetoresistance.[120] b) Radial plot of the data in a).[120] c) Normalized superconducting energy gap as a function of the in-plane magnetic field.[122]

Fig. 3.3.1 a) and b) show the main result of this effect, which is the observed two-fold rotational symmetry of the superconducting state under the application of an in-plane magnetic field. This is in contrast to the three-fold symmetry of the underlying crystal lattice. Such observation are confirmed by varying the temperature ($T > T_c$) for fixed magnetic fields, where they find a suppression of the angular modulated resistance. Such intruiging dependency on in-plane magnetic fields was explained with the existence of a subleading triplet order parameter, which mixes with the conventional s-wave singlet instability. This unconventional superconducting behaviour was confirmed in another study (Fig. 3.3.1 c), where in $NbSe_2$ at the 2D limit, the intriguingly high stability of the superconducting state at strong magnetic fields is explained by a subdominat triplet component of the order parameter. Such a triplet state is supposed to arise from the non-colinearity between the applied magnetic field and the Ising field. [122] These experiments suggest sizable electronic correlations as the origin of the competing pairing instabilities.

In this work, by means of high-resolution STS measurements at 0.35 K, we have observed a collective mode univocally associated to superconductivity, which we attribute to a related competing triplet (f-wave) pairing channel. This finding strongly suggests that many-body correlations play a dominant role in the emergence of superconductivity among TMD superconductors.

3.3.2 Superconducting properties of single layer $NbSe_2$

We investigate the superconducting properties of SL-$NbSe_2$ with samples grown by molecular beam epitaxy (MBE) on bilayer graphene on SiC(0001) substrates (see section 3.2 for details). The large scale STM image of Fig. 3.3.2 a) illustrates the typical morphology of our $NbSe_2$ monolayers. As mentioned before, SL-$NbSe_2$ exhibits charge density wave (CDW) order and superconductivity with critical temperatures of $T_{c,cdw} \approx 33$ K and $T_{c,sc} \approx 2$ K, respectively [118, 6]. Both electronic phases develop a gap feature in the density of states (DOS) at the Fermi level (E_F) that can be measured via low-bias STS measurements. The CDW gap in the dI/dV spectra (Fig. 3.3.2 b) appears as a V-shaped dip at E_F bound by coherence peaks with average locations around $\pm$ 3 - 5 mV.

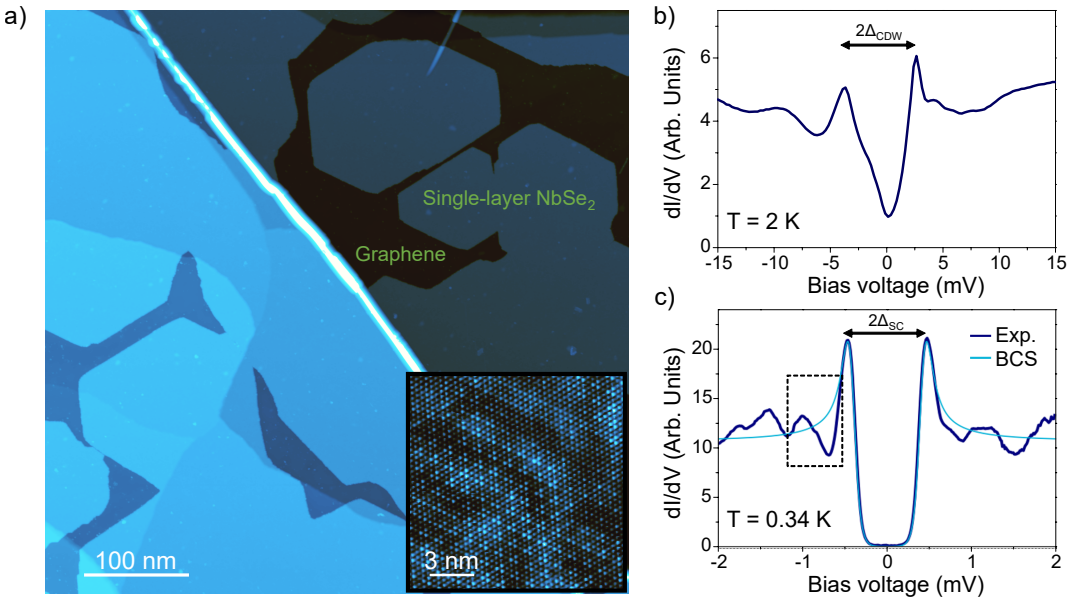

Figure 3.3.2: Morphology and low-energy electronic structure of SL-$NbSe_2$. a) Large-scale STM image of SL-$NbSe_2$/BLG/SiC(0001) in the submonolayer coverage range (V_s = +105 mV, I = 0.01 nA, T = 0.34 K). The inset shows an atomically resolved STM image of the $NbSe_2$ layer showing the 3×3 CDW order (V_s = +30 mV, I = 0.46 nA, T = 0.34 K). b-c) Low-bias STM dI/dV spectra acquired on single-layer $NbSe_2$ showing the CDW gap (Δ_{CDW}) (f = 833 Hz, $V_{a.c.}$ = 200 μV) in (b) and the superconducting gap (Δ) (f = 833 Hz, $V_{a.c.}$ = 20 μV) in (c). The boxed region in (c) shows one of the characteristic dip-hump features found in this system.

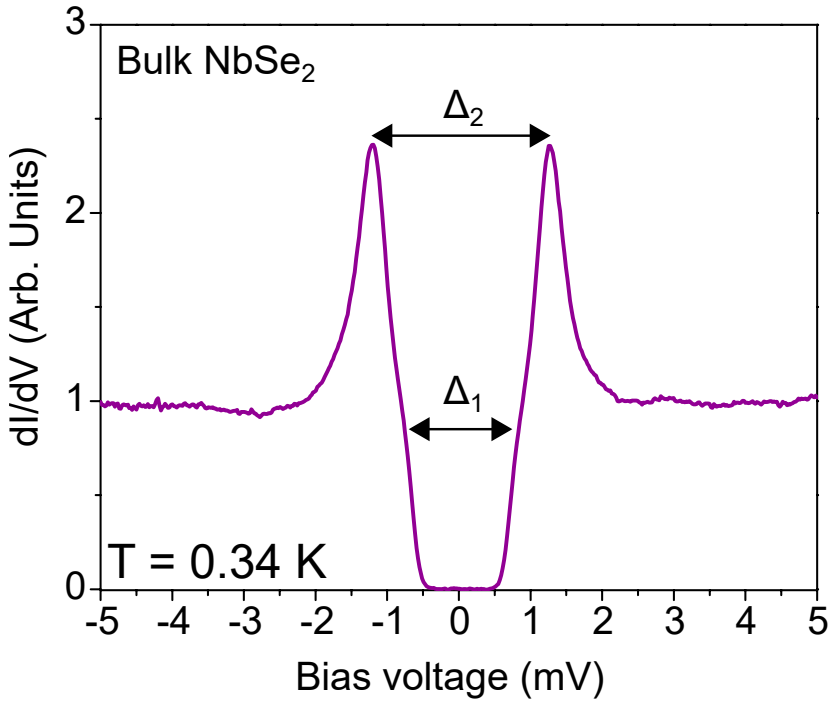

Figure 3.3.3: Low-energy electronic structure of bulk $NbSe_2$. Measuremet parameters: f = 833 Hz, $V_{a.c.} = 30\,\mu V$.

The CDW only gaps out a fraction of the Fermi surface, which allows the development of superconductivity at lower temperatures. The fingerprint of the superconducting state in single-layer $NbSe_2$ is shown in the dI/dV curve acquired at T = 0.34 K (Fig. 3.3.2 c). This spectrum reveals an absolute gap that fits the BCS gap of width $\Delta_{BCS} = 0.38$ meV (light blue curve). The averaged BCS gap over different locations is $\overline{\Delta_{BCS}} = 0.4$ meV. As can be seen, however, the experimental conductance for energies higher than the coherence peaks ($|V| > 0.6$ meV) departs from the BCS conductance and shows several dip-hump satellite features at both polarities, such as those shown in the dashed rectangle in Fig. 3.3.2 c). We note that these STS features are unique to SL-$NbSe_2$ and are not present in the bulk material.[142, 143] In order to confirm this, we have measured the differential conductance in bulk $NbSe_2$ at 0.34 K as shown in Fig. 3.3.3. The bulk $NbSe_2$ does not show any significant features in the quasi particle DOS. Furthermore, it differs from the SL-$NbSe_2$ by forming two superconducting gaps $\Delta_1 = 0.75$ mV and $\Delta_2 = 1.2$ mV, arising from two gaps in the Fermi surface.[143]

To better describe these spectral features, Fig. 3.3.4 a) shows four dI/dV curves taken in different locations. These curves reveal the existence of multiple dip-hump features (or peaks) at both polarities, which are seen usually symmetric with respect to E_F and nearly equidistant. We performed statistical analysis of over 2855 dI/dV curves acquired at T = 0.34 K in different spatial locations, using several samples and tips.

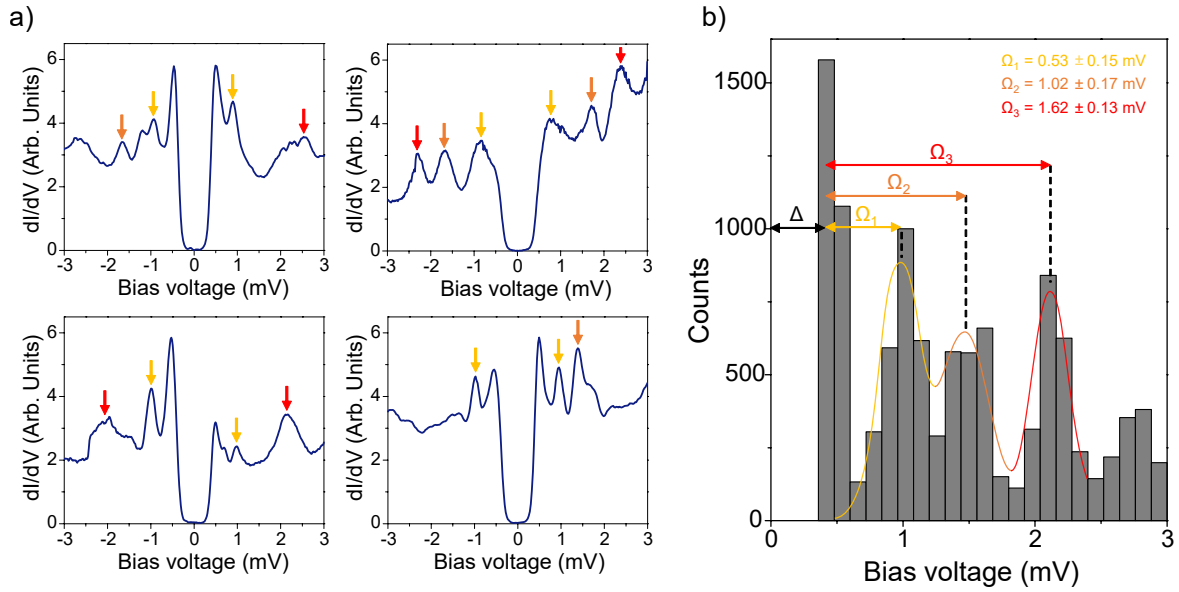

Figure 3.3.4: Statistical analysis of the STS dip-hump features. a) Four representative dI/dV curves acquired in single-layer $NbSe_2$ at T = 0.34 K. The arrows identify the fundamental Ω_1 mode (yellow) and the harmonics Ω_2 (orange) and Ω_3 (red). Parameters: f = 833 Hz, $V_{a.c.} = 20\,\mu$V. b) Histogram of 2855 dI/dV curves acquired on different locations, and using different samples and tips. Three clear peaks can be identified for energies larger than the superconducting gap (Δ). A Gaussian fit to the peaks yield the averaged values.

As seen in the histogram (Fig. 3.3.4 b), this analysis reveals the existence of three clear satellite peaks within $|V| = 3$ mV (both polarities exhibit similar statistics) at well defined energies ($\Omega_{n=1-3}$). A much weaker and wider fourth peak is also present in the histogram, but since its energy is close to the CDW coherence peaks, we will not consider it further as a replica. The main energy values of the identified peaks ($\Omega_{n=1-3}$), as defined from the nearest coherence peak ($\Omega_n = E_n - \Delta$ with E_n the energy of the n-th peak from E_F), appear to be in all cases multiple of the energy of the first peak, i.e., $\Omega_n = n \cdot \Omega_1 = n \cdot 0.53$ meV. Therefore, it appears reasonable to interpret them as harmonics of the same mode Ω_1.

3.3.3 Temperature/magnetic field dependence and spatial homogeneity

To further characterize the satellite features, we first study their temperature dependence. Fig. 3.3.5 a) shows the evolution of the Ω_1 and Ω_2 features as the temperature approaches $T_{c,sc} \approx 2$ K. As seen, the amplitude of the peaks rapidly decays in all cases, to finally disappear at 1.4 K, below $T_{c,sc} \approx 2$ K. Fig. 3.3.5 b) shows the temperature evolution of the normalized amplitude of the Ω_2 mode (measured from the conductance floor at 2 meV) for empty states (black dots).

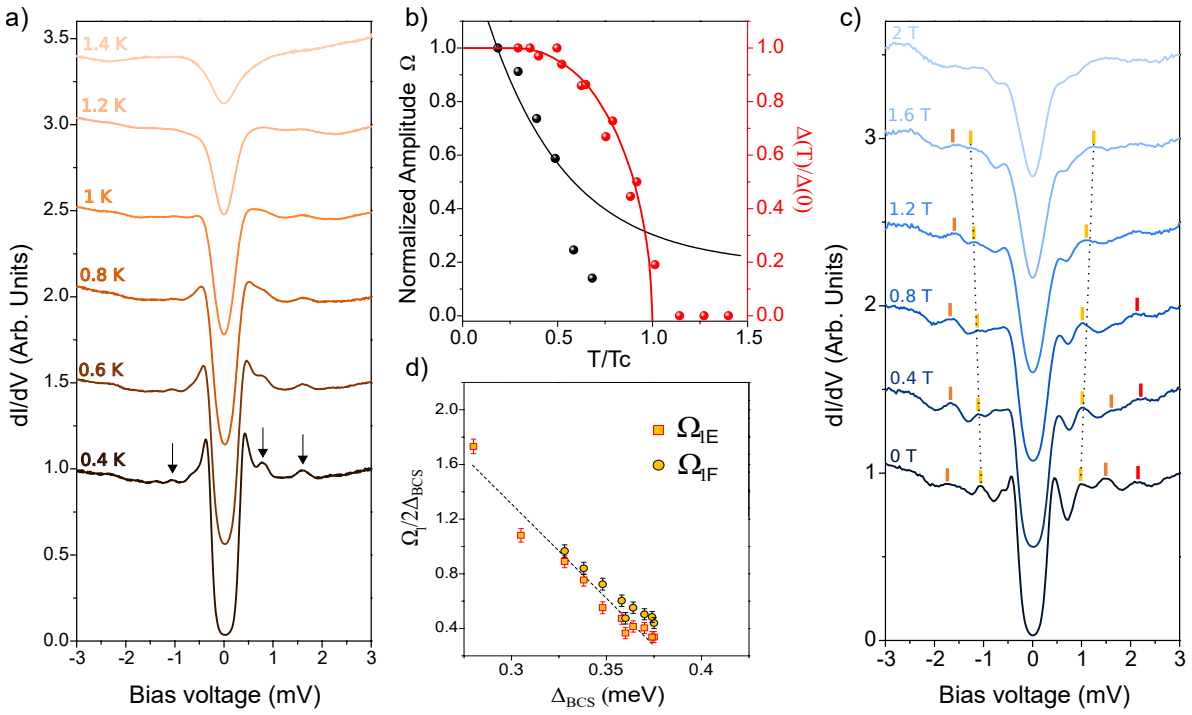

Figure 3.3.5: Temperature and magnetic field dependence of the bosonic modes. a) Evolution of the bosonic modes with temperature from 0.4 K up to 1.4 K (f = 833 Hz, $V_{a.c.} = 20\,\mu$V). b) (black dots) Normalized amplitude of the Ω_2 mode for empty states in (a) showing its decay with T below $T_{c,sc} \approx 1.9$ K. The decay of amplitude of these STS features from thermal broadening (black curve) is shown to be slower with T. In red, the evolution of the measured Δ with T (circles, fitted to BCS) along with its T-dependence in the BCS theory (line). c) Dependence of the bosonic modes with the perpendicular magnetic field (B$\perp$) up to 2 T (f = 833 Hz, $V_{a.c.} = 30\,\mu$V). Marks indicate the maxima of the resonances and dashed lines connect the energy positions of the fundamental mode Ω_1. d) Ratio $\Omega_2/2\Delta$ versus Δ extracted from the B$\perp$-evolution in c (Δ here is extracted from the BCS fit). Circles (Squares) represent the filled (empty) states Ω_{1F} (Ω_{1E}). The dashed line is the linear fit.

The amplitude decays faster than what would be expected from thermal broadening (black curve) and, therefore, their disappearance can also be attributed to the weakening of superconductivity itself, suggesting that the satellite peaks are intrinsically linked to the superconducting state. The disappearance of these features below $T_{c,sc}$ allows us to rule out other origins for these peaks unrelated to superconductivity such as band structure effects, extrinsic inelastic features and electronic renormalization due to electron-phonon interactions. Fig. 3.3.5 b) furthermore shows the reduction of the SC gap as a function of temperature (red dots), which nicely fits to the temperature dependence described in the BCS theory [58]:

$$\frac{\Delta(T)}{\Delta(T)} \approx 1.74 \cdot \left(1 - \frac{T}{T_c}\right)^{\frac{1}{2}}. \tag{3.1}$$

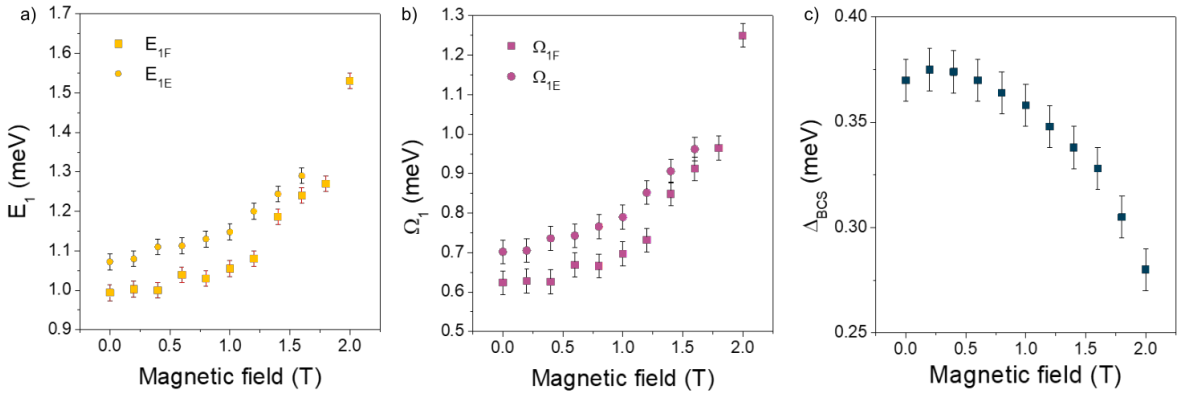

Figure 3.3.6: Magnetic field dependence of the bosonic modes. a) E_1 vs. B-field. b) Ω_1 vs. B-field. c) Δ_{BCS} vs. B-field.

Next, we examine the behaviour of the satellite peaks under a perpendicular magnetic field (B$\perp$) at 0.34 K. Fig. 3.3.5 c) shows the evolution of the Ω_1, Ω_2 and Ω_3 features in clean regions of $NbSe_2$ for B$\perp$ up to 2 T. Similar to the behaviour observed in the T-dependence, these features gradually smear out with the strength of B$\perp$ as superconductivity weakens and, ultimately, fade out within the mixed state (B_{c2}). This further confirms the intrinsic relation between these satellite features and the superconducting state in SL-$NbSe_2$. We also observe that the maxima of the satellite peaks slightly shift towards higher energies as B$\perp$ is increased. At the same time Δ_{BCS} decreases, what leads to the behavior shown in Fig. 3.3.5 d). Such anticorrelation suggests an intrinsic connection between the fundamental modes and superconductivity. In order to study the magnetic field dependence in more detail, in Fig. 3.3.6 a-c) we show the energy of E_1, Ω_1, and Δ_{BCS} as a function of the magnetic field for the data set presented in Fig. 3.3.5 c). It is evident for the fundamental mode E_1 or Ω_1, respectively, at both polarities, that they shift in a non-linear fashion. The same applies for the Δ_{BCS} what is illustrated in Fig. 3.3.6 c). While the reduction of Δ_{BCS} follows the behaviour according to BCS, at the present day, we cannot explain the non-linear increase in energy of the fundamental mode.

Apart from studying the temperature and magnetic field dependence of the fundamental mode and its connection to the superconducting gap, a different way of quantifying the relation between Ω_n and Δ is to look at local spatial variations of the superconducting order parameter $\Delta(\mathbf{r})$, and whether they correlate with the local boson energy $\Omega_n(\mathbf{r})$, as both are accessible through STS measurements. In Fig. 3.3.7, we show the correlation for the fundamental mode Ω_1 (yellow dots) and higher harmonics Ω_2 and Ω_3 (orange and red dots, respectively) from the set of dI/dV curves used to obtain the histogram of Fig. 3.3.4 b). As seen, all Ω_n modes exhibit an inverse correlation with respect to Δ with similar slope (black lines are the linear fits). This observation is consistent with the anticorrelation observed in the study of the B$\perp$-dependence (Fig. 3.3.5 d). A further key insight is the fact that the majority of the values of the fundamental mode Ω_1 are smaller than 2Δ ($\Omega_1/2\Delta < 1$).

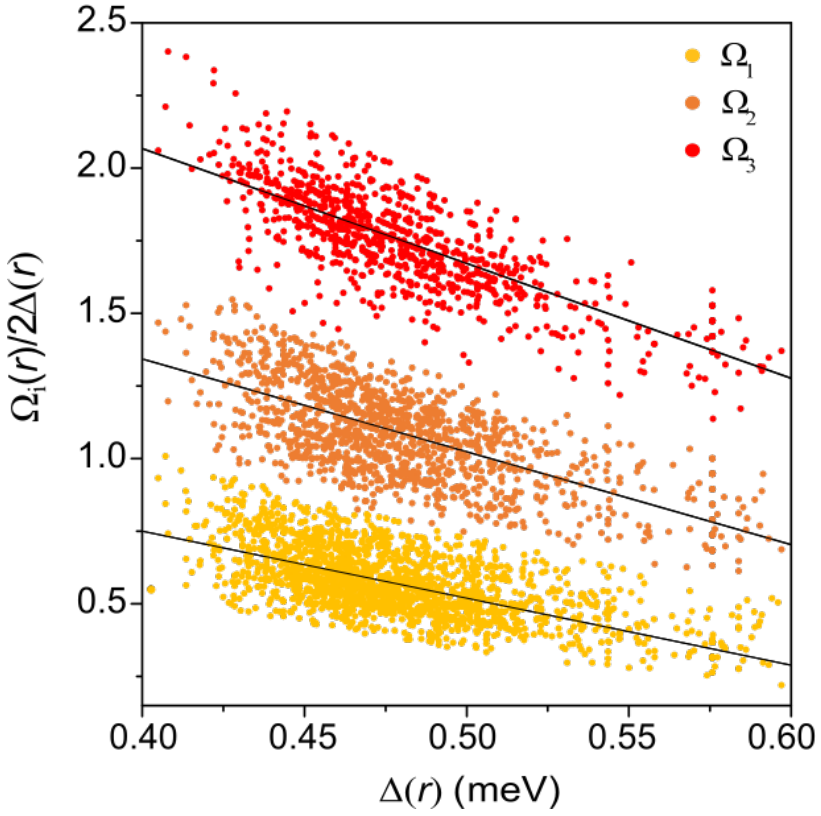

Figure 3.3.7: Local variations of the bosonic modes and the superconducting gap. Scatter plot of $\Omega/2\Delta$ against the superconducting gap (Δ) for the bosonic modes (Ω_1, Ω_2 and Ω_3), showing anticorrelation in all cases. The plot is obtained from the identification of the different Ω modes in 1974 dI/dV curves taken at T = 0.34 K in several samples, and using different calibrated STM tips. The black lines are fits for each subset of points.

This is in contrast to conventional superconductors where phonon-related features frequently lie beyond 2Δ, as for example in Pb with $\Omega_1/2\Delta \approx 1.7$ (see Fig. 3.3.9 b). The statistical confirmation that the fundamental mode has an energy below the pair breaking scale 2Δ implies that this mode cannot decay into fermionic quasiparticles and is therefore undamped, further supporting its interpretation as a superconducting collective mode.

3.3.4 Substrate effects

In order to evaluate the potential role of the substrate in the emergence of the observed STS features, we have studied the DOS of SL-$NbSe_2$ grown on h-BN on Ir(111). The mean superconducting gap energy in this system was evaluated as $\overline{\Delta_{BCS}} = 0.39 \pm 0.02$ meV (see Fig. 3.3.8 a), nearly identical with the value obtained on $NbSe_2$/BLG/SiC (see section 3.4.6 for more details). Indicated are the fundamental modes Ω_i. In order to verify the superconducting nature of the observed gap, we have

measured the DOS as a function of the magnetic field up to 5 T (illustrated in Fig. 3.3.8 b) to check if the peaks dissapear as it happens in BLG. All the dI/dV curves are normalized to the one acquired at 5 T in order to expose the contribution of superconducting order. The extracted gap energy is plotted as a function of the magnetic field (inset in Fig. 3.3.8 b) and fitted to the empirical formula $\Delta(T,H) = \Delta(T,0) \cdot \sqrt{1-(H/H_{c2})}$ according to the Ginzburg-Landau theory.[58] The fitting yields a critical field of $H_{c2} = 3.2\,\mathrm{T}$.

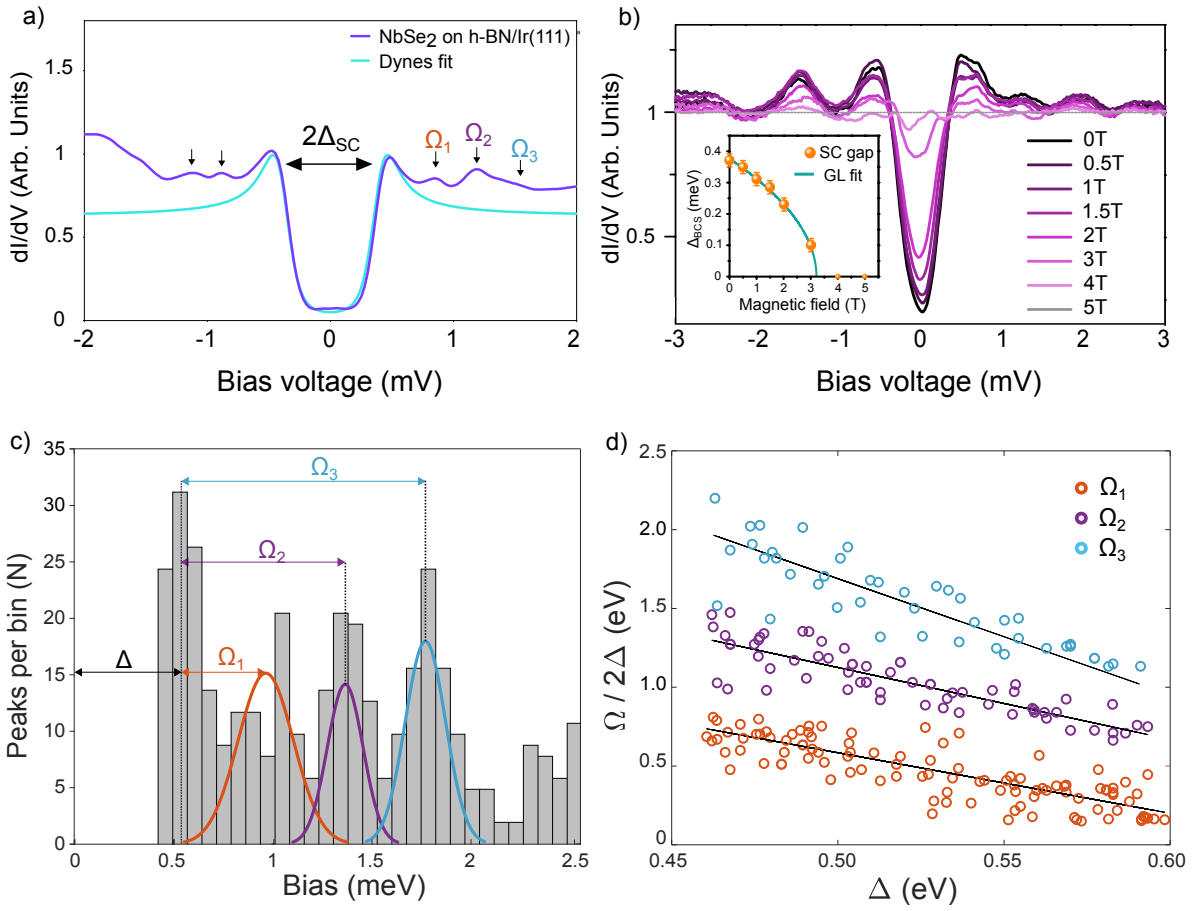

Figure 3.3.8: Statistical analysis of dip-hump features in $NbSe_2$ grown on h-BN/Ir(111). a) Dynes fits of the SC gap in $NbSe_2$/h-BN/Ir(111) for extracting Δ_{BSC}. b) Set of normalized dI/dV curves showing the evolution of the SC gap in SL-$NbSe_2$/h-BN (T = 0.35 K). The inset shows the evolution of the SC gap as a function of the applied magnetic field (dots) and Ginzburg-Landau fit. c) Histogram of detected peaks in multiple grid spectra with in total $N_{tot} = 118$ curves. Ω_1, Ω_2 and Ω_3 are fitted by Gaussian distributions, what yields $\Omega_n = n \cdot \Omega_1 = n \cdot 0.41 \pm 0.14$ meV. d) Scatter plot of $\Omega/2\Delta$ as a function of the superconducting gap (Δ) for the bosonic modes (Ω_1, Ω_2 and Ω_3) shows anti-correlation in all cases. The black lines are linear fits for each subset of points.

These results let us conclude that the observed gap is a superconducting gap and verify the superconducting nature of the gap. Superconductivity in SL-$NbSe_2$ grown on top of h-BN/Ir(111) will be further discussed in greater detail in section 3.4. Fig. 3.3.8 c) shows a histogram of observed peaks around the SC gap in SL-$NbSe_2$ on h-BN. In Fig. 3.3.8 d) the bosonic mode energies normalized by 2Δ, similarly as it is shown in Fig. 3.3.7 for SL-$NbSe_2$ grown on BLG, are plotted as a function of the SC gap energy. In the case of SL-$NbSe_2$ on h-BN we have less data (118 spectra), but we find very similar trends and a clear anticorrelation. However, the energies for the bosonic modes are different. The Gaussian fits to the histogram yield the following values: $\Omega_1 = 0.42 \pm 0.14$ meV, $\Omega_2 = 0.82 \pm 0.09$ meV and $\Omega_3 = 1.23 \pm 0.10$ meV. Although, these values differentiate from the SL-$NbSe_2$ grown on BLG case, Ω_2 and Ω_3 appear as multiples of Ω_1 as $\Omega_n = n \cdot \Omega_1 = n \cdot 0.41 \pm 0.14$ meV. Therefore, it is supposed that a similar collective mode is observed in these two systems.

3.3.5 Theoretical model and discussion of Leggett modes

To summarize our experimental evidence, the STS spectrum of superconducting monolayer $NbSe_2$ displays, in addition to the standard coherence peaks, three satellite peaks at Ω_n=Δ+nΩ_1 with $\Omega_1/2\Delta < 1$. These satellites gradually disappear with T and B as the superconducting state weakens, and their position shows a clear statistical anticorrelation between $\Omega_n/2\Delta$ and Δ. Our observations are strong evidence for the presence of a collective mode of energy Ω_1 associated to the superconducting state, which is coupled to fermionic quasiparticles and leaves its imprint in the tunnelling spectra ($\propto$ DOS). As I will show you hereafter, this hypothesis has been further explored in detail in collaboration with Daniel Muñoz-Segovia, Francisco Guinea and Fernando de Juan Sanz (DIPC).

The existence of a collective mode can impact the spectral function in two ways, via elastic scattering (the renormalization of the electron self-energy due to virtual boson emission), which leads to a peak at Δ+Ω_1, as well as inelastic scattering (where quasiparticles might emit real bosons in the tunneling process) which leads to an onset-like feature. While the relative weight of these two contributions is system-dependent, the dip-hump shape of the satellite peaks observed in single-layer $NbSe_2$ closely resembles those features previously observed in strongly correlated superconductors, dominated by elastic scattering, rather than the typical dip-shoulder shape features of conventional superconductors induced by phonons where both contributions can be comparable.

In order to illustrate the shape and properties of the phonon-related modes in conventional SC, we have performed tunneling spectroscopy measurements of bulk Pb(111) at 0.34 K shown in Fig. 3.3.9 a). The typical signatures of quasiparticle coupling to bosonic modes of phononic origin are observed and labelled as Ω_i. Furthermore, the phonon features in this case lie beyond 2Δ, in contrast to the dip-hump features in unconventional superconductors, and have a characteristic step like shape.

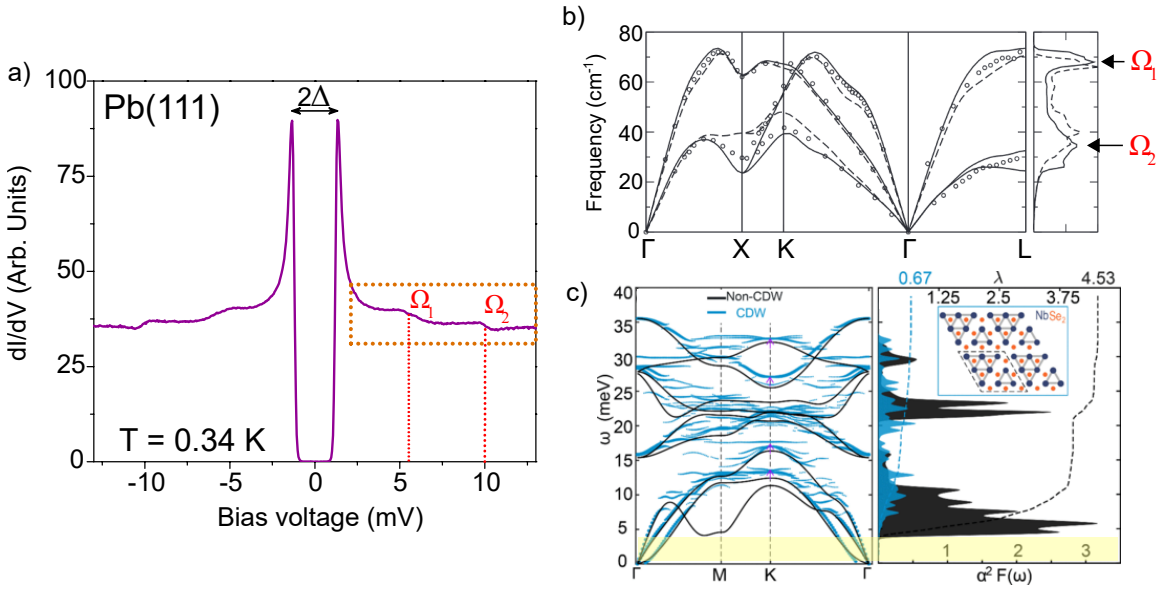

Figure 3.3.9: Virtual phonon features in conventional superconductors. a) STS spectrum acquired around the superconducting gap in Pb(111) at T = 0.34 K (f = 833 Hz, $V_{a.c.}$ = 50 μV). The orange box indicates the region where the bosonic modes are seen (shoulder-dip features labelled as Ω_1 and Ω_2). Both features lie well beyond 2Δ. b) Phonon dispersion relation of Pb(111) with indicated DOS in the right.[144] c) Phonon dispersion relation of SL-$NbSe_2$ in the CDW phase combined with the dispersion of the non-CDW phase. The right plot shows the Eliashberg spectra $\alpha^2F(\omega)$ with integrated EPC constants $\lambda(\omega)$ equivalent to the DOS. The yellow region indicates the energy range, where the satellite peaks in the STS measurements of SL-$NbSe_2$ are observed. As indicate, there are no phonon DOS in this range.[145]

Comparing the STS measurement on Pb(111) (Fig. 3.3.9 a) with the phonon dispersion curves (Fig. 3.3.9 b) indicates that the origin of these dip hump features are indeed induced by inelastic scattering of phonons because the energies of the phonon DOS (Eliashberg spectrum) correlates with the energies where the features in the STS curves are observed. Fig. 3.3.9 c) illustrates the phonon dispersion of SL-$NbSe_2$ for the CDW and non-CDW phases (left) and their corresponding phonon DOS (right). Remarkably, the intensity of $\alpha^2F(\omega)$ (electron-phonon coupling strength) in the CDW phase is greatly reduced compared to the non-CDW case, which is due to the opening of band gaps in the presence of the CDW.[145] Another remarkable point about these calculations is that there are no phonon DOS in the low energy range up to $\sim$ 4 meV as indicated by the shaded yellow area. The lowest CDW phonon mode in the monolayer occurs above $\sim$ 4 meV, way higher than the energy locations where we detect the dip-hump features in the STS experiments (0.8 - 2.2 meV).[146] We therefore exclude virtual phonon features as the origin of the observed satellite features in SL-$NbSe_2$. However, we interpret the measured peaks in SL-$NbSe_2$ as induced by elastic scattering from a collective mode intrinsic to the superconducting state, where two types of collective modes are possible. The first type are excitonic fluctuations (or particle-hole modes), which become sharper after pairing due to the removal of decay

channels into fermionic states. These modes might also be the mediators of the interaction that gives rise to superconductivity, or they may be detrimental for it, i.e. pair breaking. A common example in many unconventional superconductors is a resonant magnetic excitation of spin-1 [147] (an antiferromagnetic spin-wave) which is believed to mediate superconductivity [148] in cuprates [126–129], Fe-pnictides [130–132] and heavy fermion compounds [135, 136]. Another known example are nematic fluctuations, as found in the Fe superconductors [149]. The second type are superconducting fluctuations (or particle-particle modes), most commonly due to close competition between pairing channels, like Leggett modes [150] in two-band superconductor MgB_2 or Bardarsis-Shrieffer (BS) modes [151] in Fe superconductors where s-wave and d-wave pairings are close competitors [152]. Either type of collective mode can be observed with different experimental techniques [153–155], including tunnelling experiments, where bosonic modes are identified via the mentioned characteristic dip-hump features [129–131, 156, 157, 133, 134, 158]. While these STS experiments are mostly interpreted in terms of particle-hole modes like spin-waves, there is no reason to preclude particle-particle modes to be found with this technique. Finally, all superconductors have an amplitude or Higgs mode, which is normally not observable on its own [159], but it has been observed in bulk $NbSe_2$ due to its mixing with collective CDW modes [160]. Nevertheless, the Higgs mode can readily be discarded because in SL-$NbSe_2$ the CDW mode has much higher energy than 2Δ and their coupling is highly suppressed.

Which of the previous collective mode scenarios applies to our experiment will be discussed in the following. SL-$NbSe_2$ has been predicted to be near a ferromagnetic instability [119, 139], which competes with the CDW and, therefore, spin fluctuations could be sizable and potentially give rise to a particle-hole collective spin-wave. Such mode would indeed broaden and disappear as the temperature or magnetic field are increased to their critical values as observed in cuprates [153] and Fe-based materials [154]. In order to test the hypotheses of spin fluctuations we have studied the absorption spectra in the soft x-ray region. X-ray absorption spectroscopy (XAS) and X-ray magnetic circular dichroism (XMCD) measurements were carried out at 2 K in normal (NI) and grazing incidence (GI) by measuring the total electron yield (TEY) normalized by the incoming photon intensity. Fig. 3.3.10 a) shows the absorption spectrum of grazing incidence (GI) right polarized light (σ^+) and left polarized polarized light (σ^-). Substracting these two signals from each other yields the XMCD signal shown in Fig. 3.3.10 b), which is a direct measurement of ferromagnetic order. The same measurements have been performed at normal incidence light (see Fig. 3.3.10 c) and d). The observed resulting XMCD signals are very small and in fact negligible. We can therefore conclude that no magnetic order is present in SL-$NbSe_2$, and there is no direct evidence of strong spin fluctuations either.

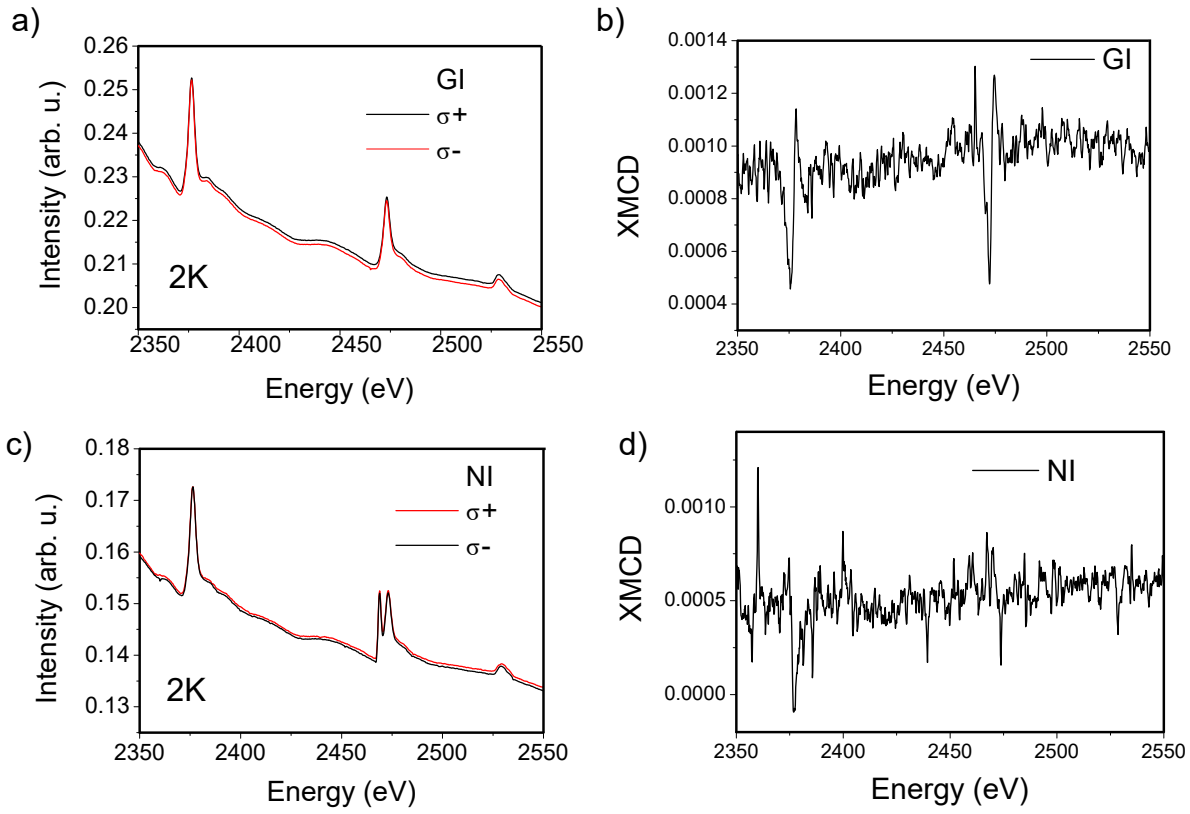

Figure 3.3.10: XMCD measurements of SL-$NbSe_2$ at 2 K. Absorption spectra for left and right circular polarized light taken at a) GI and c) NI. Corresponding XMCD signal at c) GI and d) NI.

In the particle-particle scenario, however, there is a very natural mechanism for the emergence of collective modes: the competition between pairing channels signalled by the emergence of magnetic field-induced nematic superconductivity. To substantiate the characteristics of these collective modes, we present a microscopic model of this competition which leads to explicit predictions that can be compared with our experiment.

$NbSe_2$ bands near the Fermi level are derived from the three t_{2g} Nb d orbitals, and consist of a hole pocket around the Γ point with dominant d_{z2} character and hole pockets around the K points with $d_{x2-y2} \pm i d_{xy}$ character. This difference leads to strong Ising SOC for the K pockets but negligible SOC for the Γ pocket, and to different k-independent pairing channels: while both Γ and K pockets admit the standard s-wave state, the K points can also develop spin-triplet, orbital-singlet pairing of the d_{x2-y2}, d_{xy} orbitals which has f-wave symmetry [161]. For simplicity, we therefore assume the Γ pocket is a spectator with s-wave symmetry gap and use a model with just the K pockets

$$H_0(k) = \psi^\dagger \left[(-\frac{k^2}{2m} - \mu)\tau_0\sigma_0 + \lambda\tau_z\sigma_z \right] \psi \tag{3.2}$$

where the τ_i and σ_i matrices act on the valley and spin index respectively, and λ is the Ising SOC. The pairing operators can be written as $\Delta_S = \psi\tau_x i\sigma_y\psi$ for the s-wave singlet which has A_1' symmetry, and $\Delta_T^i = \psi\tau_y\sigma_y\sigma_i\psi$ with i=x,y,z for the f-wave triplet, where Δ_T^z belongs to an A_1' irrep while $\Delta_T^{x,y}$ make an E" irrep (see Fig. 3.3.11 for a schematic). In the presence of SOC, the mixing of the A_1' singlet and A_1' triplet becomes allowed. This mixing scales with the difference of the DOS of the spin-split pockets which is however very small.

In our model with the leading k-independent SOC λ the DOS difference and the mixing actually vanish, and the only effect of λ is to disfavor the E" state. Nevertheless, if attraction in the f-wave channel is sizable, its E" part can naturally be induced with an in-plane magnetic field, which can explain the previous experiments proposing the competition of nematic [120, 121] and triplet pairing [122].

Assuming an s-wave ground state and vanishing singlet-triplet mixing, the imaginary fluctuations towards the two nearby f-wave triplets A_1' and E" represent two collective modes of the Bardarsis-Schriefer type. The fluctuation towards the E" channel is likely unobservable in practice because $\lambda >> \Delta$, which implies Tc for the E" state will nearly vanish. We therefore consider only the fluctuation towards the A_1' triplet. In the presence of singlet-triplet mixing, this second mode still exists but no longer has a well-defined Bardarsis-Schriefer character, because the gaps in the spin-split Fermi surfaces take the mixed form $\Delta_\pm = \Delta_S \pm \Delta_T^z$. This mode can alternatively be interpreted as the relative phase fluctuation of the $\Delta_\pm$ gaps, i.e. a Leggett mode [162] (see Fig. 3.3.11, which we take as the leading candidate to explain the experiments.

To model the Leggett mode explicitly, we consider attractive interactions in the s-wave singlet and f-wave triplet channels as follows

$$V = g_s\Delta_S^+\Delta_S + g_T\Delta_T^+\Delta_T \tag{3.3}$$

with g_S, $g_T < 0$. As discussed in [161], g_S might be thought of as induced by electron-phonon coupling, while g_T can have contributions from both electron-phonon and Coulomb interactions, in particular through effective spin fluctuation [119]. Depending on whether $|g_S|$ or $|g_T|$ is largest, we have a ground state with dominant singlet or triplet character, and we assume $|g_S| > |g_T|$. The energy of the Leggett mode can be computed with this model (see SM) and is obtained from the implicit equation

$$\frac{arcsin\,\Omega_1/2\Delta}{\sqrt{(2\Delta/\Omega_1)^2 - 1}} = \frac{1}{N_0|g_T|} - \frac{1}{N_0|g_S|} \tag{3.4}$$

From the measured value of $\Omega_1/2\Delta = 0.66$ we can estimate the ratio $|g_S|/|g_S|$ and hence how close the triplet state is. This first requires an estimate of $N_0\, g_S$. If we assume a weak coupling BCS limit, a gap of $\Delta \sim 0.4\,\text{meV}$ and a Debye frequency cutoff in the range of bulk estimates $\omega_D \sim 20\,\text{meV}$ [163], this corresponds to $N_0\, g_S \sim 0.2$. However, since the ratio $2\Delta/k_BT \sim 4.9$ in our experiment would denote moderate to strong coupling, the value of $N_0\, g_S$ is likely larger.

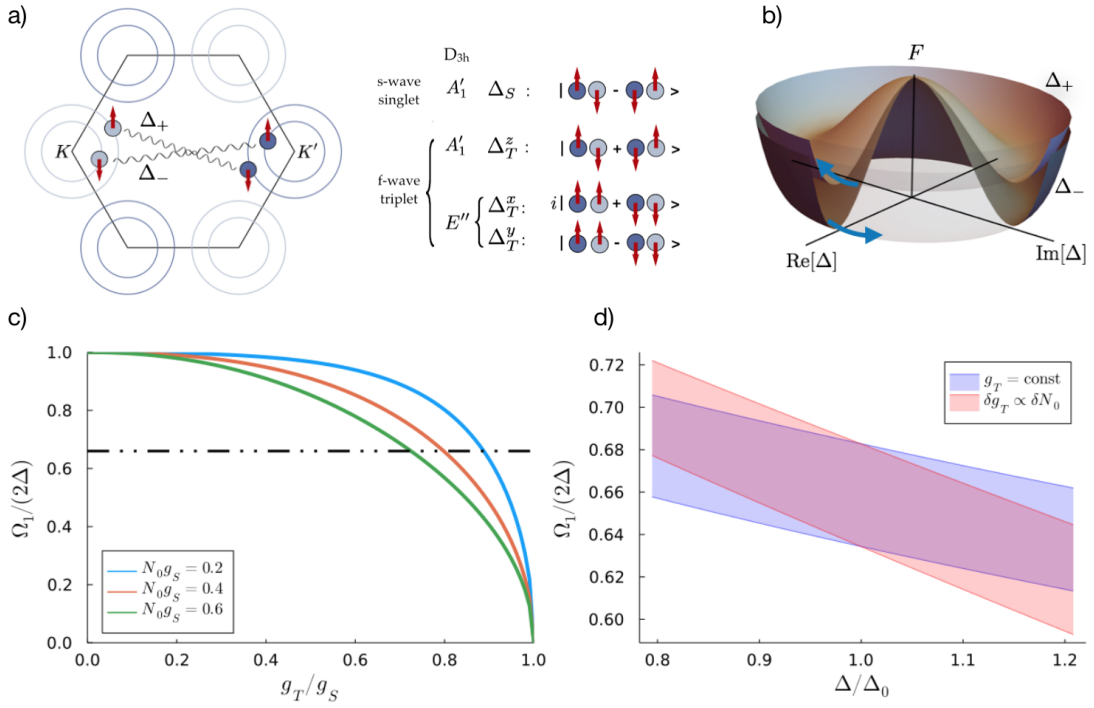

Figure 3.3.11: Pairing states and collective modes. a) Schematic Fermi surface near the K points and structure of the different pairing states considered. b) Schematic free energy for the gaps of the two spin-split Fermi surfaces, illustrating the Leggett mode as their relative phase fluctuation. c) Leggett mode energy normalized by the zero temperature gap $\Omega_1/2\Delta$ as a function of the ratio g_s/g_T. The collective mode is gapless when the two couplings are the same, and approaches 2Δ for vanishing triplet attraction $g_T = 0$. d) Allowed values of $\Omega_1/2\Delta$ when N_0 takes a range of values keeping g_S and g_T constant (blue), and when we additionally assume that g_T is correlated with N_0. Anticorrelation is generically observed but is more pronounced in the latter case.

Fig. 3.3.11 c) displays the numerical solution of $\Omega_1/2\Delta$ as a function of g_T/g_S for $N_0\, g_S = 0.2$-0.6, showing this produces a range $g_T/g_S = 0.7$-0.9. The triplet attraction must therefore be sizable, but still not enough to overcome the singlet attraction. To show that this collective mode can in fact be observed in STS measurements, we have also computed the tunneling spectra due to the renormalization of the fermionic self-energy by this collective mode following [164], showing that it indeed leads to a peak at $E_1 = \Omega_1 + \Delta$. This calculation could be extended to higher orders to show the existence of harmonics at $E_n = \Omega_1 + \mathrm{n}\Delta$ as well. A prediction of the absolute amplitude of the peaks is however beyond the scope of our calculation.

Our theory also allows to predict that the energy of the collective mode has a similar exponential dependence on temperature as the gap itself. Because of this, the collective mode energy should stay roughly constant in T for low T as we observe and only show deviations as it approaches $T \sim T_{c,sc}$,

where estimating the energy is prevented by our resolution. Similarly, the amplitude of the peak is rapidly suppressed near $T \sim T_{c,sc}$, because the weight of this boson, computed as the residue of its propagator, scales $\propto \Delta^2$. In the presence of a magnetic field, the collective mode energy shows a significant rise, surpassing 2Δ even at moderate fields B $\sim$ 1 T. While a quantitative prediction for this would involve modelling the vortex mixed state, it is clear that this change cannot originate just from changes in the gap, and we conjecture that the magnetic field might reduce g_T by hardening spin fluctuations. Complementary probes of this collective mode are needed to better understand its behaviour under magnetic fields.

To address the observed local anticorrelation with the gap, we assume that local variations of the model parameters lead to variations in the collective mode energy [165]. Fig. 3.3.11 d) shows the predicted band of allowed energies for two different scenarios. First, we consider that N_0 varies spatially, leading to variations of Δ, while g_S and g_T are kept constant. Moderate anticorrelation is obtained in this case. If we further assume that g_T depends on the DOS, as it would be for example if it relied on spin-fluctuations, we see that a larger anticorrelation is attained. Analysis of other scenarios shows the anticorrelation is quite generic for this collective mode, while a detailed match with experiments will require exact knowledge of the origin of the spatial fluctuations. Overall, we believe our model supports our hypothesis that the observed mode is the Leggett mode due to proximity of f-wave triplet and provides a consistent picture for our observations.

Finally, it is also interesting to compare the case of single-layer $NbSe_2$ with that of other superconductors where particle-hole magnetic resonances have been observed, where there is an empirical universal relation between resonance energy and the gap as $\Omega/2\Delta \sim 0.64$ over two orders of magnitude of Δ [166]. In this context, single-layer $NbSe_2$ lies in the region of the smallest Ω along with the heavy-fermion compounds [135, 136] with a very similar value $\Omega_1/2\overline{\Delta_{BCS}} = 0.53/0.8 = 0.66$ (see Fig. 3.3.12). Such intriguing similarity invokes further comparative investigation between particle-hole and particle-particle collective modes.

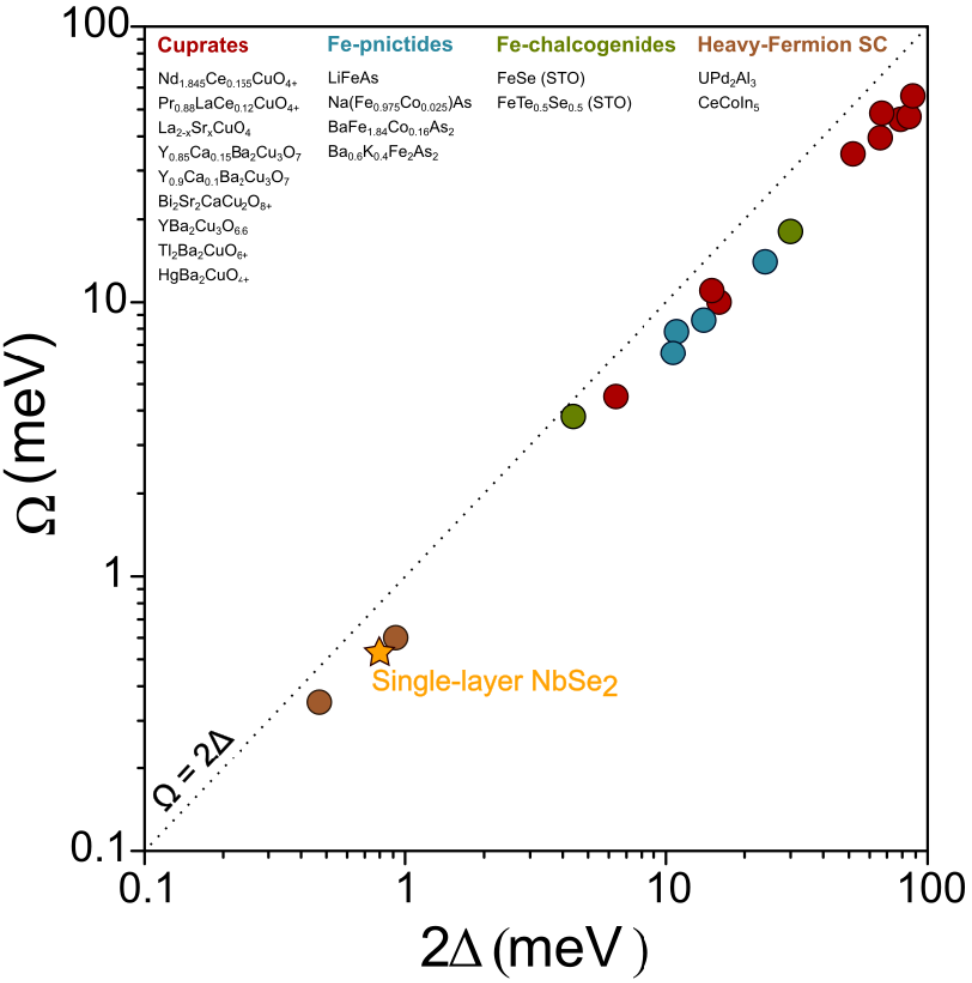

Figure 3.3.12: Universal relationship between Ω and Δ in unconventional superconductors. Plot of the bosonic mode energy versus the exciton pair-breaking energy (2Δ) for various unconventional superconductors among the most relevant families, i.e., cuprates, Fe-pnictides, Fe-chalcogenides and heavy-fermion compounds. The dashed line represents the limit $\Omega = 2\Delta$ according to the unconventional mechanism of Cooper pairing. The materials for each family are listed in increasing order of Δ. The Ω and Δ values are taken from [156] (LiFeAs), [157] ($Na(Fe_{0.975}Co_{0.025})$), [134] (FeSe), [158] ($FeTe_{0.5}Se_{0.5}$)) and [166] for the rest of the compounds.

3.3.6 Summary

In summary, our results in single-layer $NbSe_2$ have unequivocally demonstrated the existence of a bosonic, undamped collective mode associated to the superconducting state, which we have interpreted as the fluctuations to a competing f-wave triplet channel. This is the first experimental observation of Leggett collective modes in the superconducting state of a 2D TMD material. By combining high-

quality epitaxial growth of single-layer $NbSe_2$ and high-resolution tunneling spectroscopy at 0.34 K, we were able to demonstrate the emergence of collective modes in this correlated material, which is a natural scenario for the emergence of soft collective modes in the superconducting state. Our high-resolution measurements directly verify the existence of these modes in the quasiparticle spectrum, whose behavior with the temperature and magnetic field up to 11 T is systematically characterized. Our experimental observations are supported by a theoretical model based on the competition between the most natural pairing channels of this system in the monolayer limit: the ground state s-wave singlet and the subleading f-wave triplet. Our model provides an explicit calculation of the mode energy, allowing to estimate quantitatively the f-wave pairing attraction. Importantly, our theory captures two key experimental observations from our experiments, i.e., the emergence of peaks in the quasiparticle spectrum below the critical temperature as well as the observed anticorrelation between the energy (Ω) of the collective modes and the superconducting gap (Δ). The observation of superconducting collective modes in the family of materials provides key insight into our limited understanding of the microscopic mechanisms of superconductivity in two dimensions. The existence of Leggett modes highlights the emergence of unconventional properties of the superconducting state in TMDs as they are thinned down to the 2D limit. We believe this work will likely lead to further fundamental research on unconventional superconductivity in two-dimensional materials. Furthermore, this work opens new avenues for the exploration of unconventional superconductivity in unexplored environments via the combination of monolayers of TMDs with, for example, magnetic substrates to lead to topological superconductivity.

3.4 Proximity effects on CDW and SC order

This chapter discusses the role of the substrates on the collective electronic states in connection with the electronic structure in 2D materials. Specifically we are studying superconductivity (SC) and charge density wave (CDW) order in SL-$NbSe_2$ grown on various electronically distinct substrates. By combining low-temperature (0.35 K) STM/STS and angle-resolved photoemission spectroscopy (ARPES), we compare the electronic structure of this prototypical 2D superconductor on each substrate. Our results provide valuable insights into the fragile stability of such electronic ground states in 2D materials. The ARPES measurements were performed by the group of Jill Miwa at the Aarhus University in Denmark.

3.4.1 State of the art

CDW and superconductivity are electronic phases that respond dramatically to different kinds of external perturbations. In that sense, electron-phonon and electron-electron interactions, the fundamental trigger of these states, are highly susceptible to small modifications of the electronic or phononic band structures. In 2D, this brittleness becomes even more important, as the material might be completely exposed to the environment. The following outlined experiments are performed in UHV, thus chemical reactions on the surface can be neglected. However, the supporting substrate of the 2D material is capable of triggering various proximity effects as hybridization,[95, 167] strain,[168, 169] charge transfer,[95] and screening,[89] modifying fundamental properties of the material. Although these previous works have unveiled the effect of substrates, systematic and comparative studies of their properties and impact on the collective electronic phases in 2D materials remain scarce.

In metallic TMDs (MX_2 with M = Nb, Ta, Ti, V, Sn and X = S, Se, Te), CDW order and superconductivity are frequently present from the bulk form down to the single-layer limit, although with rather disparate properties in many cases. In the 2D limit, however, these electronic phases are usually influenced by the presence of the supporting substrate and, therefore, its role on the electronic structure must be carefully evaluated. So far, CDW and superconducting orders have been studied in epitaxial TMD layers on substrates that do not necessarily minimize their potential impact on the properties of the TMD layer but, instead, are suitable for ease and high quality growth of the TMD. These are mainly noble metals such as Au(111)[94, 95, 170–173] and doped graphene surfaces[6, 7, 11, 27, 174, 100, 175, 176, 113], (graphite, graphene/SiC(0001) and graphene/Ir(111)). In this work, we provide a comparative assessment of the impact of different substrates on the CDW and SC phases as well as the electronic structure of a model correlated 2D material. In particular, we study the electronic ground state of high-quality SL-$NbSe_2$ grown by molecular beam epitaxy (MBE) on four substrates with markedly distinct structural and electronic nature: BLG/SiC(0001), SL-h-BN/Ir(111), Au(111) and bulk WSe_2. Surprisingly, while both CDW and SC persist with nearly identical properties on BLG/SiC(0001) and h-BN/Ir(111), they are absent or, at least, severely weakened on Au(111) and bulk WSe_2, as summarized in Fig. 3.4.1 a). However, the electronic structure of SL-$NbSe_2$ remains

largely unaffected in all cases except for a non-uniform shift of the band structure on Au(111). The fate of these collective phases is compared and discussed in the framework of the electronic structure in each case. A discussion on the character of the electronic bands and its key features is given in the introduction of this chapter (see section 3.1). Regarding the Fermi surface of SL-$NbSe_2$, the Nb $4d$ states crossing the E_F form two hole pockets around the $\overline{\Gamma}$ and $\overline{K}$ points, as shown in Fig. 3.4.1 b). Specifically, at the center of the 2D Brillouin Zone (BZ), marked by the solid black line, there is a hexagonal-like contour, while at the corners of the BZ there are two concentric rings corresponding to the spin-split bands at $\overline{K}$. This ARPES spectrum was acquired for SL-$NbSe_2$ on BLG/SiC(0001), whose 2D BZ is also marked (dashed line). The point-like electronic structure of BLG near its $\overline{K}$ point is clearly visible in the shown data.

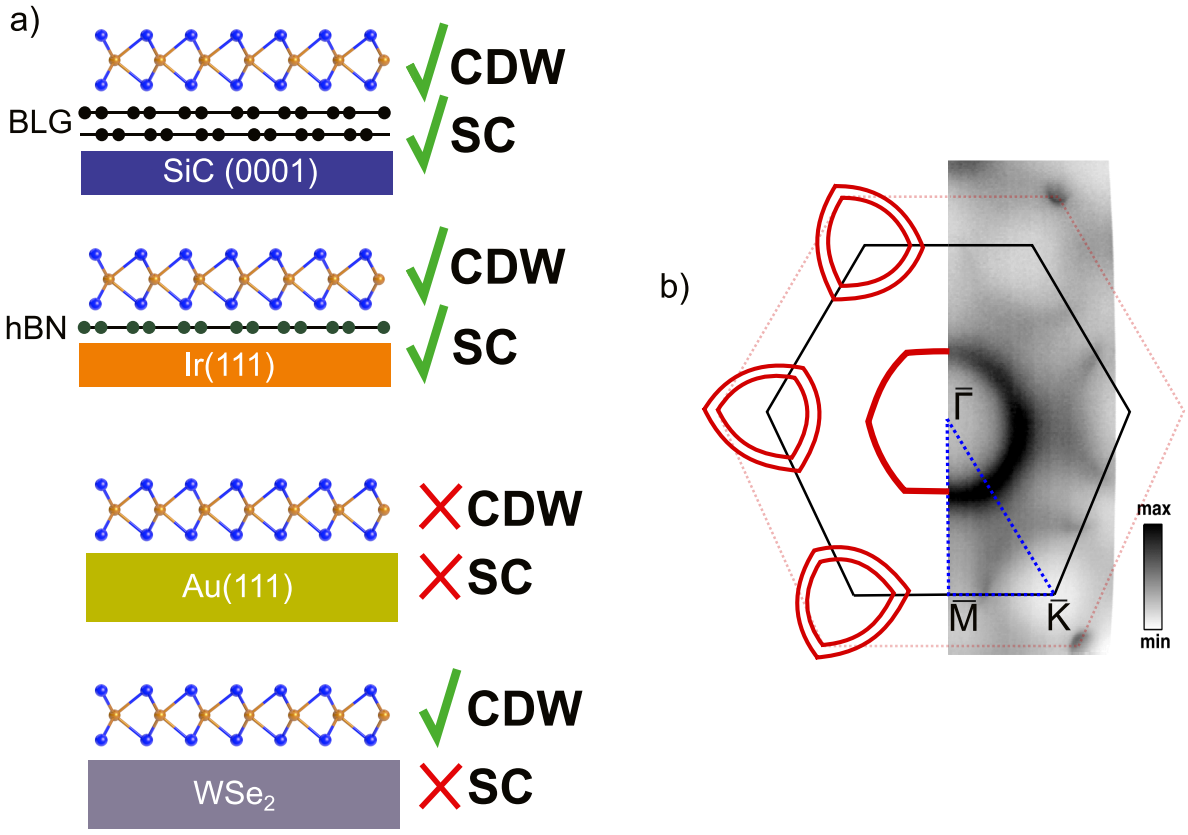

Figure 3.4.1: Material systems and Fermi surface of SL-$NbSe_2$/BLG. a) Summary of the studied SL-$NbSe_2$/substrate systems where the presence (absence) of the CDW and superconducting orders according to our experimental results is indicated. b) Sketch of the $NbSe_2$ 2D BZ (solid hexagon) and the Fermi surface of SL-$NbSe_2$ on BLG/Si(0001) measured at 55 eV photon energy. The solid red lines show the expected bands and the high-symmetry directions are indicated by the blue dashed lines. The dashed hexagon corresponds to the 2D BZ of the BLG, and the $\overline{K}$ points for BLG can be seen in the measured data. Maximum intensity corresponds to black and minimum intensity to white on the color scale.

3.4.2 Single layer $NbSe_2$ on BLG/SiC and h-BN/Ir(111)

In the first section we characterize the structural and electronic properties of SL-$NbSe_2$ grown on top of BLG/SiC and on top of h-BN/Ir(111). BLG/SiC is an extensively used substrate in the research field of 2D-TMD materials. Therefore, we aim to increase our knowledge on substrate induced proximity effects. Even when they are mostly considered to be small, especially the electronic phases of CDW order and superconductivity are supposed to be sensitive to external perturbations. Thus, we characterize these phases in SL-$NbSe_2$ and study its differences when the material is grown on electronically distinct substrates. The BLG/SiC(0001) substrate is n-doped and therefore, effectively becomes metallic. However, how the metallicity influences such collective electronic states remains unclear. Therefore we start by quantitatively asses the differences in the electronic properties between $NbSe_2$ grown on BLG/SiC and h-BN/Ir(111). The latter material, an insulator with an electronic band-gap of $\sim 6\,eV$. Due to its insulating properties we suppose that it acts as an effective decoupling layer.[177–180]

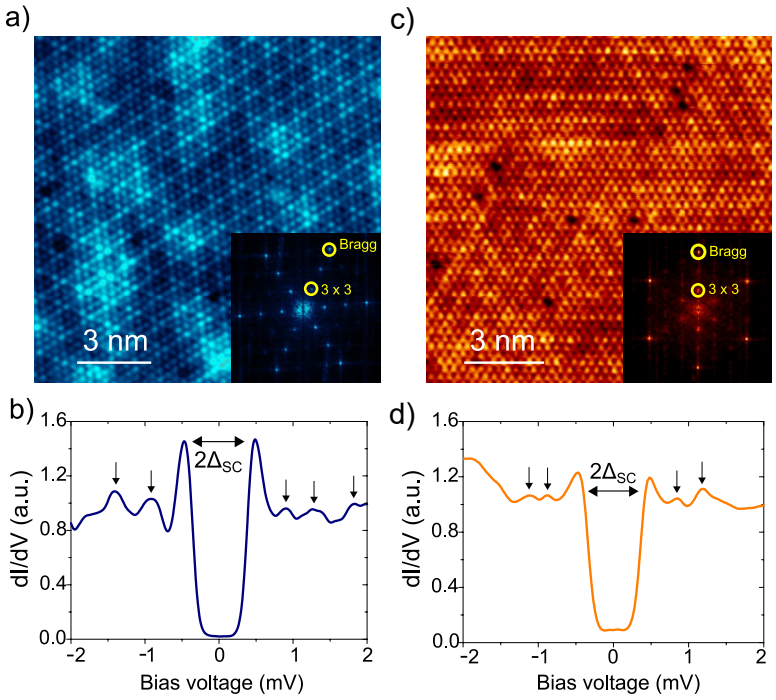

Figure 3.4.2: Structural and electronic properties of SL-$NbSe_2$ grown on BLG/SiC(0001) and h-BN/Ir(111).(a) High-resolution STM topograph of SL-$NbSe_2$ on BLG/SiC(0001), where the 3×3 CDW ordering is visible at $T = 0.35\,K$ ($V_S = +50\,mV$; $I_t = 0.86\,nA$). The corresponding FFT is shown in the inset. Low-bias (b) STM dI/dV spectra acquired on SL-$NbSe_2$/BLG at $T = 0.35\,K$. The superconducting gap (Δ_{SC}) and the position of collective modes (vertical arrows) are indicated. Equivalent STM/STS measurements on SL-$NbSe_2$ on h-BN/Ir(111) are presented in (c-d) (Parameters for (b): $V_S = -50\,mV$; $I_t = 4\,nA$).

In Fig. 3.4.2 (a-b) and (c-d) the STM/STS results for the systems SL-$NbSe_2$ on BLG/SiC(0001) and h-BN/Ir(111), respectively, are presented. If not otherwise stated, all topographic images as well as spectroscopic data shown were measured at a temperature of 0.34 K. As it can be seen from Fig. 3.4.2 (a) and (c) the $NbSe_2$ developes the 3×3 CDW pattern for both systems. However, the disorder might be slightly higher in the h-BN case, because the intensity of the CDW (as can be seen in the insets on the right bottom) is weaker. This is likely due to lower crystallinity of the SL-$NbSe_2$ when epitaxially grown on h-BN/Ir(111), compared to the BLG case.

The small scale STS measurements for both systems in Fig. 3.4.2 b) and d) reveal typical SC gaps around the Fermi energy.[10, 118] Both gaps were fitted with the Dynes formula and gaps of $\Delta_{SC,BLG} = 0.40 \pm 0.02$ meV for the BLG and $\Delta_{SC,h-BN} = 0.39 \pm 0.03$ meV for the h-BN case were extracted. These results were anticipated in section 3.3.4. Notably, the conductance does not reach 0 in the case of h-BN/Ir(111) (Fig. 3.4.2 (d), what we attribute to a direct tunneling channel to the Ir(111) underneath. This type of tunneling has already been reported before, where dI/dV spectra contained traces of the electronic structure of the metal support.[181] More details on the gap fitting as well as disorder in these two systems, can be found in section 3.4.6.

The similarity between these two systems is also very much present in the large scale electronic structure measured by means of STS as it is shown in Fig. 3.4.3 (a) and (b). As discussed in section 3.1 characteristic features could be attributed to the STS measurements and are marked as VH_i (van Hove singularities) and E_i (flat regions). Comparing the obtained dI/dV spectra on $NbSe_2$/BLG/SiC and $NbSe_2$/h-BN/Ir(111) to each other reveals their similarity. The most prominent features are a pronounced peak at sample bias $V_S = +0.43$ V (empty states) that corresponds to the flat region at the top of the Nb-derived band at $\overline{\Gamma}$ (E_2 in Fig. 3.1.2), a shallow peak near $V_S = -0.20$ V contributed by the van Hove singularities below E_F (VH_1, VH_2 and VH_3) (see also Fig. 3.4.4 for a magnification of these states), a region of low and flat DOS attributed to the bandgap of 0.4 eV, a sharp increase of the DOS at $V_S = -0.82$ V consistent with the top of the Se-derived band at the $\overline{M}$-point (VH_4), and two peaks at $V_S = -1.03$ V and $V_S = -1.30$ V that can be attributed to the V_1 and V_2 features in the band structure. All these STS features are coincident in energy in the two systems within the uncertainties (see Table 6.1).

Following, in order to complete the comparative analysis of the electronic structure, we carried out room temperature ARPES measurements, which are discussed for the two systems of SL-$NbSe_2$ on BLG/SiC(0001) and h-BN/Ir(111) (see Fig. 3.4.3 c-e) and f-h). Presented are the valence band dispersions along the $\overline{\Gamma}$–$\overline{K}$ and $\overline{\Gamma}$–$\overline{M}$ high-symmetry directions, indicated in Fig. 3.4.1 b) by the blue dashed line. In Fig. 3.4.3 e) and h) the energy distribution curves (EDC) are presented, which were used to locate the band minimum. The minima of the $\overline{\Gamma}$–$\overline{K}$ direction (VH_3) for SL-$NbSe_2$ on BLG/SiC(0001) is at ∼0.21 eV, while it is ∼0.23 eV for the case of SL-$NbSe_2$ on h-BN/Ir(111). A similar shift of the Nb 4*d* band to lower binding energy is observed in $\overline{\Gamma}$–$\overline{M}$ direction (VH_1).

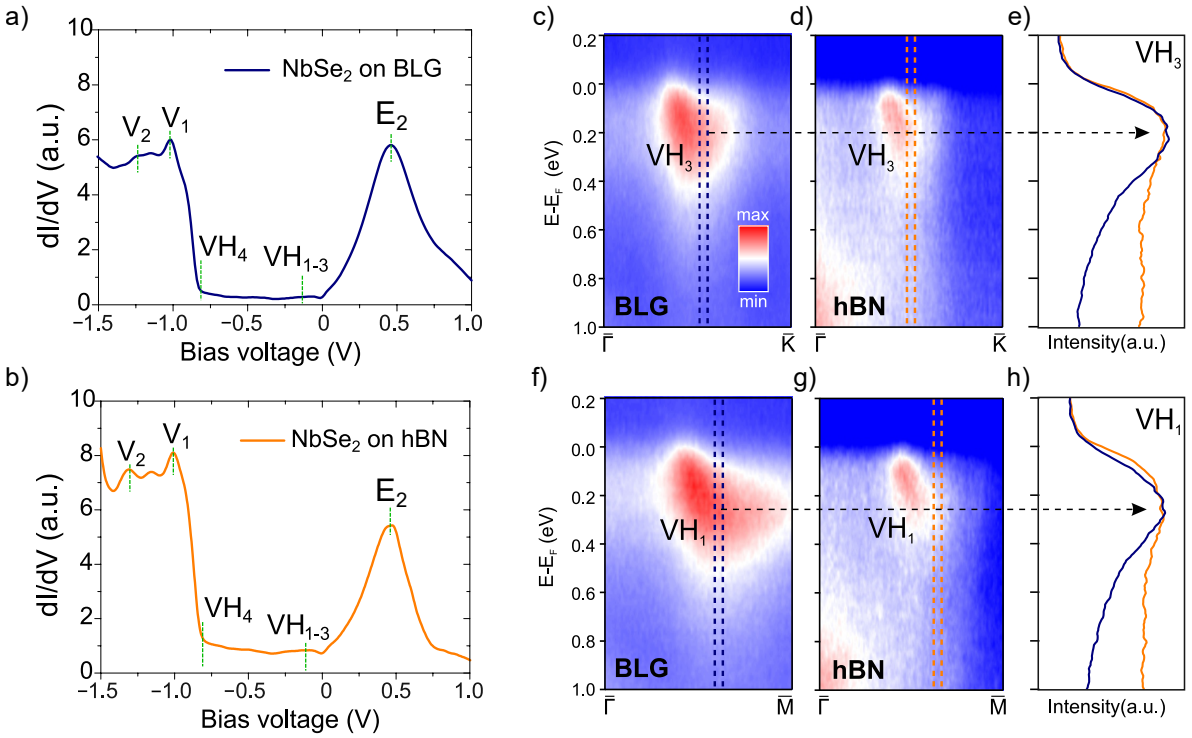

Figure 3.4.3: Large scale electronic structure of SL-$NbSe_2$ grown on BLG/SiC(0001) and h-BN/Ir(111)measured by STS and ARPES. a) Large-bias STS dI/dV spectra acquired on SL-$NbSe_2$/BLG at $T = 0.35$ K. b) Equivalent STM/STS measurements on SL-$NbSe_2$ on h-BN/Ir(111). c-d) ARPES measurements acquired with 55 eV photons, along $\overline{\Gamma}$–$\overline{K}$ and $\overline{\Gamma}$–$\overline{M}$ high-symmetry direction of (g,j) SL-$NbSe_2$ on BLG and (f-g) h-BN. Dashed lines point out the band minimum. e,h) EDCs taken at the valence band minimum along $\overline{\Gamma}$–$\overline{K}$ and $\overline{\Gamma}$–$\overline{M}$, correspondingly. Blue colour is used to represent data acquired from a SL-$NbSe_2$/BLG sample whereas orange is used for the SL-$NbSe_2$/h-BN.

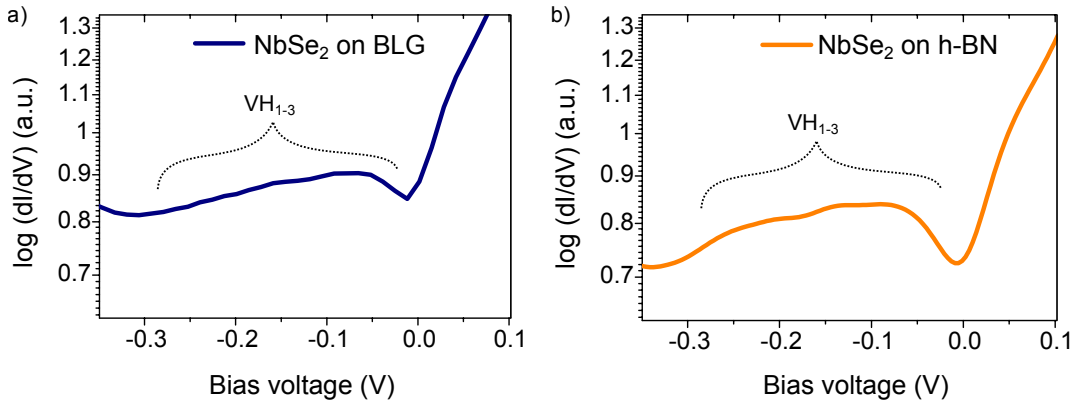

Figure 3.4.4: Magnification of states arising from VH singularities. a) and b) are logarithmic representations of the same data shown in Fig. 3.4.3 a) and b).

No hybridization between $NbSe_2$ bands with the bands of the substrates was detected, what suggests very weak substrate interactions for both systems. This conclusion is also supported by the STS measurements, where no significant differences between the two systems could be detected. This pertains for the CDW order in a similar way as for the superconductivity. Thus, regarding STS as well as ARPES measurements, the electronic structure in the $NbSe_2$ stays unmodified by interchanging the substrate from BLG/SiC to h-BN/Ir(111). This is a relevant result, because especially graphene is a preferred substrate for a high quality growth and further investigation of TMD materials.[182, 100, 6, 7, 174, 175, 11, 113, 27]. Because of such weak interactions, the SL-$NbSe_2$ on BLG/SiC(0001) system can be seen as quasi free standing SL-$NbSe_2$. Therefore, in the following section, this system was chosen as the reference system to compare it with SL-$NbSe_2$ grown on Au(111) as well as WSe_2.

3.4.3 SL-$NbSe_2$ on Au(111)

Next, we focus on the electronic structure of SL-$NbSe_2$ on Au(111) following the same procedure. Fig. 3.4.5 a) shows an atomically resolved STM image of SL-$NbSe_2$ on the Au(111) surface where, in addition to the atomic registry, a rotationally aligned superstructure is clearly observed. This superlattice has a commensurate 5×5 periodicity with respect to SL-$NbSe_2$ whose origin is a moiré pattern formed between the TMD and the Au atomic lattice.[171] FFT analysis of STM topographs (inset in Fig. 3.4.5 a) shows that the 5×5 superlattice is the only existing periodicity in SL-$NbSe_2$ on Au(111) beyond the atomic lattice and, therefore, there is no trace of 3×3 CDW ordering.

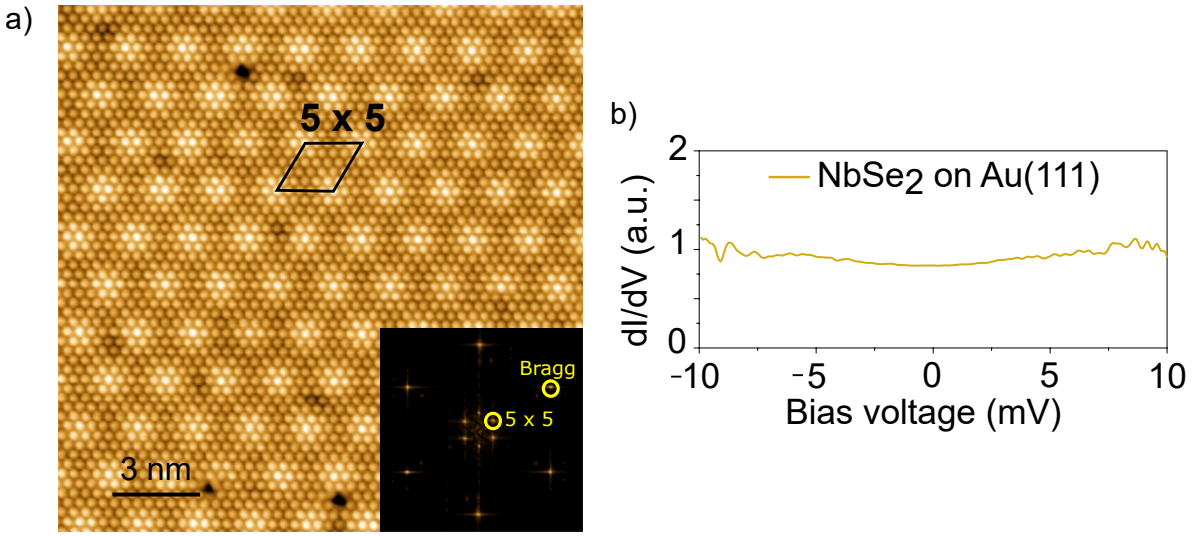

Figure 3.4.5: Structural and small scale electronic properties of SL-$NbSe_2$ on Au(111). (a) Atomically resolved STM image of SL-$NbSe_2$ on Au(111) showing the 1×1 atomic lattice and a 5×5 superlattice that corresponds to a commensurate moiré pattern of 17.3 Å ($V_S = +0.3\,\mathrm{V}$; $I_t = 1.5\,\mathrm{nA}$). The corresponding FFT of the STM image is shown in the inset. b) Low-bias STM dI/dV spectra acquired on SL-$NbSe_2$ on Au(111) at $T = 0.34\,\mathrm{K}$.

The low-energy electronic structure near E_F probed by STS at 0.34 K in Fig. 3.4.5 b) shows a flat DOS, which demonstrates the quenching of SC by the proximity of the normal metal. Fig. 3.4.6 a) shows two typical wide-bias dI/dV spectra measured for SL-$NbSe_2$ on Au(111) (yellow) and, for comparison, on BLG/SiC(0001) (blue). For occupied states, the DOS of SL-$NbSe_2$ on Au(111) exhibits a featureless monotonic increase of the DOS that we attribute to the dominant weight of the direct tunneling channel to the bulk bands of Au(111). Importantly, we do not observe any STS feature compatible with the surface state of Au(111). Lastly, although the V_1 and V_2 features from the Se p_z bands are not observed in STS in contrast to the BLG case, the dispersion and position of the former is detected in our ARPES measurements and found to be nearly unaltered with respect to the BLG system (see Table 3.2 and Fig. 3.4.7).

For unoccupied states, we find E_2 for SL-$NbSe_2$ on Au(111) to be located at $V_S = +0.16$ V. This value represents a surprisingly large shift of E_2 of 0.3 eV toward E_F with respect to the SL-$NbSe_2$/BLG system. This shift along with the simultaneous disappearance of the Au(111) surface state suggests charge transfer from the substrate to the 2D layer. This scenario is consistent with the ARPES data shown in Fig. 3.4.6 (b–d) where the Nb 4*d* band moves further below E_F compared to the weakly-interacting SL-$NbSe_2$/BLG case. However, this band does not show a rigid shift as it would be expected for a bare charge transfer. While the band position in the $\overline{\Gamma}$–$\overline{K}$ direction (VH_3) for Au(111) and BLG does not reveal any qualitative difference, there is a clear shift of the band in the $\overline{\Gamma}$–$\overline{M}$ direction (VH_1) of ∼0.1 eV. Regarding the Au(111) surface state, our ARPES data cannot resolve due to the nearly full coverage of SL-$NbSe_2$ (partial TMD coverages enable its observation).[183]

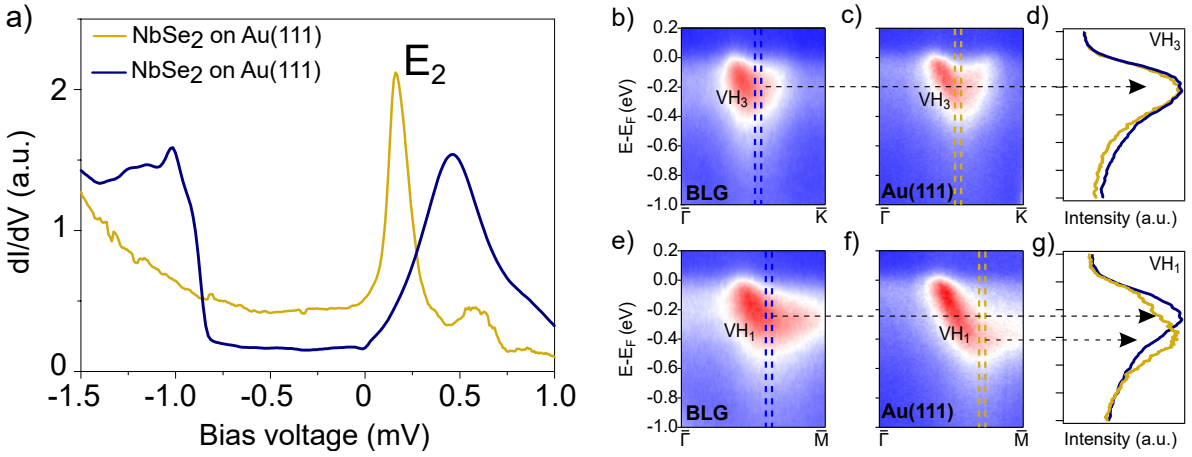

Figure 3.4.6: Electronic properties of SL-$NbSe_2$ on Au(111) measured by STS and ARPES. a) Large-bias STM dI/dV spectra acquired on SL-$NbSe_2$ on Au(111) at T = 0.34 K (yellow curves). In (a), the STM dI/dV spectrum of SL-$NbSe_2$ on BLG (blue curve) is included as a reference. ARPES measurements along $\overline{\Gamma}$–$\overline{K}$ and $\overline{\Gamma}$–$\overline{M}$ high-symmetry directions of SL-$NbSe_2$ grown (b,e) on BLG and (c,f) on Au(111). Dashed lines point out the band minimum. (d,g) EDCs taken at the Nb-derived band minimum along $\overline{\Gamma}$–$\overline{K}$ and $\overline{\Gamma}$–$\overline{M}$, correspondingly.

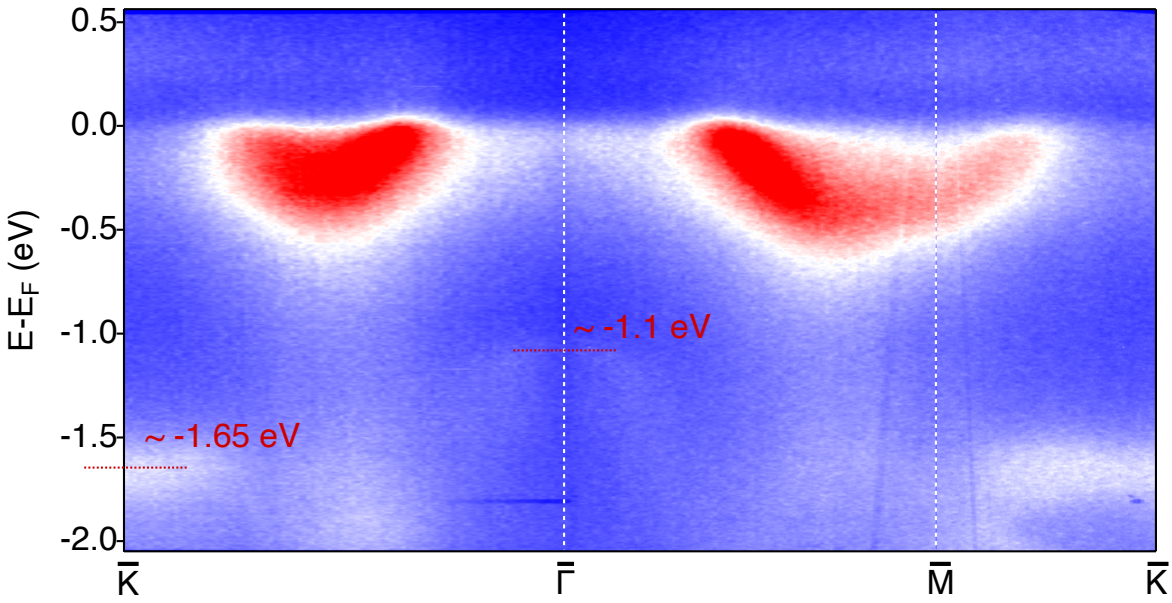

Figure 3.4.7: ARPES band dispersion for SL-$NbSe_2$ on Au(111) along the high-symmetry $\overline{K}$–$\overline{\Gamma}$–$\overline{M}$–$\overline{K}$ directions. The Nb 4*d* states cross E_F. In addition, the Se 3*p* band maximums are faintly visible at ≈ -1.1 eV (at $\overline{\Gamma}$) and -1.6 eV (near $\overline{K}$) below E_F. These band maxima are noted by the red dashed lines, and appear to be consistent with those predicted by theory in Fig. 3.1.2 of section 3.1, specifically the top Se band.

The disappearance of the Au(111) surface state, the large shift of the E_2 feature towards E_F and the non-uniform shift of the Nb-derived band is fully compatible with pseudodoping effects similar as those observed in SL-TaS_2/Au(111)[95], and arising from charge transfer and, more importantly, hybridization between the d-band of the TMD and the Au(111) surface state. First principles calculations have shown for SL-TaS_2 that the *d*-band can shift unequally in energy in different points in k-space, what is illustrated in Fig. 3.4.8.

Since the pseudodoping-induced shifts of the bands can be k-dependent within the BZ, the states above and below E_F can be affected by different amounts, which is consistent with the measured larger shift of the unoccupied E_2 STS feature ($\sim$0.3 eV) than that detected in the occupied region by ARPES ($\sim$0.1 eV) as seen in Fig. 3.4.6 (a) and (g). Therefore, the hybridization of the Nb 4*d* band with the Au surface state leads to non-uniform (k-dependent) band shifts that reshape the electronic structure of the 2D layer. Pseudodoping impacts the CDW and superconducting states in SL-$NbSe_2$ likely through a reduction of the DOS as a result of the hybridization that leads to a decrease of the effective coupling constants upon deposition on Au(111), which contribute towards their disappearance. In the case of the superconductivity, the Cooper pair leakage to the Au(111) substrate due to boundary effects is also expected to play a large role in its quenching.[184]

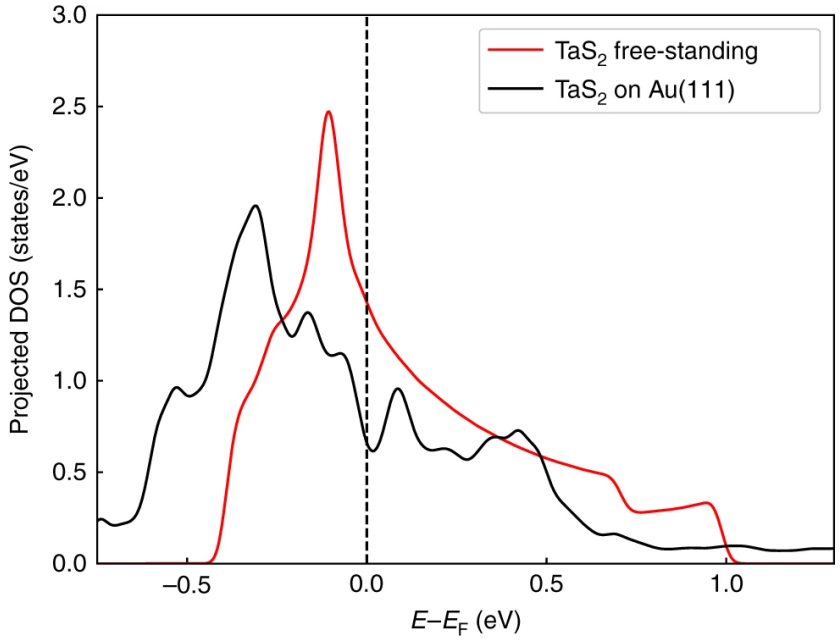

Figure 3.4.8: Influence of Au(111) substrate on the DOS of SL-TaS_2. Comparison of the DOS projected on Ta-d orbitals of 1H-TaS2 on Au(111) substrate (black line) and in its free-standing form (red line). Figure adapted from [95].

3.4.4 SL-$NbSe_2$ on WSe_2

Lastly, we investigate the case of SL-$NbSe_2$ on a large-gap ($> 1\,$eV) semiconductor, i.e., bulk WSe_2. The typical morphology of SL-$NbSe_2$ grown on WSe_2 is shown in Fig. 3.4.9 a). The high quality of the crystal structure is revealed by the uniform shape of the layer and straight edges of the domains. Fig. 3.4.9 b) shows a topographical profile and reveals a domain height of $\sim 0.8\,$nm for the SL-TMD material. Such a value is typical for monolayer TMD/BLG structures as measured before.[7, 27, 89] SL-$NbSe_2$ grows rotationally aligned with the supporting substrate. This alignment is confirmed by constant energy maps acquired by ARPES (not shown). However, due to the lattice mismatch between SL-$NbSe_2$ (3.44 Å) and WSe_2 (3.29 Å), a large moiré pattern with a periodicity of 7.8 nm is formed in the heterostructure, which is clearly visible in STM images (Fig. 3.4.9 c). High-resolution STM imaging of SL-$NbSe_2$ on bulk WSe_2 reveals a superlattice compatible with the existence of CDW order with a ratio between the Bragg (b_{1x1}) and superlattice (b_{SL}) reciprocal vectors of $b_{1x1}/b_{SL} = 3.10 \pm 0.53$. Fig. 3.4.10 presents four examples of varying strength of CDW modulation in SL-$NbSe_2$ grown on WSe_2 with topographic images on the left side and its corresponding FFT pattern on the right side. The strongest CDW ordering is visible in Fig. 3.4.10 a). This image contains also a grain boundary and the long-wavelength moiré is present. Fig. 3.4.10 b) shows a similar situation with slightly weaker CDW ordering. In c) the CDW is hardly visible, but the FFT patterns prove its existence in weakened form. The same applies for the area in d).

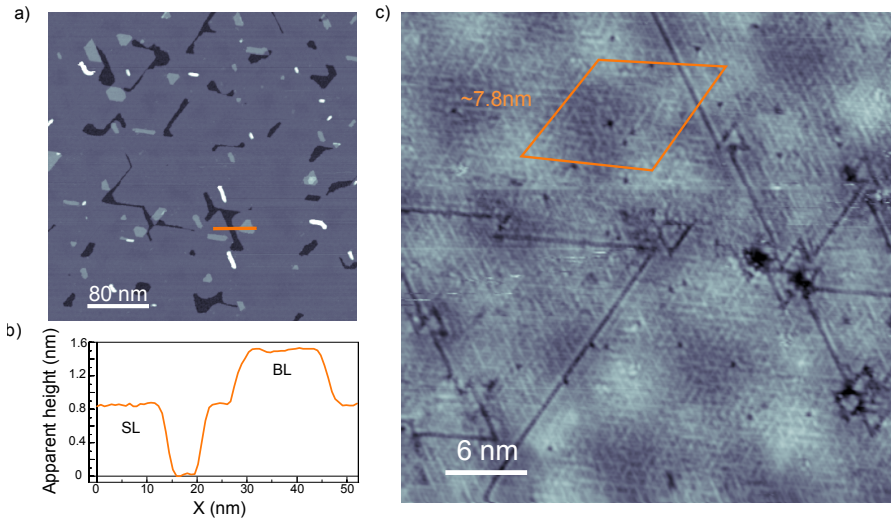

Figure 3.4.9: Morphology of SL-$NbSe_2$ on bulk WSe_2. a) Large-scale STM image of a nearly complete monolayer of $NbSe_2$ grown on bulk WSe_2 ($V_S = +0.93\,\mathrm{V}$; $I_t = 30\,\mathrm{pA}$, $T = 4.2\,\mathrm{K}$). b) Height profile taken along the orange line in (a) that illustrates the apparent heights of the monolayer and the bilayer. c) Close-up STM image of SL-$NbSe_2$/WSe_2 showing a moiré superlattice with a length of $\sim$7.8 nm arising from the lattice mismatch between SL-$NbSe_2$ (3.44 Å) and WSe_2 (3.29 Å) at zero angle between them ($V_S = +1.8\,\mathrm{V}$; $I_t = 3\,\mathrm{nA}$; $T = 4.2\,\mathrm{K}$).

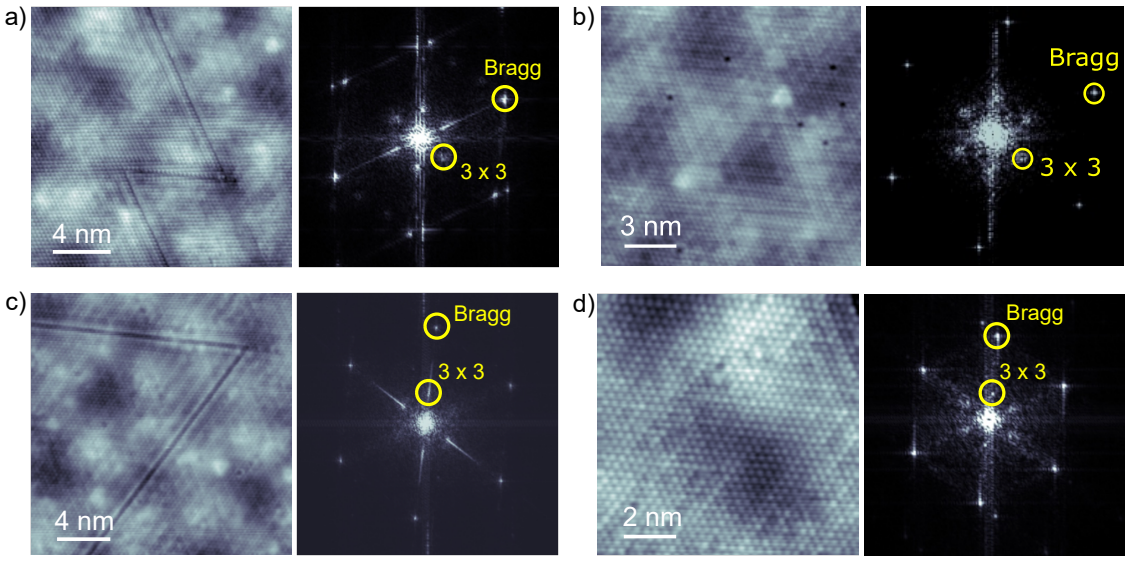

Figure 3.4.10: CDW modulation on SL-$NbSe_2$ grown on bulk WSe_2. The strength of the CDW varies as shown for four different sample areas with its strongest to weakest appearance from a) to d). Measurement parameters: a: V_s = -0.7 V, I = 100 pA, T = 4.2 K; b: V_s = 0.2 V, I = 400 pA, T = 4.2 K; c: V_s = 0.4 V, I = 100 pA, T = 4.2 K; d: V_s = -0.2 V, I = 2 nA, T = 4.2 K.

The spots of the superlattice in the corresponding FFT (insets) are blurred and poorly defined in most sample areas. This situation, and even the absence of CDW, is systematically observed in our STM images acquired in this system, which indicates an intrinsic weakening of the CDW on bulk WSe_2 as compared to the BLG and h-BN cases.

Concerning the superconducting state, the DOS near E_F usually exhibits a V-shape, whose relation with the SC state has to be considered. To do so, we consecutively acquired STM dI/dV spectra of SL-$NbSe_2$ on bulk WSe_2 below (0 T) and above (5 T) the upper critical magnetic field at 0.34 K (see Fig. 3.4.11), which show a nearly identical shape. The critical magnetic fields measured for $NbSe_2$/BLG/SiC and $NbSe_2$/hBN/Ir(111) are $H_{C2} = 2$ T and $H_{C2} = 3.2$ T, respectively. Therefore, the nearly identical shape of the curves below and above the upper critical field suggest that SC is not participating in the decrease of the DOS at E_F.

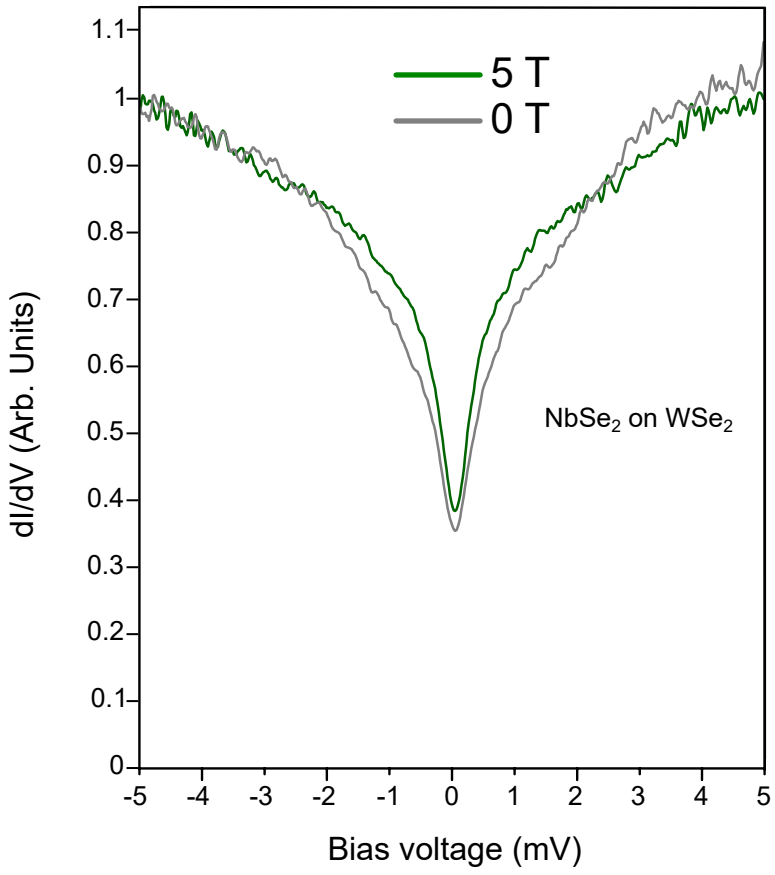

Figure 3.4.11: STM dI/dV spectra acquired on SL-$NbSe_2$ on bulk WSe_2 without an applied magnetic field (grey curve) and with a perpendicular magnetic field of $B = 5$ T (green curve). Measurement parameters for both curves: f = 833 Hz, $V_{a.c.} = 50\,\mu$V.

Surprisingly, SL-$NbSe_2$ is not SC on an insulating substrate as WSe_2. Lastly, regarding the origin of this dip feature, we tentatively attribute it to the existence of a Coulomb gap due to moderate/weak disorder. This propositions are discussed in more detail for SL-$TaSe_2$ in section 4.3.

In order to gain further knowledge about the weakening of the CDW and the disappearance of SC in SL-$NbSe_2$ grown on the semiconducting bulk WSe_2 substrate, we study and compare its electronic structure via STS and ARPES. Fig. 3.4.12 c) shows a typical large-scale bias range dI/dV spectrum of this system along with the SL-$NbSe_2$/BLG reference spectrum. For unoccupied states, the only feature is the broad E_2 peak centered at $V_S = +0.49\,\text{eV}$, nearly coincident in energy with that for SL-$NbSe_2$ on BLG/SiC(0001). For occupied states, the DOS shows a continuous and large increase from E_F that dominates over other STS features such as VH_i or $V_{1,2}$, thus rendering them not visible. We attribute the large increase of DOS to tunnelling from the bulk conduction bands of WSe_2, whose onset in SL-NbSe2 on WSe_2 is located very close to E_F (see ARPES spectra in Figs. 3.4.12 (e,h)). The bulk WSe_2 valence band maximum is located at the $\overline{\Gamma}$-point and has high intensity (red) with noticeable dispersion in the k_z direction, which maximizes the tunnelling probability to to these states and, therefore, their weight in the measured dI/dV spectra.

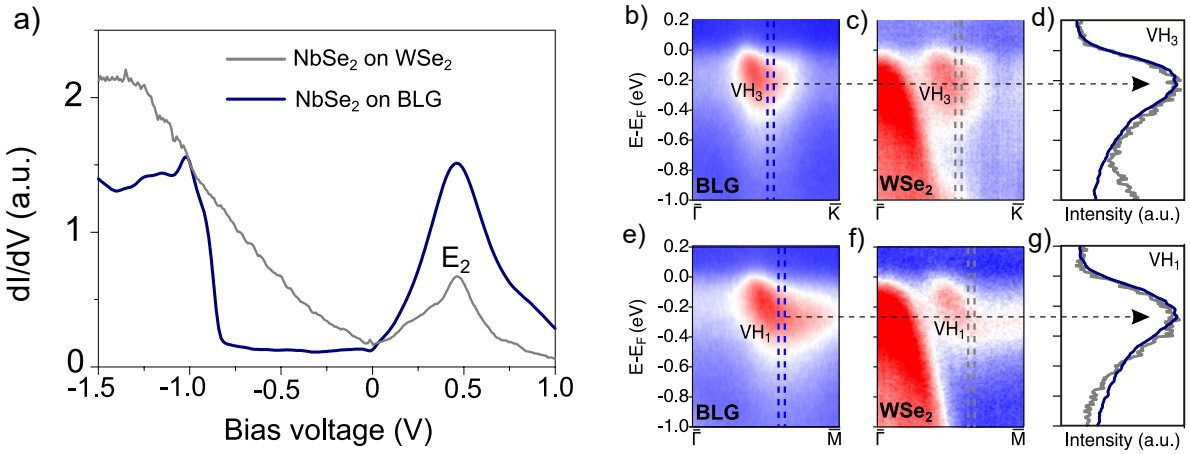

Figure 3.4.12: Structural and electronic properties of SL-$NbSe_2$ grown on bulk WSe_2. (a) Atomically resolved STM image showing a barely visible 3×3 CDW modulation that leads to a blurred 3×3 points in the FFT (this has been observed systematically with different tip apexes, see SI) ($V_S = -0.5\,\text{V}$; $I_t = 0.15\,\text{nA}$) . (b) Low-bias STM dI/dV spectrum showing the absence of the SC gap but a shallow dip feature attributed to the CDW order. (c) Wide-range STM dI/dV spectrum where only E_2 is distinguished. ARPES measurements along $\overline{\Gamma}$–$\overline{K}$ and $\overline{\Gamma}$–$\overline{M}$ high-symmetry direction of SL-$NbSe_2$ grown on (d,g) BLG/SiC(0001) and (e,h) bulk WSe_2. The black dashed lines point to the band minimum in (f,i) where EDCs acquired at the valence band minimum along the corresponding $\overline{\Gamma}$–$\overline{K}$ and $\overline{\Gamma}$–$\overline{M}$ directions. Comparison of the V_1, V_2 and VH_i features for SL-$NbSe_2$ on BLG/SiC(0001), and bulk WSe_2, they all appear to similar position in energy.

Figs. 3.4.12 (d,e) and (g,h) compare the dispersion of the SL-$NbSe_2$ states on BLG and bulk WSe_2 along the $\overline{\Gamma}$–$\overline{K}$ and $\overline{\Gamma}$–$\overline{M}$ directions, respectively. ARPES data does not reveal a significant shift of the band minimum in the $\overline{\Gamma}$–$\overline{K}$ high-symmetry direction as compared to the reference spectra for SL-$NbSe_2$ on BLG/SiC(0001) and h-BN/Ir(111) substrates. The shift of the pocket in the $\overline{\Gamma}$–$\overline{M}$ direction is equal with the SL-$NbSe_2$ on BLG/SiC(0001) and h-BN/Ir(111) samples (compare EDCs in Figs. 3.4.3 (l) and 3.4.12 (i)). In summary, from the STS and ARPES data we conclude that the electronic structure of SL-$NbSe_2$ remains unaffected within our experimental resolution by the presence of the bulk WSe_2 substrate with respect to the reference substrates of BLG/SiC(0001) and h-BN/Ir(111).

This result allows us to draw some conclusions about the behaviour of CDW and SC in this system. First, the nearly equal electronic structure of SL-$NbSe_2$ on bulk WSe_2, BLG/SiC(0001) and h-BN/Ir(111) substrates rules out significant charge transfers and/or changes in the Fermi surface that could critically affect the stability of these collective states. Similarly, hybridization between Nb 4*d* states and substrate states can also be discarded due to the absence of overlap. Furthermore, in none of the cases we observe the emergence of defect states due to a significantly high density of defects, which would be detrimental to the SC phase but not necessarily the CDW phase as we have observed CDW and SC in heavily doped SL-$Nb_{1-\delta}Mo_\delta Se_2$ alloys for large δ values up to $\delta = 0.15\%$ (see chapter 4).

Weakening of the CDW order and complete suppression of SC for SL-$NbSe_2$ could be due to minimal but measurable energy shifts of the van Hove singularities. For bulk 2H-$NbSe_2$, the energy difference between the band minima along the Γ–K and Γ–M direction is ~ 0.1 eV. In the SL case, comparison of the EDCs displayed in Fig. 3.4.12 i) reveals a plausible smaller energy difference and, therefore, a closer position of VH_1 to E_F with respect to the bulk case. Similar shifts with strong impact in the CDW and superconducting orders have been previously reported in bulk TMDs.[8] Furthermore, the presence of long-wavelength moiré pattern (7.8 nm) in SL-$NbSe_2$ on bulk WSe_2 is a distinctive feature with respect to the reference substrates (where both CDW and SC are seen) that could be affecting the stability of the CDW and SC.

Table 3.2: Energies of the main features of the electronic structure as measured by STS and ARPES. E_2, V_1, V_2 and VH_4 values were extracted from the STS data while VH_1 and VH_3 were extracted from the ARPES spectra. E_2, V_1 and V_2 values were taken as the maxima of the STS peaks and VH_4 as the onset of the Se-derived band extracted following the procedure described in ref. [89]. STS uncertainties were determined through a statistical analysis of individual STS curves obtained in multiple locations with different STM tips.

Substrate	E2 (eV)	VH_1 (eV)	VH_3 (eV)	VH_4 (eV)	V1 (eV)	V2 (eV)
BLG/SiC	0.46 ± 0.05	-0.27 ± 0.05	-0.21 ± 0.05	-0.81 ± 0.16	-1.02 ± 0.04	-1.30 ± 0.07
h-BN/Ir(111)	0.43 ± 0.06	-0.29 ± 0.05	-0.23 ± 0.05	-0.80 ± 0.02	-1.03 ± 0.03	-1.30 ± 0.01
Au(111)	0.16 ± 0.05	-0.37 ± 0.05	-0.22 ± 0.05	-	-1.10 ± 0.05	-
WSe_2	0.49 ± 0.05	-0.30 ± 0.05	-0.24 ± 0.05	-0.65 ± 0.16	-0.87 ± 0.04	-

Although long moiré patterns are present in all the heterostructures studied here, the induced structural/electronic corrugation in the $NbSe_2$ layer is only noticeable via STM on the bulk WSe_2 substrate. Further work to asses the potential impact of moirés in 2D TMD superconductors as well as other plausible factors is required to reveal the microscopic mechanisms that lead to the weakening and disappearance of the CDW and SC, respectively, in SL-$NbSe_2$ on bulk WSe_2.

3.4.5 Summary

Here, we provide a comprehensive investigation of the collective phases in parallel with the electronic band structure of single-layer $NbSe_2$, a model strongly correlated 2D material, on four substrates with markedly distinct structural and electronic nature: bilayer graphene (BLG), monolayer h-BN, Au(111) and bulk WSe_2. Each substrate here represents a family of the most typical surfaces used for the epitaxial growth and subsequent investigation of 2D metals, namely, graphene substrates, noble metals, semiconducting TMDs and 2D insulators. Here we combine low-temperature (0.34 K) scanning tunneling microscopy/spectroscopy (STM/STS) and angle-resolved photoemission spectroscopy (ARPES) measurements to probe the existence and properties of the CDW and superconductivity in single-layer $NbSe_2$ along with its electronic structure on each substrate. We demonstrate that, even when the electronic structure remains largely unaffected by the substrate, except on Au(111) where a charge transfer occurs, both the CDW and superconductivity show disparate behavior. First, we find that the CDW and superconductivity in single-layer $NbSe_2$ coexist with nearly identical properties on the insulating h-BN and the metallic bilayer graphene. In contrast, these electronic phases are absent (or severely weakened) on the insulating WSe_2 and the metallic Au(111). Of particular interest is the case of the SL-$NbSe_2$/WSe_2 heterostructure, where superconductivity is surprisingly absent at 0.34 K, while the CDW persists, although harshly depressed as compared to on the BLG and h-BN substrates, despite they all share nearly identical electronic structures.

The consequences of our findings are far-reaching. First, our results paint a clear picture of the impact of substrate-induced proximity effects on the collective phases of a model strongly-correlated 2D system. A key insight gained in this study is the significance of the fact that doped graphene substrates play a negligible role in the electronic properties of the 2D TMD metal, as demonstrated by direct comparison with the insulating h-BN case. Furthermore, the dramatic impact of a semiconducting TMD substrate observed on the CDW and superconducting orders is an unexpected result that will certainly trigger further experimental and theoretical efforts in order to fully understand its origin. Lastly, our work provides a fundamental guide for the choice of suitable substrates in future investigation of elemental aspects of 2D collective phases. More practically, the new insights that we gain into the role of substrates are also critical for future heterostructure applications and research, and may pave the way for nanodevices based on new physical principles that include substrate-tunable electronic properties.

3.4.6 Superconducting gap fit

In order to extract Δ_{bcs} we fit the measured density of states with the Dynes formula [185]

$$N(E) = N_0 Re\left[\frac{E + i\Gamma}{\sqrt{(E - i\Gamma)^2 - \Delta^2}}\right] \tag{3.5}$$

and convolute it with the fermi dirac distribution

$$f(E) = \frac{1}{e^{\frac{E}{K_B T}} + 1} \tag{3.6}$$

in order to take into account the thermal broadening of the SC gap and the effect on the Dynes parameter Γ.

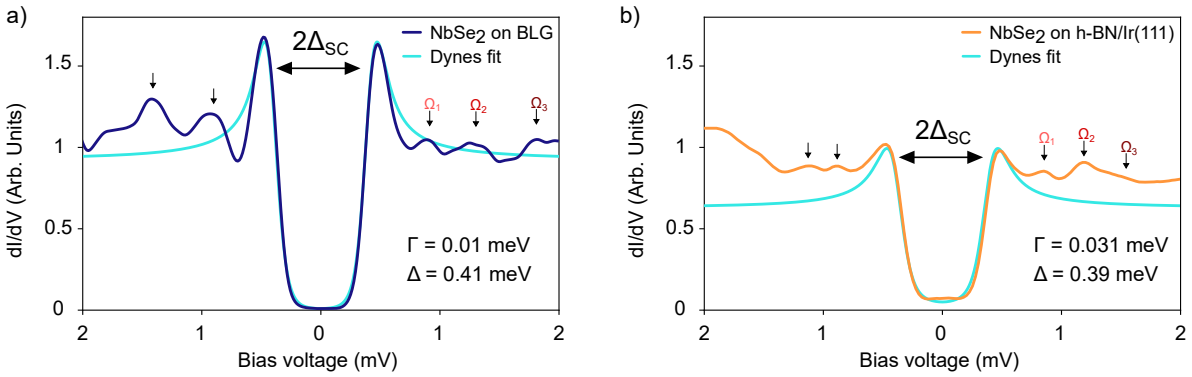

Figure 3.4.13: Dynes fits of SC gaps for extracting Δ_{bcs}. a) $NbSe_2$/BLG and b) $NbSe_2$/h-BN. Measurement parameters for (a-b): f = 833 Hz, $V_{a.c.} = 30\,\mu V$.

Different pair-breaking mechanism, comprised in Γ, constrain the lifetime of quasiparticles and broaden the superconducting coherence peaks in N(E). For the evaluation of the gap size Δ_{bsc} and comparison between the systems of $NbSe_2$ on BLG and h-BN, we have to tune Γ, because the disorder in the system on h-BN leads to broader quasiparticle peaks. We find that Γ in $NbSe_2$/h-BN is increased by a factor of 3. A direct effect is a non-vanishing tunnel conductance at zero bias. The source for this could be caused by elastic scattering of cooper pairs, realized by an additional pair-breaking disorder field, which can lead to an impurity band within the superconducting gap. However, more probable is that such electronic states are available in the underlying metal substrate. Fitting the Dynes function yields SC gaps of $\Delta_{SC} = 0.41 \pm 0.03$meV and $\Delta_{SC} = 0.37 \pm 0.03$meV for $NbSe_2$/BLG (Fig. 3.4.13 a) and $NbSe_2$/h-BN (Fig. 3.4.13 b), respectively.

CHAPTER 4

Collective electronic states in 2D Ising superconducting alloys

TMD alloys offer unprecedented versatility to engineer 2D materials with tailored properties for specific purposes. These include the unique opportunity to explore novel structural and electronic phase transitions in two dimensions (2D). Furthermore, they posses the possibility to tune electronic phases such as SC or CDW by doping the material with small amounts of impurity atoms. In this chapter, we report on the atomic-scale evolution of the electronic ground state of two novel SL-TMD alloys by means of LT (300 mK) STM/STS combined with DFT calculations. In particular, we first investigate the atomic-scale evolution of the electronic ground state of a monolayer $Nb_{1-\delta}Mo_{\delta}Se_2$ across the entire alloy composition range ($0 < \delta < 1$). Our STS measurements enable to extract the effective doping of Mo impurities, the bandgap evolution as well as the band shifts. In the second part, we study the CDW and SC phase in relation to the doping introduced disorder in the SL-$Ta_{1-\delta}W_{\delta}Se_2$ alloy. We show that by incorporating W atoms to SL-$TaSe_2$, SC can be induced with $T_c \approx 0.9$ K, which represents a significant increase with respect to its bulk counterpart ($T_c \approx 0.14$ K).[45, 186]

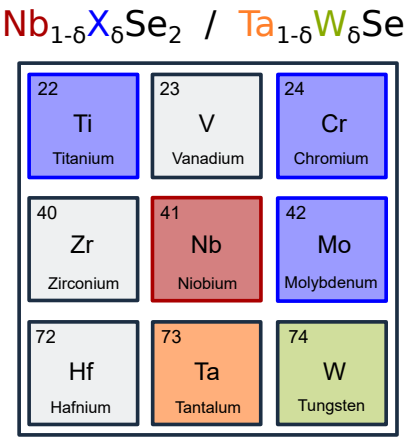

4.1 Aliovalent $Nb_{1-\delta}Mo_{\delta}Se_2$ alloy

In transition metal dichalcogenide materials, the possibility of substitute one of the atomic components, i.e., chalcogen and transition metal (TM) elements, by a different species, have greatly expanded the potential of this family of 2D materials. This route to obtain novel and stable TMD monolayers with tailored properties in form of alloys ($M_{1-\delta}N_{\delta}X_2$ or $MX_{2(1-\delta)}Y_{2\delta}$ with M, N the TM and X, Y the chalcogen for binary alloys) has been recently demonstrated [187, 188], and show significant promise in electronic [189–193], optoelectronic [188, 194–196] and catalytic applications [197–199]. So far, isovalent TMD alloys of the group VI such as $Mo_{\delta}W_{1-\delta}S_2$ and $WS_{2(1-\delta)}Se_{2\delta}$ have received most of the attention due to the possibility to tune the electronic and optical bandgaps.[188, 194–196, 200, 201] Regarding aliovalent TMD alloys where exchange of TM elements with different valence is involved, most of the efforts have focused on doping effects in the dilute limit. Moderate substitution of aliovalent species in TMD semiconductors enables stable modulation of the carrier type and carrier density.[189, 190, 202–204] A paradigmatic example is the case of Nb-doped TMD semiconductors, where doping has been investigated in alloys up to 10% of Nb impurities to demonstrate stable p-type conduction.[189, 190, 192, 193, 202, 205] Furthermore, these TMD alloys with Nb dopants have demonstrated enhanced electrocatalytic performance for hydrogen evolution reaction.[206] Other aliovalent TMD alloys such as V-doped WX_2 semiconductors have recently shown a remarkable room-temperature ferromagnetism.[207, 208]

More fundamentally, TMD alloys are also an ideal playground for the study of 2D phase transitions and critical phenomena. Monolayer alloys that connect two TMDs in different phases (structural, electronic, magnetic, etc.) should enable one to manipulate these phase transitions where the chemical composition of the alloy serves as the tuning parameter. However, the synthesis of a particular TMD alloy is subject to the miscibility of the components and its thermodynamic stability [209], which is more challenging in the case of aliovalent TMD alloys. Therefore, most of the experimental progress here has been conducted in isovalent TMD alloys. For example, structural and electronic phase transitions have been detected in the isovalent $MSe_{2(1-\delta)}Te_{2\delta}$ with M = W,Mo.[210, 211] Nonetheless, aliovalent alloys enable a bridge between TMD materials with more disparate properties and, therefore, a richer variety of phase transitions that can be accessed.[212, 213] For instance, group-V TMD materials host collective electronic phases such as CDW order [214, 6, 7, 215], SC [9, 118, 10], spin liquid behavior [27], magnetism [138, 216], and topological phases [13, 217]. These electronic phases are highly susceptible to external stimuli, and their study in TMD alloys enable access to, for example, relevant disorder and doping effects as well as their intrinsic robustness, which remain rarely explored in the SL limit.[211, 11]

In this work, we present an experimental and theoretical investigation of the aliovalent TMD alloy $Nb_{1-\delta}Mo_{\delta}Se_2$. We have successfully synthesized high-quality monolayers across the entire $0 < \delta < 1$ range, and examined the evolution of the atomic and electronic structure using low-temperature (0.3 - 4.2 K) STM/STS. First, our measurements enable us to explore the effect of electron doping on the

monolayer $NbSe_2$ and track its impact on the electronic bands. The metal-semiconductor transition in this TMD alloy occurs for Nb concentrations of 25% ($\delta = 0.75$), which enables a wide-range across which the band gap can be tuned up to a maximum band gap of 2.2 eV of monolayer $MoSe_2$.[89] Second, we also observe a nearly simultaneous disappearance of the CDW and SC, when the Mo concentration exceeds 15% ($\delta \geq 0.15$), which highlights the robustness of these collective states against disorder.

A closer look reveals that the microscopic reasons for the destruction of CDW and SC are different. While the SC undergoes an initial strengthening at low Mo doping levels followed by a monotonic weakening, the CDW gradually loses the 3x3 long-range order. The effect of Mo on SC, including the initial increase, are due to doping and therefore a monotonic reduction of the density of states (DOS) at the Fermi level. The non-monotonic behavior appears due to the competition between two factors: the electron-phonon coupling strength is directly proportional to DOS, and the proximity to magnetism is resonantly related to the DOS. As a result, at low doping concentrations of Mo, the proximity to magnetism is reduced more rapidly than the coupling strength, ensuring the initial rise of T_c, but then becomes unimportant as the weakening of the electron-phonon interactions becomes the main factor. Instead, the weakening of the CDW order is weakly dependent on doping, and is mostly due to a systematic reduction of the CDW domain sizes due to Mo pinning the domain boundaries.

For this work theory support was provided by the group of Professor Igor Mazin affiliated to the Quantum Science and Engineering Center at the George Mason University in Fairfax, USA.

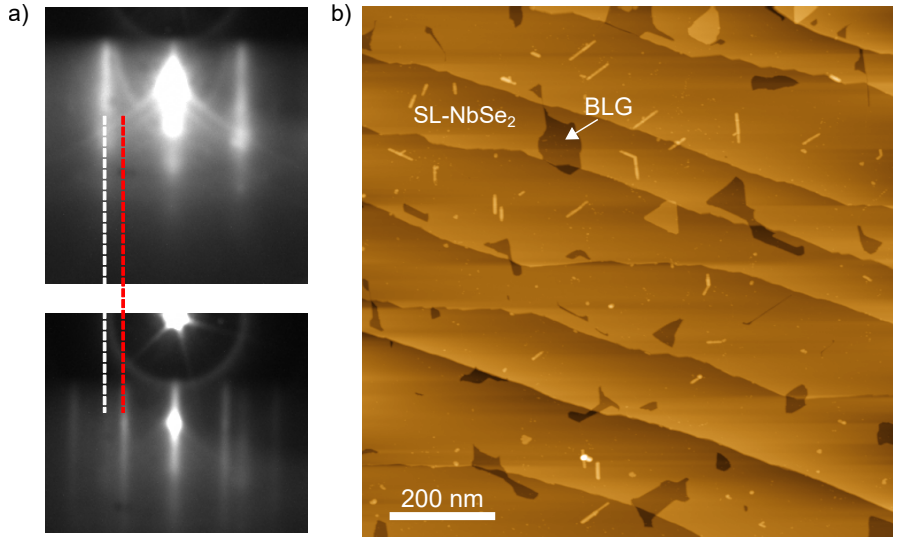

Figure 4.1.1: Morphology of single-layer $Nb_{1-\delta}Mo_\delta Se_2$. a) RHEED pattern before (upper) and after (lower) the growth of a $Nb_{1-\delta}Mo_\delta Se_2$ alloy on BLG/SiC(0001). BLG and $Nb_{1-\delta}Mo_\delta Se_2$ diffraction patterns are indicated by the white and red dash lines. b) Typical large-scale STM topography of a $Nb_{0.7}Mo_{0.3}Se_2$ monolayer on BLG/SiC(0001) ($V_s = 1.8$ V, It = 0.03 nA, T = 0.34 K).

4.1.1 Identification of substitutional transition metal dopants

We have grown monolayers of the aliovalent alloy $Nb_{1-\delta}Mo_{\delta}Se_2$ with different compositions ($0 < \delta < 1$) on bilayer graphene (BLG)/6H-SiC(0001) by molecular beam epitaxy (MBE). During the growth we have used the RHEED system to monitor its progression. An example of such a RHEED measurements and the corresponding sample topography is shown in Figure 4.1.1 a) and b). Graphene as a subsrtate (see Figure 4.1.2 a)) is both a suitable template for the synthesis of TMD materials and plays a negligible role in their electronic structure and collective electronic phases.[218] For dilute alloys ($\delta < 0.1$ and $\delta > 0.9$), STM imaging reveal that the element in minor concentration (Mo and Nb, respectively) is observed as individual point defects in the atomic lattice. This is illustrated in Figure 4.1.2 b) for $Nb_{1-\delta}Mo_{\delta}Se_2$ ($\delta = 0.07$). Figure 4.1.2 b) shows an atomically resolved STM image of the $NbSe_2$ lattice, where the 3x3 CDW ordering is also visible. In addition, several triangular features of equal orientation can also be observed. We attribute these features to Mo atoms located in substitutional positions in the Nb lattice. Since the STM images show the outermost chalcogen lattice, the triangular feature corresponds to the three Se atoms bonded to a single Mo substitutional atom underneath, whose local DOS is different from the Se atoms bonded to Nb atoms, thus link them visible.

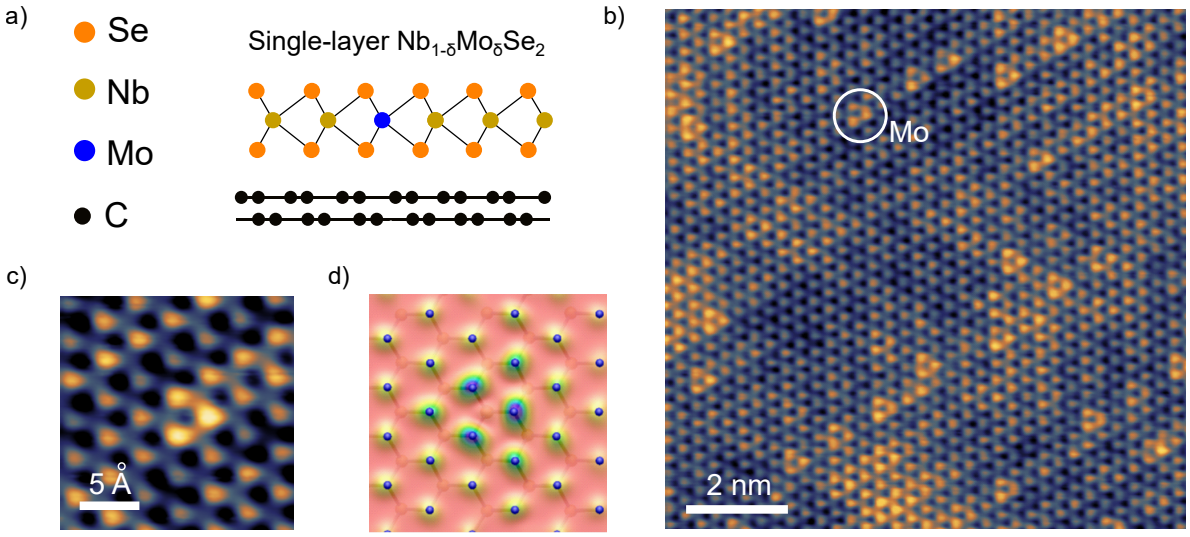

Figure 4.1.2: Atomic structure of the $Nb_{1-\delta}Mo_{\delta}Se_2$ alloy. a) Side-view sketch of the atomic structure with Mo dopant indicated in blue and the BLG substrate in black. b) High-resolution atomic-scale STM image of SL-$Nb_{0.93}Mo_{0.07}Se_2$ with 3×3 CDW modulation and the Mo defect encircled in white (V_s = -500 mV, I = 0.1 nA, T = 0.34 K). c) STM image of an individual substitutional Mo atom embedded in the $NbSe_2$ atomic lattice lattice (V_s = -550 mV, It = 0.1 nA, T = 0.34 K). d) Charge density isosurface of the occupied Mo states for Mo substituting on the Nb site.

These triangular-like features are also predicted by our first-principles density functional theory (DFT) calculations of the electron density in the vacuum region above a Mo on the Nb site in $NbSe_2$, as illustrated in Figure 4.1.2 d). The concentration of these triangular features is directly proportional to the Mo flux during the MBE growth, which further supports their identification as individual Mo atoms in the Nb lattice.

We have also analyzed the energetics of incorporating Mo in $NbSe_2$ and found it consistent with this interpretation. To this end, the group of Professor Mazin has calculated formation energies for different possible configurations of Mo incorporated into $NbSe_2$: substituting on the Nb site (Mo_{Nb}), substituting on the Se site (Mo_{Se}), or being adsorbed on top of the $NbSe_2$ surface. For the latter, there are three possible configurations; Mo adsorbed right on top of a Nb, Mo_{ads}^{Nb}, or on top of a Se, Mo_{ads}^{Se}, or above the hollow site, Mo_{ads}^{hollow}. The formation energies for these configurations are summarized in Table 4.1. In the dilute limit Mo_{Nb} has the lowest formation energy, which confirms our assertion that Mo indeed replaces Nb sites when incorporated into $NbSe_2$.

Table 4.1: Formation energy of Mo under Nb-rich and Nb-poor conditions substituted on the niobium site, Mo_{Nb}, Mo substituted on the Se site, Mo_{Se}, and Mo adsorbed above the hollow site, Mo_{ads}^{hollow}, which is the most stable adsorption site for Mo on $NbSe_2$.

Defect	Nb-rich (eV)	Nb-poor (eV)
Mo_{Nb}	1.01	-0.14
Mo_{Se}	3.41	6.12
Mo_{ads}^{hollow}	2.60	4.03

Our STM spectroscopy of these triangular features, due to Mo_{Nb}, initially identified as substitutional Mo atoms, reveals two clear fingerprints in the low-lying electronic structure. Figure 4.1.3 a) shows a typical dI/dV curve acquired on top of a triangular feature (yellow curve) along with the corresponding reference curve on pristine SL-$NbSe_2$ (blue curve).[6] The presence of this point defect induces a well-defined electronic resonance at an energy of -0.45 V below E_F. Differential conductance maps taken at this energy on a ML with a dilute concentration of Mo atoms (Figure 4.1.3 b) reveal that the intensity of this resonance has a spatial extension of ~ 5 Å around the defect. The crystal field splitting of Mo_{Nb} provides a key to understand the origin of this resonance. The Mo atom is in a trigonal prismatic coordination with Se when it is incorporated as Mo_{Nb}, which splits the five Mo 4d states into three different groups as illustrated in Figure 4.1.3 c). The density of states of Mo_{Nb} from our first-principles calculations highlights the Mo d-states where we find Mo d_{z^2} states are at a lower energy compared to the Mo d_{xy}, $d_{x^2-y^2}$ states, which is consistent with a trigonal crystal field acting on Mo^{4+}. The wavefunction of the Mo d_{z^2} states, which extend out of the $NbSe_2$ plane, have a lower decay constant compared to the in-plane Mo d_{xy}, $d_{x^2-y^2}$ states and are the most likely to contribute to tunneling.

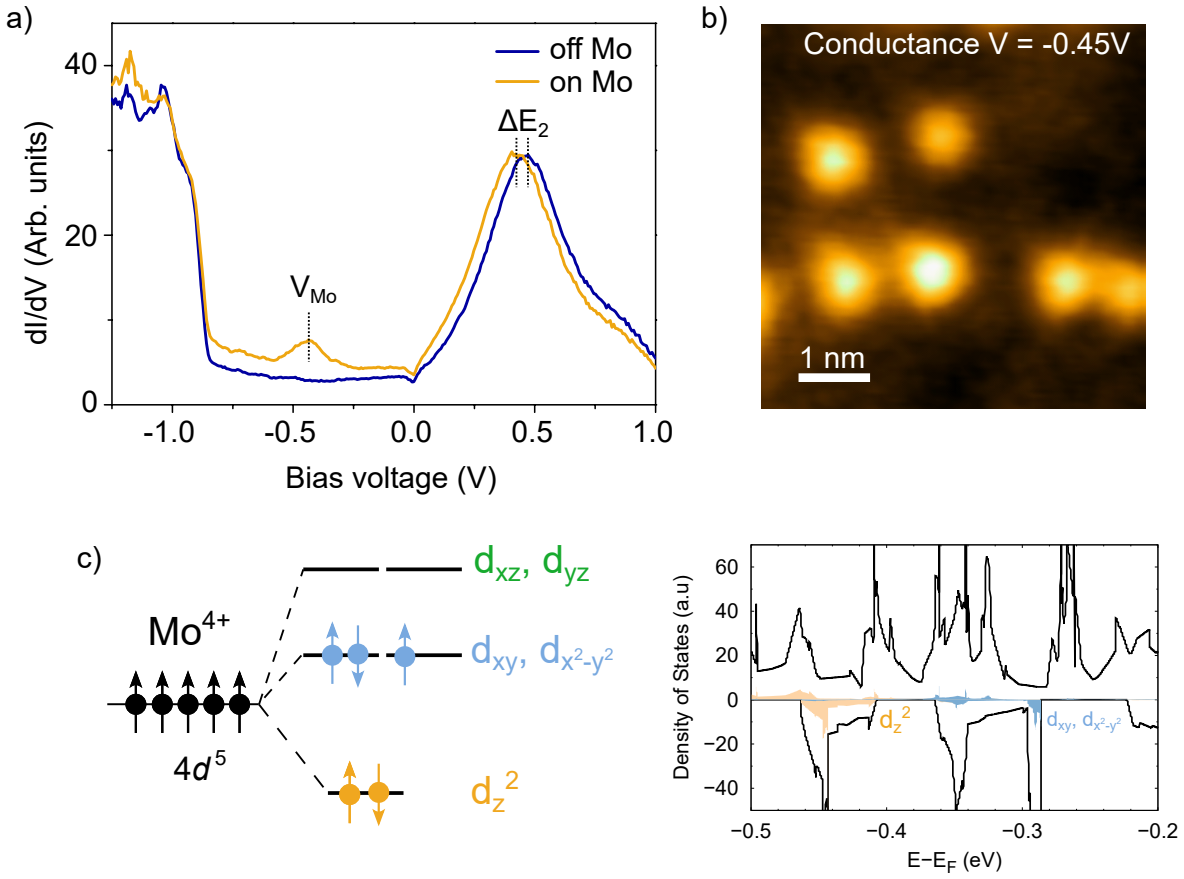

Figure 4.1.3: Electronic fingerprint of Mo substitutional atoms in monolayer $NbSe_2$. a) Wide-bias STM dI/dV spectra consecutively acquired on single-layer $Nb_{0.007}Mo_{0.993}Se_2$ on top of a substitutional Mo atom (yellow curve) and on a bare $NbSe_2$ region (blue curve). The grey arrows denote the shift in the conductance that is measured on top of the Mo atom versus off of the Mo atom. b) Experimental conductance maps taken in monolayer $Nb_{0.02}Mo_{0.98}Se_2$ taken at V_s = - 0.45 V, the maximum of the d_{z^2} states (I_t = 2 nA, T = 4.2 K). c) Trigonal crystal field acting on the 4d-states of Mo^{4+} (left) and total spin-polarized density of states of Mo in a supercell of $NbSe_2$ (black) illustrating the Mo d_{z^2} states (orange) and Mo d_{xy}, $d_{x^2-y^2}$ states (blue).

In agreement with the energy of the resonance in experiment, we find the Mo d_{z^2} states to be 0.47 eV below the $NbSe_2$ Fermi level in our calculations. In addition to the resonance, this defect also induces a rigid shift (ΔE_2) of the peak labelled as E_2, which corresponds to the flat region at the top of the Nb-derived band at $\overline{\Gamma}$ of SL-$NbSe_2$.[6, 218] We will discuss this shift in more detail in section 4.1.3 and show that it is due to Mo_{Nb} acting as a source of electron doping.

4.1.2 Atomic structure of the TMD alloy monolayers

Now that we have established the trigonal prismatic metal coordination of both TM elements by Se atoms in the TMD alloy, we first characterize the morphology of the MBE-grown monolayers of alloys for various stoichiometry values. In total, we grew 24 TMD alloy monolayers with different stoichiometries to explore the whole range ($0 < \delta < 1$) from SL-$NbSe_2$ ($\delta = 0$) to SL-$MoSe_2$ ($\delta = 1$). The stoichiometry of the grown TMD alloys rely on a calibration carried out in dilute alloys ($\delta < 0.12$ and $\delta > 0.9$), which enable to obtain a nearly exact stoichiometry by counting the number of individual dopants per area from high-resolution STM images. Figure 4.1.4 shows the obtained doping values as a function of the Mo and Nb flux we have used in the evaporation process. As it is illustrated, it is only possible to obtain an accurate doping atom number for relatively low doping concentrations. However, we have found a linear relation between the flux ratio applied at the evaporators and the synthesized samples for such low doping concentrations close to the pristine $NbSe_2$ and the pristine $MoSe_2$, respectively. Therefore we assume that this relation holds also for more equally comprised Nb/Mo alloys.

Figure 4.1.5 shows the evolution of the morphology of the TMD alloys with varying stoichiometries for six STM images. Figure 4.1.5 a) and Figure 4.1.5 f) reveal the topography of the bare TMD layers, i.e., SL-$NbSe_2$ and SL-$MoSe_2$, respectively. While both layers exhibit a high crystalline quality with a small density of point defects ($< 10^{12}$ cm^{-2}), SL-$MoSe_2$ exhibits its characteristic mirror twin boundaries forming triangular nanostructures.[219]

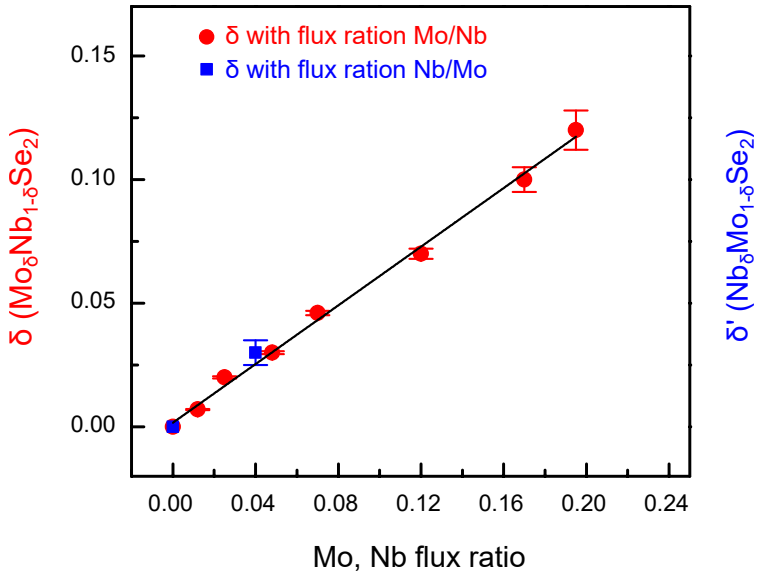

Figure 4.1.4: Stoichiometry determination of SL-$Nb_{1-\delta}Mo_\delta Se_2$ alloy. Linear relationship between the stoichiometry δ (δ') and the Mo (Nb) flux ratio for the $Nb_{1-\delta}Mo_\delta Se_2$ alloys.

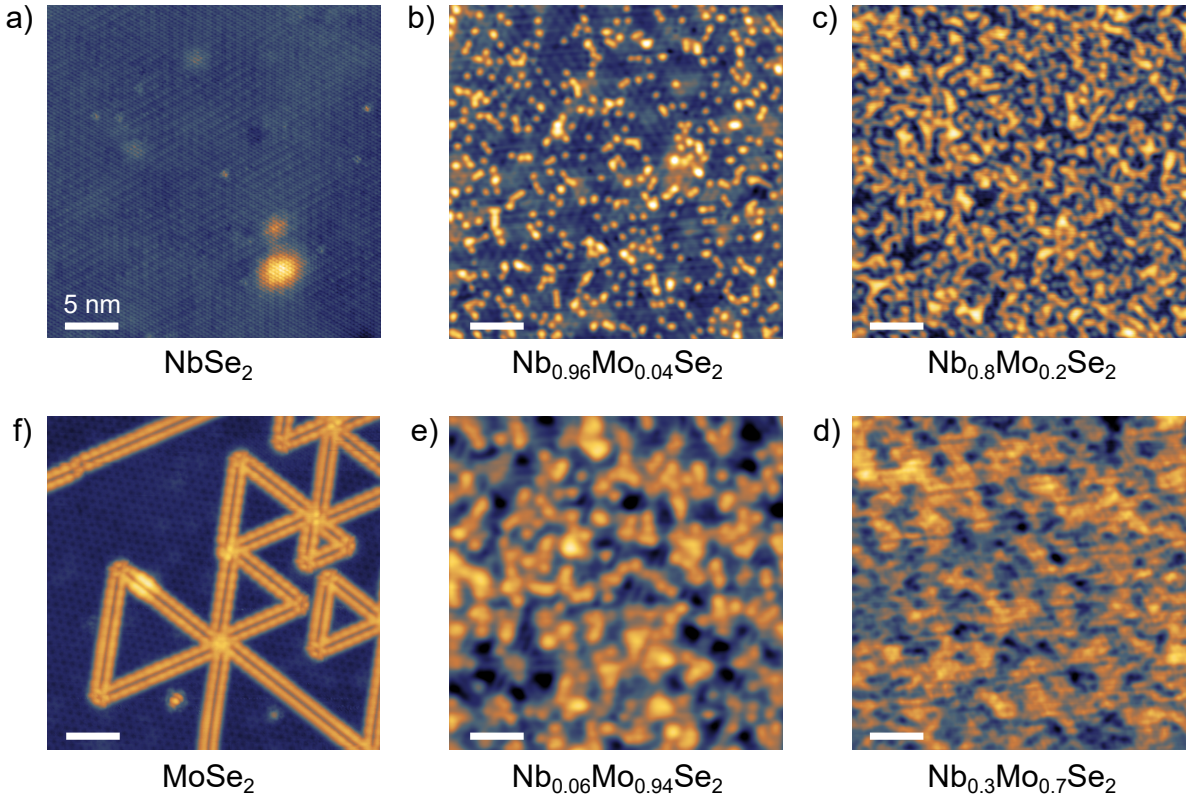

Figure 4.1.5: Atomic-scale morphology evolution of SL-$Nb_{1-\delta}Mo_{\delta}Se_2$ ($0 < \delta < 1$). a-f) High resolution STM images of several $Nb_{1-\delta}Mo_{\delta}Se_2$ MLs for different δ. All the images have the same size for an easier comparison (30×30 nm^2). Imaging parameters: a) V_s = -60 mV, I = 580 pA, T = 0.34 K. b) V_s = -550 mV, I = 200 pA, T = 0.34 K. c) V_s = -500 mV, I = 150 pA, T = 0.34 K. d) V_s = -800 mV, I = 10 pA, T = 0.34 K. e) V_s = -1500 mV, I = 20 pA, T = 0.34 K. f) V_s = -1500 mV, I = 50 pA, T = 0.34 K).

For dilute concentrations of Mo (Figure 4.1.5 b) and Nb (Figure 4.1.5 e), dopants can be observed embedded individually into the host lattice, which still preserve their most characteristic features such as the 3×3 CDW order and the presence of MTBs, respectively. For higher concentrations (Figure 4.1.5 c) and Figure 4.1.5 d), the dopants' electronic states overlap and the STM images are entirely dominated by the electronic structure.

STM imaging also allowed us to gain key information regarding the spatial distribution of the dopants across the 2D alloy monolayers. Our large-scale topographic images for $\delta < 0.5$ reveal a quite homogeneous distribution of Mo atoms except very close to the edges (~ 10 nm), where a sudden depletion of Mo is observed (see Figure 4.1.6). This behavior at the edges was not noticeable in the range $\delta > 0.5$ with Nb atoms.

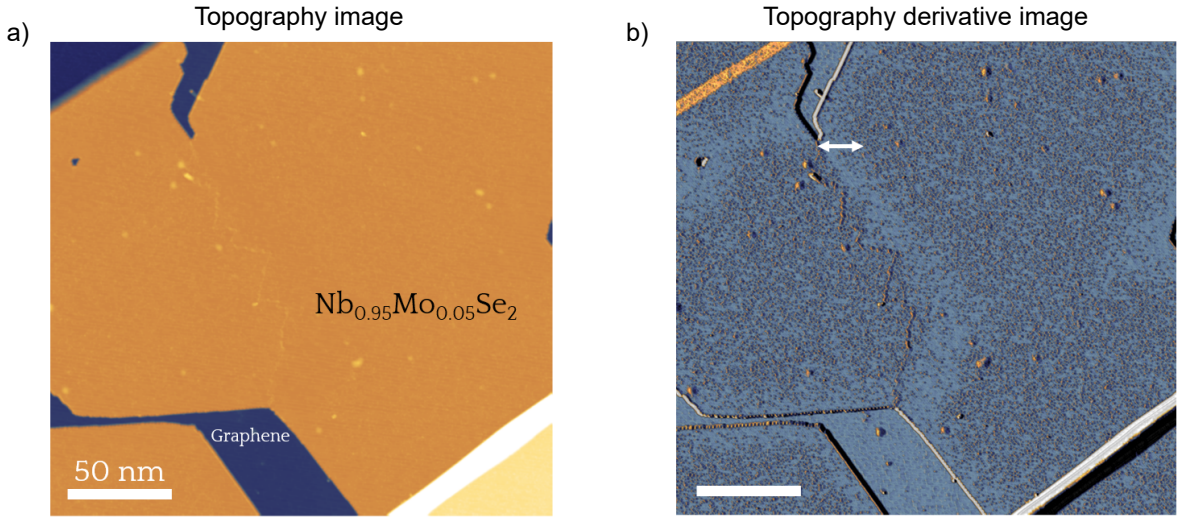

Figure 4.1.6: Homogeneity of the Mo:doped SL-$Nb_{1-\delta}Mo_{\delta}Se_2$ alloy. a) Large-scale STM image of the $Nb_{0.95}Mo_{0.05}Se_2$ monolayer (V_s = -0.5 V, It = 0.01 nA, T = 4.2 K). b) Topography derivative image of a) to enhance the contrast of the Mo dopant concentration, which is homogenous except for a Mo depletion near the edges of the domains ($\sim$ 10 nm).

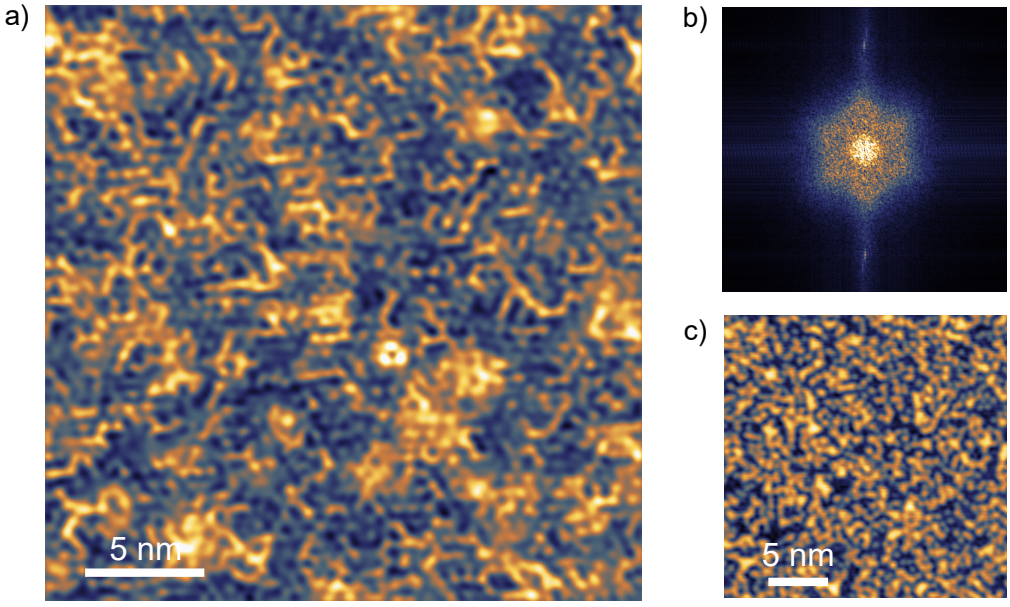

Figure 4.1.7: Striped substitutional Mo arrangement. a) STM image of the $Nb_{0.8}Mo_{0.2}Se_2$ monolayer showing stripes of Mo atoms (V_s = + 2 V, I_t = 0.15 nA, T = 4.2 K). b) FFT image of the topography in a) showing the six-fold angular stripe arrangement. c) STM image of the same region as in a) taken at the opposite polarity (occupied states) (V_s = - 0.4 V, I_t = 0.15 nA, T = 4.2 K).

Although segregation of the atomic species seems minor at large length scales, the atomic distribution of Mo dopants in the monolayer shows evidence for atomic ordering. An interesting observation in our STM images of SL-$Nb_{1-\delta}Mo_{\delta}Se_2$ with relatively high Mo concentration ($\delta > 0.15$) is the nm-sized stripes along the three crystallographic axes that likely correspond to Mo atomic chains. Figure 4.1.7 a) shows an example image of such an alloy where these stripes are visible, depending on the polarity of the bias voltage. In Figure 4.1.7 b) its corresponding FFT pattern is illustrated. At this relatively high doping level of $\delta = 0.2$, the CDW pattern is not visible anymore. Figure 4.1.7 c) shows a topographic image from the same area at the opposite bias polarity. In this case the stripes pattern cannot be identified. Although non-random dopant distributions are common in TMD alloys [196, 220, 221], striped configurations usually exhibit strong anisotropy (parallel stripes only along one crystallographic direction), which affect their most fundamental properties.[196, 221]

4.1.3 Evolution of the electronic structure: metal to semiconductor transition

We experimentally determined the evolution of the electronic structure of MLs of $Nb_{1-\delta}Mo_{\delta}Se_2$ from the metallic SL-$NbSe_2$ ($\delta = 0$) to the semiconducting SL-$MoSe_2$ ($\delta = 1$). Figure 4.1.8 a) shows this evolution through a representative series of dI/dV spectra taken over a large bias range in steps of $\triangle\delta = 0.1$. Each spectrum represents the averaged electronic structure of alloy areas of 300 – 900 nm^2 sampled measuring grids of point dI/dV curves with ~ 2 curve/nm^2. Starting from SL-$NbSe_2$ (bottom black curve), three characteristic STS features labelled as E_i are known to represent the onset of the three sets of electronic bands near E_F.[6] The E_1 feature sets the onset of the p-derived band from Se atoms, which is located at 0.81 V below E_F. The E_2 feature is a pronounced peak that corresponds to the upper onset of the d-band from the Nb lattice ($E_2 = 0.46$ V). This band is responsible for the metal character of SL-$NbSe_2$ as well as the existence of both CDW and superconductivity. Lastly, the E_3 feature is regarded as the lower onset of a second Nb band located at K with a strong d_{z^2} character, and is found approximately at 2.1 V. The energy position of these key STS features can be tracked with the Mo concentration (δ), as shown in Figure 4.1.8 b).

There the energy shift of these three features with respect to their energy position for SL-$NbSe_2$ ($\delta = 0$) is shown as the Mo concentration increases. Interestingly, E_1 remains at the same energy up to a 20% of Mo concentration, a value beyond which E_1 cannot be traced. Unlike E_1, the E_2 and E_3 features exhibit a monotonic shift towards E_F with δ. The electronic structure of these TMD alloys that evolve from SL-$NbSe_2$ to SL-$MoSe_2$ unavoidably undergoes a metal-to-semiconductor phase transition. To visualize this electronic transition, the alloy requires Mo contents larger than $\delta = 0.7$, as shown in Figure 4.1.8 a) and Figure 4.1.8 c). For $\delta = 0.7$ (SL-$Nb_{0.3}Mo_{0.7}Se_2$), while the alloy ML reaches zero DOS at E_F and ~ 0.8 V, the gap is still negligible due to persistent states originally from the d-band (E_2 feature). For $\delta = 0.8$, the phase transition has taken place, which leads to semiconducting layers with an incipient bandgap of 0.6 ± 0.2 eV with p-type behaviour.

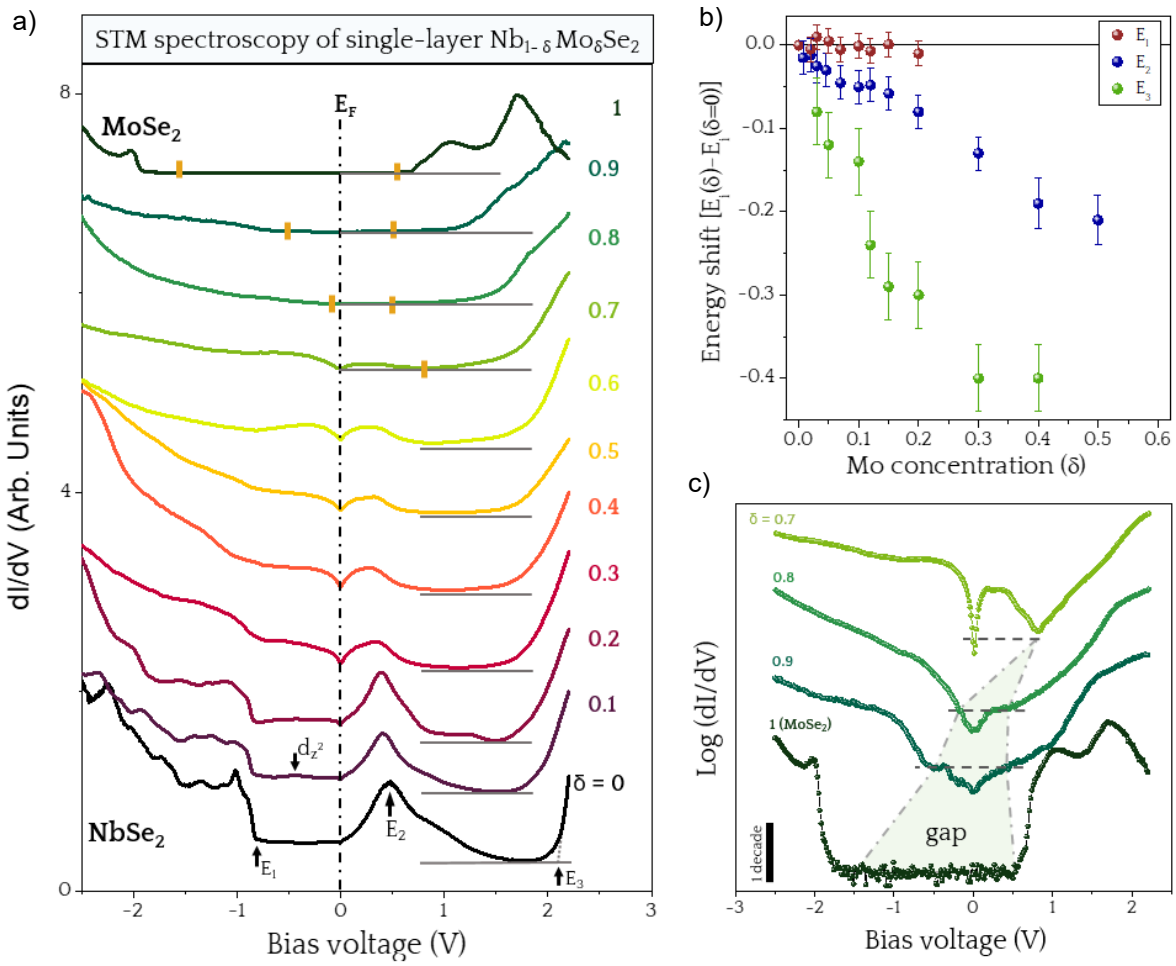

Figure 4.1.8: Electronic structure evolution of the monolayer $Nb_{1-\delta}Mo_{\delta}Se_2$ alloy. a) Representative wide-bias dI/dV spectra taken on different $Nb_{1-\delta}Mo_{\delta}Se_2$ monolayers across the full range $0 < \delta < 1$. Each curve represents the averaged electronic structure of alloy areas of $300 - 900\,nm^2$ sampled measuring grids of point dI/dV curves with ~ 2 curve/nm^2. b) Energy shift of the $E_{i=1-3}$ features with respect to their initial energy position in $NbSe_2$ ($\delta = 0$) as a function of the Mo concentration (δ). c) Logarithmic plot of the dI/dV spectra relevant for the metal-semiconductor transition ($0.7 < \delta < 1$).

From here to SL-$MoSe_2$, the bandgap develops due to the gradual depletion of the occupied states until it reaches a full electronic bandgap of 2.2 eV for SL-$MoSe_2$ ($\delta = 1$) with n-type character.[89] Interestingly, the bandgap value in this type of alloy evolves for a broad range of Nb-doping of nearly 30%, which enables a large tunability.

To provide insight into the changes in E_1, E_2 and E_3 as a function of δ we consider different factors that affect the evolution of the electronic structure with Mo doping. This includes (i) electron doping since Mo^{4+} has one more valence electron than Nb^{4+}, (ii) changes in p-d hybridization due to

differences in the Mo and Nb ionic radii and (iii) changes in the dielectric properties as the electronic structure evolves from a metal to a semiconductor. The first effect shifts E_F upwards. The second reduces the p-d separation, and therefore the separation between the corresponding bands. Indeed, the Nb bands move up by roughly $t_{pd}^2/(E_d - E_p)$, where t_{pd} is some effective hybridization strength, and the Se bands move down by the same amount. Finally, in the semiconducting regime (not relevant for Figure 4.1.8 b) the Coulomb interactions become long-range and density functional calculations need to be corrected (e.g., with the use of hybrid functionals).

We first address the shift in E_2. This can be traced to the upward shift of the Fermi level mentioned above. This is indeed what we find with our first-principles calculations illustrated in Figure 4.1.9 a).

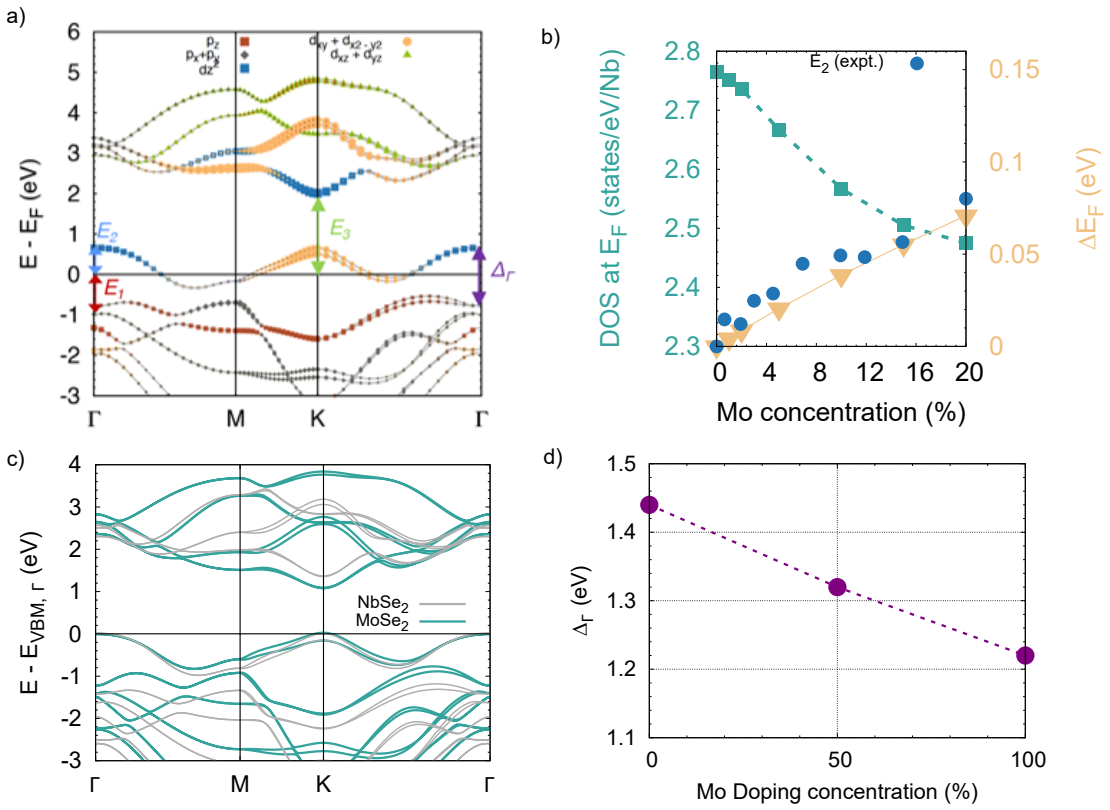

Figure 4.1.9: First-principles calculations of Mo doping in $NbSe_2$. a) Band structure of monolayer $NbSe_2$ plotted with respect to the Fermi level. The orbitals contributing to each state (listed in the legend in the top) are projected on to each band. The origin of E_1, E_2 and E_3 in our STM measurements (Figure 4.1.8) are marked with vertical arrows. b) Shift in the Fermi level (right vertical axis, orange triangle) and the magnitude of the density of states at the Fermi level (left vertical axis, teal squares) as a function of Mo concentration. Shift in the position of the peak labeled E_2 from the STM measurements (right vertical axis, blue circles) as a function of Mo content.

Doping $NbSe_2$ with Mo up to $\delta = 0.2$, we find that E_F shifts up by 0.071 eV with respect to pristine $NbSe_2$, in agreement with our experiment. For large Mo concentrations ($\delta > 0.5$), the E_2 peak amplitude is largely damped, likely due to the significant broadening of the d-band. This coincides with the emergence of a significant DOS for energies below E_F. This peak in the DOS is the origin of the valence band of Nb-doped $MoSe_2$ monolayer, which develops from the localized d_{z^2} state shown in Figure 4.1.3.

Next, we address why E_1 remains constant as a function of δ. As mentioned, the energy separation (which we define as Δ_Γ) between the highest occupied transition metal d-state at Γ and the next lower lying state (which gives rise to the feature E_1) that is comprised of Se p-orbitals with admixture of transition metal d_{xz}, d_{yz} orbitals is larger for $NbSe_2$ compared to $MoSe_2$ (see Fig. 4.1.9 a). This is accompanied by a reduction in bandwidth of the valence band around Γ when going from $NbSe_2$ to $MoSe_2$ as shown in Fig. 4.1.9 c). Since the d-d direct overlap is small, the effective d-d hopping is controlled by the same parameter $t_{pd}^2/(E_d\text{-}E_p)$, albeit maybe with a different numerical coefficient. Hence, the reduction in Δ_Γ and in turn the bandwidth can be understood by a general reduction of t_{pd}, as a function of δ. Within this line of reasoning, we expect Δ_Γ to decrease as a function of δ, which is indeed what we find with our first-principles calculations. This upward shift of the Se derived band with respect to the highest occupied state at K as a function of δ coincides with the upward shift of the Fermi level due to doping (feature E_2). The cancellation of these two upward shifts results in an approximately constant energy difference between the Se p-states and the Fermi level, which is indeed what we find in our measurements of E_1 as a function of Mo concentration.

Feature E_3 is probably the most complex of all. At first glance, it reflects the crystal field gap, as it represents transitions between the Fermi level and the conduction d-band with the minimum at K. However, this state at K has pure d_{z^2} character, similar to the band below at Γ. Therefore, the magnitude of the crystal field splitting is affected more by the dispersion of the d_{z^2} band and $d_{z^2}/(d_{xy}, d_{x^2-y^2})$ hybridization. Since the d-d hopping largely proceeds via the Se orbitals, it is again controlled by $t_{pd}^2/(E_d\text{-}E_p)$. Hence, within the simplest approximation the crystal field splitting should also decrease linearly as a function of δ, albeit with a different prefactor (note that in all three cases somewhat different combinations of $t_{pd\sigma}$ and $t_{pd\pi}$ form the effective t_{pd}. Indeed, in our experiments we find E_3 moves down roughly proportionally to, but faster than E_2. This is corroborated by our calculations (see Fig. 4.1.9 c), where we find the minimum crystal field gap in $NbSe_2$ is 1.33 eV, and in $MoSe_2$ it is 1.08 eV (both values are obtained with DFT, so for $MoSe_2$ it represents the gap in $MoSe_2$ with artificial metallic screening - which is what we need for the comparison with the experiment at $\delta < 0.6$, where the material is still metallic). The difference is 0.25 eV. Experimentally, the E_3 feature flattens out with Mo doping at 0.4 eV, larger than, but qualitatively consistent with the DFT estimate.

4.1.4 Collective electronic states against disorder

Lastly, we experimentally investigate the properties of the superconducting and CDW orders subject to disorder in the TM plane, which is key to understand their development in $NbSe_2$.

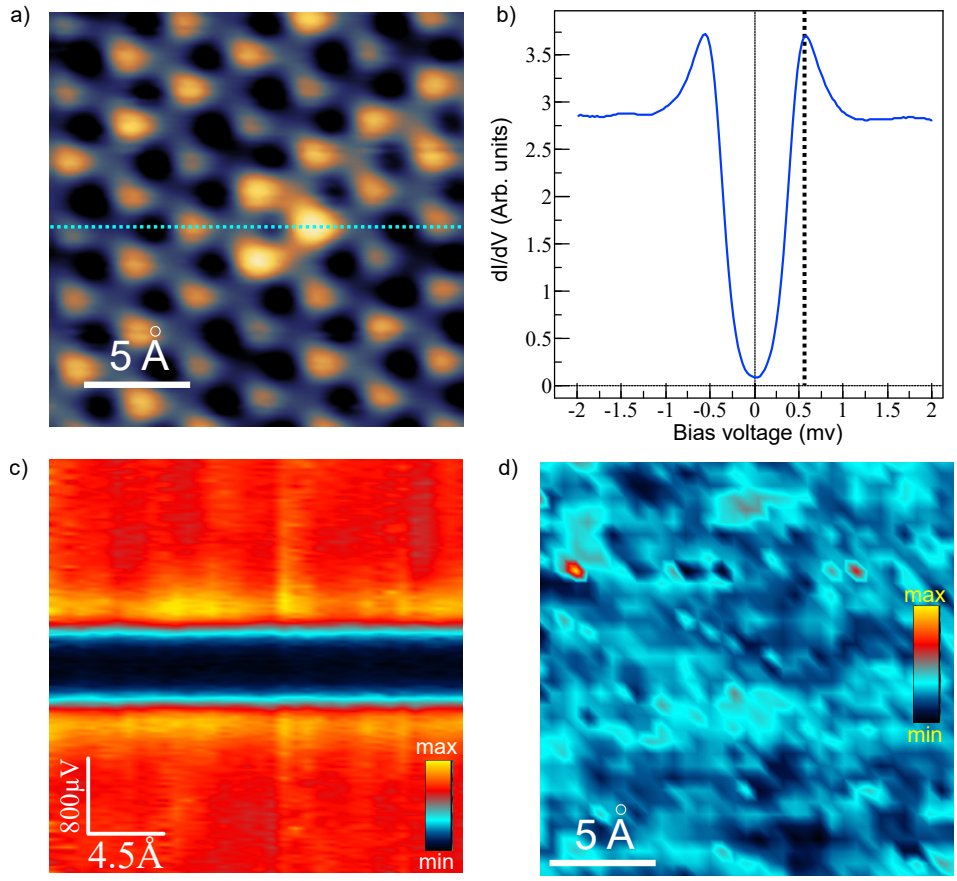

Figure 4.1.10: Robustness of superconductivity in SL-$Nb_{1-\delta}Mo_{\delta}Se_2$ against Mo impurities. a) Togographic STM image of $Nb_{1-\delta}Mo_{\delta}Se_2$ with a single Mo impurity located in the center (V_s = -550 mV, It = 0.1 nA, T = 0.34 K). b) STS dI/dV curves taken along the indicated dashed blue line in a). c) Line-spectroscopy illustration of the same data as shown in b). d) Conductance map taken in this area at V_s = 0.52 V.

Similar to the metal-semiconductor transition, the evolution of the electronic structure of SL-$Nb_{1-\delta}Mo_{\delta}Se_2$ from SL-$NbSe_2$ to SL-$MoSe_2$ implies the occurrence of two electronic phase transitions, i.e., the SC and CDW transitions. First, we focus on the behavior of the superconducting state. According to Anderson's theorem, non-magnetic impurities in conventional superconductors do not interfere with the superconducting state up to a critical defect density.[85] Therefore, the critical temperature of the material does not change by increasing the disorder in the system. However, in unconventional or non-s-wave superconductors, nonmagnetic and magnetic impurities are able to suppress T_c.[222] In order to test the theorem with our synthesized alloys we have analyzed the superconducting order parameter in an area, which comprises such a nonmagnetic Mo defect (see Fig. 4.1.10 a). Fig. 4.1.10 b) present the averaged STS dI/dV curve in the area of a).

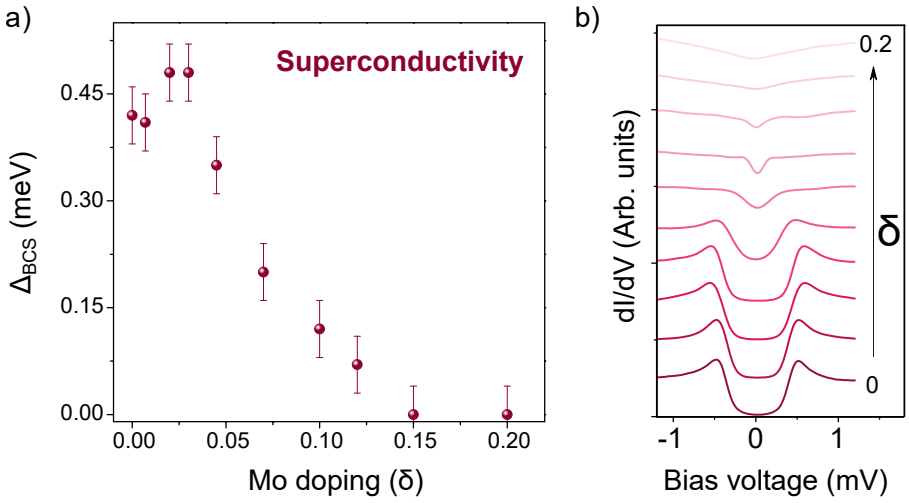

Figure 4.1.11: Superconductivity in the monolayer $Nb_{1-\delta}Mo_{\delta}Se_2$ alloy. a) Evolution of the experimental SC gap Δ with Mo concentration (δ). b) The experimental dI/dV spectra from which the Δ values are extracted. Each spectrum represents the average over regions of typically $\sim 100\,\mathrm{nm}^2$.

The variations of these curves and therefore the superconducting gap are very small and no differences can be identified in the spectra taken on top of the Mo defect. This is already a strong indication that the superconducting order is not modified by the impurity. We further prove this by plotting the dI/dV curves along the indicated line (see Fig. 4.1.10 a) as a line spectra in Fig. 4.1.10 c). The gap size remains constant over the entire length of the measured area and is not modified by the Mo impurity. A conductance map taken at $V_s = 0.52\,\mathrm{V}$ (see Fig. 4.1.10 d), the energy of the coherence peak, shows small random fluctuations in this area, but they do not correlate with the location of the Mo atom. We therefore conclude that the Anderson theorem holds for the $Nb_{1-\delta}Mo_{\delta}Se_2$ alloy and superconductivity is not altered.

Figure 4.1.11 a) shows the evolution of the averaged SC gap as a function of the Mo concentration, which comprises two regimes as seen. First, the SC gap undergoes a moderate increase of $\sim$ 20% from that of SL-$NbSe_2$ ($\Delta = 0.40$ meV) up to $\Delta = 0.48$ meV for a Mo concentration of 3% ($\delta = 0.03$). After the optimal SC at SL-$Nb_{0.97}Mo_{0.03}Se_2$, the SC gap is seen to decrease monotonically to ultimately vanish for a Mo critical concentration as large as 15% ($\delta = 0.15$). Such a large value is remarkable and highlights the robustness of the SC state in 2D against non-magnetic structural disorder.

Now, after discussing the experimental data, we want to shift the focus on the theoretical analysis and discuss the observed evolution of the superconducting state of this 2D alloy. Based on the DOS of monolayer $NbSe_2$,[119] we expect doping $NbSe_2$ with electrons to decrease the DOS at the Fermi level, $N(E_F)$, compared to pristine $NbSe_2$. Our DFT calculations in Figure 4.1.12 confirm this, showing that at about $\delta = 0.2$ doping, $N(E_F)$ decreases by 15% compared to $\delta = 0$. We expect this reduction in $N(E_F)$ with doping to also impact spin fluctuations, which have been shown to be prominent in

$NbSe_2$[119, 139, 223] and can potentially act as a source of pair-breaking. We gauge the tendency to magnetism as a function of doping by performing fixed-spin moment (FSM) calculations of monolayer $NbSe_2$ doped with Mo concentrations of δ = 0-0.2 (Figure 4.1.12). To this end, we used the virtual crystal approximation (VCA) to determine the ferromagnetic spin susceptibility, χ, defined as $\chi=(\partial^2 E/\partial m^2)^{-1}$. We find that χ decreases monotonically as a function of increasing Mo content compared to pristine $NbSe_2$ (inset of Figure 4.1.12), which implies the tendency to magnetism decreases with increasing doping. Taken together we find that doping $NbSe_2$ with Mo leads to a reduction in $N(E_F)$ and a reduction in the proximity to magnetism. This behavior of $N(E_F)$ and χ as a function of δ yields important insight into the non-monotonic change in T_c. In the first approximation, the electron-phonon coupling constant, λ_p, is proportional to $N(E_F)$, while the electron-paramagnon coupling, λ_s, is proportional to the spin susceptibility $\chi(q)$, averaged over the Brillouin zone. Using $\chi(q = 0)$ as a proxy, it is proportional, in the standard random phase approximation, to $N(E_F)/[1\text{-}IN(E_F)]$, where the Stoner parameter I is roughly independent of δ. In monolayer $NbSe_2$, $[1\text{-}IN(E_F)]$, was estimated to be rather large, ~0.7,[119] so that at small doping levels, λ_s decreases due to the reduction in $N(E_F)$ three times faster than λ_p. At the BCS level, their difference λ_p - λ_s enters in the equations for T_c.[224]

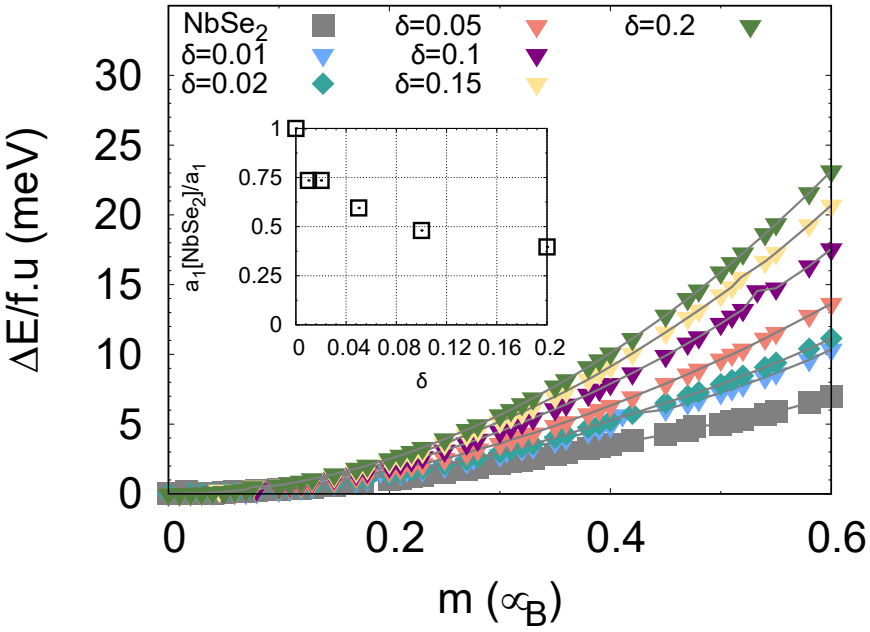

Figure 4.1.12: Collinear fixed-spin moment calculations of monolayer $Nb_{1-\delta}Mo_\delta Se_2$ alloy. Illustrated is the change in energy per formula unit with respect to the non-magnetic state as a function of magnetic moment per Nb atom. The inset shows the coefficient a_1 of $NbSe_2$ (see text) normalized by the value of a_1 obtained as a function of Mo content.

Initially, the reduction of λ_s is more important and drives Tc up. Then both constants, λ_p and λ_s, become too small and superconductivity wanes and eventually disappears. As a result of this competition, the actual dependence of T_c on δ is non-monotonic (Figure 4.1.11 a).

We now shift our focus from superconductivity to the CDW order in this system and analyse its properties as a function of Mo doping. First, we investigate the topographical evolution of the CDW order with Mo content. Figure 4.1.13 a) shows a representative series of STM images for different δ values along with their corresponding FFT images in Figure 4.1.13 b). As seen for the lowest Mo concentration ($\delta = 0.007$), the 3x3 spots in the FFT are sharp with an intensity comparable to that of the (1x1) Bragg peaks, which indicates a fully developed CDW. However, as the Mo concentration increases, the 3x3 peaks gradually broaden, become fainter and, ultimately, turn indistinguishable for $\delta \sim 0.2$, a critical value for the CDW melting. This scenario is quantitatively reproduced in the plots in Figure 4.1.13 c) and Figure 4.1.13 d) that show the averaged normalized peak intensity in the FFT (I_{3x3}/I_{1x1}) and the full width at half maximum (w_{FWHM}) of the 3x3 peaks.

One can anticipate two processes that contribute to the destruction of the CDW. First, as discussed, Mo impurities act as electron donors, and eventually turn the material semiconducting (at which point we do not anticipate a CDW to remain stable in pristine $MoSe_2$). Second, Mo impurities, as most defects, act as pinning centers for the phase domain walls.[225, 226] Because of the latter effect, the CDW phase is disrupted at a length scale $l \sim 1/\sqrt{\delta}$, where l is the average distance between two Mo impurities. At $\delta \approx 0.2$, $l \approx 2.2a$, and therefore a 3x3 CDW simply does not have room to develop. Nevertheless, as Figure 4.1.13 b) illustrates, even at $\delta \approx 0.3$ there still remains an incoherent cloud at about 1/3 r.l.u. from Γ, indicating that, while an ordered CDW is not possible any more, correlations of ionic displacement still "remember" the tendency to form the CDW with a q such that $|q| \approx 1/3$. This latter observation attests to the fact that the melting of the CDW at $\delta \sim 0.2$ is due to the disorder introduced by Mo, and not due to electron doping. Indeed, within our DFT calculations where we added electrons to $NbSe_2$ to mimic a doping of $\delta \sim 0.2$, we found the amplitude of the CDW decreases by a few tens of %, but does not disappear.

An independent test of our scenario is provided by the quantitative analysis of the visible full width at half maximum (W=FWHM, Figure 4.1.13 d). Indeed, if the finite size of the phase domains was the only source of superlattice peaks' broadening, we would expect this parameter to be proportional to $1/l \propto \sqrt{\delta}$ (black line in Figure 4.1.13 d). Indeed, this expression describes the experiment rather well, even though there are clearly additional, weaker mechanisms that are responsible for the finite width at $\delta = 0$.

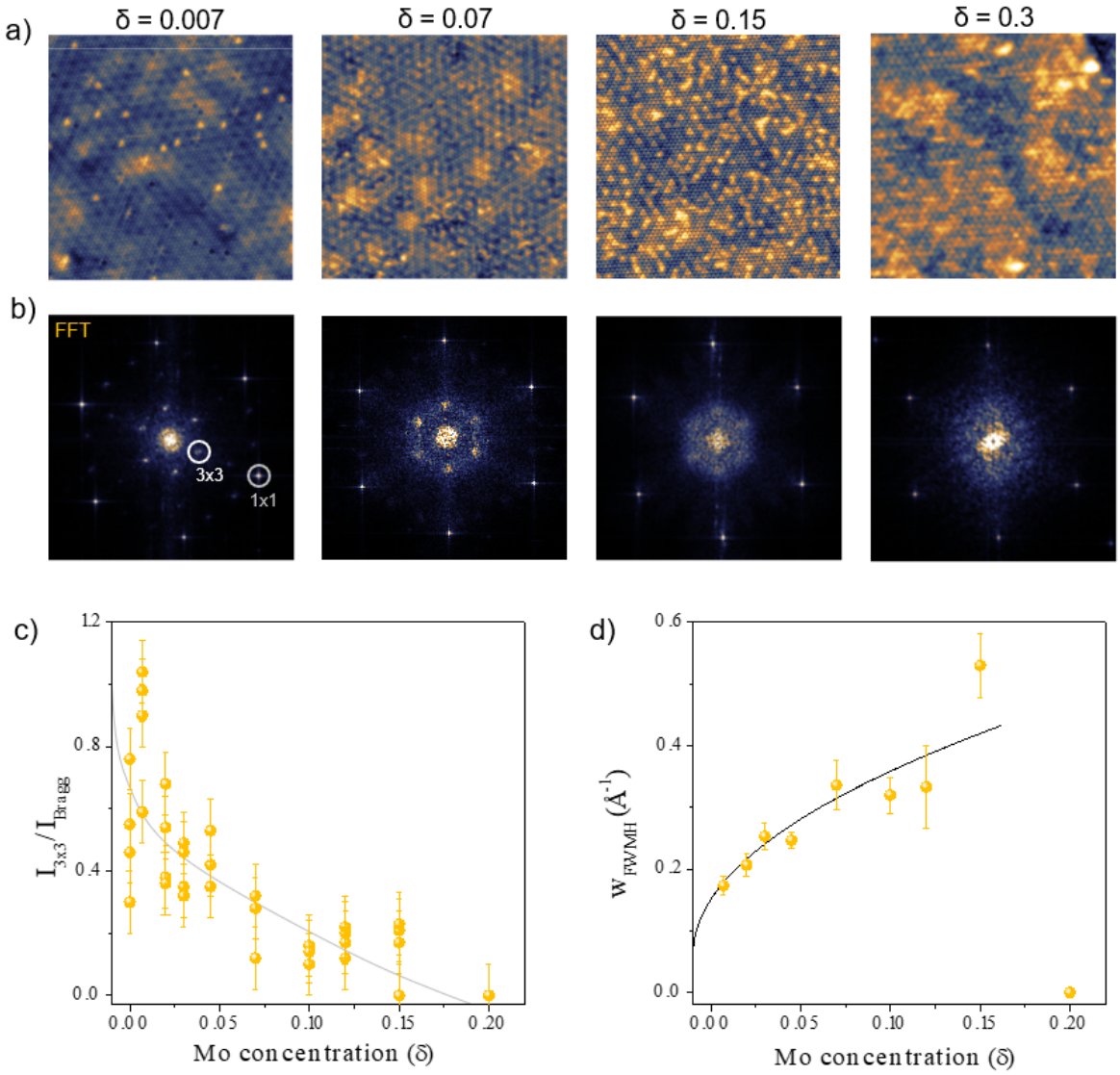

Figure 4.1.13: CDW in monolayer $Nb_{1-\delta}Mo_{\delta}Se_2$. a) High-resolution STM images for different Mo concentrations. Parameters: $\delta = 0.007$ (V_s = - 0.7 V, I_t = 1.5 nA, T = 1.2 K), $\delta = 0.07$ (Vs = - 0.09 V, I_t = 2 nA, T = 0.34 K), $\delta = 0.15$ (Vs = - 0.5 V, It = 0.67 nA, T = 1.2 K) and $\delta = 0.3$ (V_s = + 0.02 V, It = 1 nA, T = 2 K). b) Fast Fourier transform (FFT) of the STM images in a). c) Normalized intensity of the 3x3 peaks in the FFT of various experimental (yellow) atomically resolved STM images. The grey curve is a guide to the eye. d) Evolution of the width of the 3x3 peaks in the FFT as a function of Mo concentration. In black, the theoretical fit (see text).

The gradual reduction of the size of the 3x3 domains is shown in Figure 4.1.14. From left to right it illustrates topographic images, its corresponding FFT pattern and the FFT filtered 3x3 image for two different samples, a) pristine $NbSe_2$ and b) the $Nb_{0.93}Mo_{0.07}Se_2$ alloy.

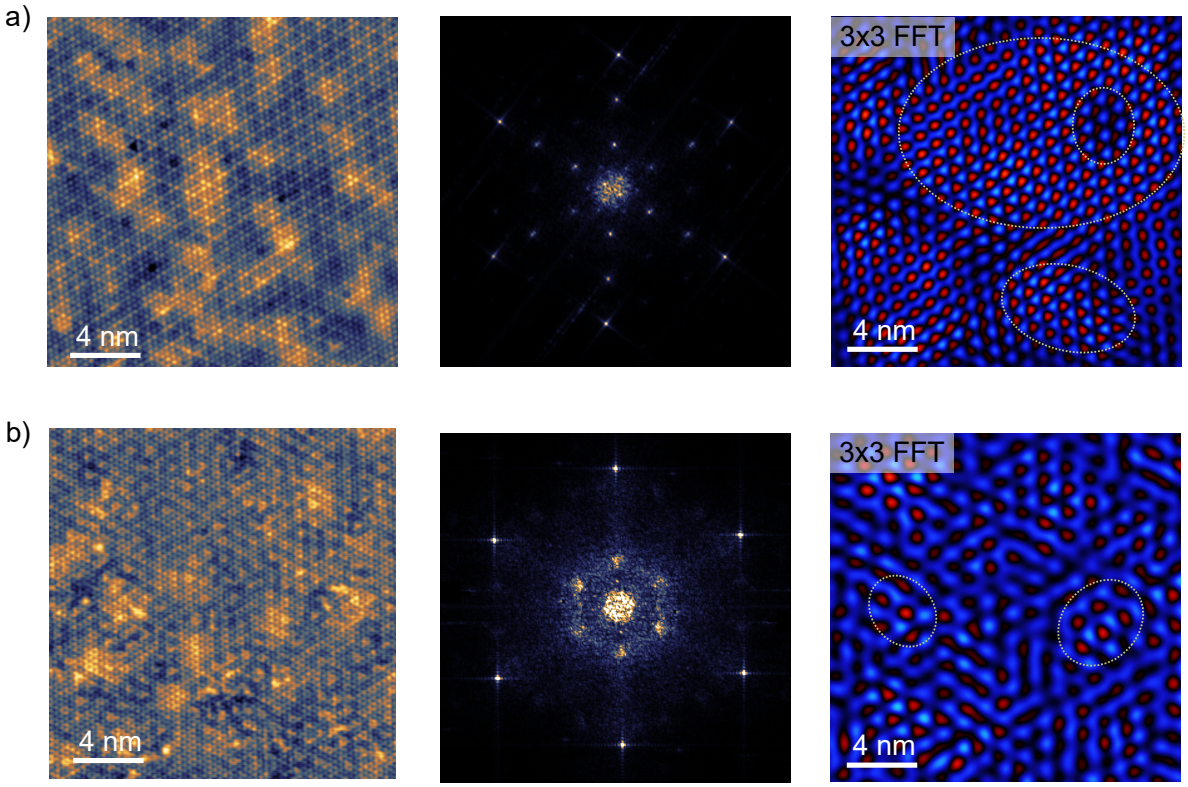

Figure 4.1.14: CDW 3x3 domains in $Nb_{1-\delta}Mo_{\delta}Se_2$. a) Left, STM Topograph of pristine NbSe2 ($\delta = 0$) and, center, its corresponding FFT. Right, inverse FFT of the integrated 3x3 peaks. Red regions indicate crystalline 3x3 domains and blue regions represent domain boundaries. Parameters: V_s = -0.09 V, I_t = 2 nA, T = 0.34 K. b) Same as a) for the $Nb_{0.93}Mo_{0.07}Se_2$ alloy shown in Figure 4.1.13 a). Parameters: V_s = + 0.05 V, I_t = 0.7 nA, T = 0.34 K.

Comparing the FFT patterns with each other reveals the broadening of the 3x3 modulation with the higher disorder. This effect can nicely be illustrated after filtering the 3x3 signal in the topographic images as shown on the right, where clearly the crystalline CDW domains are much larger in the pristine $NbSe_2$ case. In contrast, the CDW domains are already very small and almost suppressed in the $Nb_{1-\delta}Mo_{\delta}Se_2$ alloy.

4.1.5 Other substitutional elements in $NbSe_2$

In subsequent studies we have used other elements as substitutional atoms to modify the electronic structure of SL-$Nb_{1-\delta}X_{\delta}Se_2$ with X = Ti (see Fig. 4.1.15) and Cr, especially to study the effect of magnetic (Cr) and non-magnetic (Ti) impurities on SC and the CDW order. However, for both elements we have found that they trigger the T-phase of $NbSe_2$ and only a few areas can be grown in the desired superconducting H-phase. In the large scale STM image of the SL-$Nb_{1-\delta}Ti_{\delta}Se_2$ alloy shown in Fig. 4.1.15 a) one can identify areas with cluster like shapes on top and flat clean areas.

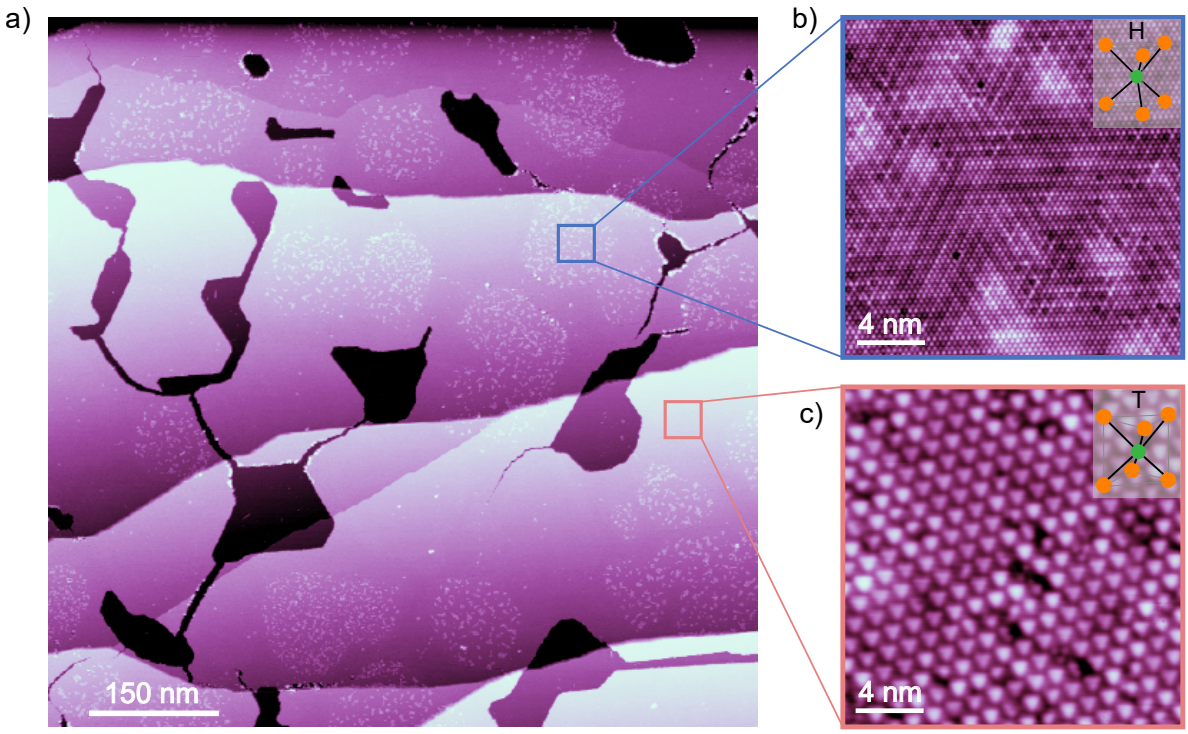

Figure 4.1.15: STM topography images of SL-$Nb_{0.97}Ti_{0.03}Se_2$. a) Large scale image (V_s = 1.8 V, I = 20 pA, T = 0.34 K). b) Zoom into H-phase area with metallic clusters on top (V_s = -0.1 V, I = 300 pA, T = 0.34 K). c) Zoom into clean T-phase area (V_s = -0.6 V, I = 1500 pA, T = 0.34 K).

Interestingly, we have found the H-phase inside the area of the clusters and the T-phase everywhere else. We suppose that these clusters are residual elements, which have been adsorbed on the surface after keeping this sample in the preparation chamber of the STM for several weeks. Due to the higher reactivity of the metallic H-phase, the sticking coefficient is higher for these non identifiable molecules and therefore mostly react within these areas. Contrary to that, the insulating T-phase is very inert and only few residual gases were deposited over time. We could not identify any dopant atoms in the H-phases of both materials (Fig. 4.1.15 b). For that we have intensively studied the topography, by taking conductance maps at different bias voltages. Therefore, we suppose that it is not possible to dope SL-$NbSe_2$ with these elements and maintain the H-phase. The T-phase is triggered already at very low doping concentrations of $\sim 3\%$ (see Fig. 4.1.15 c). For $\delta = 3\,\%$ we found that the ratio between the area of T-phase and H-phase $A_T/A_H \approx 0.32 \pm 0.07$.

It was reported before that the 1T-$NbSe_2$ as well as 1T-$TaSe_2$ can be triggered during the MBE growth by using high substrate temperature > 550°C.[106, 27] To guarantee high crystallinity of SL-$NbSe_2$ we need to grow at a minimum substrate temperature of 450°C. That is why we are limited to the temperature range of 450°C - 550°C where it was not possible to synthesize the Ti or Cr doped H-phase $NbSe_2$. More growth experiments, optimizing other growth parameters such as the Ti or Cr

to Se ratio and growth speed could possibly help to further understand the observations. However, as single-layers of $TiSe_2$ [227] and $CrSe_2$ [228] were reported to preferably crystallize in the T-phase, it appears to be complicated to mix such materials or elements, respectively.

4.1.6 Summary

In this section we have demonstrated the feasibility of synthesis and the stability of aliovalent alloys of transition metal dichalcogenide materials in the single-layer limit throughout the entire alloy composition range $Nb_{1-\delta}Mo_\delta Se_2$ ($0 \leq \delta \leq 1$). We report the first experimental and theoretical atomic-scale characterization of the evolution of the electronic ground state (both the electronic structure and the behavior of the collective electronic phases) of a 2D Ising superconductor with structural disorder. Starting with very low Mo doping concentrations we could identify the single Mo impurity as triangular features of equal orientations in the STM topographic images. The structural appearance of these features could also be predicted by our DFT calculations, which have yielded the orbitals contributing to the observed DOS and have verified Mo substituting Nb atoms as the energetically most stable doping mechanism. In the process of fabricating SL-$Nb_{1-\delta}Mo_\delta Se_2$ samples with increased doping ($0 \leq \delta \leq 1$) we could observe and study the continuous modifications of the electronic structure by STS measurements and evaluate the doping concentration where various electronic phase transitions appeared. We have investigated for the first time three different 2D phase transitions, namely, superconductor-metal, CDW-metal and metal-semiconductor. Our measurements reveal an unexpected robustness of the CDW and superconductivity against disorder in the monolayer as well as a surprising non-monotonic evolution of the SC state with disorder, which is strengthened for dilute Mo concentration and appears due to the decrease of the pair-breaking spin fluctuations. Furthermore, we provide experimental evidence that the CDW weakens with increasing disorder due to the gradual loss of long-range 3x3 order and concurrent proliferation of CDW domain boundaries. Regarding the metal-semiconductor transition, we observe it for Nb concentrations of 25% ($\delta = 0.75$), which enables a large range for gap tunability up to 2.2 eV of SL-$MoSe_2$ for low-dimensional electronic devices. Lastly, we have also used other doping atoms in order to investigate the effect of magnetic Cr (electron dopant) and non-magnetic Ti (hole dopant) impurities. However, these species could not successfully be used as substitution atoms, and instead, the T-phase of $NbSe_2$ was triggered immediately at very low doping concentrations of $\sim 3\,\%$.

The consequences of our findings are far-reaching. First, our results paint a detailed picture of the nontrivial evolution of the electronic structure in a 2D Ising superconducting alloy, which is of high relevance for future 2D materials' design. In particular, the new insights that we could gain on the large stability of aliovalent TMD alloys will potentially trigger new research directed towards the synthesis of 2D alloys with enhanced properties for high-impact applications. More fundamentally, our work will possibly provide a general methodology to study a wide variety of disorder-driven 2D electronic phase transitions, which have remained largely unexplored until now due to the lack of suitable platforms.

In the following chapter we will continue with the study of a different aliovalent single-layer TMD material, namely $Ta_{1-\delta}W_{\delta}Se_2$, and mostly focus on its low lying electronic structure. Especially, we aim to gain knowledge on the tunability of its collective electronic phases and therefore modify the critical temperatures.

4.2 Doping induced superconductivity in SL-$Ta_{1-\delta}W_{\delta}Se_2$

The successful isolation and manipulation of atomically-thin sheets of 2D crystals have recently enabled the investigation of wealth of exotic electronic phenomena in the single-layer limit. A remarkable example is the case of superconductivity (SC) in transition metal dichalcogenide (TMD) monolayers, where the strong spin orbit coupling, together with the lack of inversion symmetry, triggers the emergence of unconventional SC properties such as the Ising pairing and symmetry-allowed triplet configurations.[10, 112, 120, 121] Furthermore, most of the bulk (3D) counterparts of these TMD monolayers are SC, which enables interrogation of the effects of dimensionality and interlayer coupling. For example, the TMD metals 2H-MX_2 (M = Nb, Ta and X = S, Se) are intrinsic superconductors in bulk, but exhibit disparate behaviour as they are thinned down to the monolayer. In NbX_2 monolayers, SC shows significant weakening ($NbSe_2$) [118, 6] and even disappearance (NbS_2) [11] with respect to bulk. In contrast, electron transport experiments in ultrathin films of TaX_2 (even reaching the monolayer in TaS_2) have revealed significant increase of the critical temperature (TC) as compared to bulk [186, 229, 23, 71]. In $TaSe_2$, ionic-gating measurements reveal a substantial increase of $T_c = 1.4\,K$ of nm-thick films (~ 5 layers) as compared to the $T_c = 0.14\,K$ of bulk.[229] However, ultrathin films of TMD metals are highly susceptible to degradation in ambient conditions, which dramatically affects the properties of collective electronic states (SC and CDW). Unfortunately, experimental work carried out in inert controlled environment exploring the thickness dependence of SC is still scarce.[118, 71] This leads to disparate qualities among the TMD layers used, which often make the experimental results hardly comparable. Therefore, a clear and coherent picture about the impact of dimensionality on the SC state has not yet been achieved for this family of layered materials.

In parallel to the exploration of the intrinsic ground state of these correlated 2D systems, there has recently been an increasing interest in tuning their many-body electronic states. A successful approach here is the use of electrostatic fields by ionic gating, which has demonstrated its effectiveness to reversibly manipulate the collective phases of 2D TMDs.[230, 87, 86] An alternative method to tune the electronic properties of a layered material is by chemical doping. However, this approach has been rarely used to manipulate many-body states [191, 213], and most of the effort so far has focused on tuning the bandgap and mobility of TMD semiconductors [189, 190, 202, 204]. Furthermore, chemical-doping strategies enable to interrogate the robustness and fundamental properties of many-body states in the presence of disorder, which remain largely unexplored due to the lack of suitable platforms.

In this work, we experimentally demonstrate that a monolayer of $TaSe_2$ does not hold superconductivity down to 340 mK (using nearly isolated samples unexposed to air) by means of variable temperature (0.34 – 4.2 K) scanning tunneling spectroscopy (STS) measurements. Furthermore, we induce superconductivity in this 2D material by electron doping using W atoms given the proximity of the Fermi level (E_F) to an empty van Hove singularity in its density of states (DOS). First, our spatially resolved STS measurements confirm that W atoms are embedded in the $TaSe_2$ lattice and act

as electron donors. We subsequently probe the low-energy electronic structure of lightly doped $TaSe_2$ monolayers and unveil the emergence of a superconducting dome on the temperature-doping phase diagram. Optimized superconductivity develops for a W concentration of 1.8% with a critical temperature of $\sim 0.9\,K$, a significant increase from that of bulk $TaSe_2$ ($T_c = 0.14\,K$). The SC dome reflects the variations in the available electrons for pairing caused by the crossing of a van Hove singularity in the DOS spectrum, as the layer is electron doped. Lastly, we unambiguously identify the emergence and evolution of a Coulomb glass phase intrinsically related to disorder induced by the W dopants.

4.2.1 Sample growth and atomic scale characterization

Single-layer $Ta_{1-\delta}W_\delta Se_2$ samples ($0 < \delta < 0.07$) were grown on BLG/SiC(0001) substrates. For the growth of the TMD layer we co-evaporated high-purity Ta (99.95%), W (99.99%) and Se (99.999%) in our home-made molecular beam epitaxy (MBE) system under base pressure of $\sim 5.0\times10^{-10}$ mbar. The flux ratio between transition metals (Ta and W) and Se is about 1:30. During the growth, the temperature of BLG/SiC(0001) substrates were maintained around 570°C and the growth rate was 2.5 hours/monolayer. The flux of Ta was kept constant and the flux of W element can be proportionally changed to control the stoichiometry of the alloys. After the growth, the samples were kept annealing in Se environment for 2 minutes, and then immediately cooled down to room temperature. The in-situ RHEED was used for monitoring the whole growth process. Before taking the sample out from high vacuum for further ex-situ UHV-STM measurements, a $\sim 10\,nm$-thick Se layer was deposited on the prepared sample to prevent any contamination in air. Such Se capping layer was subsequently removed in the UHV-STM by annealing the sample at $\sim 300°C$ for 40 minutes.

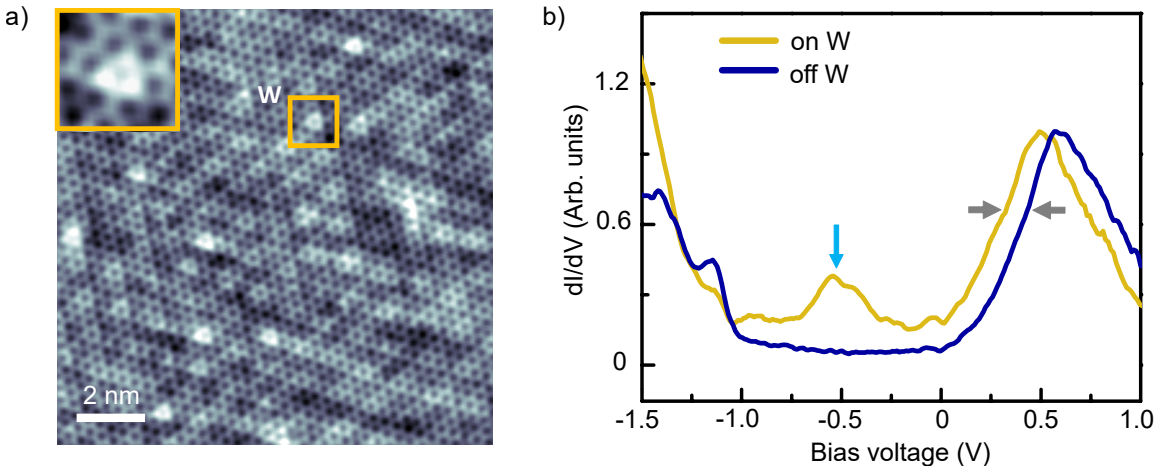

Figure 4.2.1: Identification of W impurities in SL-$Ta_{1-\delta}W_\delta Se_2$ alloy. a) Atomically resolved STM image of $Ta_{0.994}W_{0.006}Se_2$ (V_t = -1 V, I = 0.8 nA, T = 4.2 K). The inset show a zoom-in of the W atom boxed in the main image. b) Large-scale dI/dV curves on pristine $TaSe_2$ (blue) and on one of the W atoms (yellow).

Figure 4.2.1 a) shows a typical atomically resolved STM image of a single-layer $Ta_{0.994}W_{0.006}Se_2$ alloy. The W substitutional atoms can be resolved individually in the atomic lattice as triangular features of equal orientation (as the one indicated by a orange square). The triangular shape is due to the electronic perturbation that the W atom produces in the local DOS of the three upper neighbouring Se atoms. Such identification is further supported by two fingerprints in the STM spectroscopy measurements. Figure 4.2.1 b) shows two typical dI/dV curves (dI/dV $\propto$ LDOS) acquired on top of a triangular feature (yellow curve) and on pristine $TaSe_2$ (blue curve). The STS taken on the triangular feature exhibits an electronic resonance centered at -0.58 eV below E_F (light blue arrow), whose origin are the W-d_{z^2} states. Furthermore, this dopant also induces a rigid shift (indicated by grey arrows) of the main feature of the electronic structure for empty states, i.e., a large peak from the Ta-d band whose maxima at + 0.55 eV in pristine $TaSe_2$ corresponds with the energy position of this band at Γ. This is a clear indication that W atoms induce electron filling (n-type doping) into the $TaSe_2$.

4.2.2 Low-energy electronic structure in single-layer 1T-$TaSe_2$

First, we probe the existence of superconductivity in $TaSe_2$ ($\delta = 0$) in the single-layer limit. Fig. 4.2.2 a) shows a large scale topographic image of the pristine SL-$TaSe_2$/BLG. As shown in the inset, of Fig. 4.2.2 a), single-layer $TaSe_2$ retains the characteristic 3x3 CDW order shown in the bulk form. Figure 4.2.2 b) illustrates the magnetic field (B$\perp$) dependence of the low-energy electronic structure of the monolayer acquired at T = 0.34 K. As seen in the bottom dI/dV spectrum acquired at B = 0 T, the conductance shows a pronounced dip in the density of states (DOS) of width $\omega \sim 2$ meV at the Fermi level which is, in principle, compatible with the SC gap. However, this dip is an electronic feature that remains unperturbed as the magnetic field in increased, as seen in the nearly identical dI/dV spectra taken in the same region at B = 3 T (orange) and B = 5 T (yellow). To quantify this observation, we show the evolution of ω and depth (d) of the dip feature with the magnetic field. As seen, both magnitudes remain relatively constant within our resolution. Furthermore, we attribute the fluctuations of ω with B to unavoidable nm-sized drift of the regions where the STS data are taken as B is increased. In summary, the insensitive behaviour of the dip feature with the magnetic field allows us to rule out the existence of superconductivity in pristine monolayer $TaSe_2$ down to 0.34 K. The origin of the dip feature will be discussed later in combination with additional disorder-dependent STS data.

The absence of superconductivity found in our experiments is in clear contrast to recent transport experiments carried out in thin films (multilayers) of $TaSe_2$, which have reported SC critical temperatures of $\sim$ 1 K.[186, 229] A plausible origin of these opposing results is the sensitivity of the SC state to oxidation as the TD approaches the 2D limit as all the previous experiments used samples exposed to ambient conditions (and even chemical treatments). Another possibility is that the SC state follows a non-monotonic evolution from bulk down to the monolayer limit. Although unlikely, we cannot exclude this possibility and, therefore, detailed layer-dependent studies are required to fully understand the evolution of the SC state in $TaSe_2$.

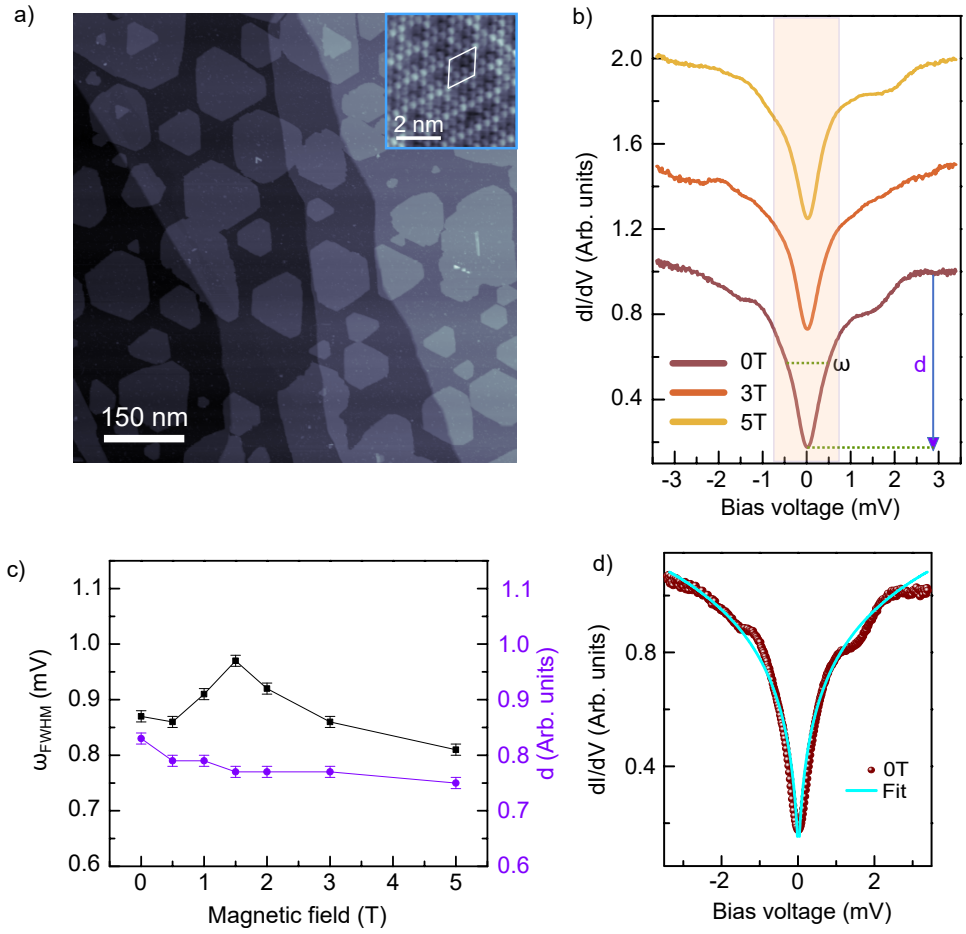

Figure 4.2.2: Low-energy electronic structure in single-layer 1T-$TaSe_2$. a) Large-scale STM image of monolayer $TaSe_2$ on BLG (V_t = 2 V, I = 20 pA). The inset shows an atomically resolved STM image of the $TaSe_2$ layer where the typical 3x3 CDW order is seen (V_t = 0.6 V, I = 100 pA). b) Perpendicular magnetic field (B⊥) dependence of the low-energy STS of monolayer $TaSe_2$ up to 5 T acquired at T = 0.34 K. The shadowed region indicates the energy range (± 1 mV) of the inner dip feature. c) The evolution of the width (ω) and depth (d) of the dip feature with B⊥ in monolayer $TaSe_2$. d) dI/dV(B⊥ = 0 T) spectrum taken on monolayer $TaSe_2$ (dots) and the DOS ∝ Ln(V) fit within ± 1 mV (line).

Here we emphasize that the role of the BLG substrate in the SC is negligible, as we previously demonstrated by comparing the SC properties of the $NbSe_2$ monolayer on the BLG and the insulating h-BN substrates.[218] Interestingly, the evolution of the SC behavior in $TaSe_2$ (H phase) with the crystal thickness departs from its parent compound TaS_2, which undergoes a significant increase of T_c in the monolayer (3.5 K) with respect to the bulk (0.8 K).

4.2.3 Chemical doping and emergence of superconductivity

The absence of superconductivity in pristine monolayer $TaSe_2$ raises the question whether electron doping could trigger its emergence. Electron doping in pristine $TaSe_2$ is expected to increase the available electrons at E_F to pair due to the proximity to a van Hove singularity in the DOS. To this purpose, individual W atoms are embedded in substitutional Ta sites in the transition metal plane. Each W^{5+} has one more valence electron than Nb^{4+} and, therefore, acts as an electron donor.

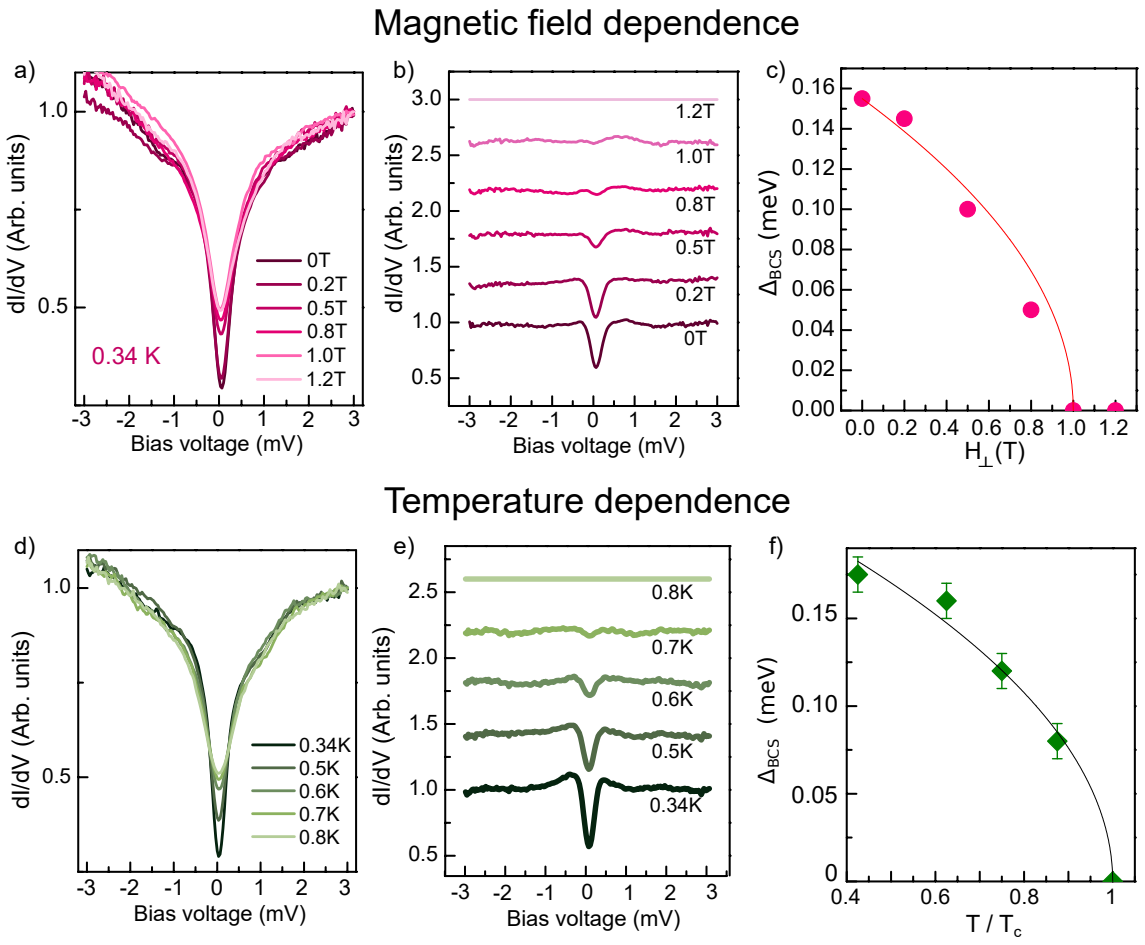

Figure 4.2.3: Low-energy electronic structure in single-layer 1T-$TaSe_2$. a) Magnetic field-dependence of the low-bias electronic structure of $Ta_{0.988}W_{0.012}Se_2$. b) Same dI/dV(B) spectra as in a) normalized to dI/dV(1.2 T). c) BCS SC fit of the dip features observed after normalization in b). The SC gap evolution with the magnetic field using the empirical formula from the Ginzburg-Landau theory (see text). d) Temperature dependence of the low-bias electronic structure of $Ta_{0.988}W_{0.012}Se_2$. e) Same dI/dV(T) spectra as in a) normalized to dI/dV(0.8K). f) BCS SC fit of the dip features observed after normalization in e). The line shows the expected BCS temperature dependence.

The resulting monolayer is an aliovalent $Ta_{1-\delta}W_{\delta}Se_2$ alloy with dilute W concentration (δ) that can be precisely characterized via STM imaging (see Fig. 4.2.1). As shown in Fig. 4.2.3, W doping levels as low as 1.2% ($\delta = 0.012$) are sufficient to trigger the superconducting state. Fig. 4.2.3 a) shows the evolution of the DOS in the $Ta_{0.988}W_{0.012}Se_2$ with the applied magnetic field. In contrast to the pristine $TaSe_2$ case (Fig. 4.2.2), the dip feature at E_F is now susceptible to the magnetic field, and its depth gradually decreases as B increases up to B = 1.2 T, a value beyond which the DOS remains unchanged. Fig. 4.2.3 b) shows the set of dI/dV(B) spectra of Fig. 4.2.3 a) normalized to dI/dV(1.2 T). As seen, a clear DOS dip centered at E_F evolves as the B field is decreased. Since this observation is compatible with the emergence of superconductivity, we have fitted these dI/dV spectra to a BCS SC gap, whose values are plotted in Fig. 4.2.3 c) as a function of B. This gap evolution with the magnetic field can be fitted to the empirical formula $\Delta(T,B) = \Delta(T,0) \cdot \sqrt{1-(B/B_{c_z})}$ from the Ginzburg-Landau theory.[55]

To confirm that the dip feature emerging in the normalized dI/dV spectra corresponds to a SC gap, we further study its temperature (T) dependence. Fig. 4.2.3 d) show a series of dI/dV spectra acquired consecutively at different temperatures. Similarly, the dip in the DOS decreases as the temperature increases up to 0.8 K, where it remains nearly unchanged. This evolution is better observed in the normalized spectra to dI/dV(0.8 K) in Fig. 4.2.3 e). We have fitted the normalized dI/dV(T) spectra to the BCS SC gap, and Fig. 4.2.3 f) shows the evolution with T. As seen, Δ(T) follows a BCS-like temperature dependence (black curve) with $\Delta(0) \approx 0.18$ meV. This gives $2\Delta(0)/k_B T_c \sim 4.6$, a value that significantly departs from that predicted by the BCS theory. This indicates that the pair-coupling interaction is strong in the W-doped $TaSe_2$ monolayer. This enhanced value is nearly coincident with that of single-layer $NbSe_2$ ($\Delta(0) = 0.4$ meV, $T_c \approx 2$ K).

Once the emergence of superconductivity in W-doped $TaSe_2$ monolayers is established, we further investigate its evolution with W concentration, which is linearly proportional to the electron doping. In total, we have studied eight alloy samples with different δ values in the range $0 < \delta < 0.07$. For each sample, we have measured both the temperature and magnetic field dependence of the low-lying electronic structure, as previously described (Fig. 4.2.3). Fig. 4.2.4 summarizes the evolution of the SC gap, the upper critical field (B_{C2}) and the critical temperature (T_c) as a function of δ. As seen, a superconducting dome spanning $0.003 < \delta < 0.03$ is found with a maximal $T_c \approx 0.85$ K for $\delta = 0.018$. The SC states develops for W concentrations as dilute as 0.5% ($\delta = 0.005$). Surprisingly, the superconducting state in the monolayer is significantly more robust against B with upper fields as large as $B_{C_2} \approx 1$ T with respect to the bulk, where B_{C_2} is in the mT range.

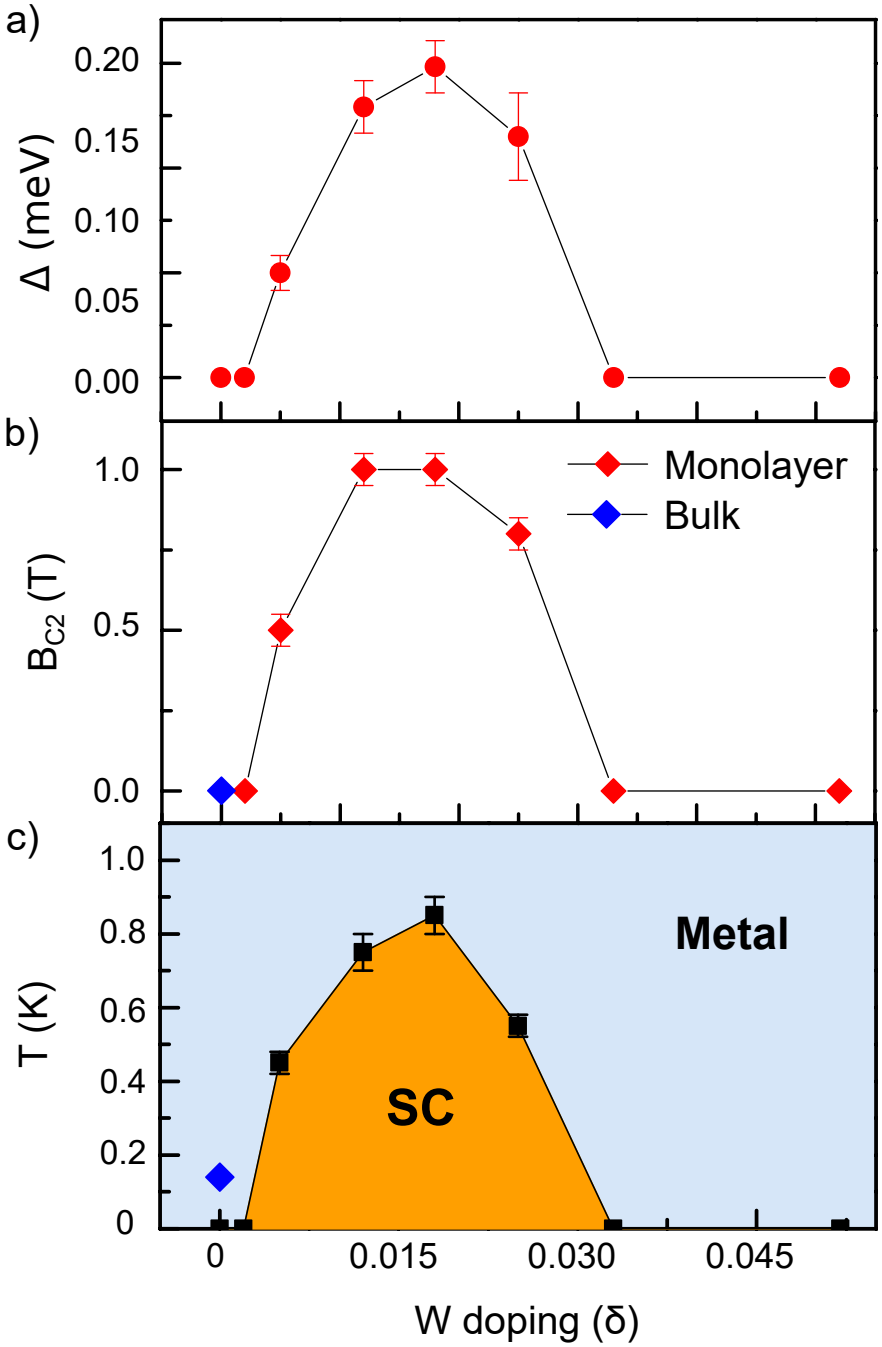

Figure 4.2.4: Low doping phase diagrams of $Ta_{1-\delta}W_{\delta}Se_2$ alloy. a) SC gap, b) upper critical field (B_{C2}), c) critical temperature (T_c) as a function of W doping δ in the studied range of $0 < \delta < 0.07$ in monolayer $Ta_{1-\delta}W_{\delta}Se_2$.

4.2.4 Superconductivity induced by tuning a van Hove singularity

Next, we discuss the origin of the superconducting state in this electron-doped $TaSe_2$. The band structure of monolayer $TaSe_2$ has a saddle point near the Fermi level, around mid-way in the $\Gamma - K$ direction, which gives rise to a logarithmic divergence in the DOS known as a Van Hove singularity. Spin-orbit coupling splits this Van Hove peak by about 0.23 eV according to DFT calculations [231, 232, 50], resulting in one peak above the Fermi level and one below it. This is also supported by ARPES experiments, which observe only one band in the $\Gamma - K$ direction.[7] As we dope electrons in $Ta_{1-\delta}W_\delta Se_2$ with increasing δ, the Fermi level is tuned through the singularity, where superconductivity should be enhanced due to the increased DOS. This is therefore a natural explanation for the emergence of the superconducting dome we observe, similar to those found in bulk 3D materials where the Van Hove singularity is tuned by chemical doping [8] or strain [233].

To estimate the amount of W needed to reach the Van Hove singularity, an accurate calculation of the DOS and the Van Hove and Fermi level positions would be required. Since this value is not accurately reported in the literature, we have used a tight binding model with hoppings up to 5 nearest neighbors and SOC, chosen to reproduce the main features of the DFT bands in Refs. [112, 120, 121]. The resulting band structure is shown in Fig. 4.2.5 a), and the corresponding DOS in Fig. 4.2.5 b). The distance from the Fermi level to the upper Van Hove peak is taken to be 5% of the VH SOC splitting, which is within the values that can be inferred from Refs. [112, 120, 121]. This model can then be used to compute the amount of electron doping needed to reach the VH peak, which we obtain to be 0.015 electrons per cell. This corresponds to a value of $\delta = 0.03$, in good agreement with the dome maximum location.

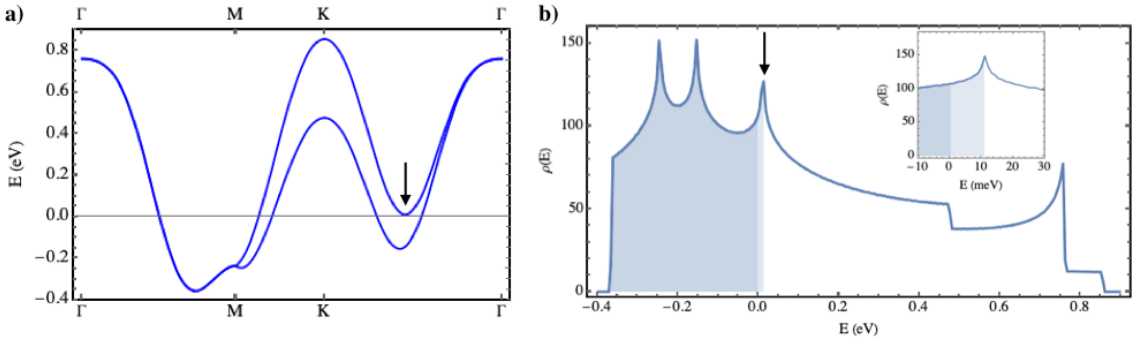

Figure 4.2.5: Tight binding model for $TaSe_2$, for parameters discussed in the text. a) Band structure obtained from the tight binding model. The Van Hove saddle point near the Fermi level is marked with a black arrow. b) Density of states for the same model, with the occupied states filled in dark blue. The amount of carriers needed to reach the Van Hove singularity (also marked with the same arrow) is coloured in light blue, and is computed to correspond to $\delta = 0.03$.

4.2.5 Development of a Coulomb glass phase by disorder

An important remaining question is the origin of the dip feature at EF intrinsically present in both pristine and W-doped $TaSe_2$. In order to gain knowledge about its nature, we have further analyzed the DOS within $\pm$ 1 meV extracted from dI/dV spectra acquired in the non-SC regime. For SC samples, we only consider dI/dV spectra taken beyond the upper critical field. As shown in Fig. 4.2.2, this dip feature is insensitive to B within our resolution, which allow us to establish a direct comparison among curves for different W concentrations. Figure 4.2.6 a) shows four typical of these dI/dV spectra for different W defect concentration from the pristine $TaSe_2$ case ($\delta = 0$) up to a 7% ($\delta = 0.07$). As seen, all the dI/dV spectra, nearly symmetric with respect to E_F, show a gradual increase of the width of the dip feature proportional to the W concentration. This is shown in Fig. 4.2.6 b), where the averaged width ω (measured from the value dI/dV(3 mV)) is plotted for the δ values studied. Furthermore, the shape of the dip feature evolves gradually from non-linear to linear for the highest W concentrations.

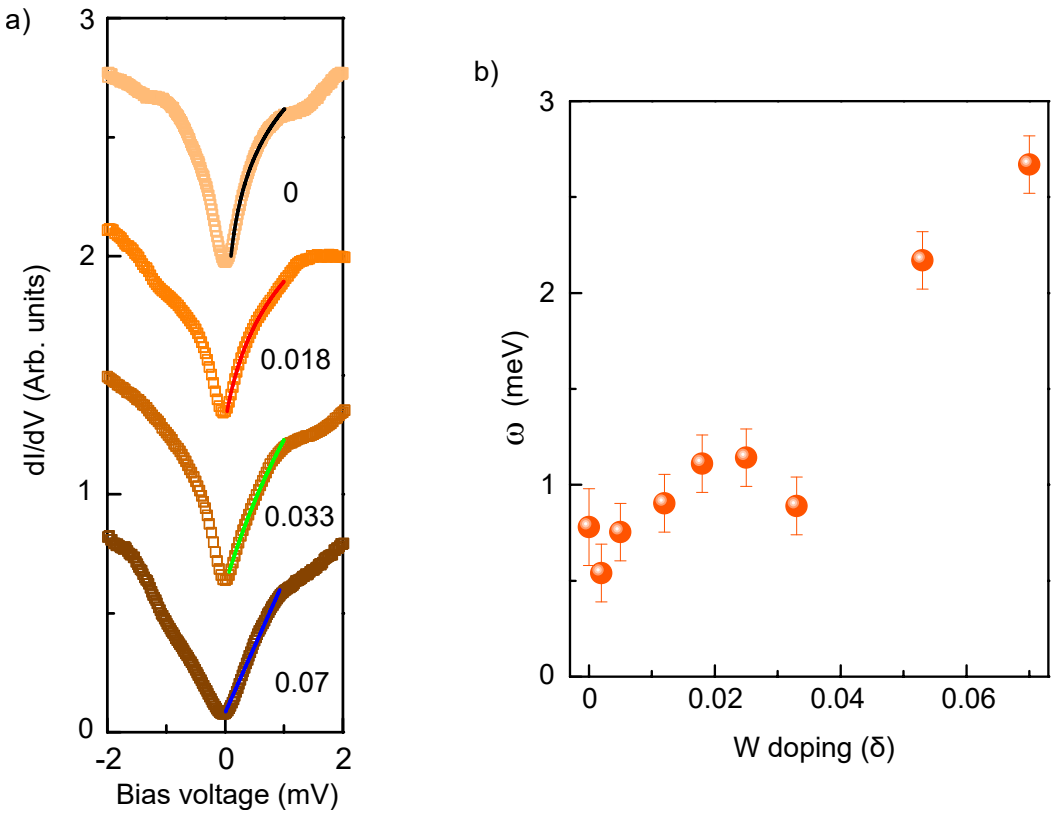

Figure 4.2.6: Electronic characterization of the observed gap in the metallic state of $Ta_{1-\delta}W_\delta Se_2$ alloy. a) DOS evolution of the dip feature within $\pm$ 1 mV in $Ta_{1-\delta}W_\delta Se_2$ monolayer from $\delta = 0$ (pristine $TaSe_2$) up to $\delta = 0.07$. All the dI/dV spectra were taken in the non-SC regime. b) Width of the dI/dV curves as a function of the W doping (δ).

At $\delta = 0$, a first plausible origin for this non-superconducting dip could be a CDW induced partial gap, as observed in $NbSe_2$, but the dip width is smaller than expected from such mechanism. In addition, the doping dependence of the dip would not conform to a CDW origin because chemical doping, in addition to increasing carrier density, introduces disorder scattering through the different potential generated by the substituted atoms, which would suppress the CDW. Since some disorder is present even in the undoped samples, we rather surmise that the dip is a disorder effect: the combination of small disorder and Coulomb interactions is known to lead to a logarithmic dip of the DOS near the Fermi level.[234, 235] When disorder is further increased, in two dimensions this dip evolves into power law one known as the Coulomb gap, which therefore appears to widen with disorder. While the power is often quoted to be linear, numerical studies often deviate from this value.[236, 237] Nevertheless, our observation of a narrow dip that widens and turns approximately linear with increasing disorder is consistent with the emergence of a Coulomb gap, fully established at doping levels where superconductivity has disappeared. Since disorder is not expected to affect superconductivity due to Anderson's theorem, our global picture of $Ta_{1-\delta}W_\delta Se_2$ is that W substitution generates superconductivity as the nominal DOS is tuned through the Van Hove singularity, while also increasing disorder so that a Coulomb gap develops at larger disorder strengths.

4.2.6 Summary

In this section we have confirmed that pristine SL-$TaSe_2$ is not superconducting down to a temperature of $T = 0.34\,K$, which is in contradiction to the proposed increase of T_c to $> 1\,K$ compared to its bulk T_c of $0.1\,K$. However, by using W doping atoms during the MBE growth of SL-$Ta_{1-\delta}W_\delta Se_2$ alloys, we were able to introduce superconducting order up to a drastically increased critical temperature of $\sim 0.8\,K$ at an optimized doping level of $\delta = 0.018$. We have further synthesized as well as electronically characterized SL-$Ta_{1-\delta}W_\delta Se_2$ alloys in the range of $0 \leq \delta \leq 0.07$. We could show that this material possesses a superconducting dome at doping levels of $0.005 \leq \delta \leq 0.033$. Lastly, we have explored the disorder in the metallic state of this system by investigating the electronic structure and therefore especially the symmetry of the low bias gap as a function of δ. We could show the progression of the logarithmically shaped gap in the low disorder regime for $\delta = 0$, to the linear shaped gap in the high disorder regime for $\delta = 0.07$. The later behaviour strongly suggests the observation of a Coulomb gap. Such Coulomb like gap features are regularly observed in SL TMD materials and should be further considered in studies on superconductivity and other collective electron phases.

CHAPTER 5

Magnetic correlations in single-layer 1T-$TaSe_2$

In this chapter we investigate the electronic structure as well as the magnetic properties of 1H-$TaSe_2$, 1T-$TaSe_2$, and particularly the heterostructure of 1T/1H-$TaSe_2$. The 1T-$TaSe_2$ phase contains an unusual orbital structure, whose nature is investigated in order to interrogate previous claims of Mott insulator phases in this material. The heterostructure of 1T/1H-$TaSe_2$ introduces a magnetic moment and therefore a zero bias anomaly (ZBA) at the Fermi level. Investigation of this ZBA at very low temperature of 350 mK and as a function of the magnetic field suggests that this system undergoes antiferromagnetic order at low temperatures.

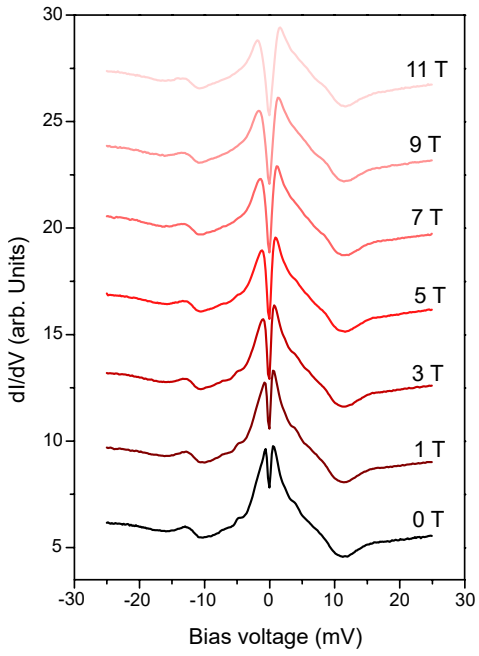

5.1 Unusual orbital texture in 1T-$TaSe_2$

The first section focuses on the unusual orbital texture of 1T-$TaSe_2$ and discusses the existence of a Mott insulating phase, or, by the contrary, the existence of a trivial insulating phase. To this purpose, we have performed high-resolution 350 mK STM/STS measurements supported by DFT calculations carried out by the group of Ion Errea (CFM, UPV-CSIC).

5.1.1 Introduction

At the 2D limit, enhanced electronic correlations are capable of triggering intriguing states of matter such as Mott insulating behaviour, which can lead to quantum spin liquids.[25–27] Materials presenting narrow electronic bands close to the Fermi level are especially susceptible for such states of matter, because the kinetic energy of the electrons in these bands is strongly reduced.[26, 238] If the Fermi level lies within the energy of the band width, Coulomb interactions are enhanced, exceed the kinetic energy of the electrons and can thus trigger correlated phases.[239] Such dynamics were intensively studied in 1T-TaS_2, which was found to undergo a Mott-insulator-to-superconductor transition induced by high pressure [240], charge doping [241, 242], or isovalent substitution [243, 244].

$TaSe_2$ has two thermodynamically stable phases, the H-phase (metallic) as well as the T-phase (semiconducting) and can therefore be investigated individually or stacked on top of each other, by optimizing MBE growth parameters. The 2H-$TaSe_2$ (bulk) possesses two CDW transitions. A normal to incommensurate transition at $T_{N-IC} \sim 122$ K and a incommensurate to commensurate transition at $T_{N-IC} \sim 90$ K.[7] Bulk 1T-TaS_2 and bulk 1T-$TaSe_2$ have been known to exhibit unusual insulating phases, which are being believed to be Mott insulating phases.[245, 246] In these materials, the so-called star-of-David CDW state is well characterized.[247, 245] The exact description of their insulating phases, however, remains elusive, because these systems contain complicated interlayer CDW stacking what is not fully understood at the present day.[248] Without such interlayer couplings in the SL limit of 1T-$TaSe_2$ similar physical behaviour was reported, whereas strong electronic correlations are supposed to introduce the Mott insulating behaviour with an electronic band gap of 109 ± 18 mV and unusual orbital texture, what was not found in multilayer samples.[27]

These interpretations remain controversial, as it was pointed out in another study, where 1T-$TaSe_2$ was identified as a conventional band insulator.[249] In the following section I describe our experiments carried out aiming to shed light on this open question.

5.1.2 Growth and structural characterization

In the scope of the following outlined experiments we have grown monolayers of $TaSe_2$ in various different phases or forms, respectively. These are SL-1H-$TaSe_2$/BLG/SiC(0001), SL-1T-$TaSe_2$/BLG/SiC(0001) as well as 1T-$TaSe_2$ on top of 1H-$TaSe_2$/BLG/SiC(0001).

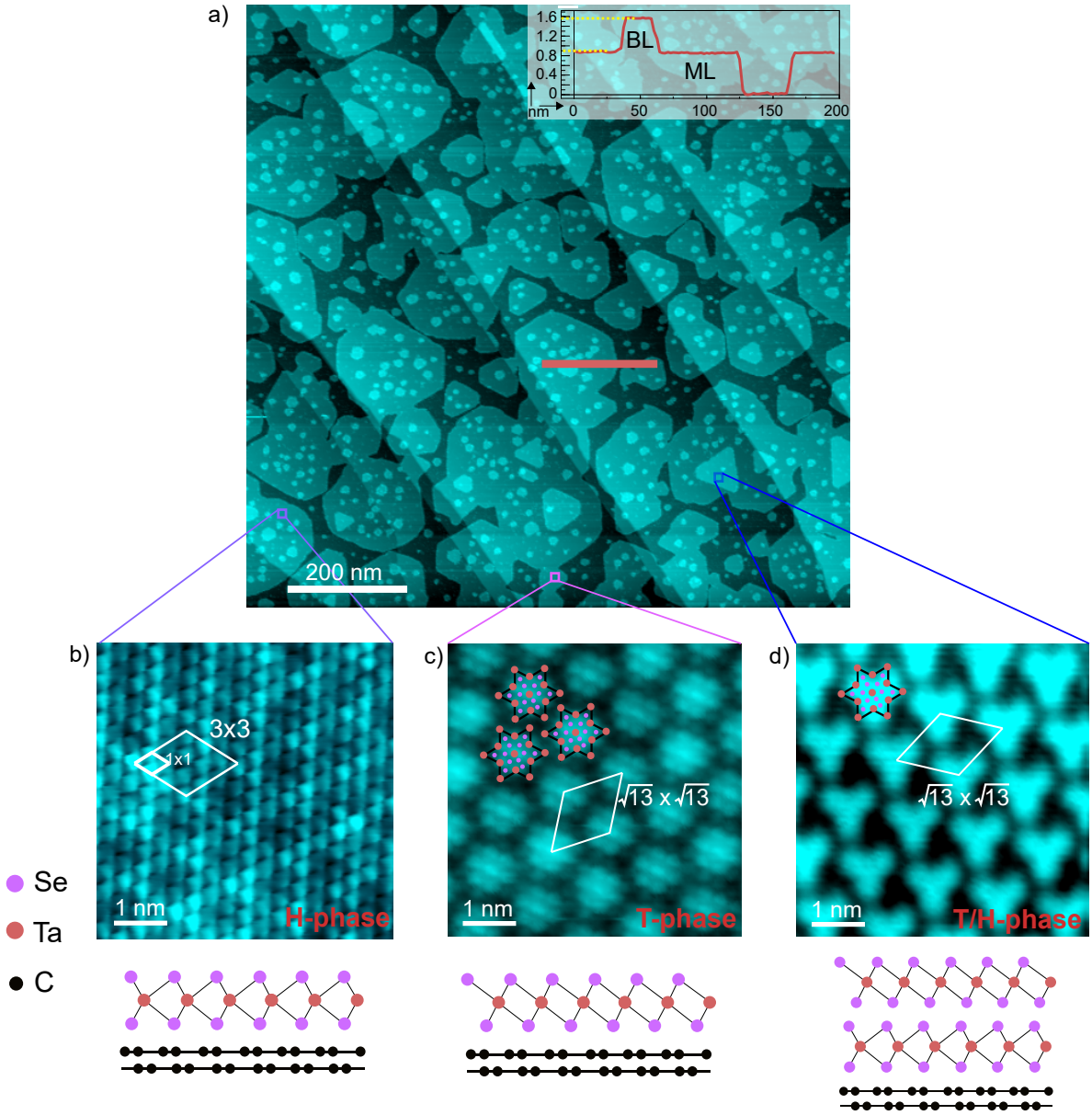

Figure 5.1.1: Structural characterization of MBE grown ML (H-phase, T-phase) and 1T/1H heterostructure $TaSe_2$. a) Large scale STM image showing domains of $TaSe_2$ on top of the BLG substrate. The inset depicts a height profile along the red line indicated in the image (V_s = + 1.5 V, I_t = 0.03 nA, T = 4.2 K). b) Atomic scale STM image of the 1H-phase. Indicated are the atomic unit cell and the 3×3 CDW super structure (V_s = + 0.3 V, I_t = 0.2 nA, T = 4.2 K). c) A small scale image of a 1T-phase area shows the star-of-David CDW pattern. The unit cell as well as the atomic arrangement within the star-of-David are depicted (V_s = + 0.105 V, I_t = 0.02 nA, T = 4.2 K). d) Atomic scale image of 1T/1H $TaSe_2$ (V_s = - 1.54 V, I_t = 0.1 nA, T = 4.2 K).

We have grown these samples by MBE at a Ta:Se flux of 1:30, similarly to the growth of $NbSe_2$. However, the growth time is much longer, depending on the desired coverage. For the sample shown in Fig. 5.1.1 a) with a coverage of $\sim$ 1 ML, containing several patches of bilayer, the growth time was 100 min. The substrate temperature is decisive of which phase will be dominating. At temperatures $\sim$ 550°C only the H-phase was synthesized. Instead, at higher temperatures $\sim$ 650°C the T-phase is much more dominant. Within this temperature range a mixture of both phases as well as the mentioned bilayer structures could be grown on the BLG surface. The inset in Fig. 5.1.1 a) shows an apparent height profile along the indicated red line comprised of SL-$TaSe_2$, BL-$TaSe_2$ and BLG areas. The SL-$TaSe_2$ has a height of 0.83 $\pm$ 0.03 nm, the bilayer height is 0.72 $\pm$ 0.03 nm. These apparent heights are nearly coincident with those reported by previous STM works on TMDs on graphene.[250, 105] In Fig. 5.1.1 b) the 3×3 CDW modulation of 1H-$TaSe_2$ is shown. In Fig. 5.1.1 c) a T-phase area is presented. A triangular $\sqrt{13} \times \sqrt{13}$ CDW modulation is indicated, which is similar to the observed commensurate CDW modulation of bulk 1T-$TaSe_2$.[251] Each triangular structure corresponds to a star-of-David unit cell. The Ta atoms (red) and Se atoms (violet) are illustrated for three unit cells. It contains 13 Ta^{4+} ions and is therefore predicted to be metallic, because of the odd Ta ion number. It has a single d-electron localized in the center of the unit cell.[27] In the case of the 1T/1H-phase shown in Fig. 5.1.1 d) the similar $\sqrt{13} \times \sqrt{13}$ CDW pattern is observed. However, the image has less resolution and was measured at a different bias voltage (see figure captions). The critical temperature of the CDW transition in the single-layer limit was measured as $T_{N-IC} = 130 \pm 5$ k, which is slightly higher than in the bulk.[7] This result confirms a robust CDW order, similar to $NbSe_2$, even in the 2D limit.

5.1.3 Electronic characterization of 1H-$TaSe_2$/BLG

We have performed an electronic characterization by low temperature (340 mK) STS measurements of the SL-H-phase of $TaSe_2$ and compared it with the H-phase of SL-$NbSe_2$ (see Fig. 5.1.2 a) and b)). The typical STS dI/dV curve of 1H-$TaSe_2$ exhibits a rather flat area of DOS in the negative bias range (filled states regime $V < 0$) up to a indicated onset at E_1 (-1.17 $\pm$ 0.05 V), where a step rise of the DOS is observed. In the positive bias range above the Fermi energy, the most significant feature is the E_2 (0.53 $\pm$ 0.05 V) condcution band peak. The origin of this peak is most probably a van Hove singularity around Γ, as reported in a combined STS/ARPES study on this material.[7] The comparison to the dI/dV spectrum of SL-1H-$NbSe_2$ reveals a slight shift of the E_2 feature, which was found to be a SOC effect due to higher mass of Ta compared to Nb.[231] Overall, the shape of the curves are quite similar, as both curves contain a relatively flat and featureless DOS between E_F and E_1. These observations suggest that the Fermi level is moving upwards in energy and that the electronic bands have a similar shape as in the case of 1H-$NbSe_2$. The STS measurement is mostly sensitive to the electronic states around Γ, therefore, STS measurements alone cannot tell the exact electronic band dispersion. However, the displacement of E_2 suggests that E_F is moving upwards in energy as it was suggested in various studies.[7, 231]

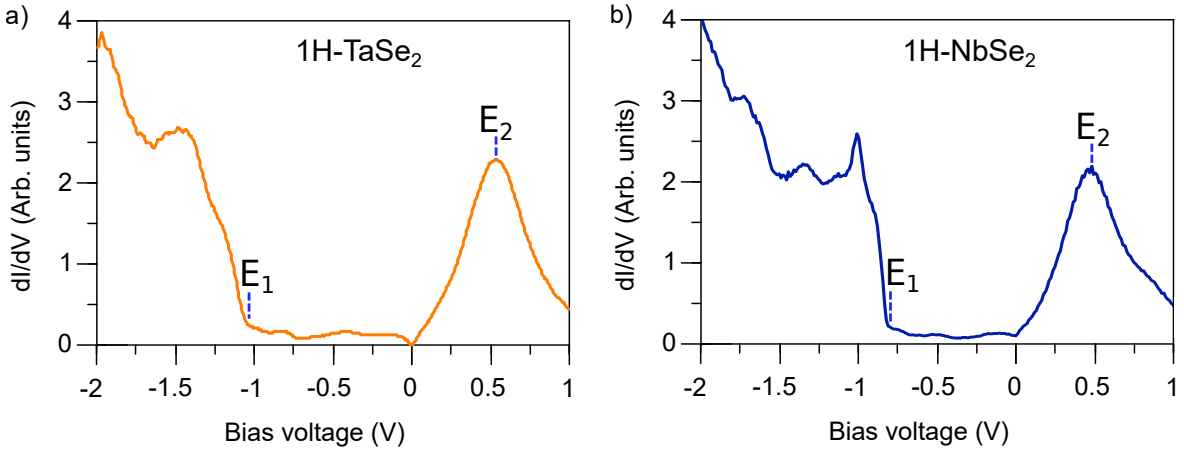

Figure 5.1.2: Large-bias STS electronic structure of 1H-$TaSe_2$ compared to 1H-$NbSe_2$. a) 1H-$TaSe_2$: E_1 = -1.17 ± 0.05 V, E_2 = 0.53 ± 0.05 V,. b) 1T-$NbSe_2$: E_1 = -0.81± 0.16 V, E_2 = 0.46 ± 0.06 V. Measurement parameters for (a-b): f = 833 Hz, $V_{a.c.}$ = 1 mV, 4.2 K.

5.1.4 Electronic characterization of 1T-$TaSe_2$/BLG

Next, we discuss the electronic structure of SL-1T-$TaSe_2$/BLG (Fig. 5.1.3 a) and compare it with the case of SL-1T-$NbSe_2$/BLG (Fig. 5.1.3 b). The dI/dV spectrum for 1T-$TaSe_2$ shows the insulating nature of this material with the opening of a gap Δ_E = 0.30 ± 0.07 mV. Two significant valence band features in the filled states are indicated as a steep onset at V_1 = -0.11 ± 0.03 mV and large increase of DOS at V_2 = -0.34 ± 0.05 mV.

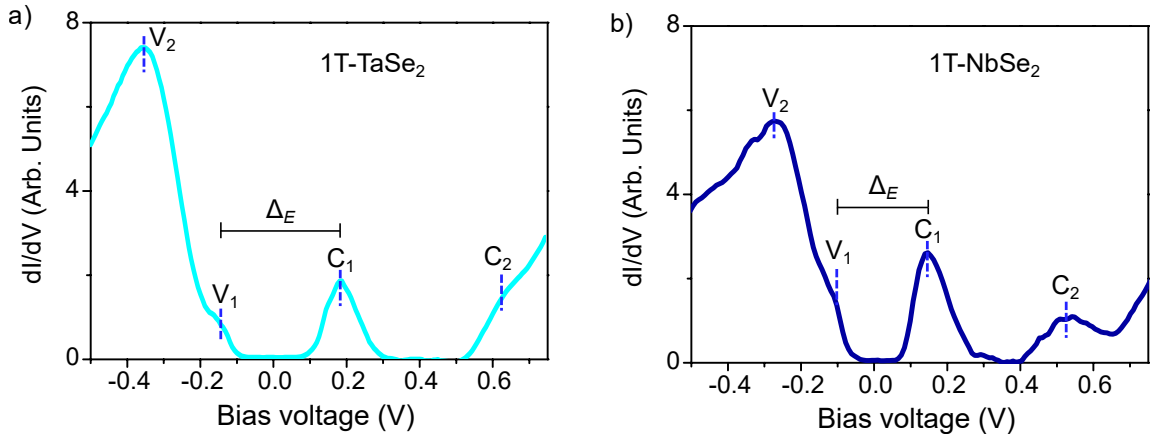

Figure 5.1.3: Large-bias STS electronic structure of 1T-$TaSe_2$ and 1T-$NbSe_2$. a) 1H-$TaSe_2$: V_1 = -0.11 ± 0.05 V, V_2 = -0.34 ± 0.05 V, C_1 = 0.19 ± 0.05 V, C_2 = 0.62 ± 0.15 V. b) 1T-$NbSe_2$: V_1 = -0.28 ± 0.05 V, V_2 = -0.12 ± 0.05 V, C_1 = 0.15 ± 0.05 V, C_2 = 0.53 ± 0.12 V. Measurement parameters for (a-b): f = 833 Hz, $V_{a.c.}$ = 1 mV, T = 4.2 K.

The gap in the DOS around E_F extends to the positive bias range up to $C_1 = 0.19 \pm 0.05$ mV where the first conduction band feature is detected. At higher energies another conduction band peak is observed at $C_2 = 0.62 \pm 0.15$ mV. The electronic structure for the two materials 1T-$TaSe_2$ and 1T-$NbSe_2$ are almost identical. Both materials develop a gap Δ_E around E_F which is slightly higher in the case of $TaSe_2$. In 1T-$NbSe_2$ we measure a gap of $\Delta_E = 0.27 \pm 0.07$ mV.

Reported DFT calculations in the CDW state of the T-phase of $TaSe_2$ have yielded a metallic state of this material.[27] However, the experimental results obtained by STS measurements show an insulating behaviour. It was argued that the half-filled metallic band at E_F splits into a LHB and UHB, because of a high Coulomb repulsion due to its narrow bandwidth (~ 20 meV). Such a behaviour transitions a metallic state to the Mott insulator state. However, if this is the case, the orbital textures should be similar for spectroscopic imaging at opposite polarities, e.g. $V = \pm 0.2$ V, what is not the case. In the study by Chen et al., it is further argued that injected electrons from the STM tip experience additional correlation effects from the coulomb interactions with electrons occupying the states.[27]

In order to better understand the electronic structure of this system we have acquired spatially resolved high-resolution STM/STS data, which is illustrated in Fig. 5.1.4. A significant observation during these experiments was that the electronic structure is spatially dependent with a key difference, depending where exactly the dI/dV curve is taken. As shown in Fig. 5.1.4 a) two distinct curves are observed depending on the location, the center of the CDW unit cell, or in between (indicated in Fig. 5.1.4 b). The unit cell of the star-of-David $\sqrt{13} \times \sqrt{13}$ CDW modulation is illustrated in b). Taking the STS spectra at different positions leads to a variation in the DOS with two significant differences. At the center of the star-of-David at $V_1 = -0.1 \pm 0.05$ V a new sharp peak appears with a width of 35 ± 10 mV. This peak is not present outside of the star-of-David, however a shoulder like feature is located at slightly smaller energy $\sim 0.15 \pm 0.05$ V. More differences in the spectra are the intensities of the features, what is especially significant for the C_1 peak. In Fig. 5.1.4 c) a line spectra is shown crossing multiple unit cells along the indicated green line in Fig. 5.1.4 b). From this results one can see the periodic modulation of all the indicated band features $V_{1,2}$ and $C_{1,2}$. These observations point to a different interpretation from that previously suggested where a Mott insulating phase was identified. Namely, not a split band consisting of LHB and UHB, but two different bands, leading to a conventional insulating gap.

To further analyze this hypothesis we have acquired spatially resolved conductance maps at the energies of the peak features (compare to STS measurement in Fig. 5.1.4). Fig. 5.1.5 shows three different maps acquired at a) $V_s = -0.3$ V (V_2 feature), b) $V_s = -0.1$ V (V_1 feature) and c) $V_s = +0.2$ V (C_1 feature). The DOS in the case of V_1 and V_2 are mostly located in the center of the star-of-David (green circle) unit cell. In contrast, the measurement at the energy of the C_1 feature reveals that the DOS are located outside of the star-of-David.

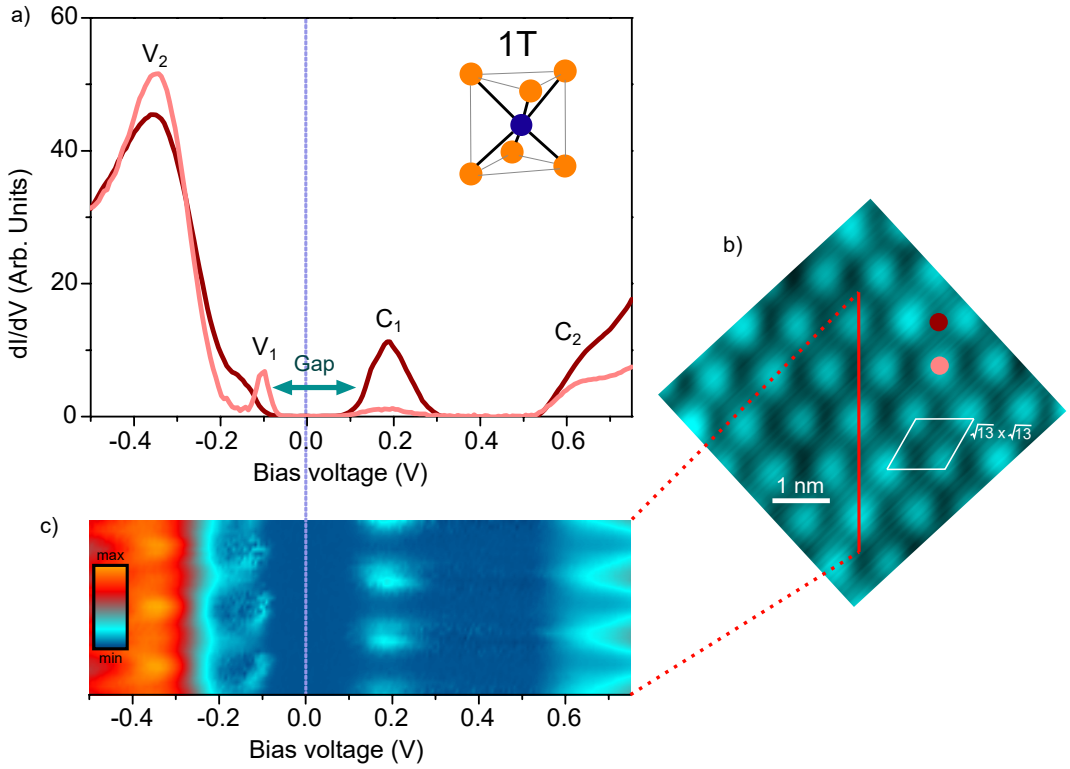

Figure 5.1.4: Location dependent DOS. a) The 1T-$TaSe_2$ exhibits basically two different electronic structures, which are classified as the light blue curve taken in the center of the star-of-David unit cell and the dark blue curve taken outside the star-of-David. Indicated are the valence bands as $V_{1,2}$ and the conduction bands as $C_{1,2}$. b) Small scale atomic resolution image with depicted star-of-David CDW unit cell and the locations where the STS curves shown in a) were taken (V_s = - 1 V, I_t = 0.1 nA, T = 4.2 K). c) Line spectra taken over three CDW unit cells indicating the variation of the peak intensities.

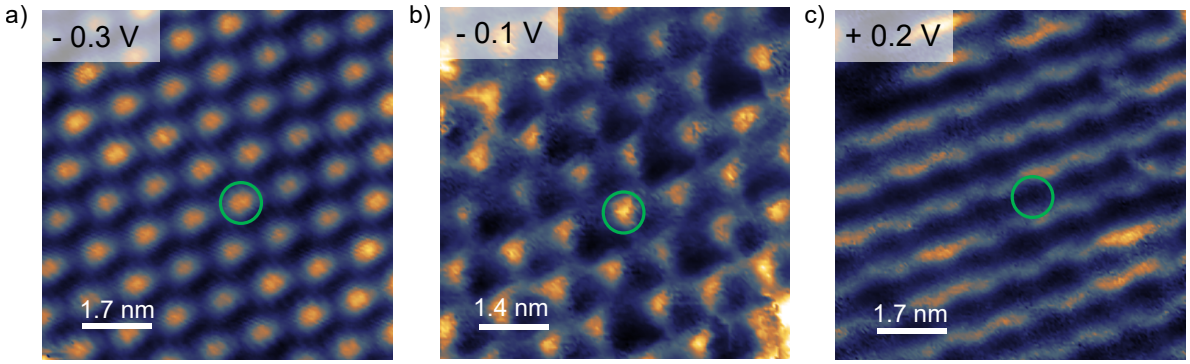

Figure 5.1.5: STS dI/dV conductance maps for different energies. a) - 0.3 V, b) - 0.1 V, c) + 0.2 V.

This observations suggests a different orbital origin of the bands involved in the DOS of V_1 and C_1. In the Mott insulator picture, where the narrow band at E_F splits into the LHB (V_1) and the UHB (C_1), the DOS for both of these bands should appear similar. However, this is not the case in our STM/STS measurements, where Fig. 5.1.5 b) and c) clearly differ from each other.

In order to help solving this puzzle, we have established a collaboration with the group of Dr. Ion Errea (UPV/EHU-CSIC) and Dr. Fernando de Juan aiming to perform calculations on this system by means of DFT methods. Figure 5.1.6 shows the band structure of an isolated layer of 1T-$TaSe_2$ in the CDW phase ($\sqrt{13} \times \sqrt{13}$) along with the DOS from the Se (purple) and Ta (blue), and the total DOS (green). As seen, a large peak develops at the Fermi level due to the presence of a half-filled narrow band, which provides all the relevance to this system. This narrow band is followed by a gap of 0.5 eV for empty states. These two features are qualitatively consistent, in principle, with our STS observations (see Fig. 5.1.4), which would imply the conventional nature of the bandgap, thus ruling out strong electron correlations and the existence of a Mott gap for this system. However, there are two important differences between the calculated DOS and our STS spectra. First, our STS data locates the narrow V_1 feature (candidate to be identified as the flat band) well below E_F (-100 mV), where the DFT calculations predict it. A plausible explanation for this is the presence of the graphene substrate, as recent theoretical calculations report that graphene acts as an electron donor to the 1T-$TaSe_2$ monolayer.[252] With this picture, the flat band is filled and electron correlations are not present.

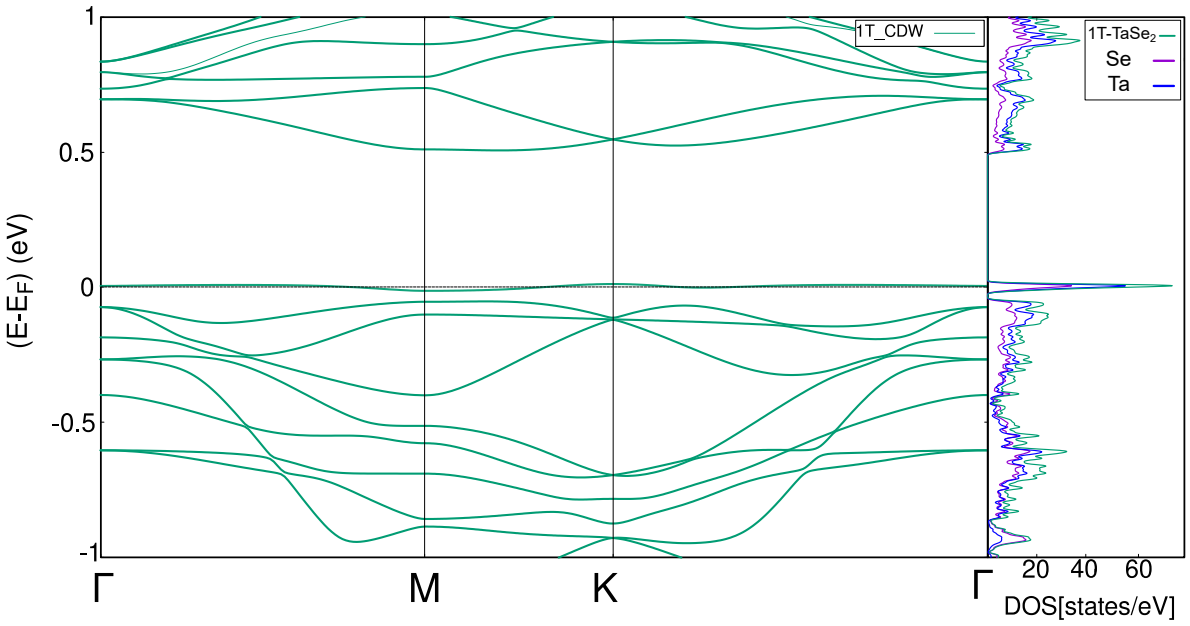

Figure 5.1.6: DFT calculations. (Left) Electronic band structure calculated using the Quantum expresso package within the Pardew-Burke-Enzerhof approximation. (Right) Calculated DOS.

The second difference between theory/experiment concerns the size of the gaps, as the experimental gap is significantly smaller ($\sim 0.3\,\mathrm{eV}$) than the calculated one ($0.5\,\mathrm{eV}$). However, again, the presence of the substrate seems to play an important role here and is expected to reduce the gap by a factor of two approximately, thus leading to a value very close to the experimental one. In summary, while this is still an ongoing project by the time of submission of the present thesis, our experimental results together with the DFT calculations paint a picture clearly different from the proposed many-body physics (Mott insulating phase), and point towards a scenario where both the unusual orbital texture and the band gap result from a conventional semiconducting behaviour.

5.2 Magnetism in 1T/1H-$TaSe_2$ heterostructure

In this section we study the effects of the magnetic moment induced by the unpaired electron located at the center of the star-of-David CDW unit-cell in 1T-$TaSe_2$ when it is on a metallic substrate, namely 1H-$TaSe_2$. Particularly, we compare our 340 mK STM/STS results with two distinct theories: the Kondo lattice and magnetic ordering.

5.2.1 Introduction

As described in the previous section, the 1T-$TaSe_2$ develops a triangular $\sqrt{13}\times\sqrt{13}$ CDW modulation. Each star-of-David unit cell has a single unpaired d-electron localized in its center. Generally, if an atomic orbital cannot be doubly occupied owing to strong on-site Coulomb repulsion a local magnetic moment can arise.[253] In 1T/1H-$TaSe_2$, a triangular lattice of magnetic moments emerging from the unpaired electron, interacts with the underlying metallic substrate. Such circumstances are capable of triggering intriguing states of matter, from heavy fermion physics to magnetic order.[254–256]

In the proximity of one isolated magnetic moment to a metallic system, the conduction electrons at the Fermi surface are capable of antiferromagnetically screen the spin of the magnetic moment. Thus, when the coupling J between the localized moment and the spins of the conduction electrons is strong enough, or the temperature reaches a certain low-lying threshold, called the Kondo temperature T_K, respectively, a many-body spin-singlet state is formed. In this mechanism, where the electron spins in the metal screen the impurity spin, the impurity spin effectively gets removed from the system. The Kondo temperature relates to the spin-exchange coupling constant J_0 in the form of $T_K = D_0\, exp\,[-1/2N(0)J_0)]$, where D_0 is the conduction band width and N_0 the DOS at E_F. In the case of more than one localized magnetic moment in proximity to a metal, an additional interaction, the one between these two localized moments, also largely dependent on J, has to be considered. The interaction of isolated spins is mediated by conduction electrons scattering between them. This long-range spin-exchange coupling, called K, is proportional to the square of the spin-exchange coupling as $K \propto N(0)J_0^2$. It can be ferromagnetic or antiferromagnetic. The interaction between two isolated spins was first described by Ruderman-Kittel-Kasuya-Yosida and is therefore called the RKKY interaction.[257] Within this picture one can compare two distinct temperatures, the Kondo temperature T_K and the RKKY temperature T_{RKKY} describing the two different regimes.

In a lattice of localized magnetic moments the Kondo coupling and the RKKY interactions stipulate the ground state of the system, deciding if it is Kondo screened (paramagnetic) or magnetically ordered. Figure 5.2.1 presents the so-called Doniach phase diagram, which illustrates the interplay between these two interactions. If the Kondo coupling exceeds the RKKY interaction, a Fermi liquid state with fully screened magnetic moments is formed. However, if the RKKY interaction exceeds the Kondo coupling, the spin screening can be overcome and a magnetically ordered state is developed.[257]

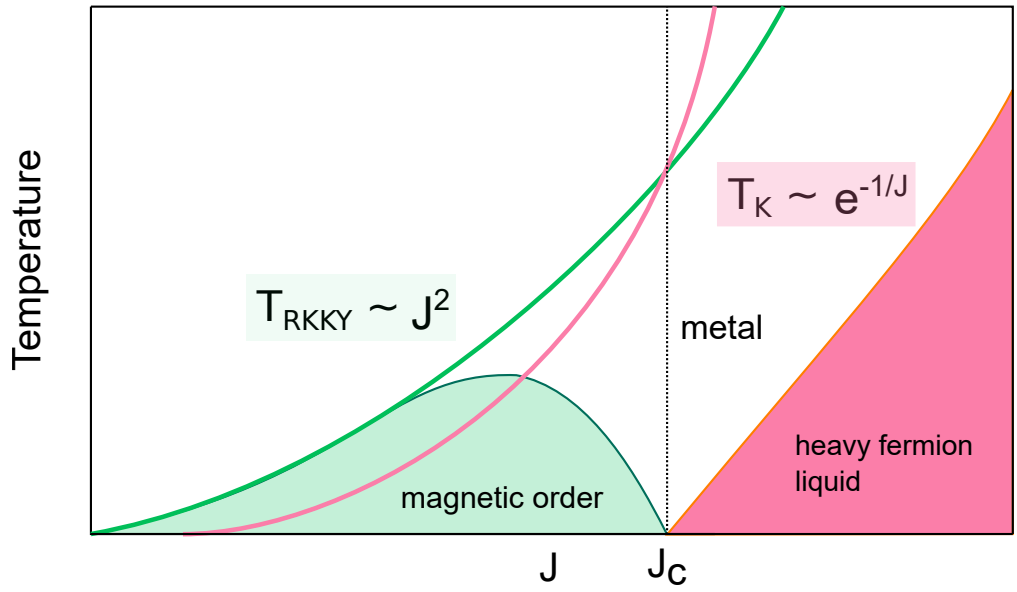

Figure 5.2.1: Doniach's phenomenological phase diagram. In the low coupling regime $J < J_C$, the RKKY interaction dominates and a magnetically ordered state can be formed. In the strong coupling regime $J > J_C$ the Kondo coupling screens the magnetic moments and the system is paramagnetic. The quantum critical point J_C is reached when the RKKY coupling becomes equal to the Kondo coupling.

To bring this into a more formal perspective, it follows a discussion about the bandstructure effects arising from such magnetic impurities (Figure 5.2.2) in the case of $J > J_C$ ($T_K > T_{RKKY}$). As it is shown in the top right corner of Figure 5.2.2 a), the spin of the Kondo impurity (red) interacts with the spins of the surrounding conduction electrons, what implies anomalous transport properties and a zero bias peak (ZBP) in the dI/dV spectrum.[258, 259] As described in the introduction of this section, an atomic lattice consisting of a dilute concentration of such magnetic moments in proximity to a metal experiences a collective magnetic screening below the characteristic Kondo temperature T_K.[254] If the magnetic moments are arranged periodically a Kondo lattice is formed, whose spectroscopic fingerprints are two peaks in the dI/dV spectrum as illustrated in Figure 5.2.2 b). As previously discussed, two decisive interactions are of great importance, namely the Kondo coupling and RKKY interaction. The topology of the FS mediates the interaction of the magnetic moments with its surroundings.[260] Following from the mean-field approximation of the periodic Anderson model, including strong Coulomb interactions, two renormalized hybridized and spin degenerate bands are formed by the interaction of the localized states (ϵ_f) with the conduction band (ϵ_k) [256]:

$$E_{k\pm} = \frac{1}{2}\{\epsilon_k + \lambda \pm \sqrt{(\epsilon - \lambda)^2 + 4V^2}\} \tag{5.1}$$

In eq. (5.1) λ is the renormalized f level and $V = z^{1/2}V_0$ the renormalized hybridization matrix amplitude with $z = 1 - n_f$ (n_f, f-level occupancy).

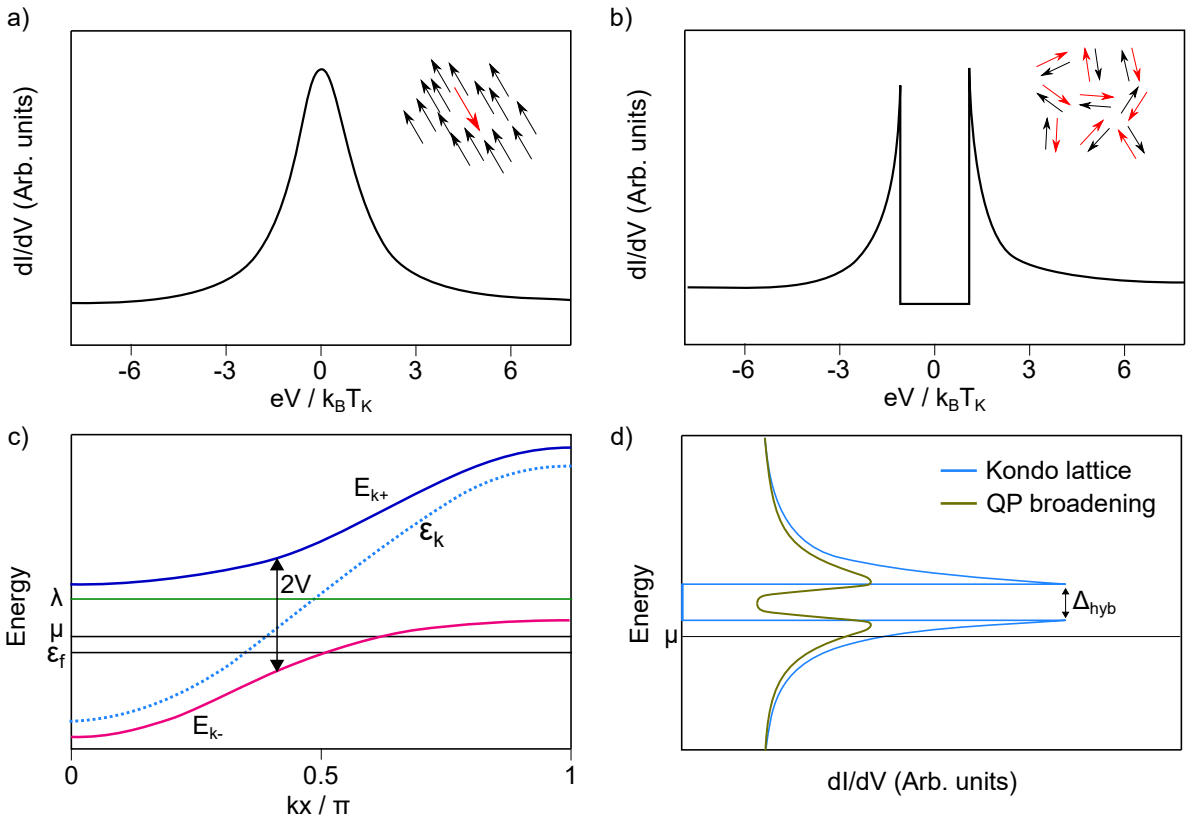

Figure 5.2.2: Kondo-lattice. a) The spin of single magnetic impurity (red arrow) is screened by the spins of the conduction electrons, what leads to a zero bias Fano resonance in the DOS. b) Such a peak becomes a gap feature in the Kondo lattice. c) In such a Kondo lattice hybridization of the conduction band (ϵ_k) with the localized states (ϵ_f) leads to the opening of a gap. d) The DOS are broadened due to various quasi particle effects.[255]

A hybridization gap of 2V opens up (Figure 5.2.2 c), what leads to a gap in the DOS (Figure 5.2.2 d) in the form of $\Delta_{hyb} = 2V^2/D$ with 2D the conduction bandwidth.[255] The resulting deconfinement leads to low-energy excitations with a heavy effective mass.[261] Manipulating the interaction of the f-orbital and itinerant electrons might trigger quantum phase transitions such as antiferromagnetic ordering or unconventional topological superconductivity.[262–264]

Recently, it was claimed that such artificial heavy fermion systems can be synthesized by MBE growth of designer TMD heterostructures 1T-TaS_2 on top of 1H-TaS_2.[265] In this system the Kondo coupling between the magnetic moments of the 1T layer and the itinerant electrons of the 1H layer create such a heavy fermion system, measurable with the STM tip. Specifically, the Kondo lattice formed by the Kondo impurities, defined by the CDW unit cell, creates a nearly flat pseudo-fermion band at the Fermi energy.

Bulk 1T-$TaSe_2$ is an intensively studied system known to exhibit the discussed Mott insulating phase.[245, 246] The star-of-David CDW state is also well characterized.[247, 245] However, no magnetic order has been detected. Compared to the single layer form of 1T-$TaSe_2$ the bulk material contains complicated interlayer CDW stacking what is not fully understood at the present day.[248] Without such interlayer couplings in the SL limit, especially when grown on top of the metallic 1H-$TaSe_2$, the intrinsic physics change drastically.

In a recent STM/STS study carried out at 5 K on the 1T-$TaSe_2$/1H-$TaSe_2$ heterostructure a zero bias peak was detected, which was attributed to a Kondo resonance with an estimated Kondo temperature of $T_K = 57 \pm 3$ K. In this experiment in combination with theoretical calculations [266], long-wavelength modulations of the Hubbard band energies (arising from the possible Mott insulating phase) were measured, which are identified as fingerprints of itinerant spinons. In that sense, the 1T/1H-$TaSe_2$ heterostructure is an ideally suited system for the study of magnetic correlations in this class of 2D materials.

If quantum fluctuations in such a system are very strong, and particularly stronger than the coupling between the Kondo sites, a magnetically ordered ground state is prevented and quantum spin liquids can develop.[267–270] Various studies have shown that bulk 1T-TaS_2 is a QSL material with a Mott insulating groundstate arising from the star-of-David CDW ordering.[271, 266, 272] The QSL ground state in bulk 1T-TaS_2 has been verified by experiments proving the absence of magnetic order down to the Millikelvin range.[272, 273] In a recent study, a similar QSL ground state was suggested in SL-1T-$TaSe_2$ on BLG.[270] However, few controversies remain, which are addressed in the following sections. Particularly, the ground state of the 1T/1H-$TaSe_2$ heterostructure regarding its magnetic nature has not been explored in the single-layer limit and shall be further discussed in this chapter.

5.2.2 Low-lying electronic structure

Based on the recent advancements in the study of low-dimensional QSL materials and the intriguing results regarding magnetic correlations in 2D TMD heterostructures, in this section we provide an exploration and discussion of the low-lying electronic structure of the 1T/1H-$TaSe_2$ heterostructure. Fig. 5.2.3 a) presents an atomic scale STM topographic image of a heterostructure domain consisting of 1T/1H-$TaSe_2$ grown on top of BLG. The H-phase acts as a metal substrate for the T-phase, which allows us to probe the interactions between the localized spin with the Fermi sea and examine the magnetic properties. Fig. 5.2.3 b) shows a typical dI/dV spectrum taken on the top of a bright spot of the $\sqrt{13} \times \sqrt{13}$ CDW on 1T/1H-$TaSe_2$. As seen, a clear, sharp peak appears at E_F. Such a peak at the Fermi energy is not present in the SL of 1H-$TaSe_2$, nor in the SL of 1T-$TaSe_2$. Only in the present heterostructure such a peak can be detected. A similar result was reported by Ruan et al., at 5 K.[270] Also indicated in the figure are the V_1 and C_1 states, which likely correspond to the same bands of 1T-$TaSe_2$ on BLG (compare to Fig. 5.1.4).

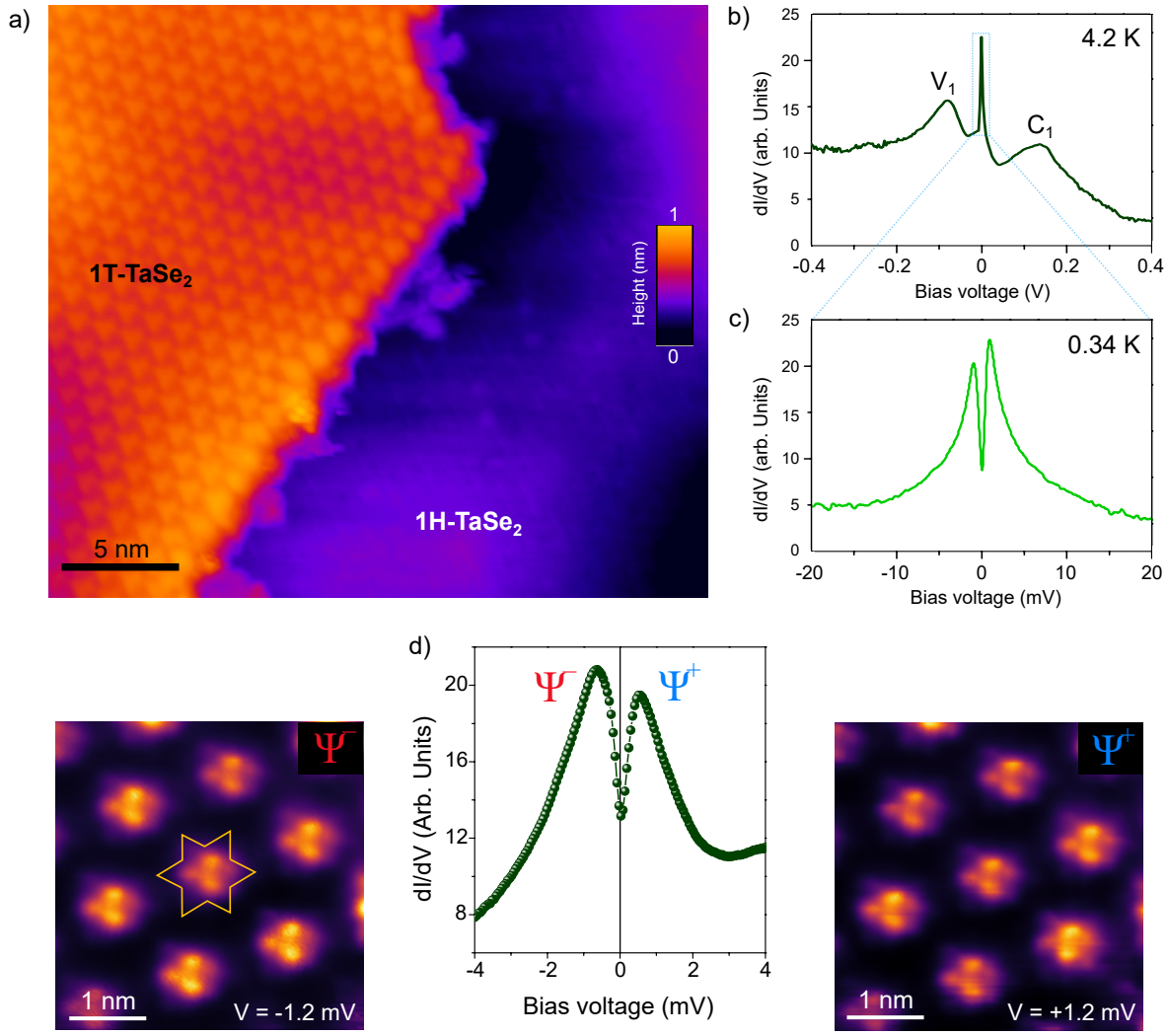

Figure 5.2.3: Topographic STM image and low temperature STS characterization of zero bias anomaly on 1T/1H-$TaSe_2$. a) STM image of 1T-$TaSe_2$ grown on 1H-$TaSe_2$ (V_s = - 1.6 V, I_t = 0.5 nA, T = 4.2 K). b) Low lying electronic structure (f = 833 Hz, $V_{a.c.}$ = 1 mV). c) High resolution dI/dV curve around E_F reveals to peaks (f = 833 Hz, $V_{a.c.}$ = 50 μV). d) Spatial extension of the wave function measured for ± 1 mV (f = 833 Hz, $V_{a.c.}$ = 25 μV).

Lowering the temperature down to 0.34 K, thus increasing the resolution of the spectroscopic measurements along with fine tuning the STS parameters and noise levels yield the ZBP feature shown in Fig. 5.2.3 c). This measurement reveals an internal structure of this feature, which consists of two equidistantly separated (with reference to E_F) peaks of ∼ 5 meV in width. The average energy separation between the peaks is $U_{\Delta V}$ = 1.2 ± 0.3 meV. Compared to previous works [270] on this system, we have not measured the expected single Kondo peak (at 0 T), but instead, the ZBP is split

in two peaks. This could be due to the lower temperature in our measurements, which was 0.35 K compared to 5 K in [270]. However, in another STM/STS study (measured at 0.3 K) on a similar system, namely 1T/1H-TaS_2, only one resonance feature is detected.[265] In order to probe the spatial extension of the wave function and the origin of the DOS in the atomic registry, we measure conductance maps at V = ± 1.2 mV as shown in Figure 5.2.3 d). The measurements allow us to spatially resolve the DOS within the star-of-David $\sqrt{13} \times \sqrt{13}$ CDW unit cell. Remarkably, for both polarities, the states are located in the center of the star-of-David, what signifies that they arise from the same atoms.

In order to gain knowledge on the nature of these intriguing peaks, we now study the temperature dependence in the range of 0.34 K - 4.2 K. As shown in Fig. 5.2.4 a), we find that the peaks get weaker and the gap vanishes as a function of increasing temperature.

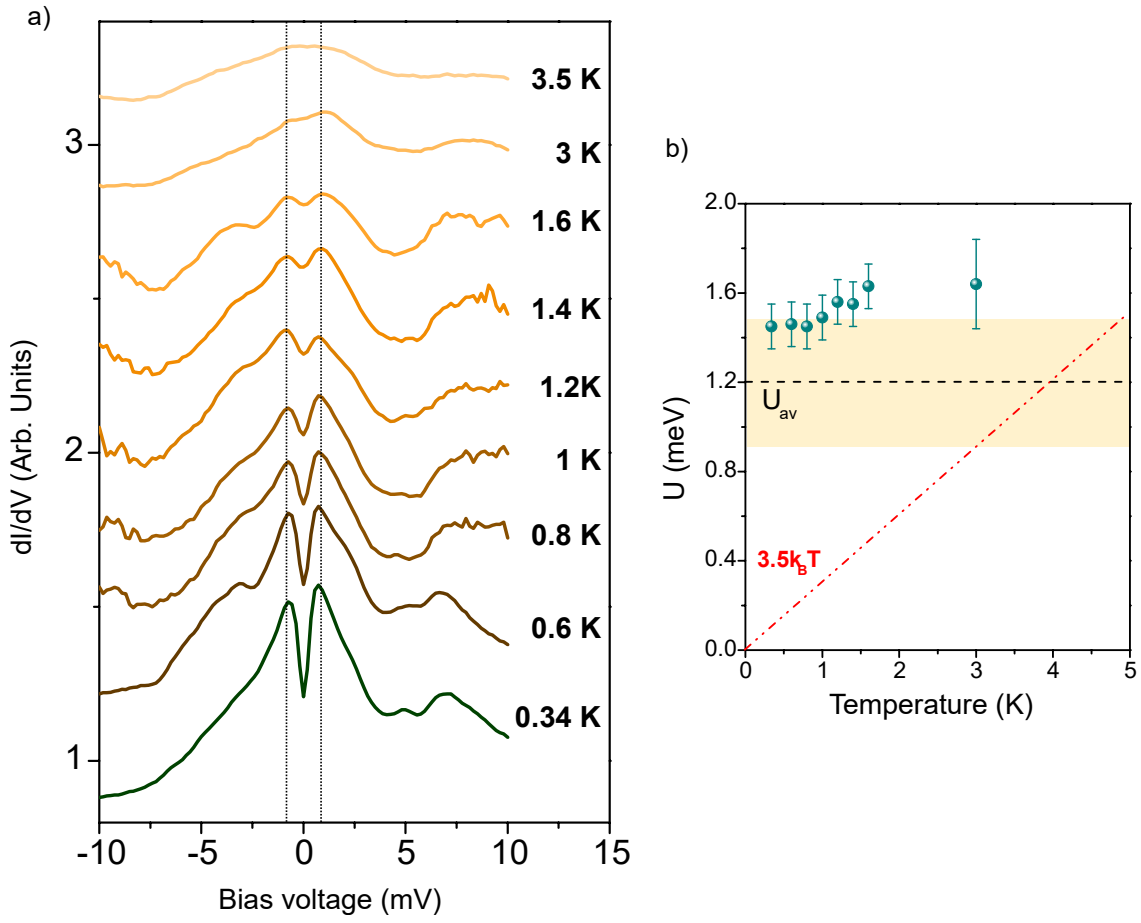

Figure 5.2.4: Temperature dependence of low lying electronic structure of 1T/1H-$TaSe_2$. a) Evolution of the dI/dV curves as a function of temperature (f = 833 Hz, $V_{a.c.} = 100\,\mu V$). b) The peak separation U for different temperatures.

A single ZBP remains in the electronic structure when increasing the temperature to a threshold of $\sim 3.5 \pm 0.3$ K. As indicated with the black dashed lines, the energy location of the peaks remain constant. In order to evaluate the role of thermal broadening in this observation, we compare the measured gap energies U with the expected thermal broadening. In Fig. 5.2.4 b) the separation U of the two peaks, or the gap, is plotted as a function of the temperature for one specific dataset. We have repeated this temperature variation experiment various times and found that within the error margin, U remains constant. Also indicated are the average gap value of $U_{av} = 1.2$ meV and the expected thermal broadening $3.5k_BT$ (red dashed line). At 3 K the gap is already almost totally suppressed; however, from the thermal broadening effect alone we expect it not to be strong enough to be capable of fully suppress the peaks (compare red dashed line with energy U). Even at 3.5 K, the remaining resolution, decreased by the thermal broadening effect, should still be high enough to resolve both of the peaks. Therefore, we believe that another intrinsic temperature dependent effect plays a role in this observation, which is capable of modifying the electronic structure.

In summary, the existence of two peaks and the gap like feature is, in principle, compatible with a Kondo lattice, as illustrated in Fig. 5.2.2. This is however contradictory to discoveries made in the system of 1T/1H-TaS_2, where a single peak was reported.[265] In the same study, by applying an out-of-plane magnetic field, they could split this single peak according to the expected behaviour of a Kondo resonance.

5.2.3 Magnetic field dependence

In order to gain further knowledge about the intrinsic nature of these feature, in the following section, we study it as a function of applied out-of-plane magnetic fields up to ± 11 T. Figure 5.2.5 a) illustrates the dI/dV curves acquired at 0.35 mK as a function of the magnetic field ($0 < B < 11$ T). The two peaks forming the opening of the gap are symmetrically moving away from the Fermi energy. At the same time, the broadening of the width of the peaks is very small. Plotting the position of the maxima of the peaks as a function of the magnetic field shows a linear increase for both peaks (Fig. 5.2.5 b) below and above E_F caused by a Zeeman splitting. The total gap energy dependency on the B-field is shown in Fig. 5.2.5 c). The Landé factor g can be extracted by fitting the data points to $2\Delta = g\mu_B B$ with μ_B the Bohr magneton and B the applied magnetic field. The fit yields $g \approx 3.7$.

The existence of only two peaks (one gap) in the presence of a magnetic field was probed for various grown samples with various different tips and can therefore be considered as a robust result. However, the observations contain a peculiar finding, which is not compatible with the Kondo lattice theory as outlined in Fig. 5.2.2. The incompatibility arises from the observation that the two hybridized bands ($E_{k\pm}$ in Fig. 5.2.2), which are spin degenerate, do not split in two sub peaks with increasing or reducing the magnetic field.

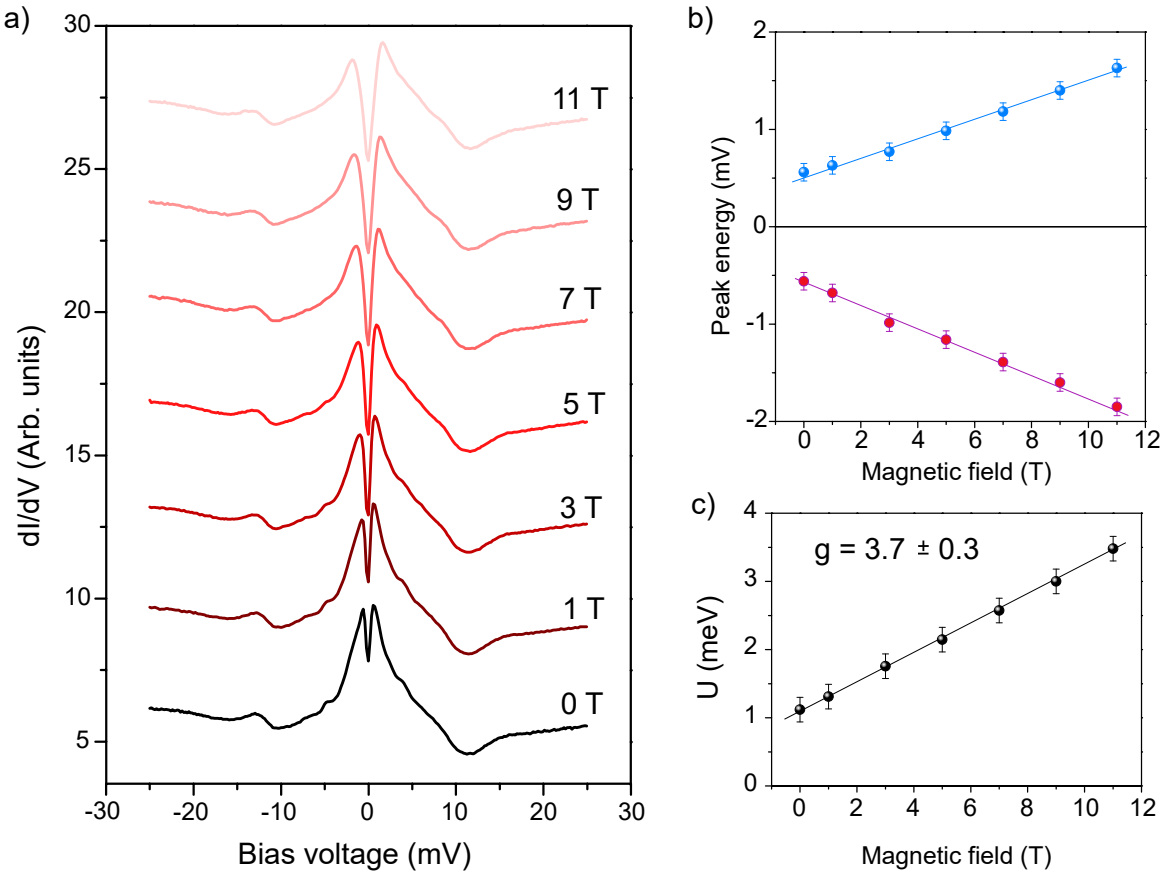

Figure 5.2.5: Magnetic field dependence of the low-energy electronic structure. a) Opening of the gap as a function of B-field (f = 833 Hz, $V_{a.c.}$ = 100 μV). b) Shift in energy for the peak in the occupied states (violet) and unoccupied states (blue) as a function of B-field. c) Hybridization gap as a function of the magnetic field (measured from dI/dV curves shown in a).

In principle, a gap arising from the mixing of f-electrons with the conduction band (see Fig. 5.2.2) should be able to be split into two gaps, as outlined in Fig. 5.2.6. As shown in 5.2.6 a), the generated bands are spin degenerate and split with increasing the magnetic field approaching $B \sim \Delta_0/gJ\mu_B$. In this scenario, the Kondo gap Δ_0 is reduced with increasing magnetic field and two peaks split into two individual sub-peaks. Such behaviour was reported in various studies on different kinds of Kondo insulators.[274–276] As discussed before, in our measurements we do not observe this splitting. Therefore, the Kondo lattice picture in this case can not explain the results.

In order to further investigate this peculiar behaviour we have probed the gap feature U in our system with particular focus on low magnetic fields (< 1 T) to verify the slope of this curve. During these measurements, we have observed systematic non-linearities (see Fig. 5.2.7 a) and b), which are not compatible with the heavy fermion picture as outlined in Figure 5.2.2.

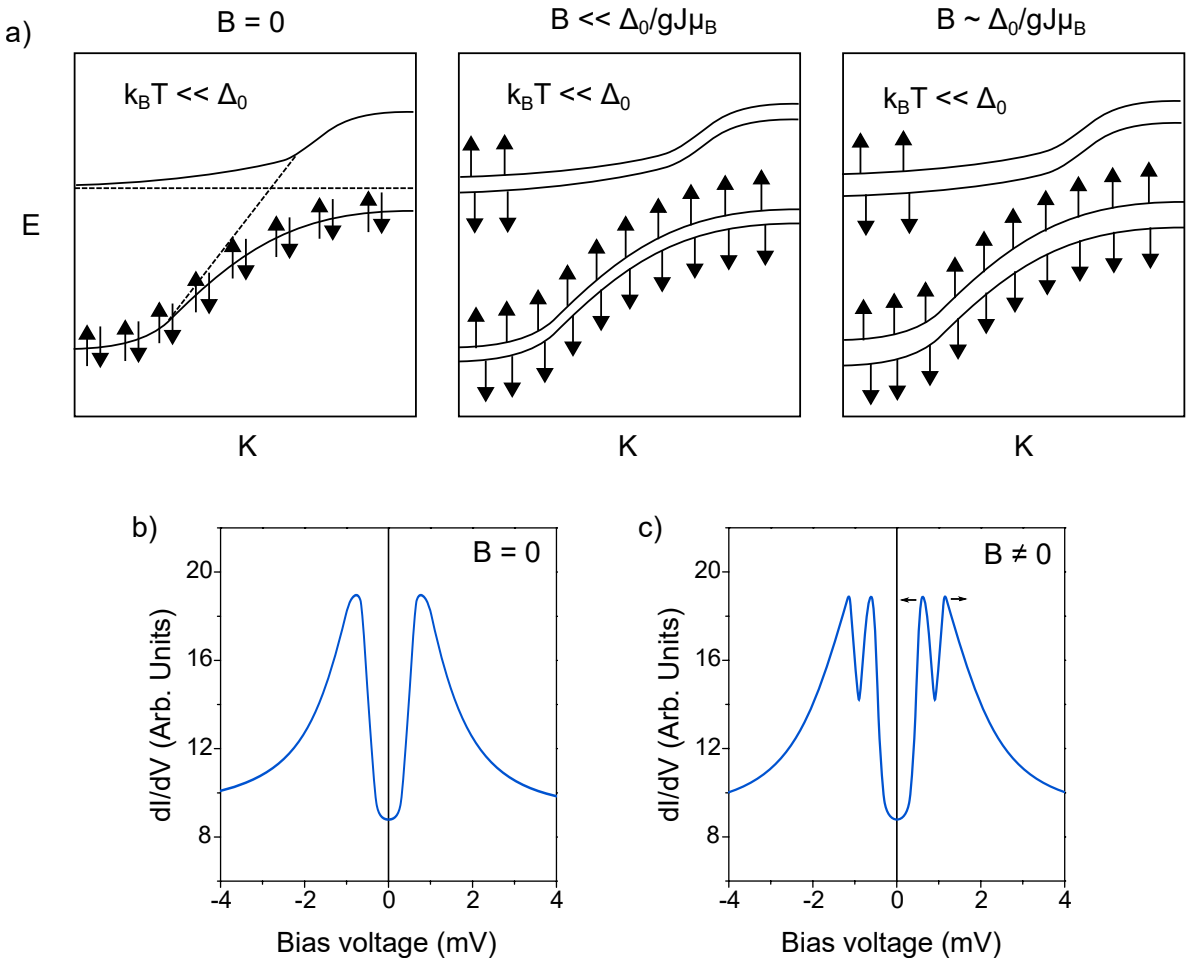

Figure 5.2.6: Theoretical gap evolution as a function of the magnetic field for a Kondo insulator. a) Splitting of the spin degenerate bands with application of a magnetic field is increased with higher fields from B = 0 (left) to B $\sim \Delta_0/gJ\mu_B$ (right). Expected dI/dV spectra at B = 0 (b) and B $\neq$ 0 (c). Reproduced from [275, 274]

As it is illustrated in Figure 5.2.7 a) in the shaded red area the gap energy is changing faster for very low magnetic fields, compared to the linear slope at at magnetic fields B > 1 T. Such behaviour has been observed in different locations of the samples. Figure 5.2.7 b) shows U for a measurement in a different location of the sample at a smaller field range. Again, a non-linear declination below 1 T is observed; however, the slope is different compared to Figure 5.2.7 a). Interestingly, most curves have a global minimum slightly above and below 0 T (for both polarities). However, due to different environments and different locations in the unit cell, the behaviour of U is also modified. This behaviour has been always found to be symmetric at both polarities of the magnetic field.

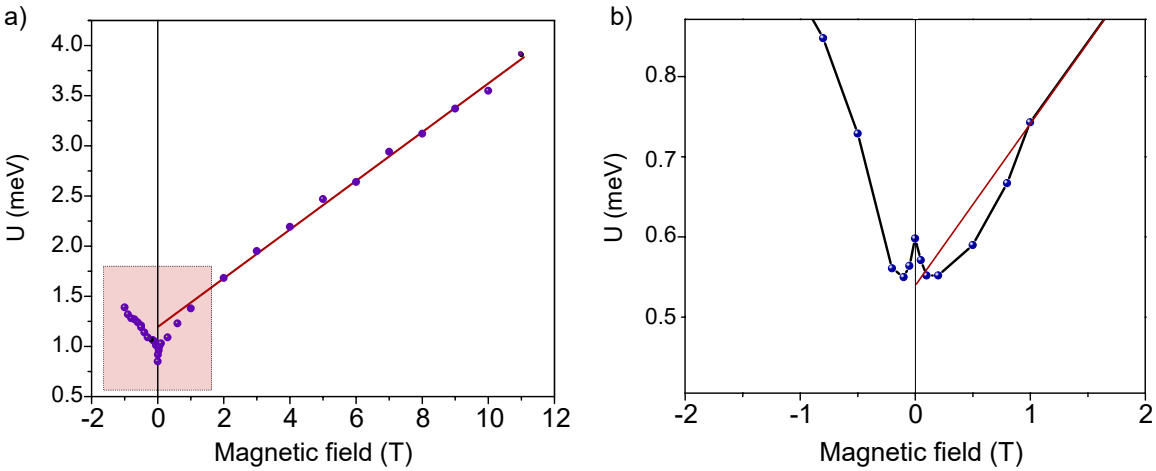

Figure 5.2.7: Gap feature U as a function of the B-field. a) The curve has a linear behaviour in the range of 1 - 11 T. AT low B-field (0 - 1 T) the curve shows unexpected non-linearities. b) Another dataset shows a different kind of non-linear behaviour between 0 - 1 T in another location of the unit-cell.

CHAPTER 6

Charge density wave order in single-layer 1T-$TiSe_2$

In this chapter we explore the structural and electronic properties (including the CDW state) of SL-1T-$TiSe_2$ grown on top of two different substrates: BLG/SiC(0001) and bulk WSe_2. Especially the CDW domain walls (DW) are interesting features as fluctuations of the charge order could possibly introduce superconductivity [87, 88, 277, 227] and networks of DWs could potentially be used as transport channels [278]. We first perform a topographic and electronic characterization of our MBE grown SL-$TiSe_2$/BLG/SiC(0001) and SL-$TiSe_2$/WSe_2 samples by means of low temperature (340 mK) STM/STS measurements. Furthermore, we explore the large scale CDW order and examine its symmetry, which varies when the SL domains are grown on the diverse substrates.

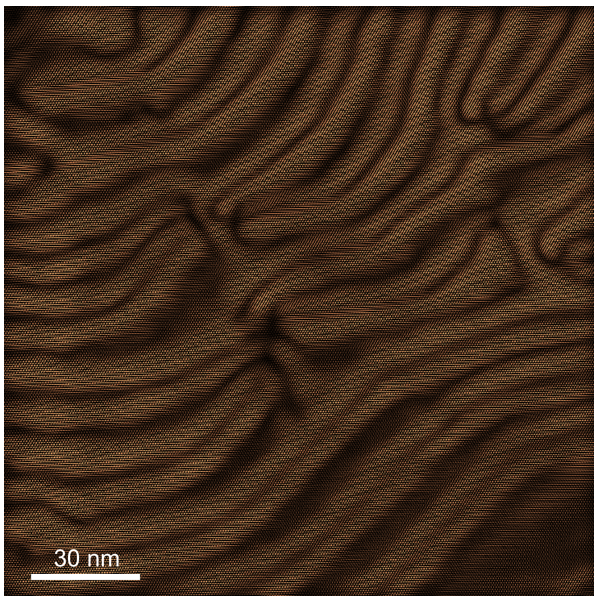

6.1 Theory and State of the art

Since its first structural characterization by neutron scattering experiments in 1976 [46] and later following topographic measurements by STM in 1988 [279], the fundamental trigger and the properties of the CDW modulation in the group-IV TMD 1T-$TiSe_2$ have been a captivating mystery in the field of condensed matter physics. As described in the introduction of this thesis, the two most favoured possible explanations for its existence are the excitonic insulator phase mechanism and the band-type Jahn-Teller effect.[48, 49] A CDW transition driven by the formation of excitons can appear, if the bandgap or band overlap of a semiconductor or semimetal is smaller than the exciton binding energy. The band-structure of free-standing SL-$TiSe_2$ (see Fig. 6.1.1) satisfies this condition.[280] In Fig. 6.1.1 a-b) electronic band structure calculations are presented for SL-1T-$TiSe_2$ in the normal 1x1 (a) and the 2x2 charge density wave (b) phase.[182]

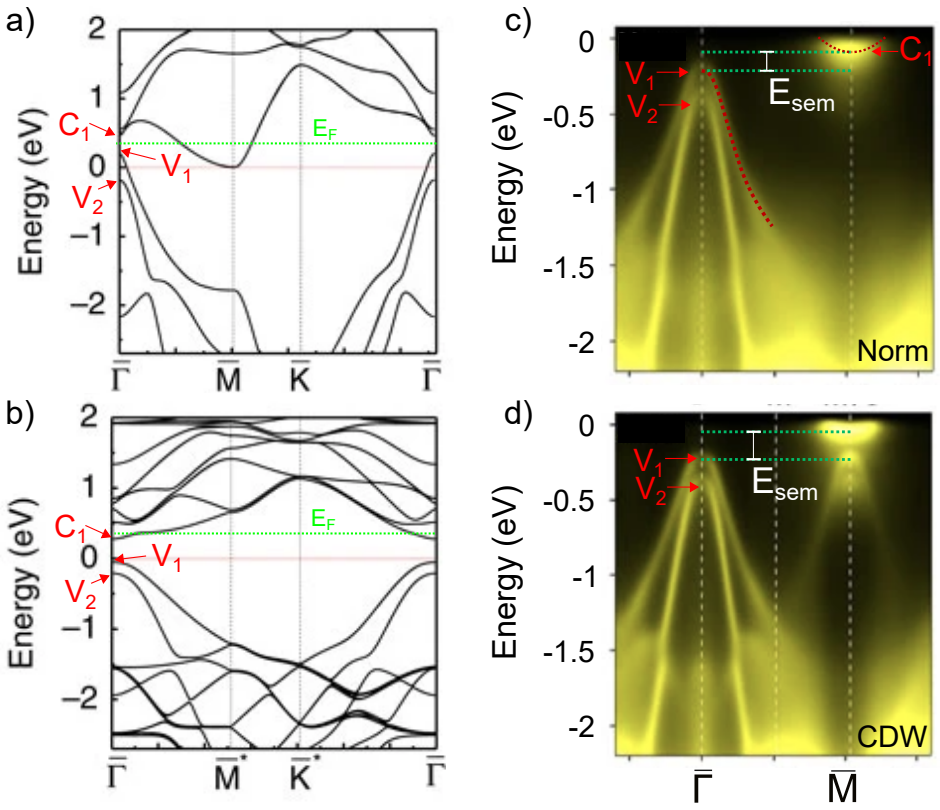

Figure 6.1.1: Electronic bandstructure calculations and ARPES measurements of SL-$TiSe_2$. a-b) DFT calculated bands with characteristic features indicated as C_1 (conduction band) and V_i (valence bands) near to E_F for the 1x1 normal phase (a) and the 3x3 CDW phase (b).[182] c-d) ARPES measurement of the band structure in the normal (1×1) phase (c) and the 2×2 CDW phase (d). Indicated by the green dashed lines is the semi metallic bandgap.[182]

Figures c-d) represent ARPES results in the two different phases.[182] Several characteristic features, traceable in STS measurements, arising from the electronic bands at Γ, are indicated in the plots. Also delineated is the Fermi energy (dashed green line), where we believe it to be, because of our STS results. A discussion about it follows further below in the text (see section 6.2). Interestingly, the electronic bands in the calculation show an overlap of $E_{sem} = 0.327\,eV$ (1x1 phase), which is in agreement with previous theoretical DFT studies [182, 281], but contrary to experimental results (see Fig. 6.1.1 c-d). These experimental ARPES measurements indicate a much smaller indirect gap of $\sim 98\,meV$ (1x1 phase).[182, 282] Such variations are supposed to arise from the tendency of DFT calculations to under estimate bandgaps.[283] In the normal 1×1 phase (Fig. 6.1.1 c) one can identify a pair of concave bands (V_1, V_2) centred at the $\overline{\Gamma}$ point, which are derived from Se 4p states. At the $\overline{M}$ point, the convex conduction band C_1, which is mainly derived from Ti 3d states, reaches below the Fermi level and becomes visible in the ARPES measurement. The bandgap of $\sim 98\,meV$ is calculated as the gap between the top of the Se band (V_1) and the bottom of the Ti band at $\overline{M}$.[182] In the CDW phase (Fig. 6.1.1 b) and d)), the bands are folded and repeated at the $\overline{M}$ point, which is a consequence of the 2×2 modulation. The gap increases in the CDW phase from 98 meV to 153 meV, what excludes Fermi surface nesting as the trigger of this modulation. Through opening a larger gap, the occupied Se 4p states are pushed to lower energies, what results in reducing the total energy primarly, but is counteracted by an increase in elastic energy.[182] These ARPES results suggest a band structure effect as the origin of the CDW. However, a low concentration of mobile charge carriers and therefore weakly screened Coulomb interactions can trigger an excitonic insulator instability. These circumstances are present in 1T-$TiSe_2$, where the formation of Ti 3d - Se 4p excitons can possibly destabilize the system and introduce a new periodicity emerging from the wave vector connecting the corresponding valence and conduction band pockets.[284]

Experimental evidence for this purely electronic mechanism was presented by ultrafast response time measurements conducted within another ARPES study [285] and recently by means of momentum-resolved electron energy-loss spectroscopy, a technique which was particularly developed to study electronic collective excitations.[286] In a different experiment, it was shown that this material can undergo a semimetal-to-semiconductor transition by sulfur (S) substitution as 1T-$TiSe_{2-x}S_x$. Within the same study it was revealed how the CDW phase can be suppressed with this method.[287] A similar behaviour was found when Cu was used as the doping source. Such experiments have also shown that SC is triggered in Cu_xTiSe_2 with the right amount of Cu doping (starting from $x \sim 0.04$ and maximum at $x \sim 0.08$).[88] These studies suggest that SC and CDW order are somewhat more fundamentally connected through a quantum critical point (QCP), at which $T_{c,cdw}$ reaches zero and $T_{c,sc}$ is finite. A QCP without CDW order indeed was discovered through pressurizing the material ($P = 5.1 \pm 0.2\,GPa$); however, at such high pressure SC could not develop anymore. Instead what was found is a relation between the transition of commensurate CDW (CCDW) to incommensurate CDW (ICDW) and superconducting order. This relation is attributed to SC appearing in the CDW domain walls.[227] SC in 1T-$TiSe_2$ can also be triggered by increasing the charge-carrier density through applying an electric field to $TiSe_2$ nanosheets (thickness $< 10\,nm$).[87] Remarkably, a phase diagram

comprised of temperature and charge-carrier density shows a domain between the well known CDW order and SC, which is explained as a mixed CDW phase made up of a CCDW and an ICDW. Such areas of ICDW are described as the domain walls in between the CCDW, similarly to the study [227] mentioned above. Interestingly, fluctuations of the charge order parameters have led to the appearance of SC in various systems, what makes the intermediate mixed phase particularly exciting for further studies, as it could potentially host SC order. Dynamic phase fluctuation, comprised of ICDW phonon modes, can exist in the domain walls. Such phonons are capable of inducing SC and therefore strongly localize the Cooper pairs in the DWs.[277]

Another interesting aspect of the CDW order in $TiSe_2$ is its controversial chiral symmetry. As it was suggested by various experimental probes, including STM, below 7 K another phase transition occurs, which is attributed to a chiral phase transition.[288–290] As shown by Fourier Transformations of topographic STM images, the intensities of the CDW peaks break the expected threefold symmetry. However, such observations remain controversial.

In this study we have epitaxially grown 1T-$TiSe_2$ on two electronically distinct substrates, namely BLG/SiC(0001) and bulk WSe_2. Low temperature STM/STS measurements are deployed for an electronic characterization of the different systems. We further study the large scale evolution and the symmetry of the CDW domain walls, which behave surprisingly different in the two investigated systems. Spectroscopic measurements reveal the absence of SC (at 340 mK) in the domain walls as it was suggested by various previous studies.[227, 291, 87]

6.2 Topographic and electronic characterization

First, the synthesis as well as the large scale topographic and electronic characterization by STM/STS is described. For the MBE growth of SL-$TiSe_2$ we have used high purity Ti (99.99%) and Se (99.999%) as the elemental sources. As described in a previous section (3.2), we need to prepare BLG/SiC(0001) substrates first, which is done by high temperature annealing (1400°C for 35 min). The WSe_2 substrate does not need to be annealed at a very high temperature. We expect that annealing at a similar temperature than the actual growth temperature is enough, because the crystals are cleaved inside the UHV of the MBE chamber with the conventional sticky tape method. This process reveals the clean and flat surface of pristine WSe_2, which is therefore optimally suited for the epitaxial growth of TMD materials. In the process of tuning the growth dynamics, we found an ideal substrate growth temperature of 450°C for both BLG/SiC(0001) and WSe_2 through a continuous cycle of sample synthesis and characterization by AFM. The growth time varies, depending on the desired coverage; however, an optimized crystal quality was found at a growth rate of ~ 0.1 ML / min, with a Ti:Se flux ratio of 1:30. Topographic images obtained by STM at 4.2 K are shown in Fig. 6.2.1 a) for 1T-$TiSe_2$/BLG/SiC(0001) and d) for 1T-$TiSe_2$/WSe_2.

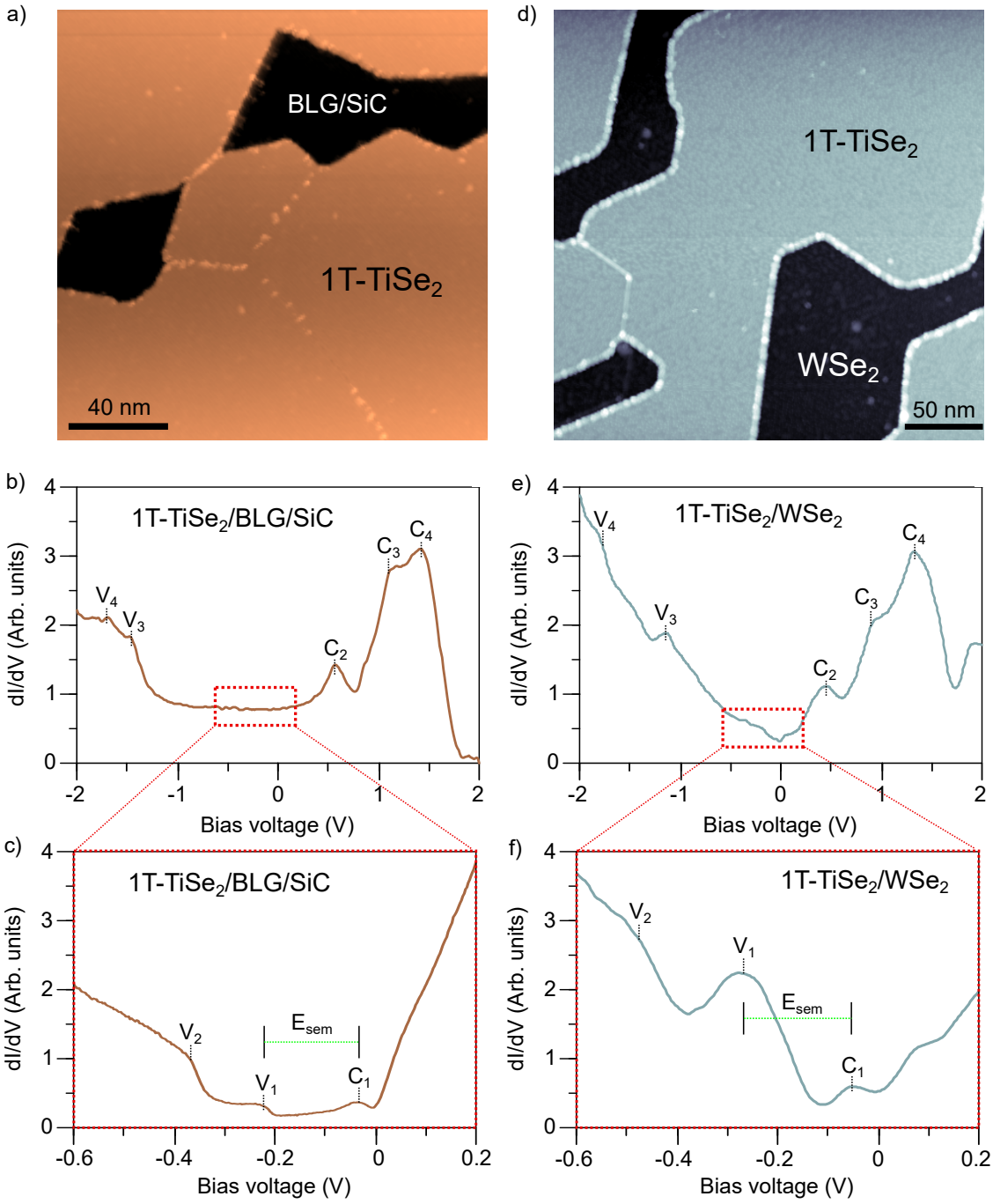

Figure 6.2.1: Topographic (STM) and electronic characterization (STS) of 1T-TiSe$_2$. a) Topography ($V_S = +1\,\mathrm{V}$; $I_t = 20\,\mathrm{pA}$; $T = 4.2\,\mathrm{K}$), b) large scale and c) small scale dI/dV curve of SL-TiSe$_2$ grown on BLG/SiC. d) Topography ($V_S = +2.8\,\mathrm{V}$; $I_t = 8\,\mathrm{pA}$; $T = 4.2\,\mathrm{K}$), e) large scale and f) small scale dI/dV curve of SL-TiSe$_2$ grown on WSe$_2$. Measurement parameters: (b,e): f = 833 Hz, $V_{a.c.}$ = 5 mV; (c,f): f = 833 Hz, $V_{a.c.}$ = 0.15 mV.

Table 6.1: Energies of the main low lying features of the electronic structure as measured by STS (see Fig. 6.2.1 (c,f). The values were taken as the maxima of the STS peaks. STS uncertainties were determined through a statistical analysis of individual STS curves obtained in multiple locations with different STM tips.

Substrate	C_1 (meV)	V_1 (meV)	V_2 (meV)	E_{sem} (meV)
BLG/SiC	-38 ± 8	-223 ± 12	-358 ± 10	185 ± 15
WSe_2	-49 ± 8	-272 ± 10	-477 ± 45	223 ± 15
BLG/SiC [182]	-76	-229	-	153
Bulk $TiSe_2$ [182]	-24	-106	-	82

The crystallinity of the grown domains is very high, as can be seen from the sharp edges of the SL materials. Few grain boundaries are visible for both cases. Figures 6.2.1 b) and d) show the acquired large scale dI/dV spectra measured by STS for the two studied systems, which reveal subtle differences. Indicated in the figures are the main STS features we have observed in the bias range of ± 2 V. In order to compare the low lying electronic structure, including the bandgap of the two studied system, with the reported electronic structure calculations and ARPES measurements (see Fig. 6.1.1), figures 6.2.1 c) and f) represent magnifications of the DOS in a smaller energy range around E_F. The observed energy locations of these features are summarized in table 6.1. As it is indicated in the band structure shown in Fig. 6.1.1, V_1 is the top of the Se valence band and C_1 represents the bottom of the Ti conductance band. Therefore, the band overlap energy from our STS measurements yield band gaps of $E_{sem} = 185 \pm 15$ meV for 1T-$TiSe_2$/BLG/SiC(0001) and $E_{sem} = 223 \pm 15$ meV for 1T-$TiSe_2$/WSe_2. These results are in good agreement with the reported ARPES studies.[182, 284]

For the empty states we found a shift of the C_2 peak. Its energy is$C_2 = 552 \pm 15$ mV (BLG) and $VH_{1,4} = 442 \pm 15$ mV (WSe_2). Such a difference of $\triangle E = 110$ mV is intriguing and unexpected as it was shown in section 3.4 for the case of SL-$NbSe_2$/WSe_2, the substrate has only a marginal effect on the electronic structure of the TMD material grown on top. From these previous results we assume that there should not be any significant charge transfer to the SL-TMD material when using WSe_2 as a substrate. However, in the case of 1T-$TiSe_2$/WSe_2 compared to $NbSe_2$/WSe_2 the observation a this shift points to this direction. Two circumstances might affect these finding, which are the remnant Se clusters on the surface when the sample is grown on WSe_2, or other emerging defects on the top layer of WSe_2 arising from the annealing and outgassing process, respectively. Such defects could act as electron dopants and shift the peak towards the Fermi energy. Another distinctive feature in the dI/dV spectrum on 1T-$TiSe_2$/WSe_2 compared to 1T-$TiSe_2$/BLG/SiC is the increase of DOS approaching -1 V (compare Fig. 6.2.1 b) with e)), which is an effect of the WSe_2 bulk valence band maximum, located at the Γ point just below the Fermi energy.[292] This observation is in agreement with the $NbSe_2$/WSe_2 measurements.

6.3 CDW domain walls in 1T-$TiSe_2$/BLG/SiC(0001)

In order to learn more about the intriguing properties of the 2×2 CDW modulation in this material, we have studied its large scale modulations and symmetry through topographic imaging by STM in combination with the analysis of its FFT patterns. Fig. 6.3.1 shows an example image of the atomic structure of 1T-$TiSe_2$/BLG/SiC(0001) measured by STM at 4.2 K. Several periodicities are visible, which are highlighted in the FFT pattern in the right bottom corner of Fig. 6.3.1 a). Very pronounced are the 2×2 CDW and 1×1 Bragg peaks. Taking a close look on the CDW pattern in the FFT reveals that this modulation contains two slightly different CDW wave vectors, similar to what was already described in a study on Cu intercalated 1T-$TiSe_2$ mentioned in the introduction of this chapter.[291] In the quoted study it is suggested that the Cu intercalation changes the nature of the CDW from a CCDW phase to an ICDW phase by pinning it and creating DWs. It is further elaborated that such an ICDW modulation can be triggered by a phase shift of the CCDW between two domains, or by two rotated ICDW interfering with each other.[291] However, in the pristine 1T-$TiSe_2$ they detect only a single domain CCDW and no domain walls. Similar results were found in Pt doped $TiSe_2$ samples.[278] In this study they suggest that the low energy insulating behaviour is caused by a combination of electron correlations with an increased disorder in those samples, accompanied by the arising of CDW DWs, which act as narrow channels for the low energy transport.[278] Both of this studies on atomically doped bulk 1T-$TiSe_2$ are in contrast to our results on SL-$TiSe_2$/BLG/SiC(0001) shown in Fig. 6.3.1, where DWs are clearly visible even in the pristine case.

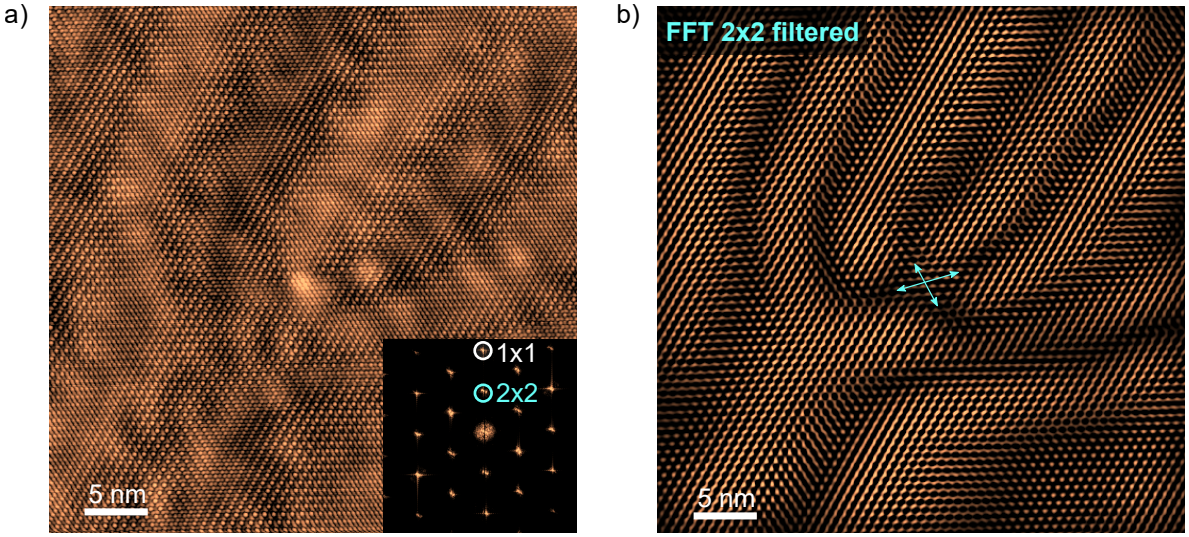

Figure 6.3.1: Atomic structure and CDW modulation in 1T-$TiSe_2$/BLG/SiC(0001). a) Atomic resolution STM image ($V_S = -150$ mV; $I_t = 100$ pA; $T = 4.2$ K). b) Filtered 2×2 CDW components reveals the symmetry of the domain walls.

By filtering the 2×2 modulation (see Fig. 6.3.1 b) and therefore removing all other q vectors from the FFT spectrum, the topographic modulation of the CDW with appearing domain walls is exposed and easily identified. Interestingly, these domain walls do not have a three-fold symmetry, as it was suggested before.[291, 87] Instead, they follow a curvilinear path, merging at various locations almost every time in the number of four distinct domains.

The behaviour of these domain walls is further studied and represented in the large scale 2×2 filtered topographic image in Fig. 6.3.2. As can be seen from the inset in the bottom right corner, the CDW domains have a cross section of $\sim 9.4\,\mathrm{nm}$. Furthermore, they possess extended shapes exceeding the length scale of the image, which has a size of $150\times150\,\mathrm{nm}^2$.

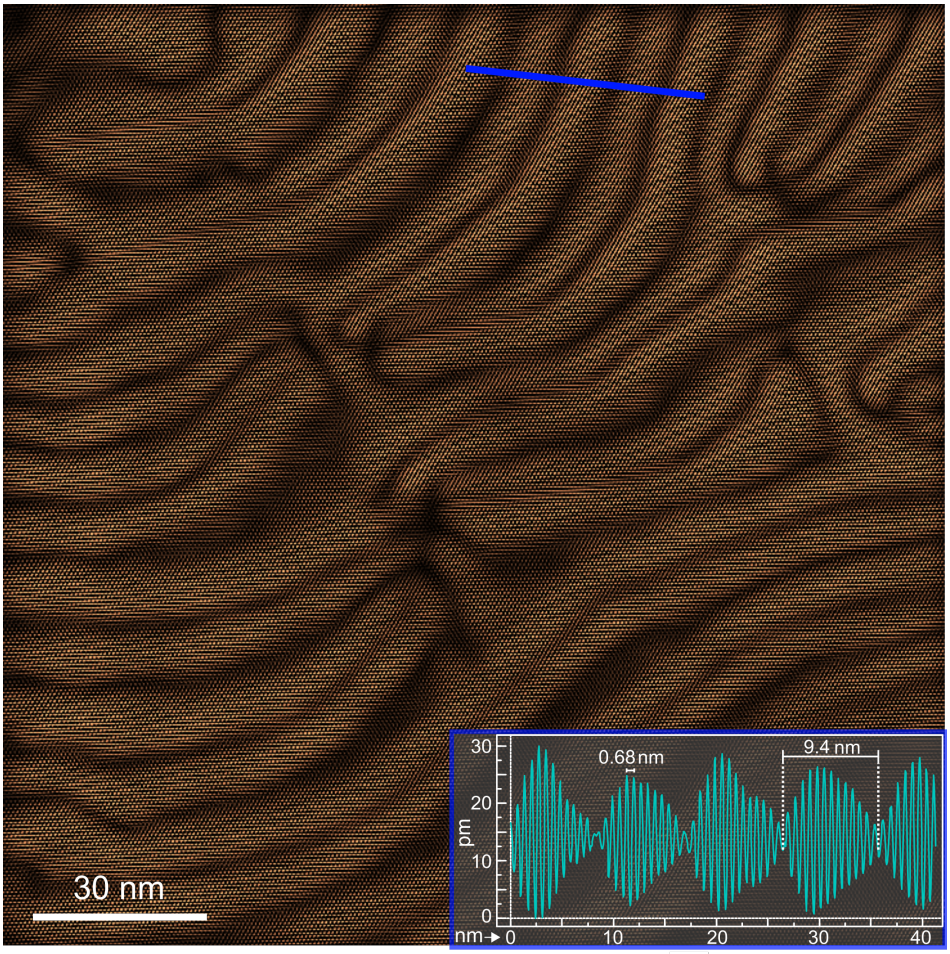

Figure 6.3.2: Large scale topographic image of CDW domain walls in SL-1T-$TiSe_2$/BLG/SiC(0001). The inset shows the electronic corrugation measured across multiple CDW domain walls ($V_S = -50\,\mathrm{V}$; $I_t = 60\,\mathrm{pA}$; $T = 4.2\,\mathrm{K}$).

A recent study examines the structural and electronic properties of the CDW domain walls in 1T-TaS_2 by STM, where multiple different types of DWs are identified.[293] Similar results were observed for Cu-doped and Pt-doped 1T-$TiSe_2$ [291, 278], where in all of these systems the CDW DWs are linear features and they are in accordance with the three-fold symmetry of the lattice. This is not the case in our observations. A possible reason for this discrepancy could be atomic defects incorporated into, or underneath, the grown SL material. Such defect would act as CDW pinning potentials modifying the phase of the CDW in a similar manner as it was described in the case of Mo doped $NbSe_2$ in section 4.1.4.

We have further assessed the appearance of SC in the observed DWs in 1T-TiSe2/BLG. The topography and the DWs do not change when applying a magnetic field up to 10 T. In order to measure a possible superconducting state, we have performed grid spectroscopy measurements on top of various DWs at different magnetic fields in the range of 0 - 10 T. In the scope of these experiments, we could not detect any superconducting order and conclude that these DWs do not host superconductivity.

6.4 CDW order and QPI in 1T-$TiSe_2$/WSe_2

In this section, we investigate the CDW order in SL-$TiSe_2$/WSe_2, which varies significantly compared to the case when grown on BLG/SiC(0001). Similar to another investigated system described in this thesis, namely SL-$NbSe_2$ grown on top of WSe_2, the CDW order is drastically weakened in SL-$TiSe_2$/WSe_2. The reason for this suppression is not clear. We suggest that due to subtle differences in the epitaxial growth on WSe_2, van Hove singularities might shift incrementaly in energy, what could lead to the weakening of the CDW order. This interpretation is consistent with the observed shifts in the large scale STS measurements (see Fig. 6.2.1). However, more experiments need to be performed in order to identify the exact microscopic mechanism leading to this effect.

Instead, what we have found in this novel heterostructure are very intriguing features in FFT patterns. The features appear at similar wave vectors as what is expected from the 2×2 CDW modulation. By changing the measurement mode from constant current to constant height, and simultaneously record the conductance, we were able to identify modifications of the FFT features as a function of bias voltage. The patterns in the range of ± 950 mV are shown in Fig. 6.4.1. Clearly, these features change its structure by varying the bias voltage, what indicates a band structure effect instead of the CDW modulation.

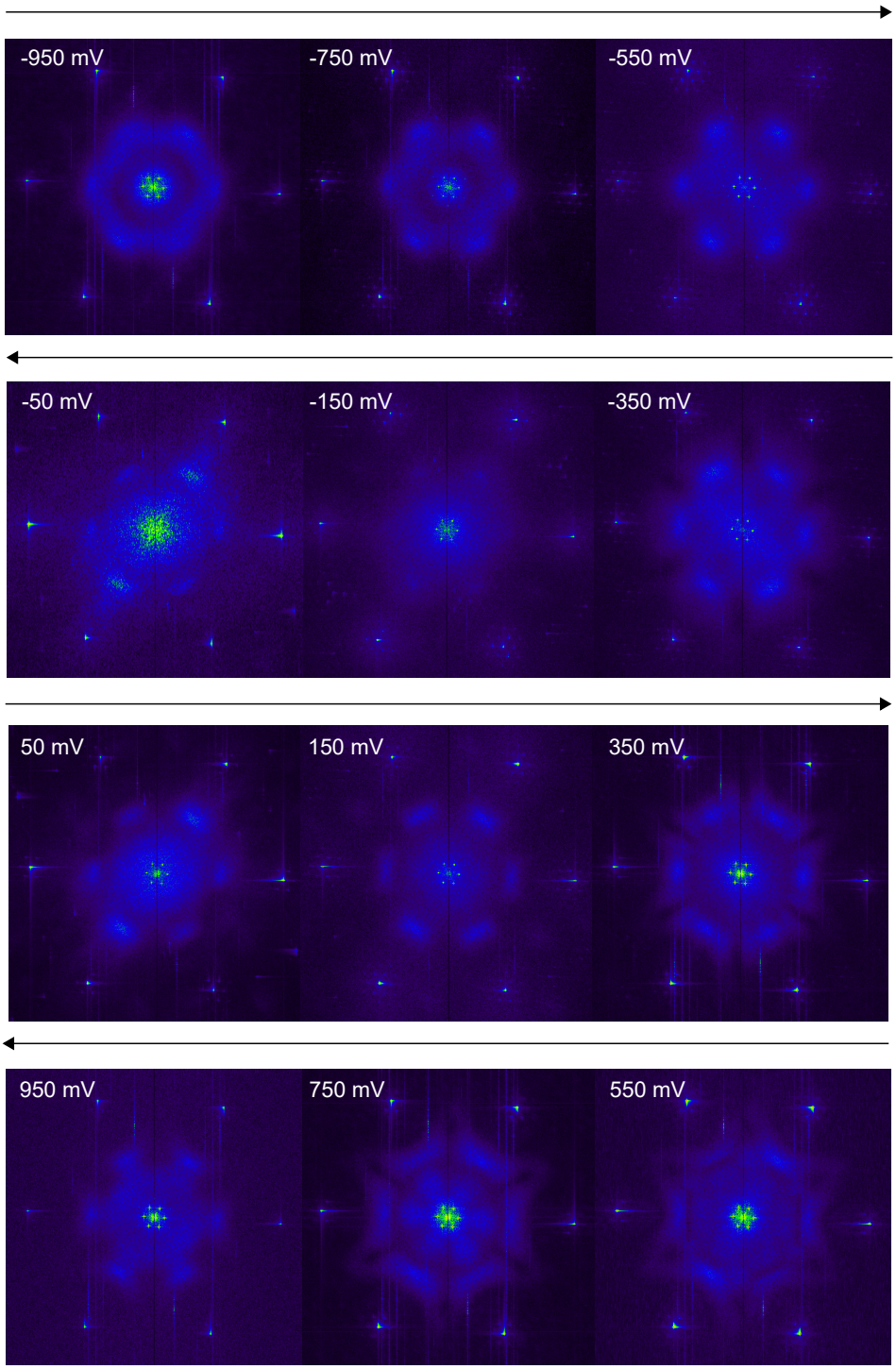

Figure 6.4.1: FFT pattern evolution of SL-$TiSe_2$/WSe_2 for different bias voltages. The measured FFT structures are extracted from constant height conductance maps.

6.5 Summary

We have successfully grown SL-1T-$TiSe_2$ on two electronically distinct substrates and have compared their atomic and electronic structure by STM/STS measurements. Within this atomic scale characterization we could demonstrate the semi metallic nature of this material reported from varying ARPES experiments. Although the band gap does not change significantly when the SL-TMD is grown on the distinct substrates, the appearing 2×2 CDW and especially its DWs has crucial differences. The DWs appear even in undoped 1T-$TiSe_2$/BLG what is contrasting previous works on this material. The reason for this matter could be a dilute number of defects interfering with the phase of the CDW and therefore creating the DWs. Why the DWs almost always show a 4-fold symmetry at specific locations remains unclear. However, these could be the sites of the atomic defects. In contrast, when the 1T-$TiSe_2$ is grown on bulk WSe_2, the symmetry of the DWs is different and is much more similar to the reported behaviour in doped $TiSe_2$. We suspect that due to a larger number of defects ($\sim 10\,\%$) the interferences of the CDW become much larger and therefore, the DWs become shorter. Finally, by large scale constant height conductance maps at different energies in the range of $\pm$ 950 mV we were able to reveal a band structure effect with similar 2x2 modulation than what is expected from the CDW. How these observations interfere with the CDW order remains unknown and shall hopefully be a motivation for future experimental as well as theoretical works.

CHAPTER 7

Conclusions and Outlook

In this work, we have studied collective electronic phases such as superconductivity, charge density wave order, and magnetic correlations in therefore fabricated novel single-layer TMD materials. We have started with optimizing MBE growth parameters in order to be able to grow highly crystalline, uniform single layers of a variety of TMD materials. Such samples allowed us to perform high resolution topographic imaging and precise spectroscopic measurements. The possibility to perform these measurements at very low temperatures of 0.34 K in combination with the applicability of a 11 T magnetic field has helped us to deeply understand the underlying mechanisms of the collective electronic phases in these SL-TMD materials.

The experimental work has started with a thorough characterization of the quasi particle density of states of SL-$NbSe_2$. Therefore, first, we have optimized the MBE growth of SL-$NbSe_2$/BLG/SiC(0001) until we could obtain highly crystalline domains of up to 700 nm in diameter. Acquisition of more than 3000 dI/dV curves in various different samples with distinct tips has allowed us to perform a coherent statistical analysis of the observed dip-hump features outside of the superconducting gap. With help of a therefore developed theoretical model, we could show that these features correspond to a soft collective mode, a so-called Leggett mode, which is a phase fluctuation of the superconducting order parameter. We could show that these observations are evidence for a f-wave triplet pairing channel competing with the conventional s-wave singlet ground state.

In the second part, we have assessed the role of the substrates on the collective electronic states (SC and CDW) in SL-TMD-materials. Therefore we have grown SL-$NbSe_2$ on four electronically distinct substrates, namely BLG/SiC(0001), h-BN/Ir(111), Au(111), and WSe_2 and we have studied its electronic structure by STM/STS and ARPES. Interestingly, we have found that the BLG/SiC(0001) substrate plays a negligible role on the electronic properties of the SL-TMD material grown on top of it and is therefore optimally suited for the MBE growth and the consecutive study of 2D TMD materials. Furthermore, we have observed similar spectroscopic signatures in SL-$NbSe_2$ when it was grown on h-BN/Ir(111). However, when the material is grown on WSe_2, SC and CDW order are

critically impacted, whereas SC vanishes and CDW order is drastically weakened. Lastly, we found that the Au(111) substrate is not suitable for the investigation of collective electronic states in TMD materials, because the electronic structure of the TMD is strongly impacted and it cannot sustain SC nor CDW order.

We have continued with the synthesis and characterization of SL-TMD alloys. We were able to grow high-quality monolayers of $Nb_{1-\delta}Mo_{\delta}Se_2$ across the entire alloy composition range ($0 < \delta < 1$) in order to bridge two electronically distinct 2D TMD materials. This aliovalent alloy allowed us to investigate the atomic-scale evolution of the electronic ground state across three different phase transitions, i.e., superconductor-metal, CDW-metal and metal-semiconductor. Our measurements have revealed a remarkable robustness of the collective electronic states (CDW and SC) against disorder. Furthermore, a non-monotonic evolution of the SC state with disorder was discovered, which is strengthened for dilute Mo concentration. Our work provides a general methodology to study a wide variety of disorder-driven 2D electronic phase transitions, which remain largely unexplored due to the lack of suitable platforms. In the second part of this chapter we have synthesised alloys of $Ta_{1-\delta}W_{\delta}Se_2$ in order to examine if it is possible to tune E_F and thus increase $T_{c,sc}$ to a detectable temperature. Indeed, we could show that by an optimized doping level of $\delta = 0.018$, $T_{c,sc}$ can be enhanced from 0.2 K in the bulk to 0.88 K in the fabricated alloy. We have followed with a discussion of the phase diagram of this alloy as a function of W doping, where we could define a superconducting dome. Finally we have discussed the disorder in this system, which triggers a gap like feature in the DOS even in the metallic state. These results could be helpful for future studies in the field of superconductivity in SL-TMD materials as it exemplifies a versatile approach of tuning $T_{c,sc}$.

We have continued with the synthesis as well as the electronic and magnetic characterization of the H-phase and T-phase of $TaSe_2$. In the first part of this chapter, we have investigated the nature of the electronic gap, appearing in the DOS of the 1T-$TaSe_2$. A careful assessment and comparison of our spectroscopic measurements with DFT calculations suggests a conventional band structure effect instead of the widely believed Mott insulator theory. In the second part we investigate magnetic correlations in the heterostructure of 1T/1H-$TaSe_2$ and have found unexpected behaviour in the low-lying electronic structure. We discuss two distinct theories including the creation of heavy fermions and the appearance of magnetic order.

In the last chapter of this thesis, we have performed an electronic characterization of the MBE grown single-layer samples of $TiSe_2$/BLG and $TiSe_2/WSe_2$ and have confirmed the semi metallic nature of this material. Furthermore, we have investigated the CDW domain walls in these two systems. Especially when grown on top of BLG/SiC(0001), we were able to image the dispersion of the CDW domains at large scales of more than 100 nm and could show that they appear in a four-fold symmetry. When $TiSe_2$ is grown on bulk WSe_2 on the other hand, the CDW is drastically weakened. However, by analysing FFT patterns of constant height conductance maps, we could reveal intriguing QPI band structure effects.

In conclusion, this thesis aimed to expand the knowledge on MBE growth of single-layer TMD materials, combined with the study of their fundamental collective electronic phases. A remarkable result from this thesis is the first demonstration of the existence of a Leggett mode in the quasiparticle spectrum of a 2D TMD superconductor. These results have unveiled the rather unconventional superconducting properties in SL-$NbSe_2$ and, therefore, could change the current understanding of the microscopic mechanisms behind superconductivity in two dimensions. If the discovered Leggett mode in $NbSe_2$ is something universal for all superconducting single-layer TMD materials remains however an open question. Fine spectroscopy measurements of other TMD superconductors such as TaS_2 or WS_2 could potentially clarify this matter. In this thesis it was also shown that single-layer TMD alloy materials host great potential for tuning the electronic properties of 2D designer materials. By increasing atomic substitutional doping the possibility to tune the electronic band gap of $Mo_\delta Nb_{1-\delta}Se_2$ was described. However, also the collective electronic phases such as superconductivity can be modified and even strengthened to a large degree by the same approach, what opens up a rather new way of controlling superconductivity at the 2D limit. We hope that the obtained results and formulated ideas will help other researchers in the future to continue expanding the fundamental knowledge of the intriguing physics of collective electronic and magnetic states in two-dimensional TMD materials.

Bibliography

[1]K. S. Novoselov, A. K. Geim, S. V. Morozov, D. Jiang, Y. Zhang, S. V. Dubonos, I. V. Grigorieva, and A. A. Firsov, "Electric Field Effect in Atomically Thin Carbon Films", Science **306**, 666–669 (2004).

[2]P. Johari and V. B. Shenoy, "Tuning the Electronic Properties of Semiconducting Transition Metal Dichalcogenides by Applying Mechanical Strains", ACS Nano **6**, 5449–5456 (2012).

[3]K. P. Dhakal, S. Roy, H. Jang, X. Chen, W. S. Yun, H. Kim, J. Lee, J. Kim, and J.-H. Ahn, "Local Strain Induced Band Gap Modulation and Photoluminescence Enhancement of Multilayer Transition Metal Dichalcogenides", Chemistry of Materials **29**, 5124–5133 (2017).

[4]S.-H. Su, W.-T. Hsu, C.-L. Hsu, C.-H. Chen, M.-H. Chiu, Y.-C. Lin, W.-H. Chang, K. Suenaga, J.-H. He, and L.-J. Li, "Controllable Synthesis of Band-Gap-Tunable and Monolayer Transition-Metal Dichalcogenide Alloys", Frontiers in Energy Research **2**, 27 (2014).

[5]S. Borghardt, J.-S. Tu, F. Winkler, J. Schubert, W. Zander, K. Leosson, and B. E. Kardynał, "Engineering of Optical and Electronic Band Gaps in Transition Metal Dichalcogenide Monolayers through External Dielectric Screening", Physical Review Materials **1**, 054001 (2017).

[6]M. M. Ugeda, A. J. Bradley, Y. Zhang, S. Onishi, Y. Chen, W. Ruan, C. Ojeda-Aristizabal, H. Ryu, M. T. Edmonds, H.-Z. Tsai, A. Riss, S.-K. Mo, D. Lee, A. Zettl, Z. Hussain, Z.-X. Shen, and M. F. Crommie, "Characterization of Collective Ground States in Single-Layer $NbSe_2$", Nature Physics **12**, 92–97 (2016).

[7]H. Ryu, Y. Chen, H. Kim, H.-Z. Tsai, S. Tang, J. Jiang, F. Liou, S. Kahn, C. Jia, A. A. Omrani, J. H. Shim, Z. Hussain, Z.-X. Shen, K. Kim, B. I. Min, C. Hwang, M. F. Crommie, and S.-K. Mo, "Persistent Charge-Density-Wave Order in Single-Layer $TaSe_2$", Nano Letters **18**, 689–694 (2018).

[8]A. Chikina, A. Fedorov, D. Bhoi, V. Voroshnin, E. Haubold, Y. Kushnirenko, K. H. Kim, and S. Borisenko, "Turning Charge-Density Waves into Cooper Pairs", npj Quantum Materials **5**, 22 (2020).

[9]J. T. Ye, Y. J. Zhang, R. Akashi, M. S. Bahramy, R. Arita, and Y. Iwasa, "Superconducting Dome in a Gate-Tuned Band Insulator", Science **338**, 1193–1196 (2012).

[10]X. Xi, Z. Wang, W. Zhao, J.-H. Park, K. T. Law, H. Berger, L. Forro, J. Shan, and K. F. Mak, "Ising Pairing in Superconducting $NbSe_2$ Atomic Layers", Nature Physics **12**, 139–143 (2016).

[11]K. Zhao, H. Lin, X. Xiao, W. Huang, W. Yao, M. Yan, Y. Xing, Q. Zhang, Z.-X. Li, S. Hoshino, J. Wang, S. Zhou, L. Gu, M. S. Bahramy, H. Yao, N. Nagaosa, Q.-K. Xue, K. T. Law, X. Chen, and S.-H. Ji, "Disorder-Induced Multifractal Superconductivity in Monolayer Niobium Dichalcogenides", Nature Physics **15**, 904–910 (2019).

[12]Y.-T. Hsu, W. S. Cole, R.-X. Zhang, and J. D. Sau, "Inversion-Protected Higher-Order Topological Superconductivity in Monolayer WTe_2", Phys. Rev. Lett. **125**, 097001 (2020).

[13]S. Tang et al., "Quantum Spin Hall State in Monolayer 1T'-WTe_2", Nature Physics **13**, 683–687 (2017).

[14]Y. Chen et al., "Strong Correlations and Orbital Texture in Single-Layer 1T-$TaSe_2$", Nature Physics **16**, 218–224 (2020).

[15]M. M. Ugeda, A. Pulkin, S. Tang, H. Ryu, Q. Wu, Y. Zhang, D. Wong, Z. Pedramrazi, A. Martín-Recio, Y. Chen, F. Wang, Z.-X. Shen, S.-K. Mo, O. V. Yazyev, and M. F. Crommie, "Observation of Topologically Protected States at Crystalline Phase Boundaries in Single-Layer WSe_2", Nature Communications **9**, 3401 (2018).

[16]S. A. Han, R. Bhatia, and S.-W. Kim, "Synthesis, Properties and Potential Applications of Two-Dimensional Transition Metal Dichalcogenides", Nano Convergence **2**, 17 (2015).

[17]K. F. Mak, C. Lee, J. Hone, J. Shan, and T. F. Heinz, "Atomically Thin MoS_2: A New Direct-Gap Semiconductor", Phys. Rev. Lett. **105**, 136805 (2010).

[18]T. Akama, W. Okita, R. Nagai, C. Li, T. Kaneko, and T. Kato, "Schottky Solar Cell using Few-Layered Transition Metal Dichalcogenides toward Large-Scale Fabrication of Semitransparent and Flexible Power Generator", Scientific Reports **7**, 11967 (2017).

[19]W. Bao, X. Cai, D. Kim, K. Sridhara, and M. S. Fuhrer, "High Mobility Ambipolar MoS_2 Field-Effect Transistors: Substrate and Dielectric Effects", Applied Physics Letters **102**, 042104 (2013).

[20]G. L. Frey, S. Elani, M. Homyonfer, Y. Feldman, and R. Tenne, "Optical-Absorption Spectra of Inorganic Fullerenelike MS_2 (M = Mo, W)", Phys. Rev. B **57**, 6666–6671 (1998).

[21]N. Choudhary, M. R. Islam, N. Kang, L. Tetard, Y. Jung, and S. I. Khondaker, "Two-Dimensional Lateral Heterojunction Through Bandgap Engineering of MoS_2 via Oxygen Plasma", Journal of Physics: Condensed Matter **28**, 364002 (2016).

[22]X. Cui, G.-H. Lee, Y. D. Kim, G. Arefe, P. Y. Huang, C.-H. Lee, D. A. Chenet, X. Zhang, L. Wang, F. Ye, F. Pizzocchero, B. S. Jessen, K. Watanabe, T. Taniguchi, D. A. Muller, T. Low, P. Kim, and J. Hone, "Multi-Terminal Transport Measurements of MoS_2 using a Van der Waals Heterostructure Device Platform", Nature Nanotechnology **10**, 534–540 (2015).

[23]E. Navarro-Moratalla, J. O. Island, S. Mañas-Valero, E. Pinilla-Cienfuegos, A. Castellanos-Gomez, J. Quereda, G. Rubio-Bollinger, L. Chirolli, J. A. Silva-Guillén, N. Agraït, G. A. Steele, F. Guinea, H. S. J. van der Zant, and E. Coronado, "Enhanced Superconductivity in Atomically Thin TaS_2", Nature Communications **7**, 11043 (2016).

[24]S. C. de la Barrera, M. R. Sinko, D. P. Gopalan, N. Sivadas, K. L. Seyler, K. Watanabe, T. Taniguchi, A. W. Tsen, X. Xu, D. Xiao, and B. M. Hunt, "Tuning Ising Superconductivity with Layer and Spin-Orbit Coupling in Two-Dimensional Transition-Metal Dichalcogenides", Nature Communications **9**, 1427 (2018).

[25]N. F. MOTT, "Metal-Insulator Transition", Rev. Mod. Phys. **40**, 677–683 (1968).

[26]Y. Cao, V. Fatemi, S. Fang, K. Watanabe, T. Taniguchi, E. Kaxiras, and P. Jarillo-Herrero, "Unconventional Superconductivity in Magic-Angle Graphene Superlattices", Nature **556**, 43–50 (2018).

[27]Y. Chen et al., "Strong Correlations and Orbital Texture in Single-Layer 1T-$TaSe_2$", Nature Physics **16**, 218–224 (2020).

[28]X. Zhu, J. Guo, J. Zhang, and E. W. Plummer, "Misconceptions associated with the Origin of Charge Density Waves", Advances in Physics: X **2**, 622–640 (2017).

[29]R. Peierls, *Quantum Theory of Solids*, Oxford University Press, London (1955).

[30]E. J. Woll and W. Kohn, "Images of the Fermi Surface in Phonon Spectra of Metals", Phys. Rev. **126**, 1693–1697 (1962).

[31]D. S. Inosov, V. B. Zabolotnyy, D. V. Evtushinsky, A. A. Kordyuk, B. Büchner, R. Follath, H. Berger, and S. V. Borisenko, "Fermi Surface Nesting in Several Transition Metal Dichalcogenides", New Journal of Physics **10**, 125027 (2008).

[32]D. Moncton, J. Axe, and F. DiSalvo, "Study of Superlattice Formation in 2H-$NbSe_2$ and 2H-$TaSe_2$ by Neutron Scattering", Physical Review Letters **34**, 734 (1975).

[33]D. E. Moncton, J. D. Axe, and F. J. DiSalvo, "Neutron Scattering Study of the Charge-Density Wave Transitions in $2H-TaSe_2$ and $2H-NbSe_2$", Phys. Rev. B **16**, 801–819 (1977).

[34]X. Zhu, Y. Cao, J. Zhang, E. W. Plummer, and J. Guo, "Classification of Charge Density Waves based on their Nature", Proceedings of the National Academy of Sciences **112**, 2367–2371 (2015).

[35]F. Weber, S. Rosenkranz, J.-P. Castellan, R. Osborn, R. Hott, R. Heid, K.-P. Bohnen, T. Egami, A. H. Said, and D. Reznik, "Extended Phonon Collapse and the Origin of the Charge-Density Wave in $2H-NbSe_2$", Phys. Rev. Lett. **107**, 107403 (2011).

[36]T. Valla, A. V. Fedorov, P. D. Johnson, P.-A. Glans, C. McGuinness, K. E. Smith, E. Y. Andrei, and H. Berger, "Quasiparticle Spectra, Charge-Density Waves, Superconductivity, and Electron-Phonon Coupling in $2H-NbSe_2$", Phys. Rev. Lett. **92**, 086401 (2004).

[37]C. J. Arguello, E. P. Rosenthal, E. F. Andrade, W. Jin, P. C. Yeh, N. Zaki, S. Jia, R. J. Cava, R. M. Fernandes, A. J. Millis, T. Valla, R. M. Osgood, and A. N. Pasupathy, "Quasiparticle Interference, Quasiparticle Interactions, and the Origin of the Charge Density Wave in $2H-NbSe_2$", Phys. Rev. Lett. **114**, 037001 (2015).

[38]J. Laverock, D. Newby, E. Abreu, R. Averitt, K. E. Smith, R. P. Singh, G. Balakrishnan, J. Adell, and T. Balasubramanian, "k-Resolved Susceptibility Function of $2H$-$TaSe_2$ from Angle-Resolved Photoemission", Phys. Rev. B **88**, 035108 (2013).

[39]M. D. Johannes, I. I. Mazin, and C. A. Howells, "Fermi-Surface Nesting and the Origin of the Charge-Density Wave in $NbSe_2$", Phys. Rev. B **73**, 205102 (2006).

[40]M. D. Johannes and I. I. Mazin, "Fermi Surface Nesting and the Origin of Charge Density Waves in Metals", Phys. Rev. B **77**, 165135 (2008).

[41]T. Kiss, T. Yokoya, A. Chainani, S. Shin, T. Hanaguri, M. Nohara, and H. Takagi, "Charge-Order-Maximized Momentum-Dependent Superconductivity", Nature Physics **3**, 720–725 (2007).

[42]F. Weber, R. Hott, R. Heid, K.-P. Bohnen, S. Rosenkranz, J.-P. Castellan, R. Osborn, A. H. Said, B. M. Leu, and D. Reznik, "Optical phonons and the Soft Mode in $2H$-$NbSe_2$", Phys. Rev. B **87**, 245111 (2013).

[43]C. Bessis, M. L. Della Rocca, C. Barraud, P. Martin, J. C. Lacroix, T. Markussen, and P. Lafarge, "Probing Electron-Phonon Excitations in Molecular Junctions by Quantum Interference", Scientific Reports **6**, 20899 (2016).

[44]D. Lin, S. Li, J. Wen, H. Berger, L. Forro, H. Zhou, S. Jia, T. Taniguchi, K. Watanabe, X. Xi, and M. S. Bahramy, "Patterns and Driving Forces of Dimensionality-Dependent Charge Density Waves in 2H-Type Transition Metal Dichalcogenides", Nature Communications **11**, 2406 (2020).

[45]T. Kumakura, H. Tan, T. Handa, M. Morishita, and H. Fukuyama, "Charge Density Waves and Superconductivity in 2H-$TaSe_2$", Czechoslovak Journal of Physics **46**, 2611–2612 (1996).

[46]F. J. Di Salvo, D. E. Moncton, and J. V. Waszczak, "Electronic Properties and Superlattice Formation in the Semimetal $TiSe_2$", Phys. Rev. B **14**, 4321–4328 (1976).

[47]D. Jérome, T. M. Rice, and W. Kohn, "Excitonic Insulator", Phys. Rev. **158**, 462–475 (1967).

[48]K. Rossnagel, L. Kipp, and M. Skibowski, "Charge-Density-Wave Phase Transition in $1T - TiSe_2$: Excitonic Insulator versus Band-Type Jahn-Teller Mechanism", Phys. Rev. B **65**, 235101 (2002).

[49]H. P. Hughes, "Structural Distortion in $TiSe_2$ and Related Materials - a Possible Jahn-Teller effect?", Journal of Physics C: Solid State Physics **10**, L319–L323 (1977).

[50]C.-S. Lian, C. Heil, X. Liu, C. Si, F. Giustino, and W. Duan, "Coexistence of Superconductivity with Enhanced Charge Density Wave Order in the Two-Dimensional Limit of $TaSe_2$", The Journal of Physical Chemistry Letters **10**, 4076–4081 (2019).

[51]J. Bardeen, L. N. Cooper, and J. R. Schrieffer, "Theory of Superconductivity", Phys. Rev. **108**, 1175–1204 (1957).

[52]D. van Delft and P. Kes, "The Discovery of Superconductivity", Physics Today **63**, 38–43 (2010).

[53]W. Meissner and R. Ochsenfeld, "Ein neuer Effekt bei Eintritt der Supraleitfähigkeit", Naturwissenschaften **21**, 787–788 (1933).

[54]R. Kleiner, W. Buckel, and R. Huebener, *Superconductivity: An Introduction* (Wiley, 2016).

[55]V. L. Ginzburg and L. D. Landau, "On the Theory of Superconductivity", Zh. Eksp. Teor. Fiz. **20**, 1064–1082 (1950).

[56]E. M. Lifshitz and L. P. Pitaevskii, *Statistical Physics: Theory of the Condensed State*, Vol. 9 (Elsevier, 2013).

[57]M. Milošević and R. Geurts, "The Ginzburg–Landau Theory in Application", Physica C: Superconductivity **470**, Vortex Matter in Nanostructured Superconductors, 791–795 (2010).

[58]M. Tinkham, *Introduction to Superconductivity*, Dover Books on Physics Series (Dover Publications, 2004).

[59]W. S. Corak, B. B. Goodman, C. B. Satterthwaite, and A. Wexler, "Exponential Temperature Dependence of the Electronic Specific Heat of Superconducting Vanadium", Phys. Rev. **96**, 1442–1444 (1954).

[60]W. S. Corak, B. B. Goodman, C. B. Satterthwaite, and A. Wexler, "Atomic Heats of Normal and Superconducting Vanadium", Phys. Rev. **102**, 656–661 (1956).

[61]J. Bardeen, L. N. Cooper, and J. R. Schrieffer, "Theory of Superconductivity", Phys. Rev. **108**, 1175–1204 (1957).

[62]H. Fröhlich, "Theory of the Superconducting State. I. The Ground State at the Absolute Zero of Temperature", Phys. Rev. **79**, 845–856 (1950).

[63]*Isotope Effect in Superconductivity* (Proc. Phys. Soc. London A63 778-778, 1950).

[64]N. N. Bogoljubov, V. V. Tolmachov, and D. V. Širkov, "A New Method in the Theory of Superconductivity", Fortschritte der Physik **6**, 605–682 (1958).

[65]J. G. Valatin and D. Butler, "On the Collective Properties of a Boson System", Il Nuovo Cimento (1955-1965) **10**, 37–54 (1958).

[66]A. F. Andreev, "Thermal Conductivity of the Intermediate State of Supercondcutors", Zh. Eksperim. i Teor. Fiz. **46** (1964).

[67]N. E. Staley, J. Wu, P. Eklund, Y. Liu, L. Li, and Z. Xu, "Electric Field Effect on Superconductivity in Atomically Thin Flakes of $NbSe_2$", Phys. Rev. B **80**, 184505 (2009).

[68]J. M. Lu, O. Zheliuk, I. Leermakers, N. F. Q. Yuan, U. Zeitler, K. T. Law, and J. T. Ye, "Evidence for Two-Dimensional Ising Superconductivity in Gated MoS_2", Science **350**, 1353–1357 (2015).

[69]Y. Saito, Y. Nakamura, M. S. Bahramy, Y. Kohama, J. Ye, Y. Kasahara, Y. Nakagawa, M. Onga, M. Tokunaga, T. Nojima, Y. Yanase, and Y. Iwasa, "Superconductivity Protected by Spin-Valley Locking in Ion-Gated MoS_2", Nature Physics **12**, 144–149 (2016).

[70]J.-F. Ge, Z.-L. Liu, C. Liu, C.-L. Gao, D. Qian, Q.-K. Xue, Y. Liu, and J.-F. Jia, "Superconductivity above 100 K in Single-Layer FeSe Films on Doped $SrTiO_3$", Nature Materials **14**, 285–289 (2015).

[71]Y. Yang, S. Fang, V. Fatemi, J. Ruhman, E. Navarro-Moratalla, K. Watanabe, T. Taniguchi, E. Kaxiras, and P. Jarillo-Herrero, "Enhanced Superconductivity upon Weakening of Charge Density Wave Transport in 2H-TaS_2 in the Two-Dimensional Limit", Phys. Rev. B **98**, 035203 (2018).

[72]K. M. Bastiaans, D. Chatzopoulos, J.-F. Ge, D. Cho, W. O. Tromp, J. M. van Ruitenbeek, M. H. Fischer, P. J. de Visser, D. J. Thoen, E. F. C. Driessen, T. M. Klapwijk, and M. P. Allan, "Direct Evidence for Cooper Pairing Without a Spectral Gap in a Disordered Superconductor above T_c", Science **374**, 608–611 (2021).

[73]J. G. Bednorz and K. A. Müller, "Possible highTc Superconductivity in the Ba-La-Cu-O System", Zeitschrift für Physik B Condensed Matter **64**, 189–193 (1986).

[74]M. K. Wu, J. R. Ashburn, C. J. Torng, P. H. Hor, R. L. Meng, L. Gao, Z. J. Huang, Y. Q. Wang, and C. W. Chu, "Superconductivity at 93 K in a New Mixed-Phase Y-Ba-Cu-O Compound System at Ambient Pressure", Phys. Rev. Lett. **58**, 908–910 (1987).

[75]P. Monthoux, D. Pines, and G. G. Lonzarich, "Superconductivity Without Phonons", Nature **450**, 1177–1183 (2007).

[76]S. . Nakajima, "Paramagnon Effect on the BCS Transition in H3", **50**, 1101–1109 (1973).

[77]W. F. Brinkman, J. W. Serene, and P. W. Anderson, "Spin-Fluctuation Stabilization of Anisotropic Superfluid States", Phys. Rev. A **10**, 2386–2394 (1974).

[78]D. Fay and J. Appel, "Coexistence of p-State Superconductivity and Itinerant Ferromagnetism", Phys. Rev. B **22**, 3173–3182 (1980).

[79]Y. Maeno, H. Hashimoto, K. Yoshida, S. Nishizaki, T. Fujita, J. G. Bednorz, and F. Lichtenberg, "Superconductivity in a Layered Perovskite without Copper", Nature **372**, 532–534 (1994).

[80]S. S. Saxena, P. Agarwal, K. Ahilan, F. M. Grosche, R. K. W. Haselwimmer, M. J. Steiner, E. Pugh, I. R. Walker, S. R. Julian, P. Monthoux, G. G. Lonzarich, A. Huxley, I. Sheikin, D. Braithwaite, and J. Flouquet, "Superconductivity on the Border of Itinerant-Electron Ferromagnetism in UGe_2", Nature **406**, 587–592 (2000).

[81]F. Steglich, J. Aarts, C. D. Bredl, W. Lieke, D. Meschede, W. Franz, and H. Schäfer, "Superconductivity in the Presence of Strong Pauli Paramagnetism: $CeCu_2Si_2$", Phys. Rev. Lett. **43**, 1892–1896 (1979).

[82]H. R. Ott, H. Rudigier, Z. Fisk, and J. L. Smith, "UBe_{13}: An Unconventional Actinide Superconductor", Phys. Rev. Lett. **50**, 1595–1598 (1983).

[83]G. R. Stewart, "Heavy-Fermion Systems", Rev. Mod. Phys. **56**, 755–787 (1984).

[84]Z. FISK, D. W. HESS, C. J. PETHICK, D. PINES, J. L. SMITH, J. D. THOMPSON, and J. O. WILLIS, "Heavy-Electron Metals: New Highly Correlated States of Matter", Science **239**, 33–42 (1988).

[85]P. Anderson, "Theory of Dirty Superconductors", Journal of Physics and Chemistry of Solids **11**, 26–30 (1959).

[86]X. Xi, H. Berger, L. Forró, J. Shan, and K. F. Mak, "Gate Tuning of Electronic Phase Transitions in Two-Dimensional $NbSe_2$", Phys. Rev. Lett. **117**, 106801 (2016).

[87]L. J. Li, E. C. T. O'Farrell, K. P. Loh, G. Eda, B. Özyilmaz, and A. H. Castro Neto, "Controlling Many-Body States by the Electric-Field Effect in a Two-Dimensional Material", Nature **529**, 185–189 (2016).

[88]E. Morosan, H. W. Zandbergen, B. S. Dennis, J. W. G. Bos, Y. Onose, T. Klimczuk, A. P. Ramirez, N. P. Ong, and R. J. Cava, "Superconductivity in Cu_xTiSe_2", Nature Physics **2**, 544–550 (2006).

[89]M. M. Ugeda, A. J. Bradley, S.-F. Shi, F. H. da Jornada, Y. Zhang, D. Y. Qiu, W. Ruan, S.-K. Mo, Z. Hussain, Z.-X. Shen, F. Wang, S. G. Louie, and M. F. Crommie, "Giant Bandgap Renormalization and Excitonic Effects in a Monolayer Transition Metal Dichalcogenide Semiconductor", Nature Materials **13**, 1091–1095 (2014).

[90]B. Shao, A. Eich, C. Sanders, A. S. Ngankeu, M. Bianchi, P. Hofmann, A. A. Khajetoorians, and T. O. Wehling, "Pseudodoping of a Metallic Two-Dimensional Material by the Supporting Substrate", Nature Communications **10**, 180 (2019).

[91]M. Dendzik, A. Bruix, M. Michiardi, A. S. Ngankeu, M. Bianchi, J. A. Miwa, B. Hammer, P. Hofmann, and C. E. Sanders, "Substrate-Induced Semiconductor-to-Metal Transition in Monolayer WS_2", Phys. Rev. B **96**, 235440 (2017).

[92]C. Zhang, M.-Y. Li, J. Tersoff, Y. Han, Y. Su, L.-J. Li, D. A. Muller, and C.-K. Shih, "Strain Distributions and their Influence on Electronic Structures of WSe_2-MoS_2 Laterally Strained Heterojunctions", Nature Nanotechnology **13**, 152–158 (2018).

[93]S. Gao, F. Flicker, R. Sankar, H. Zhao, Z. Ren, B. Rachmilowitz, S. Balachandar, F. Chou, K. S. Burch, Z. Wang, J. van Wezel, and I. Zeljkovic, "Atomic-Scale Strain Manipulation of a Charge Density Wave", Proceedings of the National Academy of Sciences **115**, 6986–6990 (2018).

[94]R.-M. Stan, S. K. Mahatha, M. Bianchi, C. E. Sanders, D. Curcio, P. Hofmann, and J. A. Miwa, "Epitaxial Single-Layer NbS_2 on Au(111): Synthesis, Structure, and Electronic Properties", Phys. Rev. Materials **3**, 044003 (2019).

[95]B. Shao, A. Eich, C. Sanders, A. S. Ngankeu, M. Bianchi, P. Hofmann, A. A. Khajetoorians, and T. O. Wehling, "Pseudodoping of a Metallic Two-Dimensional Material by the Supporting Substrate", Nature Communications **10**, 180 (2019).

[96]S. Franchi, "Chapter 1 - Molecular Beam Epitaxy: Fundamentals, Historical Background and Future Prospects", in *Molecular Beam Epitaxy*, edited by M. Henini (Elsevier, Oxford, 2013), pp. 1–46.

[97]X. Zhang, Q. Lu, W. Liu, W. Niu, J. Sun, J. Cook, M. Vaninger, P. F. Miceli, D. J. Singh, S.-W. Lian, T.-R. Chang, X. He, J. Du, L. He, R. Zhang, G. Bian, and Y. Xu, "Room-Temperature Intrinsic Ferromagnetism in Epitaxial $CrTe_2$ Ultrathin Films", Nature Communications **12**, 2492 (2021).

[98]W. Chen, Z. Sun, Z. Wang, L. Gu, X. Xu, S. Wu, and C. Gao, "Direct Observation of Van der Waals Stacking–dependent interlayer magnetism", Science **366**, 983–987 (2019).

[99]C. Gong and X. Zhang, "Two-dimensional Magnetic Crystals and Emergent Heterostructure Devices", Science **363**, `10.1126/science.aav4450` (2019).

[100]J.-P. Peng, J.-Q. Guan, H.-M. Zhang, C.-L. Song, L. Wang, K. He, Q.-K. Xue, and X.-C. Ma, "Molecular Beam Epitaxy Growth and Scanning Tunneling Microscopy Study of $TiSe_2$ Ultrathin Films", Phys. Rev. B **91**, 121113 (2015).

[101]B. Hunt, J. D. Sanchez-Yamagishi, A. F. Young, M. Yankowitz, B. J. LeRoy, K. Watanabe, T. Taniguchi, P. Moon, M. Koshino, P. Jarillo-Herrero, and R. C. Ashoori, "Massive Dirac Fermions and Hofstadter Butterfly in a Van der Waals Heterostructure", Science **340**, 1427–1430 (2013).

[102]B. Li et al., "Van der Waals Epitaxial Growth of Air-Stable $CrSe_2$ Nanosheets with Thickness-Tunable Magnetic Order", Nature Materials **20**, 818–825 (2021).

[103]K. Lasek, J. Li, S. Kolekar, P. M. Coelho, L. Guo, M. Zhang, Z. Wang, and M. Batzill, "Synthesis and Characterization of 2D Transition Metal Dichalcogenides: Recent Progress from a Vacuum Surface Science Perspective", Surface Science Reports **76**, 100523 (2021).

[104]S. Tiefenbacher, C. Pettenkofer, and W. Jaegermann, "Moiré Pattern in LEED Obtained by Van der Waals Epitaxy of Lattice Mismatched $WS_2/MoTe_2$ (0001) Heterointerfaces", Surface Science **450**, 181–190 (2000).

[105]C. Zhang, Y. Chen, J.-K. Huang, X. Wu, L.-J. Li, W. Yao, J. Tersoff, and C.-K. Shih, "Visualizing Band Offsets and Edge States in Bilayer-Monolayer Transition Metal Dichalcogenides Lateral Heterojunction", Nature Communications **7**, 10349 (2016).

[106]Y. Nakata, K. Sugawara, R. Shimizu, Y. Okada, P. Han, T. Hitosugi, K. Ueno, T. Sato, and T. Takahashi, "Monolayer 1T-$NbSe_2$ as a Mott insulator", NPG Asia Materials **8**, e321–e321 (2016).

[107]S. Hasegawa, "Reflection High-Energy Electron Diffraction", in *Characterization of Materials* (John Wiley & Sons, Ltd, 2012), pp. 1–14.

[108]G. Binnig and H. Rohrer, "Scanning Tunneling Microscopy", Surface Science **126**, 236–244 (1983).

[109]B. Voigtlaender, *Scanning Probe Microscopy* (Springer-Verlag Berlin Heidelberg, 2015).

[110]J. Bardeen, "Tunnelling from a Many-Particle Point of View", Phys. Rev. Lett. **6**, 57–59 (1961).

[111]S. H. Pan, E. W. Hudson, and J. C. Davis, "3He Refrigerator Based Very Low Temperature Scanning Tunneling Microscope", Review of Scientific Instruments **70**, 1459–1463 (1999).

[112]E. Sohn, X. Xi, W.-Y. He, S. Jiang, Z. Wang, K. Kang, J.-H. Park, H. Berger, L. Forro, K. T. Law, J. Shan, and K. F. Mak, "An Unusual Continuous Paramagnetic-Limited Superconducting Phase Transition in 2D $NbSe_2$", Nature Materials **17**, 504–508 (2018).

[113]C. Rubio-Verdú, A. M. García-García, H. Ryu, D.-J. Choi, J. Zaldívar, S. Tang, B. Fan, Z.-X. Shen, S.-K. Mo, J. I. Pascual, and M. M. Ugeda, "Visualization of Multifractal Superconductivity in a Two-Dimensional Transition Metal Dichalcogenide in the Weak-Disorder Regime", Nano Letters **20**, 5111–5118 (2020).

[114]M. S. El-Bana, D. Wolverson, S. Russo, G. Balakrishnan, D. M. Paul, and S. J. Bending, "Superconductivity in Two-Dimensional $NbSe_2$ Field Effect Transistors", Superconductor Science and Technology **26**, 125020 (2013).

[115]J. N. Coleman et al., "Two-Dimensional Nanosheets Produced by Liquid Exfoliation of Layered Materials", Science **331**, 568–571 (2011).

[116]M. Calandra, I. I. Mazin, and F. Mauri, "Effect of Dimensionality on the Charge-Density Wave in Few-Layer 2H-$NbSe_2$", Phys. Rev. B **80**, 241108 (2009).

[117]J. Á. Silva-Guillén, P. Ordejón, F. Guinea, and E. Canadell, "Electronic Structure of 2H-$NbSe_2$ Single-Layers in the CDW State", 2D Materials **3**, 035028 (2016).

[118]Y. Cao et al., "Quality Heterostructures from Two-Dimensional Crystals Unstable in Air by Their Assembly in Inert Atmosphere", Nano Letters **15**, 4914–4921 (2015).

[119]D. Wickramaratne, S. Khmelevskyi, D. F. Agterberg, and I. I. Mazin, "Ising Superconductivity and Magnetism in $NbSe_2$", Phys. Rev. X **10**, 041003 (2020).

[120]A. Hamill, B. Heischmidt, E. Sohn, D. Shaffer, K.-T. Tsai, X. Zhang, X. Xi, A. Suslov, H. Berger, F. J. Burnell, J. Shan, K. F. Mak, R. M. Fernandes, K. Wang, and V. S. Pribiag, "Two-Fold Symmetric Superconductivity in Few-Layer $NbSe_2$", Nature Physics **17**, 949–954 (2021).

[121]C.-W. Cho, J. Lyu, T. Han, C. Y. Ng, Y. Gao, G. Li, M. Huang, N. Wang, J. Schmalian, and R. Lortz, "Distinct Nodal and Nematic Superconducting Phases in the 2D Ising Superconductor $NbSe_2$", arXiv (2020).

[122]M. Kuzmanović, T. Dvir, D. LeBoeuf, S. Ilić, D. Möckli, M. Haim, S. Kraemer, M. Khodas, M. Houzet, J. S. Meyer, M. Aprili, H. Steinberg, and C. H. L. Quay, "Tunneling Spectroscopy of Few-Monolayer $NbSe_2$ in High Magnetic Field: Ising Protection and Triplet Superconductivity", arXiv (2021).

[123]Q. Wang, W. Zhang, L. Wang, K. He, X. Ma, and Q. Xue, "Large-Scale Uniform Bilayer Graphene Prepared by Vacuum Graphitization of 6H-SiC(0001) Substrates", Journal of Physics: Condensed Matter **25**, 095002 (2013).

[124]A. B. Migdal, "INTERACTION BETWEEN ELECTRONS AND THE LATTICE VIBRATIONS IN A NORMAL METAL", Zhur. Eksptl'. i Teoret. Fiz. **34** (1958).

[125]G. M. Eliashberg, "Interactions Between Electrons and Lattice Vibrations in a Superconductor", Sov. Phys. - JETP (Engl. Transl.); (United States) **11:3** (1960).

[126]H. F. Fong, P. Bourges, Y. Sidis, L. P. Regnault, A. Ivanov, G. D. Gu, N. Koshizuka, and B. Keimer, "Neutron Scattering From Magnetic Excitations in $Bi_2Sr_2CaCu_2O8+\delta$", Nature **398**, 588–591 (1999).

[127]H. He, P. Bourges, Y. Sidis, C. Ulrich, L. P. Regnault, S. Pailhès, N. S. Berzigiarova, N. N. Kolesnikov, and B. Keimer, "Magnetic Resonant Mode in the Single-Layer High-Temperature Superconductor $Tl_2Ba_2CuO_{6+\delta}$", Science **295**, 1045–1047 (2002).

[128]S. Pailhès, Y. Sidis, P. Bourges, C. Ulrich, V. Hinkov, L. P. Regnault, A. Ivanov, B. Liang, C. T. Lin, C. Bernhard, and B. Keimer, "Two Resonant Magnetic Modes in an Overdoped High T_c Superconductor", Phys. Rev. Lett. **91**, 237002 (2003).

[129]S. Pailhès, C. Ulrich, B. Fauqué, V. Hinkov, Y. Sidis, A. Ivanov, C. T. Lin, B. Keimer, and P. Bourges, "Doping Dependence of Bilayer Resonant Spin Excitations in $(Y, Ca)Ba_2Cu_3O_{6+x}$", Phys. Rev. Lett. **96**, 257001 (2006).

[130]A. D. Christianson, E. A. Goremychkin, R. Osborn, S. Rosenkranz, M. D. Lumsden, C. D. Malliakas, I. S. Todorov, H. Claus, D. Y. Chung, M. G. Kanatzidis, R. I. Bewley, and T. Guidi, "Unconventional Superconductivity in $Ba_{0.6}K_{0.4}Fe_2As_2$ from Inelastic Neutron Scattering", Nature **456**, 930–932 (2008).

[131]L. Shan, J. Gong, Y.-L. Wang, B. Shen, X. Hou, C. Ren, C. Li, H. Yang, H.-H. Wen, S. Li, and P. Dai, "Evidence of a Spin Resonance Mode in the Iron-Based Superconductor $Ba_{0.6}\mathbf{K}_{0.4}Fe_2As_2$ from Scanning Tunneling Spectroscopy", Phys. Rev. Lett. **108**, 227002 (2012).

[132]M. Liu, L. W. Harriger, H. Luo, M. Wang, R. A. Ewings, T. Guidi, H. Park, K. Haule, G. Kotliar, S. M. Hayden, and P. Dai, "Nature of Magnetic Excitations in Superconducting $BaFe_{1.9}Ni_{0.1}As_2$", Nature Physics **8**, 376–381 (2012).

[133]C.-L. Song, Y.-L. Wang, Y.-P. Jiang, Z. Li, L. Wang, K. He, X. Chen, J. E. Hoffman, X.-C. Ma, and Q.-K. Xue, "Imaging the Electron-Boson Coupling in Superconducting FeSe Films Using a Scanning Tunneling Microscope", Phys. Rev. Lett. **112**, 057002 (2014).

[134]C. Liu, Z. Wang, S. Ye, C. Chen, Y. Liu, Q. Wang, Q.-H. Wang, and J. Wang, "Detection of Bosonic Mode as a Signature of Magnetic Excitation in One-Unit-Cell FeSe on $SrTiO_3$", Nano Letters **19**, 3464–3472 (2019).

[135]N. K. Sato, N. Aso, K. Miyake, R. Shiina, P. Thalmeier, G. Varelogiannis, C. Geibel, F. Steglich, P. Fulde, and T. Komatsubara, "Strong Coupling Between Local Moments and Superconducting 'Heavy' Electrons in UPd_2Al_3", Nature **410**, 340–343 (2001).

[136]C. Stock, C. Broholm, J. Hudis, H. J. Kang, and C. Petrovic, "Spin Resonance in the *d*-Wave Superconductor $CeCoIn_5$", Phys. Rev. Lett. **100**, 087001 (2008).

[137]Y. Cao, V. Fatemi, S. Fang, K. Watanabe, T. Taniguchi, E. Kaxiras, and P. Jarillo-Herrero, "Unconventional Superconductivity in Magic-Angle Graphene Superlattices", Nature **556**, 43–50 (2018).

[138]M. Bonilla, S. Kolekar, Y. Ma, H. C. Diaz, V. Kalappattil, R. Das, T. Eggers, H. R. Gutierrez, M.-H. Phan, and M. Batzill, "Strong Room-Temperature Ferromagnetism in VSe_2 Monolayers on Van der Waals Substrates", Nature Nanotechnology **13**, 289–293 (2018).

[139]S. Divilov, W. Wan, P. Dreher, E. Bölen, D. Sánchez-Portal, M. M. Ugeda, and F. Ynduráin, "Magnetic Correlations in Single-Layer $NbSe_2$", Journal of Physics: Condensed Matter **33**, 295804 (2021).

[140]Y. Cao et al., "Quality Heterostructures from Two-Dimensional Crystals Unstable in Air by Their Assembly in Inert Atmosphere", Nano Letters **15**, 4914–4921 (2015).

[141]L. P. Gor'kov and E. I. Rashba, "Superconducting 2D System with Lifted Spin Degeneracy: Mixed Singlet-Triplet State", Phys. Rev. Lett. **87**, 037004 (2001).

[142]H. Hess, R. Robinson, and J. Waszczak, "STM Spectroscopy of Vortex Cores and the Flux Lattice", Physica B: Condensed Matter **169**, 422–431 (1991).

[143]I. Guillamon, H. Suderow, F. Guinea, and S. Vieira, "Intrinsic Atomic-Scale Modulations of the Superconducting Gap of $2H-NbSe_2$", Phys. Rev. B **77**, 134505 (2008).

[144]M. J. Verstraete, M. Torrent, F. ç. Jollet, G. Zérah, and X. Gonze, "Density Functional Perturbation Theory with Spin-Orbit Coupling: Phonon Band Structure of Lead", Phys. Rev. B **78**, 045119 (2008).

[145]F. Zheng and J. Feng, "Electron-Phonon Coupling and the Coexistence of Superconductivity and Charge-Density Wave in Monolayer $NbSe_2$", Phys. Rev. B **99**, 161119 (2019).

[146]X. Xi, L. Zhao, Z. Wang, H. Berger, L. Forro, J. Shan, and K. F. Mak, "Strongly Enhanced Charge-Density-Wave Order in Monolayer $NbSe_2$", Nature Nanotechnology **10**, 765–769 (2015).

[147]M. Eschrig, "The Effect of Collective Spin-1 Excitations on Electronic Spectra in High-Tc Superconductors", Advances in Physics **55**, 47–183 (2006).

[148]D. J. Scalapino, "A Common Thread: The Pairing Interaction for Unconventional Superconductors", Rev. Mod. Phys. **84**, 1383–1417 (2012).

[149]V. K. Thorsmølle, M. Khodas, Z. P. Yin, C. Zhang, S. V. Carr, P. Dai, and G. Blumberg, "Critical Quadrupole Fluctuations and Collective Modes in Iron Pnictide Superconductors", Phys. Rev. B **93**, 054515 (2016).

[150]A. J. Leggett, "Number-Phase Fluctuations in Two-Band Superconductors", Progress of Theoretical Physics **36**, 901–930 (1966).

[151]A. Bardasis and J. R. Schrieffer, "Excitons and Plasmons in Superconductors", Phys. Rev. **121**, 1050–1062 (1961).

[152]F. Kretzschmar, B. Muschler, T. Böhm, A. Baum, R. Hackl, H.-H. Wen, V. Tsurkan, J. Deisenhofer, and A. Loidl, "Raman-Scattering Detection of Nearly Degenerate s-Wave and d-Wave Pairing Channels in Iron-Based $Ba_{0.6}K_{0.4}Fe_2As_2$ and $Rb_{0.8}Fe_{1.6}Se_2$ Superconductors", Phys. Rev. Lett. **110**, 187002 (2013).

[153]P. Dai, H. A. Mook, G. Aeppli, S. M. Hayden, and F. Doğan, "Resonance as a Measure of Pairing Correlations in the High-Tc Superconductor $YBa_2Cu_3O_{6.6}$", Nature **406**, 965–968 (2000).

[154]T. Chen, Y. Chen, D. W. Tam, B. Gao, Y. Qiu, A. Schneidewind, I. Radelytskyi, K. Prokes, S. Chi, M. Matsuda, C. Broholm, and P. Dai, "Anisotropic Effect of a Magnetic Field on the Neutron Spin Resonance in FeSe", Phys. Rev. B **101**, 140504 (2020).

[155]G. Blumberg, A. Mialitsin, B. S. Dennis, M. V. Klein, N. D. Zhigadlo, and J. Karpinski, "Observation of Leggett's Collective Mode in a Multiband MgB_2 Superconductor", Phys. Rev. Lett. **99**, 227002 (2007).

[156]S. Chi, S. Grothe, R. Liang, P. Dosanjh, W. N. Hardy, S. A. Burke, D. A. Bonn, and Y. Pennec, "Scanning Tunneling Spectroscopy of Superconducting LiFeAs Single Crystals: Evidence for Two Nodeless Energy Gaps and Coupling to a Bosonic Mode", Phys. Rev. Lett. **109**, 087002 (2012).

[157]Z. Wang, H. Yang, D. Fang, B. Shen, Q.-H. Wang, L. Shan, C. Zhang, P. Dai, and H.-H. Wen, "Close Relationship between Superconductivity and the Bosonic Mode in $Ba_{0.6}K_{0.4}Fe_2As_2$ and $Na(Fe_{0.975}Co_{0.025})As$", Nature Physics **9**, 42–48 (2013).

[158]C. Chen, C. Liu, Y. Liu, and J. Wang, "Bosonic Mode and Impurity-Scattering in Monolayer Fe(Te,Se) High-Temperature Superconductors", Nano Letters **20**, 2056–2061 (2020).

[159]P. B. Littlewood and C. M. Varma, "Gauge-Invariant Theory of the Dynamical Interaction of Charge Density Waves and Superconductivity", Phys. Rev. Lett. **47**, 811–814 (1981).

[160]M.-A. Méasson, Y. Gallais, M. Cazayous, B. Clair, P. Rodière, L. Cario, and A. Sacuto, "Amplitude Higgs mode in the $2H - NbSe_2$ superconductor", Phys. Rev. B **89**, 060503 (2014).

[161]D. Shaffer, J. Kang, F. J. Burnell, and R. M. Fernandes, "Crystalline Nodal Topological Superconductivity and Bogolyubov Fermi Surfaces in Monolayer $NbSe_2$", Phys. Rev. B **101**, 224503 (2020).

[162]N. Bittner, D. Einzel, L. Klam, and D. Manske, "Leggett Modes and the Anderson-Higgs Mechanism in Superconductors without Inversion Symmetry", Phys. Rev. Lett. **115**, 227002 (2015).

[163]V. Eremenko, V. Sirenko, V. Ibulaev, J. Bartolomé, A. Arauzo, and G. Rényi, "Heat Capacity, Thermal Expansion and Pressure Derivative of Critical Temperature at the Superconducting and Charge Density Wave (CDW) Transitions in $NbSe_2$", Physica C: Superconductivity **469**, 259–264 (2009).

[164]A. Abanov, A. V. Chubukov, and J. Schmalian, "Fingerprints of Spin Mediated Pairing in Cuprates", Journal of Electron Spectroscopy and Related Phenomena **117-118**, 129–151 (2001).

[165]A. V. Balatsky and J.-X. Zhu, "Local Strong-Coupling Pairing in *d*-Wave Superconductors with Inhomogeneous Bosonic Modes", Phys. Rev. B **74**, 094517 (2006).

[166]G. Yu, Y. Li, E. M. Motoyama, and M. Greven, "A Universal Relationship Between Magnetic Resonance and Superconducting Gap in Unconventional Superconductors", Nature Physics **5**, 873–875 (2009).

[167]M. Dendzik, A. Bruix, M. Michiardi, A. S. Ngankeu, M. Bianchi, J. A. Miwa, B. Hammer, P. Hofmann, and C. E. Sanders, "Substrate-Induced Semiconductor-to-Metal Transition in Monolayer WS_2", Phys. Rev. B **96**, 235440 (2017).

[168]C. Zhang, M.-Y. Li, J. Tersoff, Y. Han, Y. Su, L.-J. Li, D. A. Muller, and C.-K. Shih, "Strain Distributions and their Influence on Electronic Structures of WSe_2-MoS_2 Laterally Strained Heterojunctions", Nature Nanotechnology **13**, 152–158 (2018).

[169]S. Gao, F. Flicker, R. Sankar, H. Zhao, Z. Ren, B. Rachmilowitz, S. Balachandar, F. Chou, K. S. Burch, Z. Wang, J. van Wezel, and I. Zeljkovic, "Atomic-Scale Strain Manipulation of a Charge Density Wave", Proceedings of the National Academy of Sciences **115**, 6986–6990 (2018).

[170]C. E. Sanders, M. Dendzik, A. S. Ngankeu, A. Eich, A. Bruix, M. Bianchi, J. A. Miwa, B. Hammer, A. A. Khajetoorians, and P. Hofmann, "Crystalline and Electronic Structure of Single-Layer TaS_2", Phys. Rev. B **94**, 081404 (2016).

[171]F. Cheng, Z. Ding, H. Xu, S. J. R. Tan, I. Abdelwahab, J. Su, P. Zhou, J. Martin, and K. P. Loh, "Epitaxial Growth of Single-Layer Niobium Selenides with Controlled Stoichiometric Phases", Advanced Materials Interfaces **5**, 1800429 (2018).

[172]H. M. Lefcochilos-Fogelquist, O. R. Albertini, and A. Y. Liu, "Substrate-Induced Suppression of Charge Density Wave Phase in Monolayer $1H-TaS_2$ on Au(111)", Phys. Rev. B **99**, 174113 (2019).

[173]S. S. Grønborg, S. Ulstrup, M. Bianchi, M. Dendzik, C. E. Sanders, J. V. Lauritsen, P. Hofmann, and J. A. Miwa, "Synthesis of Epitaxial Single-Layer MoS_2 on Au(111)", Langmuir **31**, 9700–9706 (2015).

[174]J. Feng et al., "Electronic Structure and Enhanced Charge-Density Wave Order of Monolayer VSe_2", Nano Letters **18**, 4493–4499 (2018).

[175]H. Lin, W. Huang, K. Zhao, C. Lian, W. Duan, X. Chen, and S.-H. Ji, "Growth of Atomically Thick Transition Metal Sulfide Films on Graphene/6H-SiC(0001) by Molecular Beam Epitaxy", Nano Research **11**, 4722–4727 (2018).

[176]J. Hall, N. Ehlen, J. Berges, E. van Loon, C. van Efferen, C. Murray, M. Rösner, J. Li, B. V. Senkovskiy, M. Hell, M. Rolf, T. Heider, and Asensio, M. C.; Avila, J.; Plucinski, L.; Wehling, T.; Grüneis, A.; Michely, T., "Environmental Control of Charge Density Wave Order in Monolayer 2H-TaS_2", ACS Nano **13**, 10210–10220 (2019).

[177]X. Blase, A. Rubio, S. G. Louie, and M. L. Cohen, "Quasiparticle Band Structure of Bulk Hexagonal Boron Nitride and Related Systems", Phys. Rev. B **51**, 6868–6875 (1995).

[178]I. Brihuega, C. H. Michaelis, J. Zhang, S. Bose, V. Sessi, J. Honolka, M. Alexander Schneider, A. Enders, and K. Kern, "Electronic Decoupling and Templating of Co Nanocluster Arrays on the Boron Nitride Nanomesh", Surface Science **602**, L95–L99 (2008).

[179]S. Bose, A. M. García-García, M. M. Ugeda, J. D. Urbina, C. H. Michaelis, I. Brihuega, and K. Kern, "Observation of Shell Effects in Superconducting Nanoparticles of Sn", Nature Materials **9**, 550–554 (2010).

[180]W. Auwärter, "Hexagonal Boron Nitride Monolayers on Metal Supports: Versatile Templates for Atoms, Molecules and Nanostructures", Surface Science Reports **74**, 1–95 (2019).

[181]F. Schulz, R. Drost, S. K. Hämäläinen, T. Demonchaux, A. P. Seitsonen, and P. Liljeroth, "Epitaxial Hexagonal Boron Nitride on Ir(111): A Work Function Template", Phys. Rev. B **89**, 235429 (2014).

[182]P. Chen, Y.-H. Chan, X.-Y. Fang, Y. Zhang, M. Y. Chou, S.-K. Mo, Z. Hussain, A.-V. Fedorov, and T.-C. Chiang, "Charge Density Wave Transition in Single-Layer Titanium Diselenide", Nature Communications **6**, 8943 (2015).

[183]J. A. Miwa, S. Ulstrup, S. G. Sørensen, M. Dendzik, A. G. ć. Čabo, M. Bianchi, J. V. Lauritsen, and P. Hofmann, "Electronic Structure of Epitaxial Single-Layer MoS_2", Phys. Rev. Lett. **114**, 046802 (2015).

[184]P. G. DE Gennes, "Boundary Effects in Superconductors", Rev. Mod. Phys. **36**, 225–237 (1964).

[185]F. Herman and R. Hlubina, "Microscopic Interpretation of the Dynes Formula for the Tunneling Density of States", Phys. Rev. B **94**, 144508 (2016).

[186]J. A. Galvis, P. Rodière, I. Guillamon, M. R. Osorio, J. G. Rodrigo, L. Cario, E. Navarro-Moratalla, E. Coronado, S. Vieira, and H. Suderow, "Scanning Tunneling Measurements of Layers of Superconducting 2H-$TaSe_2$: Evidence for a Zero-Bias Anomaly in Single Layers", Phys. Rev. B **87**, 094502 (2013).

[187]D. O. Dumcenco, H. Kobayashi, Z. Liu, Y.-S. Huang, and K. Suenaga, "Visualization and Quantification of Transition Metal Atomic Mixing in $Mo_{1-x}W_xS_2$ Single Layers", Nature Communications **4**, 1351 (2013).

[188]Y. Chen, J. Xi, D. O. Dumcenco, Z. Liu, K. Suenaga, D. Wang, Z. Shuai, Y.-S. Huang, and L. Xie, "Tunable Band Gap Photoluminescence from Atomically Thin Transition-Metal Dichalcogenide Alloys", ACS Nano **7**, 4610–4616 (2013).

[189]J. Gao, Y. D. Kim, L. Liang, J. C. Idrobo, P. Chow, J. Tan, B. Li, L. Li, B. G. Sumpter, T.-M. Lu, V. Meunier, J. Hone, and N. Koratkar, "Transition-Metal Substitution Doping in Synthetic Atomically Thin Semiconductors", Advanced Materials **28**, 9735–9743 (2016).

[190]H. Gao, J. Suh, M. C. Cao, A. Y. Joe, F. Mujid, K.-H. Lee, S. Xie, P. Poddar, J.-U. Lee, K. Kang, P. Kim, D. A. Muller, and J. Park, "Tuning Electrical Conductance of MoS_2 Monolayers through Substitutional Doping", Nano Letters **20**, 4095–4101 (2020).

[191]S. Li, J. Hong, B. Gao, Y.-C. Lin, H. E. Lim, X. Lu, J. Wu, S. Liu, Y. Tateyama, Y. Sakuma, K. Tsukagoshi, K. Suenaga, and T. Taniguchi, "Tunable Doping of Rhenium and Vanadium into Transition Metal Dichalcogenides for Two-Dimensional Electronics", Advanced Science **8**, 2004438 (2021).

[192]X. Tang, G. Murali, H. Lee, S. Park, S. Lee, S. M. Oh, J. Lee, T. Y. Ko, C. M. Koo, Y. J. Jeong, T. K. An, I. In, and S. H. Kim, "Aggregation-Resistant MXene Nanosheets: Engineering Aggregation-Resistant MXene Nanosheets As Highly Conductive and Stable Inks for All-Printed Electronics", Advanced Functional Materials **31**, 2170206 (2021).

[193]V. T. Vu, T. T. H. Vu, T. L. Phan, W. T. Kang, Y. R. Kim, M. D. Tran, H. T. T. Nguyen, Y. H. Lee, and W. J. Yu, "One-Step Synthesis of $NbSe_2$/Nb-Doped-WSe_2 Metal/Doped-Semiconductor Van der Waals Heterostructures for Doping Controlled Ohmic Contact", ACS Nano **15**, 13031–13040 (2021).

[194]J. Mann, Q. Ma, P. M. Odenthal, M. Isarraraz, D. Le, E. Preciado, D. Barroso, K. Yamaguchi, G. von Son Palacio, A. Nguyen, T. Tran, M. Wurch, A. Nguyen, V. Klee, S. Bobek, D. Sun, T. F. Heinz, T. S. Rahman, R. Kawakami, and L. Bartels, "2-Dimensional Transition Metal Dichalcogenides with Tunable Direct Band Gaps: $MoS_{2(1-x)}Se_{2x}$ Monolayers", Advanced Materials **26**, 1399–1404 (2014).

[195]M. Zhang, J. Wu, Y. Zhu, D. O. Dumcenco, J. Hong, N. Mao, S. Deng, Y. Chen, Y. Yang, C. Jin, S. H. Chaki, Y.-S. Huang, J. Zhang, and L. Xie, "Two-Dimensional Molybdenum Tungsten Diselenide Alloys: Photoluminescence, Raman Scattering, and Electrical Transport", ACS Nano **8**, 7130–7137 (2014).

[196]A. Azizi, Y. Wang, Z. Lin, K. Wang, A. L. Elias, M. Terrones, V. H. Crespi, and N. Alem, "Spontaneous Formation of Atomically Thin Stripes in Transition Metal Dichalcogenide Monolayers", Nano Letters **16**, 6982–6987 (2016).

[197]V. Kochat, A. Apte, J. A. Hachtel, H. Kumazoe, A. Krishnamoorthy, S. Susarla, J. C. Idrobo, F. Shimojo, P. Vashishta, R. Kalia, A. Nakano, C. S. Tiwary, and P. M. Ajayan, "Re Doping in 2D Transition Metal Dichalcogenides as a New Route to Tailor Structural Phases and Induced Magnetism", Advanced Materials **29**, 1703754 (2017).

[198]X. Duan, C. Wang, Z. Fan, G. Hao, L. Kou, U. Halim, H. Li, X. Wu, Y. Wang, J. Jiang, et al., "Synthesis of $WS_{2x}Se_{2-2x}$ Alloy Nanosheets with Composition-Tunable Electronic Properties", Nano letters **16**, 264–269 (2016).

[199]Y. Zhao, K. Xu, F. Pan, C. Zhou, F. Zhou, and Y. Chai, "Doping, Contact and Interface Engineering of Two-Dimensional Layered Transition Metal Dichalcogenides Transistors", Advanced Functional Materials **27**, 1603484 (2017).

[200]Y. Gong, Z. Liu, A. R. Lupini, G. Shi, J. Lin, S. Najmaei, Z. Lin, A. L. ElÃfÂas, A. Berkdemir, G. You, H. Terrones, M. Terrones, R. Vajtai, S. T. Pantelides, S. J. Pennycook, J. Lou, W. Zhou, and P. M. Ajayan, "Band Gap Engineering and Layer-by-Layer Mapping of Selenium-Doped Molybdenum Disulfide", Nano Letters **14**, 442–449 (2014).

[201]V. Klee, E. Preciado, D. Barroso, A. E. Nguyen, C. Lee, K. J. Erickson, M. Triplett, B. Davis, I.-H. Lu, S. Bobek, J. McKinley, J. P. Martinez, J. Mann, A. A. Talin, L. Bartels, and F. Laonard, "Superlinear Composition-Dependent Photocurrent in CVD-Grown Monolayer $MoS_{2(1-x)}Se_{2x}$ Alloy Devices", Nano Letters **15**, 2612–2619 (2015).

[202]J. Suh, T.-E. Park, D.-Y. Lin, D. Fu, J. Park, H. J. Jung, Y. Chen, C. Ko, C. Jang, Y. Sun, R. Sinclair, J. Chang, S. Tongay, and J. Wu, "Doping Against the Native Propensity of MoS_2: Degenerate Hole Doping by Cation Substitution", Nano Letters **14**, 6976–6982 (2014).

[203]T. Zhang, K. Fujisawa, F. Zhang, M. Liu, M. C. Lucking, R. N. Gontijo, Y. Lei, H. Liu, K. Crust, T. Granzier-Nakajima, H. Terrones, A. L. ElÃfÂas, and M. Terrones, "Universal In Situ Substitutional Doping of Transition Metal Dichalcogenides by Liquid-Phase Precursor-Assisted Synthesis", ACS Nano **14**, 4326–4335 (2020).

[204]P. Mallet, F. Chiapello, H. Okuno, H. Boukari, M. Jamet, and J.-Y. Veuillen, "Bound Hole States Associated to Individual Vanadium Atoms Incorporated into Monolayer WSe_2", Phys. Rev. Lett. **125**, 036802 (2020).

[205]Z. Qin, L. Loh, J. Wang, X. Xu, Q. Zhang, B. Haas, C. Alvarez, H. Okuno, J. Z. Yong, T. Schultz, N. Koch, J. Dan, S. J. Pennycook, D. Zeng, M. Bosman, and G. Eda, "Growth of Nb-Doped Monolayer WS_2 by Liquid-Phase Precursor Mixing", ACS Nano **13**, 10768–10775 (2019).

[206]I. S. Kwon, I. H. Kwak, J. Y. Kim, T. T. Debela, Y. C. Park, J. Park, and H. S. Kang, "Concurrent Vacancy and Adatom Defects of $Mo_{1-x}Nb_xSe_2$ Alloy Nanosheets Enhance Electrochemical Performance of Hydrogen Evolution Reaction", ACS Nano **15**, 5467–5477 (2021).

[207]S. J. Yun, D. L. Duong, D. M. Ha, K. Singh, T. L. Phan, W. Choi, Y.-M. Kim, and Y. H. Lee, "Ferromagnetic Order at Room Temperature in Monolayer WSe_2 Semiconductor via Vanadium Dopant", Advanced Science **7**, 1903076 (2020).

[208]F. Zhang et al., "Monolayer Vanadium-Doped Tungsten Disulfide: A Room-Temperature Dilute Magnetic Semiconductor", Advanced Science **7**, 2001174 (2020).

[209]Z. Hemmat, J. Cavin, A. Ahmadiparidari, A. Ruckel, S. Rastegar, S. N. Misal, L. Majidi, K. Kumar, S. Wang, J. Guo, R. Dawood, F. Lagunas, P. Parajuli, A. T. Ngo, L. A. Curtiss, S. B. Cho, J. Cabana, R. F. Klie, R. Mishra, and A. Salehi-Khojin, "Quasi-Binary Transition Metal Dichalcogenide Alloys: Thermodynamic Stability Prediction, Scalable Synthesis, and Application", Advanced Materials **32**, 1907041 (2020).

[210]P. Yu, J. Lin, L. Sun, Q. L. Le, X. Yu, G. Gao, C.-H. Hsu, D. Wu, T.-R. Chang, Q. Zeng, F. Liu, Q. J. Wang, H.-T. Jeng, H. Lin, A. Trampert, Z. Shen, K. Suenaga, and Z. Liu, "Metal Semiconductor Phase-Transition in $WSe_{2(1-x)}Te_{2x}$ Monolayer", Advanced Materials **29**, 1603991 (2017).

[211]P. Li, J. Cui, J. Zhou, D. Guo, Z. Zhao, J. Yi, J. Fan, Z. Ji, X. Jing, F. Qu, C. Yang, L. Lu, J. Lin, Z. Liu, and G. Liu, "Phase Transition and Superconductivity Enhancement in Se-Substituted $MoTe_2$ Thin Films", Advanced Materials **31**, 1904641 (2019).

[212]L. Zhang, T. Yang, X. He, W. Zhang, G. Vinai, C. S. Tang, X. Yin, P. Torelli, Y. P. Feng, P. K. J. Wong, and A. T. S. Wee, "Molecular Beam Epitaxy of Two-Dimensional Vanadium-Molybdenum Diselenide Alloys", ACS Nano **14**, 11140–11149 (2020).

[213]S. Wang, J. Cavin, Z. Hemmat, K. Kumar, A. Ruckel, L. Majidi, H. Gholivand, R. Dawood, J. Cabana, N. Guisinger, R. F. Klie, F. Khalili-Araghi, R. Mishra, and A. Salehi-Khojin, "Phase-Dependent Band Gap Engineering in Alloys of Metal-Semiconductor Transition Metal Dichalcogenides", Advanced Functional Materials **30**, 2004912 (2020).

[214]G. M. Pang, M. Smidman, W. B. Jiang, J. K. Bao, Z. F. Weng, Y. F. Wang, L. Jiao, J. L. Zhang, G. H. Cao, and H. Q. Yuan, "Evidence for Nodal Superconductivity in Quasi-One-Dimensional $K_2Cr_3As_3$", Phys. Rev. B **91**, 220502 (2015).

[215]J. Feng et al., "Electronic Structure and Enhanced Charge-Density Wave Order of Monolayer VSe_2", Nano Letters **18**, 4493–4499 (2018).

[216]A. O. Fumega, M. Gobbi, P. Dreher, W. Wan, C. González-Orellana, M. Peña-Díaz, C. Rogero, J. Herrero-Martín, P. Gargiani, M. Ilyn, M. M. Ugeda, V. Pardo, and S. Blanco-Canosa, "Absence of Ferromagnetism in VSe_2 Caused by Its Charge Density Wave Phase", The Journal of Physical Chemistry C **123**, 27802–27810 (2019).

[217]Z. Fei, T. Palomaki, S. Wu, W. Zhao, X. Cai, B. Sun, P. Nguyen, J. Finney, X. Xu, and D. H. Cobden, "Edge Conduction in Monolayer WTe_2", Nature Physics **13**, 677–682 (2017).

[218]P. Dreher, W. Wan, A. Chikina, M. Bianchi, H. Guo, R. Harsh, S. Mañas-Valero, E. Coronado, A. J. Martinez-Galera, P. Hofmann, J. A. Miwa, and M. M. Ugeda, "Proximity Effects on the Charge Density Wave Order and Superconductivity in Single-Layer NbSe2", ACS Nano **15**, 19430–19438 (2021).

[219]S. Barja, S. Wickenburg, Z.-F. Liu, Y. Zhang, H. Ryu, M. M. Ugeda, Z. Hussain, Z.-X. Shen, S.-K. Mo, E. Wong, M. B. Salmeron, F. Wang, M. F. Crommie, D. F. Ogletree, J. B. Neaton, and A. Weber-Bargioni, "Charge Density Wave Order in 1D Mirror Twin Boundaries of Single-Layer $MoSe_2$", Nature Physics **12**, 751–756 (2016).

[220]A. Azizi, M. Dogan, J. D. Cain, R. Eskandari, X. Yu, E. C. Glazer, M. L. Cohen, and A. Zettl, "Frustration and Atomic Ordering in a Monolayer Semiconductor Alloy", Phys. Rev. Lett. **124**, 096101 (2020).

[221]S. M. Loh, X. Xia, N. R. Wilson, and N. D. M. Hine, "Strong In-Plane Anisotropy in the Electronic Properties of Doped Transition Metal Dichalcogenides Exhibited in $W_{1-x}Nb_xS_2$", Phys. Rev. B **103**, 245410 (2021).

[222]A. P. Mackenzie, R. K. W. Haselwimmer, A. W. Tyler, G. G. Lonzarich, Y. Mori, S. Nishizaki, and Y. Maeno, "Extremely Strong Dependence of Superconductivity on Disorder in Sr_2RuO_4", Phys. Rev. Lett. **80**, 161–164 (1998).

[223]S. Das and I. I. Mazin, "Quantitative Assessment of the Role of Spin Fluctuations in 2D Ising Superconductor $NbSe_2$", Computational Materials Science **200**, 110758 (2021).

[224]O. V. Dolgov, A. A. Golubov, I. I. Mazin, and E. G. Maksimov, "Critical Temperature and the Giant Isotope Effect in the Presence of Paramagnons", Journal of Physics: Condensed Matter **20**, 434226 (2008).

[225]H. Fukuyama and P. A. Lee, "Dynamics of the Charge-Density Wave. I. Impurity Pinning in a Single Chain", Phys. Rev. B **17**, 535–541 (1978).

[226]P. A. Lee and T. M. Rice, "Electric Field Depinning of Charge Density Waves", Phys. Rev. B **19**, 3970–3980 (1979).

[227]Y. I. Joe, X. M. Chen, P. Ghaemi, K. D. Finkelstein, G. A. de la Peña, Y. Gan, J. C. T. Lee, S. Yuan, J. Geck, G. J. MacDougall, T. C. Chiang, S. L. Cooper, E. Fradkin, and P. Abbamonte, "Emergence of Charge Density Wave Domain Walls above the Superconducting Dome in 1T-$TiSe_2$", Nature Physics **10**, 421–425 (2014).

[228]B. Li et al., "Van der Waals Epitaxial Growth of Air-Stable $CrSe_2$ Nanosheets with Thickness-Tunable Magnetic Order", Nature Materials **20**, 818–825 (2021).

[229]Y. Wu, J. He, J. Liu, H. Xing, Z. Mao, and Y. Liu, "Dimensional Reduction and Ionic Gating Induced Enhancement of Superconductivity in Atomically Thin Crystals of 2H-$TaSe_2$", Nanotechnology **30**, 035702 (2018).

[230]J. T. Ye, Y. J. Zhang, R. Akashi, M. S. Bahramy, R. Arita, and Y. Iwasa, "Superconducting Dome in a Gate-Tuned Band Insulator", Science **338**, 1193–1196 (2012).

[231]Y. Ge and A. Y. Liu, "Effect of Dimensionality and Spin-Orbit Coupling on Charge-Density-Wave Transition in 2H-$TaSe_2$", Phys. Rev. B **86**, 104101 (2012).

[232]J.-A. Yan, M. A. D. Cruz, B. Cook, and K. Varga, "Structural, Electronic and Vibrational Properties of Few-Layer 2H- and 1T-$TaSe_2$", Scientific Reports **5**, 16646 (2015).

[233]V. Sunko, E. Abarca Morales, I. Marković, M. E. Barber, D. Milosavljević, F. Mazzola, D. A. Sokolov, N. Kikugawa, C. Cacho, P. Dudin, H. Rosner, C. W. Hicks, P. D. C. King, and A. P. Mackenzie, "Direct Observation of a Uniaxial Stress-Driven Lifshitz Transition in Sr_2RuO_4", npj Quantum Materials **4**, 46 (2019).

[234]P. Kopietz, "Coulomb Gap in the Density of States of Disordered Metals in Two Dimensions", Phys. Rev. Lett. **81**, 2120–2123 (1998).

[235]V. Y. Butko, J. F. DiTusa, and P. W. Adams, "Coulomb Gap: How a Metal Film Becomes an Insulator", Phys. Rev. Lett. **84**, 1543–1546 (2000).

[236]A. Möbius, M. Richter, and B. Drittler, "Coulomb Gap in Two- and Three-Dimensional Systems: Simulation Results for Large Samples", Phys. Rev. B **45**, 11568–11579 (1992).

[237]M. Sarvestani, M. Schreiber, and T. Vojta, "Coulomb Gap at Finite Temperatures", Phys. Rev. B **52**, R3820–R3823 (1995).

[238]A. L. Sharpe, E. J. Fox, A. W. Barnard, J. Finney, K. Watanabe, T. Taniguchi, M. A. Kastner, and D. Goldhaber-Gordon, "Emergent Ferromagnetism near Three-Quarters Filling in Twisted Bilayer Graphene", Science **365**, 605–608 (2019).

[239]C. Wen, J. Gao, Y. Xie, Q. Zhang, P. Kong, J. Wang, Y. Jiang, X. Luo, J. Li, W. Lu, Y.-P. Sun, and S. Yan, "Roles of the Narrow Electronic Band near the Fermi Level in $1T-TaS_2$-Related Layered Materials", Phys. Rev. Lett. **126**, 256402 (2021).

[240]B. Sipos, A. F. Kusmartseva, A. Akrap, H. Berger, L. Forró, and E. Tutiš, "From Mott State to Superconductivity in 1T-TaS_2", Nature Materials **7**, 960–965 (2008).

[241]R. Ang, Y. Tanaka, E. Ieki, K. Nakayama, T. Sato, L. J. Li, W. J. Lu, Y. P. Sun, and T. Takahashi, "Real-Space Coexistence of the Melted Mott State and Superconductivity in Fe-Substituted $1T-TaS_2$", Phys. Rev. Lett. **109**, 176403 (2012).

[242]Y. Yu, F. Yang, X. F. Lu, Y. J. Yan, Y.-H. Cho, L. Ma, X. Niu, S. Kim, Y.-W. Son, D. Feng, S. Li, S.-W. Cheong, X. H. Chen, and Y. Zhang, "Gate-Tunable Phase Transitions in thin Flakes of 1T-TaS_2", Nature Nanotechnology **10**, 270–276 (2015).

[243]R. Ang, Y. Miyata, E. Ieki, K. Nakayama, T. Sato, Y. Liu, W. J. Lu, Y. P. Sun, and T. Takahashi, "Superconductivity and Bandwidth-Controlled Mott Metal-Insulator Transition in $1T$-$TaS_{2-x}Se_x$", Phys. Rev. B **88**, 115145 (2013).

[244]Y. Liu, R. Ang, W. J. Lu, W. H. Song, L. J. Li, and Y. P. Sun, "Superconductivity Induced by Se-Doping in Layered Charge-Density-Wave System 1T-$TaS_{2-x}Se_x$", Applied Physics Letters **102**, 192602 (2013).

[245]P. Fazekas and E. Tosatti, "Electrical, Structural and Magnetic Properties of Pure and Doped 1T-TaS_2", Philosophical Magazine B **39**, 229–244 (1979).

[246]E. Tosatti and P. Fazekas, "On the Nature of the Low-Temperature Phase of 1T-TaS_2", Le Journal de Physique Colloques **37**, C4–165 (1976).

[247]J. Wilson and A. Yoffe, "The Transition Metal Dichalcogenides Discussion and Interpretation of the Observed Optical, Electrical and Structural Properties", Advances in Physics **18**, 193–335 (1969).

[248]T. Ritschel, J. Trinckauf, K. Koepernik, B. Büchner, M. v. Zimmermann, H. Berger, Y. I. Joe, P. Abbamonte, and J. Geck, "Orbital Textures and Charge Density Waves in Transition Metal Dichalcogenides", Nature Physics **11**, 328–331 (2015).

[249]H. Lin, W. Huang, K. Zhao, S. Qiao, Z. Liu, J. Wu, X. Chen, and S.-H. Ji, "Scanning Tunneling Spectroscopic Study of Monolayer 1T-TaS_2 and 1T-$TaSe_2$", Nano Research **13**, 133–137 (2020).

[250]A. J. Bradley, M. M. Ugeda, F. H. da Jornada, D. Y. Qiu, W. Ruan, Y. Zhang, S. Wickenburg, A. Riss, J. Lu, S.-K. Mo, Z. Hussain, Z.-X. Shen, S. G. Louie, and M. F. Crommie, "Probing the Role of Interlayer Coupling and Coulomb Interactions on Electronic Structure in Few-Layer $MoSe_2$ Nanostructures", Nano Letters **15**, PMID: 25775022, 2594–2599 (2015).

[251]F. Di Salvo, R. Maines, J. Waszczak, and R. Schwall, "Preparation and Properties of 1T-$TaSe_2$", Solid State Communications **14**, 497–501 (1974).

[252]J. W. Park and H. W. Yeom, "Atomic Structures and Electronic Correlation of Monolayer 1T-$TaSe_2$", arXiv (2020).

[253]P. W. Anderson, "Localized Magnetic States in Metals", Phys. Rev. **124**, 41–53 (1961).

[254]S. Sasaki and S. Tarucha, "The Kondo Effect Enhanced by State Degeneracy", Journal of the Physical Society of Japan **74**, 88–94 (2005).

[255]W. K. Park, P. H. Tobash, F. Ronning, E. D. Bauer, J. L. Sarrao, J. D. Thompson, and L. H. Greene, "Observation of the Hybridization Gap and Fano Resonance in the Kondo Lattice URu_2Si_2", Phys. Rev. Lett. **108**, 246403 (2012).

[256]D. Newns and N. Read, "Mean-Field Theory of Intermediate Valence/Heavy Fermion Systems", Advances in Physics **36**, 799–849 (1987).

[257]J. Kroha, "Interplay of Kondo Effect and RKKY Interaction", Lecture Notes: Physikalisches Institut, Universität Bonn (2017).

[258]J. Kondo, G. Grüner, and A. Zawadowski, "Prog. Theor. Phys.", (1964).

[259]V. Madhavan, W. Chen, T. Jamneala, M. F. Crommie, and N. S. Wingreen, "Tunneling into a Single Magnetic Atom: Spectroscopic Evidence of the Kondo Resonance", Science **280**, 567–569 (1998).

[260]K. M. Döbrich, A. Bostwick, J. L. McChesney, K. Rossnagel, E. Rotenberg, and G. Kaindl, "Fermi-Surface Topology and Helical Antiferromagnetism in Heavy Lanthanide Metals", Phys. Rev. Lett. **104**, 246401 (2010).

[261]P. Aynajian, E. H. da Silva Neto, A. Gyenis, R. E. Baumbach, J. D. Thompson, Z. Fisk, E. D. Bauer, and A. Yazdani, "Visualizing Heavy Fermions Emerging in a Quantum Critical Kondo lattice", Nature **486**, 201–206 (2012).

[262]A. Schröder, G. Aeppli, R. Coldea, M. Adams, O. Stockert, H. Löhneysen, E. Bucher, R. Ramazashvili, and P. Coleman, "Onset of Antiferromagnetism in Heavy-Fermion Metals", Nature **407**, 351–355 (2000).

[263]P. Coleman, C. Pépin, Q. Si, and R. Ramazashvili, "How do Fermi Liquids get Heavy and Die?", **13**, R723–R738 (2001).

[264]L. Jiao, S. Howard, S. Ran, Z. Wang, J. O. Rodriguez, M. Sigrist, Z. Wang, N. P. Butch, and V. Madhavan, "Chiral Superconductivity in Heavy-Fermion Metal UTe_2", Nature **579**, 523–527 (2020).

[265]V. Vaňo, M. Amini, S. C. Ganguli, G. Chen, J. L. Lado, S. Kezilebieke, and P. Liljeroth, "Artificial Heavy Fermions in a Van der Waals Heterostructure", Nature **599**, 582–586 (2021).

[266]W.-Y. He, X. Y. Xu, G. Chen, K. T. Law, and P. A. Lee, "Spinon Fermi Surface in a Cluster Mott Insulator Model on a Triangular Lattice and Possible Application to $1T-TaS_2$", Phys. Rev. Lett. **121**, 046401 (2018).

[267]P. A. Lee, "An End to the Drought of Quantum Spin Liquids", Science **321**, 1306–1307 (2008).

[268]L. Balents, "Spin liquids in Frustrated Magnets", Nature **464**, 199–208 (2010).

[269]Y. Shimizu, K. Miyagawa, K. Kanoda, M. Maesato, and G. Saito, "Spin Liquid State in an Organic Mott Insulator with a Triangular Lattice", Phys. Rev. Lett. **91**, 107001 (2003).

[270]W. Ruan, Y. Chen, S. Tang, J. Hwang, H.-Z. Tsai, R. L. Lee, M. Wu, H. Ryu, S. Kahn, F. Liou, C. Jia, A. Aikawa, C. Hwang, F. Wang, Y. Choi, S. G. Louie, P. A. Lee, Z.-X. Shen, S.-K. Mo, and M. F. Crommie, "Evidence for Quantum Spin Liquid Behaviour in Single-Layer 1T-$TaSe_2$ from Scanning Tunnelling Microscopy", Nature Physics **17**, 1154–1161 (2021).

[271]K. T. Law and P. A. Lee, "1T-TaS_2 as a Quantum Spin Liquid", Proceedings of the National Academy of Sciences **114**, 6996–7000 (2017).

[272]M. Klanjšek, A. Zorko, R. Žitko, J. Mravlje, Z. Jagličić, P. K. Biswas, P. Prelovšek, D. Mihailovic, and D. Arčon, "A High-Temperature Quantum Spin Liquid with Polaron Spins", Nature Physics **13**, 1130–1134 (2017).

[273]M. Kratochvilova, A. D. Hillier, A. R. Wildes, L. Wang, S.-W. Cheong, and J.-G. Park, "The Low-Temperature Highly Correlated Quantum Phase in the Charge-Density-Wave 1T-TaS_2 Compound", npj Quantum Materials **2**, 42 (2017).

[274]K. Sugiyama, F. Iga, M. Kasaya, T. Kasuya, and M. Date, "Field-Induced Metallic State in YbB_{12} under High Magnetic Field", Journal of the Physical Society of Japan **57**, 3946–3953 (1988).

[275]M. Jaime, R. Movshovich, G. R. Stewart, W. P. Beyermann, M. G. Berisso, M. F. Hundley, P. C. Canfield, and J. L. Sarrao, "Closing the Spin Gap in the Kondo Insulator $Ce_3Bi_4Pt_3$ at High Magnetic Fields", Nature **405**, 160–163 (2000).

[276]K. S. D. Beach, P. A. Lee, and P. Monthoux, "Field-Induced Antiferromagnetism in the Kondo Insulator", Phys. Rev. Lett. **92**, 026401 (2004).

[277]W. L. McMillan, "Time-Dependent Laudau Theory of Charge-Density Waves in Transition-Metal Dichalcogenides", Phys. Rev. B **12**, 1197–1199 (1975).

[278]K. Lee, J. Choe, D. Iaia, J. Li, J. Zhao, M. Shi, J. Ma, M. Yao, Z. Wang, C.-L. Huang, M. Ochi, R. Arita, U. Chatterjee, E. Morosan, V. Madhavan, and N. Trivedi, "Metal-to-Insulator Transition in Pt-doped $TiSe_2$ driven by Emergent Network of Narrow Transport Channels", npj Quantum Materials **6**, 8 (2021).

[279]C. G. Slough, B. Giambattista, A. Johnson, W. W. McNairy, C. Wang, and R. V. Coleman, "Scanning Tunneling Microscopy of 1T-$TiSe_2$ and 1T-TiS_2 at 77 and 4.2 K", Phys. Rev. B **37**, 6571–6574 (1988).

[280]J. Tseng and X. Luo, "First-Principles Investigation of Low-Dimension MSe_2 (M = Ti, Hf, Zr) Configurations as Promising Thermoelectric Materials", Journal of Physics and Chemistry of Solids **139**, 109322 (2020).

[281]B. Singh, C.-H. Hsu, W.-F. Tsai, V. M. Pereira, and H. Lin, "Stable Charge Density Wave Phase in a $1T - TiSe_2$ Monolayer", Phys. Rev. B **95**, 245136 (2017).

[282]K. Sugawara, Y. Nakata, R. Shimizu, P. Han, T. Hitosugi, T. Sato, and T. Takahashi, "Unconventional Charge-Density-Wave Transition in Monolayer 1T-$TiSe_2$", ACS Nano **10**, 1341–1345 (2016).

[283]P. Johari and V. B. Shenoy, "Tuning the Electronic Properties of Semiconducting Transition Metal Dichalcogenides by Applying Mechanical Strains", ACS Nano **6**, 5449–5456 (2012).

[284]M. D. Watson, O. J. Clark, F. Mazzola, I. Markovi ć, V. Sunko, T. K. Kim, K. Rossnagel, and P. D. C. King, "Orbital- and k_z-Selective Hybridization of Se $4p$ and Ti $3d$ States in the Charge Density Wave Phase of $TiSe_2$", Phys. Rev. Lett. **122**, 076404 (2019).

[285]T. Rohwer, S. Hellmann, M. Wiesenmayer, C. Sohrt, A. Stange, B. Slomski, A. Carr, Y. Liu, L. M. Avila, M. Kalläne, S. Mathias, L. Kipp, K. Rossnagel, and M. Bauer, "Collapse of Long-Range Charge Order Tracked by Time-Resolved Photoemission at High Momenta", Nature **471**, 490–493 (2011).

[286]A. Kogar, M. S. Rak, S. Vig, A. A. Husain, F. Flicker, Y. I. Joe, L. Venema, G. J. MacDougall, T. C. Chiang, E. Fradkin, J. van Wezel, and P. Abbamonte, "Signatures of Exciton Condensation in a Transition Metal Dichalcogenide", Science **358**, 1314–1317 (2017).

[287]M.-L. Mottas, T. Jaouen, B. Hildebrand, M. Rumo, F. Vanini, E. Razzoli, E. Giannini, C. Barreteau, D. R. Bowler, C. Monney, H. Beck, and P. Aebi, "Semimetal-to-Semiconductor Transition and Charge-Density-Wave Suppression in 1T-$TiSe_{2-x}S_x$ Single Crystals", Phys. Rev. B **99**, 155103 (2019).

[288]J. Ishioka, Y. H. Liu, K. Shimatake, T. Kurosawa, K. Ichimura, Y. Toda, M. Oda, and S. Tanda, "Chiral Charge-Density Waves", Phys. Rev. Lett. **105**, 176401 (2010).

[289]J.-P. Castellan, S. Rosenkranz, R. Osborn, Q. Li, K. E. Gray, X. Luo, U. Welp, G. Karapetrov, J. P. C. Ruff, and J. van Wezel, "Chiral Phase Transition in Charge Ordered $1T-TiSe_2$", Phys. Rev. Lett. **110**, 196404 (2013).

[290]S.-Y. Xu, Q. Ma, Y. Gao, A. Kogar, A. Zong, A. M. Mier Valdivia, T. H. Dinh, S.-M. Huang, B. Singh, C.-H. Hsu, T.-R. Chang, J. P. C. Ruff, K. Watanabe, T. Taniguchi, H. Lin, G. Karapetrov, D. Xiao, P. Jarillo-Herrero, and N. Gedik, "Spontaneous Gyrotropic Electronic Order in a Transition-Metal Dichalcogenide", Nature **578**, 545–549 (2020).

[291]S. Yan, D. Iaia, E. Morosan, E. Fradkin, P. Abbamonte, and V. Madhavan, "Influence of Domain Walls in the Incommensurate Charge Density Wave State of Cu Intercalated $1T-TiSe_2$", Phys. Rev. Lett. **118**, 106405 (2017).

[292]J. M. Riley, F. Mazzola, M. Dendzik, M. Michiardi, T. Takayama, L. Bawden, C. Granerød, M. Leandersson, T. Balasubramanian, M. Hoesch, T. K. Kim, and Takagi, H; Meevasana, W.; Hofmann, Ph.; Bahramy, M.S.; Wells, J. W.; King, P. D. C., "Direct Observation of Spin-Polarized Bulk Bands in an Inversion-Symmetric Semiconductor", Nature Physics **10**, 835–839 (2014).

[293]J. W. Park, J. Lee, and H. W. Yeom, "Zoology of Domain Walls in Quasi-2D Correlated Charge Density Wave of 1T-TaS_2", npj Quantum Materials **6**, 32 (2021).

List of publications

Articles, which are part of the thesis are marked with a red bullet.

Articles in preparation

- "Magnetic Correlations in the 1T/1H-$TaSe_2$ Bilayer Heterostructure"
- "Charge Density Wave Domain Walls in 1T-$TiSe_2$"
- **Paul Dreher**, Wen Wan, Carmen Gonzalez-Orellana, Max Ilyn, Pierluigi Gargiani, Pablo Ares, Julio Gomez-Herrero, Marco Gobbi, Santiago Blanco-Canosa, Miguel M. Ugeda, "Synthesis and Atomic-Scale Characterization of Self-Intercalated Chromium-Based Selenide Ultrathin Films"

Articles in review process

- Wen Wan, Rishav Harsh, **Paul Dreher**, Fernando de Juan and Miguel M. Ugeda, "Superconducting Dome by Tuning through a Van Hove Singularity in a Two-Dimensional Metal", In review (2022)
- Wen Wan, Darshana Wickramaratne, **Paul Dreher**, Rishav Harsh, I. I. Mazin and Miguel M. Ugeda, "Nontrivial Doping Evolution of Electronic Properties in Ising-Superconducting Alloys", In review (2022)
- W. Wan, **P. Dreher**, D. Muñoz-Segovia, R. Harsh, F. Guinea, F. Juan and M. M. Ugeda, "Observation of Superconducting Leggett Modes from Competing Pairing Instabilities in Single-Layer $NbSe_2$", arXiv (2021)

Published articles

- **P. Dreher**, W. Wan, A. Chikina, M. Bianchi, H. Guo, R. Harsh, S. M. Valero, E. Coronado, A. J. M. Galera, P. Hofmann, J. A. Miwa and M. M. Ugeda, "Proximity Effects on the Charge

Density Wave Order and Superconductivity in Single-Layer $NbSe_2$", ACS Nano 15, 19430-19438 (2021)

- S. Divilov, Wen Wan, **Paul Dreher**, Emre Bölen, Daniel Sanchez Portal, Miguel M. Ugeda and Felix Ynduráin, "Magnetic Correlations in Single-Layer $NbSe_2$", Journal of Physics: Condensed Matter 33, 295804 (2021)

- Francesco Calavalle, **Paul Dreher**, Ananthu P. Surdendran, Wen Wan, Melanie Timpel, Roberto Verucchi, Celia Rogero, Thilo Bauch, Floriana Lombardi, Fèlix Casanova, Marco Vittorio Nardi, Miguel M. Ugeda, Luis E. Hueso, and Marco Gobbi, "Tailoring Superconductivity in Large-Area Single-Layer $NbSe_2$ via Self-Assembled Molecular Adlayers", Nano Letters 21, 1, 136 (2021)

- S. Kezilebieke, Md N. Huda, **Paul Dreher**, I. Manninen, Y. Zhou, J. Sainio, R. Mansell, Miguel M. Ugeda, S. van Dijken, H. P. Komsa, P. Liljeroth, "Electronic and Magnetic Characterization of Epitaxial VSe_2 Monolayers on Superconducting $NbSe_2$", Communication Physics 3, 116 (2020)

- A. O. Fumega, M. Gobbi, **P. Dreher**, W. Wan, C. González, M. Peña, C. Rogero, J. Herrero-Martin, P. Gargiani, M. Ilin, Miguel M. Ugeda, V. Pardo, S. Blanoc-Canosa, "Absence of Ferromagnetism in VSe_2 Caused by Its Charge Density Wave", Journal of Physical Chemistry C 123, 27802 (2019)

- B. Guster, C. Rubio-Verdú, R. Robles, J. Zaldívar, **P. Dreher**, M. Pruneda, J. A. Silva-Guillén, D. J. Choi, J. I. Pascual, M. M. Ugeda, P. Ordejón, and E. Canadell, "Coexistence of Elastic Modulations in the Charge Density Wave State of 2H-$NbSe_2$", Nano Letters 19, 5, 3027 (2019)